TU Delft

Delft University of Technology

Bacterial chromosome organization by ParB proteins

Tišma, M.

DOI
10.4233/uuid:19906f66-bca0-46e6-9af8-584a8ee0a73c

Publication date
2024

Document Version
Final published version

Citation (APA)
Tišma, M. (2024). *Bacterial chromosome organization by ParB proteins*. [Dissertation (TU Delft), Delft University of Technology]. https://doi.org/10.4233/uuid:19906f66-bca0-46e6-9af8-584a8ee0a73c

Important note
To cite this publication, please use the final published version (if applicable).
Please check the document version above.

Copyright
Other than for strictly personal use, it is not permitted to download, forward or distribute the text or part of it, without the consent of the author(s) and/or copyright holder(s), unless the work is under an open content license such as Creative Commons.

Takedown policy
Please contact us and provide details if you believe this document breaches copyrights.
We will remove access to the work immediately and investigate your claim.

This work is downloaded from Delft University of Technology.
For technical reasons the number of authors shown on this cover page is limited to a maximum of 10.

BACTERIAL CHROMOSOME ORGANIZATION BY PARB PROTEINS

BACTERIAL CHROMOSOME ORGANIZATION BY PARB PROTEINS

Dissertation

for the purpose of obtaining the degree of doctor
at Delft University of Technology
by the authority of the Rector Magnificus, Prof.dr.ir. T.H.J.J. van der Hagen
chair of the Board for Doctorates
to be defended publicly on
Thursday 21st March 2024 at 15:00 o'clock

by

Miloš TIŠMA

Master of Science in Molecular Bioengineering, Technische Universität Dresden, Germany
born in Belgrade, Serbia.

This dissertation has been approved by the promotors.

Composition of the doctoral committee:

Rector Magnificus	Chairperson
Prof. Dr. C. Dekker	Delft University of Technology, promotor
Prof. Dr. A. M. Dogterom	Delft University of Technology, promotor

Independent members:

Prof. Dr. B. Rowland	Delft University of Technology
Prof. Dr. R. T. Dame	Leiden University
Prof. Dr. A. Vecchiarelli	University of Michigan, USA
Dr. F. Moreno Herrero	Centro Nacional de Biotecnologia, Spain
Prof. Dr. N. H. Dekker	Delft University of Technology, reserve

Other members:

Prof. Dr. S. Gruber	University of Lausanne, Switzerland







Keywords: Single-molecule Biophysics, Single-molecule fluorescence, In vitro Assays, Magnetic Tweezers, ParABS, Chromosome Segregation, ParB Protein, Supercoiling, DNA Dyes, ParB-ParB Recruitment, DNA Condensation, Live Cell Imaging

Printed by: Proefschrift Specialist

Front & back: Milica Jeličić

Copyright © 2024 by M. Tišma

Casimir PhD Series, Delft-Leiden 2023-30

An electronic version of this dissertation is available at:

http://repository.tudelft.nl

To those who seek not answers
but deeper understanding of the questions.

TABLE OF CONTENTS

1. Introduction to bacterial genome organization 1
1.1 The Why? 2
1.2 Bacterial chromosome organization 2
1.2.1 Physical confinement and crowding 4
1.2.2 Macrodomains 4
1.2.3 Supercoiling 5
1.2.4 Nucleoid-associated proteins 6
1.3 Bacterial chromosome dynamics 7
1.4 Bacterial chromosome segregation 8
1.4.1 Early stages - segregating the origin 8
1.4.2 Late stages - segregating the chromosome terminus and partitioning to daughter cells 9
1.4.3 Late stages – delaying division ring formation 10
1.5 Final thoughts 10
1.6 References 12
2. Connecting the dots: key insights into the ParB protein for chromosome segregation from single-molecule studies 23
2.1 Introduction 24
2.2 Single-molecule techniques to study ParB-DNA interactions 28
2.2.1 Magnetic tweezers: DNA condensation 29
2.2.2 Optical tweezers: *parS* binding and spreading 32
2.2.3 Single-molecule stretching assays: ParB spreading, recruitment, and DNA condensation 33
2.2.4 Atomic Force Microscopy: ParB-ParB bridging 36
2.2.5 Cargo transport assay: ParB-ParA interactions 37
2.3 Future perspectives: ParB interaction partners, ParB variants, and ParB-like proteins 39
2.4 Concluding remarks 41
2.5 References 43
3. Supercoiling-dependent dna binding: quantitative modeling and applications to bulk and single-molecule experiments 53
3.1 Introduction 54
3.2 Results 56
3.2.1 Model for ligand binding under topological constraint 56
3.2.2 DNA supercoiling modulates intercalation 59
3.2.3 Topology dependent binding depends on initial topology and intercalator affinity 60
3.2.4 Psoralen-based DNA crosslinking to detect DNA torsional tension 62
3.2.5 Single-molecule assay monitors supercoiling-dependent binding in real time 64
3.2.6 High-speed fluorescence tracking reveals binding dynamics 66
3.3 Discussion 69

3.4 Materials and methods 71
3.4.1 Plasmid DNA preparation 71
3.4.2 DNA dilution series 71
3.4.3 AFM imaging of DNA plasmids 72
3.4.4 Gel electrophoresis 72
3.4.5 Gel electrophoresis image analysis 72
3.4.6 Bulk fluorescence experiments 73
3.4.7 Single-molecule fluorescence experiments 73
3.4.8 Numerical implementation of the binding model under topological constraint 75
3.5 Supplementary data 77
3.6 References 87
4. ParB proteins can bypass dna-bound roadblocks via dimer-dimer recruitment 97
4.1 Introduction 98
4.2 Results 98
4.2.1 CTP-hydrolysis determines residence of ParB on DNA 100
4.2.2 Diffusing ParB proteins can recruit new dimers onto the DNA 101
4.2.3 *In-trans* ParB-ParB recruitment can overcome DNA-bound roadblocks 103
4.2.4 CTP hydrolysis in ParB-ParB recruitment 105
4.3 Discussion 106
4.3.1 Model of ParB spreading in presence of DNA-bound roadblocks 106
4.4 Materials and methods 109
4.4.1 ParB purification and fluorescent labelling 109
4.4.2 ParBs CTP-hydrolysis assays 109
4.4.3 Biolayer interferometry 110
4.4.4 Construction and purification of 42kb DNA$_{parS}$ construct 110
4.4.5 Preparation and binding dCas9 roadblock to DNAparS 111
4.4.6 Single-molecule visualization assay 111
4.4.7 Crossed DNA$_{parS}$-DNA$_X$ assay 112
4.4.8 Image processing 112
4.4.9 Data analysis of single-molecule imaging traces 112
4.4.10 Modeling the distribution of residence times 114
4.4.11 Fitting of the dwell time distributions 115
4.4.12 CTP hydrolysis rates and ParB dissociation rates 116
4.4.13 Accidental recruitment co-localization simulations 116
4.4.14 Modelling and molecular dynamics simulations 117
4.5 Supplementary data 119
4.6 References 130
5. Dynamic parb-dna interactions initiate and maintain a partition condensate for bacterial chromosome segregation 135
5.1 Introduction 136
5.2 Results 137
5.2.1 ParB proteins condense DNA with a single *parS* site 137

5.2.2 DNA condensation by ParB proteins is dynamic and reversible 140
5.2.3 DNA condensation starts with loop formation 142
5.2.4 CTP hydrolysis at the ParB N-terminal is required for partition complex formation 143
5.2.5 Cooperativity of ParB multimers drives ParB:DNA condensation..... 146
5.2.6 Transcription by RNA Polymerase can occur in the presence of dynamic ParB:DNA clusters 149
5.3 Discussion 152
5.4 Material & Methods 156
5.4.1 ParB purification and fluorescent labeling 156
5.4.2 ParB storage and handling 156
5.4.3 ParBs crosslinking assays 157
5.4.4 Biolayer interferometry assay (BLI) 158
5.4.5 Construction and purification of 42 kbp DNA$_{parS}$ construct and 38 kbp T7A1+parS for fluorescence experiments 158
5.4.6 Single-molecule visualization assay 159
5.4.7 Fluorescence recovery after photobleaching experiments 161
5.4.8 Image processing and analysis 161
5.4.9 Construction of DNA$_{parS}$ construct for atomic force microscopy experiments 163
5.4.10 Atomic force microscopy experiments and imaging 163
5.4.11 Construction of DNA$_{parS}$ construct for Magnetic Tweezers experiments 164
5.4.12 *E. coli* RNAP-biotin, GreB, and σ^{70} purification 165
5.4.13 Magnetic tweezers instrument and experiments 165
5.4.14 Modelling and molecular dynamics simulations 168
5.4.15 Implementation of Dimer-of-Dimers and Multimer-of-Dimers bridging 170
5.5 Supplementary data 171
5.6 References 181
6. Direct observation of a crescent-shape chromosome in bacillus subtilis 189
6.1 Introduction 190
6.2 Results 191
6.2.1 Cell-shape manipulation of *Bacillus subtilis* bacteria 191
6.2.2 Observation of a crescent chromosome *in Bacillus subtilis* in single cells 192
6.2.3 DNA is highly compacted in the origin region 194
6.2.4 BsSMC proteins spread along the entire contour of the crescent chromosome 197
6.2.5 Disruption of the BsSMC complex opens the crescent-shaped chromosome into a toroidal shape 199
6.3 Discussion 201
6.4 Methods 205
6.4.1 Strain construction 205
6.4.2 Bacterial growth conditions 205

6.4.3 Conversion to L-form spheroid cells 206
6.4.4 Fluorescence imaging 206
6.4.5 Solid agar plating assays 207
6.4.6 Growth curves 207
6.4.7 Quantitative RT-PCR on genomic DNA 207
6.4.8 Deconvolution microscopy 208
6.4.9 Structured illumination microscopy imaging 209
6.4.10 Image processing and analysis 209
6.4.11 Chromosome shape selection 211
6.4.12 Chromosomal loci counting – *ori* and *ter* 211
6.4.13 Visualization and representation 211
6.5 Supplementary data 213
6.6 References 229
7. Future perspectives and outlook 237
7.1 Mechanistic insights of ParB closure and dissociation using FRET 238
7.2 ParB interaction and DNA supercoiling 238
7.3 *In vitro* reconstitution of the ParABS system 239
7.4 *In vitro* reconstitution of bacterial SMC loading onto the DNA 239
7.5 *In vivo* investigation of SMC dynamics on bacterial chromosomes 240
7.6 Final outlook 241
7.7 References 242
SAMENVATTING 245
SUMMARY 248
ACKNOWLEDGEMENTS 253
CURRICULUM VITAE 255
LIST OF PUBLICATIONS 257

1

INTRODUCTION TO BACTERIAL GENOME ORGANIZATION

Despite being markedly simpler than their eukaryotic counterparts, bacterial cells embody a remarkable level of organizational complexity that allows their fast propagation and adaptation. Devoid of subcellular compartmentalization into organelles, bacteria have developed many mechanisms of precise cell and chromosome organization within a single cellular compartment. This chapter covers the general principles and players involved in bacterial chromosome organization and segregation. This theme will resonate and be revisited throughout this thesis. Furthermore in this chapter, I will discuss the genome organization studied in standard bacterial model species.

1.1 The Why?

1

"God blessed them. And God said to them, 'Be fruitful and multiply and fill the earth and subdue it, and have dominion over the fish of the sea and over the birds of the heavens and over every living thing that moves on the earth.'" (Genesis 1:28).

And so they did…

Bacteria have evolved to thrive in vastly different environments, essentially colonizing every ecological niche on Earth. While they developed various life strategies, cellular organizations, and DNA sequences, they all adhere to the same goal – replicate and divide. The fundamental principles underlying this prolificacy are rooted in their cellular organization and cell cycle dynamics.

So why study the chromosome organization in bacteria? Studying bacterial cell organization and dynamics not only provides insights into the fundamental principles of cell operations in these ancient systems but also illuminates processes that are mirrored in more complex organisms within the animal kingdom, such as ourselves.

1.2 Bacterial chromosome organization

Bacterial genomes tremendously vary in size in different species, from ~150 000 bp[1] to 15 000 000 bp[2]. Regardless of the species, the physical size of the genome is always many times larger than the bacterial cell that it resides in. To illustrate, consider a model system bacterium *B. subtilis*: it has a genome that is ~1.4 mm in length (~4.2 Mbp)[3], which is confined within the cell of a typical size of ~3 μm. This means that the genome needs to be efficiently packed and condensed up to 1000x to fit into the tiny confines of the bacterial cell. To do this, bacteria have evolved an array of physical and molecular mechanisms to architecturally arrange a large genome within the threedimensional space of the cell. These include physical confinement, formation of macrodomains, DNA supercoiling and DNA-binding proteins that alter the threedimensional structure of the chromosome (Fig. 6.1.1).

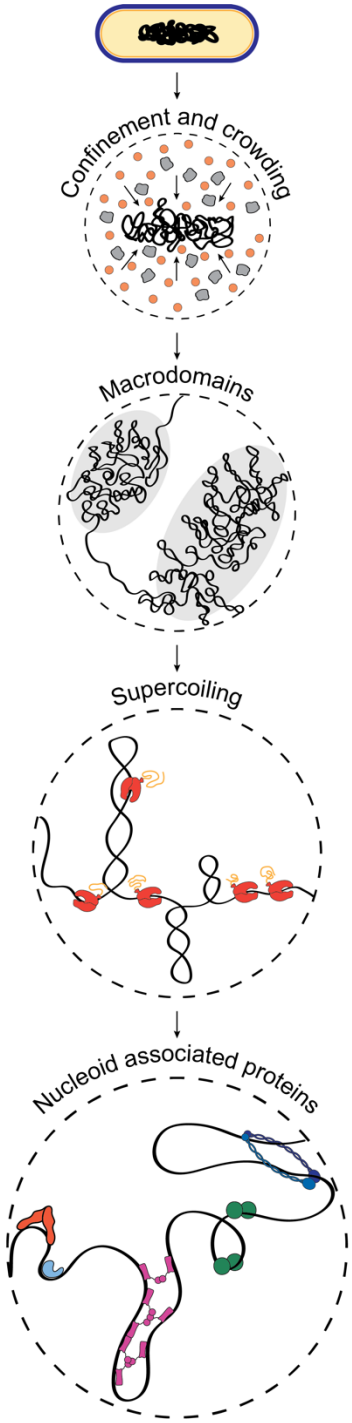


Figure 1.1. Hierarchical bacterial chromosome organization.

1.2.1 Physical confinement and crowding

The most apparent way that bacteria compact their genomes is the confinement of the genome within the bacterial cell. In fact, for a long time bacterial genomes were viewed as unstructured polymers simply confined within the cell membrane of the bacterial cell[4]. This notion was shifted after the initial observations of the bacterial chromosomes, revealing that the chromosome occupies a central volume within the cylindrical cell[4], avoiding regions close to the cell wall or cell poles. The bacterial cell is also full of macromolecular complexes, RNA molecules, proteins, and smaller metabolites essential for its metabolism. These molecules act as molecular crowders[5], which restrict the bacterial chromosome from expanding in 3D[6] and adopting the globular structure typical of an isolated polymer in a simpler solution[7].

1.2.2 Macrodomains

Delving deeper into the structural organization of bacterial chromosomes, the concept of macrodomains emerges. Macrodomains can be visualized as large chromosomal regions, embodying a more organized structure compared to random DNA coils[8-10]. While their exact origin, function, and maintenance are all topics of long-standing research, it is evident that the genome organization in macrodomains is maintained over time in individual cells and in different cells of the same species[11].

In *E. coli* cells, for example, the chromosome is packed in four macrodomains: the origin (Ori), the terminus (Ter), and two chromosomal arms connecting them[8]. The origin and terminus macrodomains represent the beginning and end regions of DNA replication. The Ori macrodomain is where DNA replication initiates, a region rich in A-T sequence that allows initiation proteins easy opening of the two strands and loading of the replication machinery[12]. At the opposite end of the circular chromosome, the Ter macrodomain is where replication finishes, and is equipped with a distinct set of proteins, ensuring the process terminates accurately[13,14]. The two chromosomal arms, spanning between the Ori and Ter macrodomains, contain the bulk of the *E. coli* genome[15]. These arms are not mere passive stretches of DNA; they are condensed yet dynamic entities that allow continuous interactions with various proteins.

Macrodomain organization differs between different bacterial species. Unlike the four macrodomains in *E. coli*, a second prominent model system, *B. subtilis*, has only two distinct macrodomains[16]. The origin region, where replication begins, is highly condensed, making it a distinct entity both structurally and functionally[16]. In contrast, the rest of the chromosome is less condensed and structured. Instead of a rigid, well-defined architecture like in *E. coli*, *B. subtilis* has non-origin chromosomal regions that exhibit less structure and rigididty[16].

While these macrodomains facilitate compartmentalization and localized regulation of the genome, they also possess some degree of flexibility in each species, allowing the chromosome to adapt to various cellular conditions and stresses.

1.2.3 Supercoiling

The next level of compaction comes from the phenomenon termed "supercoiling". DNA molecule is a double-stranded helix that naturally adopts a helical structure. Due to intrinsic molecular interactions, DNA makes a single turn every 10.5 base pairs. If the DNA molecule is twisted more or less than the natural 10.5 bp/turn, DNA becomes twisted which results in changes of the higher-order structure[17] of the DNA but also significantly changes the accessibility to DNA-binding proteins[18]. Overtwisting the DNA, enforcing a turn in the helix that is <10.5 bp results in positive supercoiling. Conversely, undertwisting the helix such that it is >10.5 bp/turn results in negative supercoiling.

Cells exploit both positive and negative supercoiling to fine-tune gene expression[19], but a high presence of supercoiling inadvertently causes genomic instability. Positive supercoiling can obstruct DNA-binding proteins and even halt important cellular machinery like DNA and RNA polymerases[20-22], which could result in DNA breaks or mutations. On the other hand, negative supercoiling can untwist the DNA helix, creating "DNA bubbles" where the two strands separate making them more vulnerable and prone to breakage[23-25]. For this reason, there are many proteins dedicated to specific regulation of the supercoiling levels in bacterial cells[20]. The most prominent sources of positive and negative supercoiling are DNA and RNA polymerases[20,26]. These enzymes move along the DNA by using the energy of nucleotide incorporation into the nascent DNA or RNA strand, respectively[27-29]. In this process, polymerases introduce positive supercoiling downstream of their position and negative supercoiling upstream of their position[30]. While supercoiling caused by RNA polymerases can be used in the regulation of gene expression[19], most of the supercoiling needs to be rapidly removed to avoid potential DNA damage[31]. This is done by topoisomerases – enzymes that can recognize positively or negatively supercoiled DNA and release the tension within the molecule[32,33]. An active introduction of additional supercoiling by the cell requires external energy, and this is catalyzed by the enzymes called – gyrases[34,35]. Gyrases introduce negative supercoils (and thus counteract positive ones) by making controlled double-stranded DNA breaks, releasing the torsional tension, and subsequently ligating the DNA back to its relaxed form[36,37]. To avoid excessive damage during highly abundant processes as RNA transcription, cells predominantly maintain their genomes in a negatively

supercoiled state[38]. This lowers the negative impacts of positive supercoiling that is caused downstream of cellular machinery.

Supercoiling throughout the genome orchestrates the birth of higher-order structures known as plectonemes[38]. These are helically twisted DNA configurations wherein torsional stress in the DNA molecule is dissipated by introducing writhe, causing 3D bends. This process brings distant DNA segments into close proximity. Such arrangements not only help prevent the formation of precarious DNA bubbles but also foster co-regulation proximal of genes[39]. Some genes are ensnared within the same higher-order structure[40], where transcription factors are limited by the plectonemes encompassing these regions and additional proteins that can stabilize these structures[41], likely making them inaccessible for transcription machinery[42,43]. Although a nick in one of the DNA strands can facilitate the relaxation of supercoiling within a plectoneme, it is inadequate to relax the entire chromosome[44]. This observation hints that a chromosome is segmented into multiple topologically distinct supercoiling domains, which are dynamically maintained[44,45].

1.2.4 Nucleoid-associated proteins

At the smallest scale of compaction, bacteria use DNA-binding proteins that can locally as well as globally change the threedimensional structure of the DNA. For example, *E. coli* has multiple nucleoid-associated proteins (NAPs)[46] (i.e., HUα[47], HUβ[48], IHF[49], Fis[50], H-NS[51], Dps[52]), which bind across the entire chromosome, changing its global structure[38]. These proteins can bend, kink, or bridge different DNA regions[38]. While most of the NAPs are not essential to the survival of bacteria under laboratory conditions, they all serve to modulate chromosome organization and gene expression with subtle environmental changes[53]. For example, Fis (Factor for inversion stimulation protein) will be highly expressed and bind the chromosome in exponentially growing bacteria[54], while it will be replaced by Dps (DNA-binding protein from starved cells) when the bacterial culture enters the stationary phase[52,55]. Homologous subunits of HU (Heat unstable) protein – HUα and HUβ, show different expression levels and protein interactions depending on the growth phase of the bacterial culture[56]. In the early stages, HUα forms a homodimer that uniformly covers the chromosome[57], while in the late exponential stage, when the bacterial culture is low on nutrients, HUα and HUβ form a heterodimer, which has stronger DNA affinity[56,58]. These are a few of many examples of regulations where perturbations do not fatally impact cell growth but provide subtle advantages in the environmental conditions that allow the bacterial culture to prosper.

Next to the global regulators, bacteria also employ proteins that locally change the structure of the genome within a specific chromosomal area. A notable example is the

ParB (Partition protein B) of the ParABS system[59]. This protein binds to its recognition site, called – *parS*, found near the origin region[60] and condenses only that fraction of the chromosome[16]. Another example is the H-HS protein which, aside from being a global regulator[61], shows tendencies towards A-T-rich regions within promotor regions[62]. This mode of binding can strongly affect specific genes by forming tight, bridged structures that locally restrict proteins from accessing these promotor regions[41,63].

Bacteria also utilize active motor proteins whose actions significantly alter the threedimensional structure of the chromosome. Most notably are SMC (Structural maintenance of chromosomes) protein complexes that hydrolyze ATP nucleotide as energy to perform loop extrusion on the chromosome[64-66]. SMC proteins span all domains of life[67] and have a conserved structure that is adapted to various cellular processes such as bacterial chromosome segregation[65,66,68], eukaryotic cell division[69], DNA repair[70], homologous recombination[70,71], and many more.

1.3 Bacterial chromosome dynamics

As mentioned, bacteria use various physical mechanisms and protein factors to achieve sufficient chromosome compaction within the bacterial cells. On top of this, bacteria ensure the chromosome is positioned in a specific orientation throughout the cell cycle, to allow sufficient genome access during RNA transcription and DNA replication, as well as faithful chromosome segregation prior to cell division.

Two general modes of chromosome arrangement are recognized throughout the currently studied bacteria: "longitudinal" (i.e., *B. subtilis, C. crescentus*) and "transverse" (i.e., *E. coli*). In longitudinal chromosome arrangement, Ori and Ter macrodomains are positioned towards opposite cell poles[72,73], with chromosomal arms juxtaposed between them[68,74] (often facilitated by the action of SMC proteins[65,75]). In transverse chromosome arrangement, Ori and Ter are positioned close to the cell middle, while the two chromosomal arms are closer to the opposite cell poles[76]. These arrangements are dynamically changing with the changing environment or cell cycle stage[77,78], and are still the subject of ongoing research that questions even the basic paradigms of these two models.

Bacteria further need to accommodate their chromosome compaction and chromosomal arrangement to their dynamic life cycle as bacteria, unlike eukaryotes, do not possess temporal separation of their key processes: DNA replication, chromosome segregation, and cell division. As soon as DNA replication is initiated at the replication origin, the two chromosomes undergo progressive genome segregation in parallel to ongoing DNA replication. While both processes, replication and segregation, need to be finished before the cell division occurs, the division septum formation initiates very early into the

replication process. In fact, different protein factors ensure that the Z-ring formation and the division septum are sufficiently delayed until the chromosomes are segregated[79]. This Chapter further covers the basic principles of chromosome segregation in its early and late stages, and though being dynamically regulated together with cell division, this chapter and thesis will not extensively detail the division process.

A typical picture of the bacterial cell cycle envisions segregating two chromosomes during a binary division, whereas in many species, the number of nascent chromosomes can be significantly higher[80,81]. Therefore, bacteria use different systems that promote accurate and fast chromosome segregation of daughter cells, allowing cell division to occur and leaving every progeny cell with a full chromosome.

1.4 Bacterial chromosome segregation

Bacterial chromosome segregation starts immediately after the replication of the origin region[82]. Simultaneous chromosome replication and segregation is a typical feature of bacterial cell cycle, which ensures a short cell cycle and faster propagation of the progeny. As chromosomes progress in their spatial segregation to the cell poles, different protein factors serve as major drivers in these stages. Therefore we can distinguish **early** and **late stages** of protein segregation, whereby early in the chromosome segregation the chromosomes directionally move to opposite cell poles, while later in the chromosome segregation the chromosome serves as a scaffold for proteins that regulate divisome formation and cell division.

1.4.1 Early stages - segregating the origin

Most bacterial species use ParABS to initiate the segregation of chromosome origins[83]. This system relies on two main protein components - ParA and ParB protein[59]. ParB proteins, mentioned previously, have a role in both chromosome organization and segregation. They bind locally near the origin of replication to condense the DNA[16], which results in the formation of a nucleoprotein structure called a “partition complex” or “segregosome” [84,85]. Unlike ParB, ParA proteins uniformly bind across the chromosome irrespective of the DNA sequence[86] and specifically interact with ParB proteins to support the movement of the partition complex[87,88]. Quickly after the DNA replication initiates, the two nascent origins are specifically recognized by ParB proteins which form two partition complexes, one at each ori[72,89,90]. Both nascent partition complexes will be moved and positioned to the cell poles, dragging the continuously replicating bulk of the chromosome along[90].

In the minority of bacteria (mostly γ-proteobacteria[83]) that do not encode for the ParABS system the chromosomes are segregated using other mechanisms, many of which remain

undescribed. In *E. coli* DNA condensation by the MukBEF complex (a homolog of SMC-complex[91]) increases the fidelity of chromosome segregation[64,92]. Moreover, chromosome segregation is entropically supported by the high confinement of the bacterial cells[93]. With further exploration we will discover not only novel chromosome segregation principles, but also further understand the fundamental requirements for high-fidelity chromosome segregation.

1.4.2 Late stages - segregating the chromosome terminus and partitioning to daughter cells

As the process of DNA replication nears its completion, bacteria simultaneously initiate the cell division process. This means that the two chromosomes must be faithfully separated to ensure the healthy distribution of the genome to daughter cells. These two processes are closely regulated, such the division does not proceed if the chromosomes are not sufficiently separated[94].

The biggest challenge in the final stages of chromosome segregation is resolving concatenated and topologically intertwined chromosomes[95]. Due to the inherent mutation rate of the replication machinery, as well as other cellular processes that cause mutations, DNA breaks and nicks, bacteria face DNA damage that would carry to the new generation. To prevent the propagation of potentially detrimental mutations, bacteria use nascent chromosomes to repair DNA damage at the damaged chromosome[96,97]. However, this repair mechanism can create concatenated or topologically linked chromosomes[98,99], which can fragment and result in multiple dsDNA breaks if forcedly pulled to the cell poles. To ensure the nascent chromosomes are properly separated and ready to segregate, bacteria use a conserved system composed of FtsK-XerCD [95,100,101].

The FtsK protein is an efficient DNA pump that forms at the division ring along with other Fts-proteins[102-105]. It specifically recognizes “KOPS sequences” to bind the DNA[106,107] and uses external energy from ATP to pump the DNA molecules to soon-to-be daughter cells[102]. FtsK works in close relation with XerCD complex[102]. This complex identifies specific loci on the chromosomes known as *dif* sites and undertakes site-specific recombination[98,108,109]. During this process, one of the chromosomes is intentionally cleaved and then re-ligated[110]. This action alters the topology of the two chromosomes. The procedure is executed repetitively until the nascent chromosomes are entirely separated, and the cell division can proceed.

After the chromosomes are fully separated and not topologically linked, chromosome segregation is entropically favored[93]. While this would largely ensure chromosome segregation, bacteria employ different mechanisms to increase the precision of division

ring and septum formation precisely in between nascent chromosomes[111]. Strategies to ensure precise division ring formation are not conserved across bacterial species, as is the case for the FtsK-XerCD system, as these mechanisms support a process such as entropy.

1.4.3 Late stages – delaying division ring formation

In *E. coli* for example, a protein SlmA (Synthetically lethal with a defective Min system protein A) binds along the chromosome and, through a process termed nucleoid occlusion, inhibits the formation of the division ring[112]. This ensures that the division does not proceed across the area where the chromosome is found. In *B. subtilis*, an analogous system employs a protein called Noc (Nucleoid occlusion protein)[113]. Noc displays a distinct binding pattern: it attaches extensively across the chromosomal origin and arms but scarcely in the terminus region[114]. This ensures that the division ring forms where the concentration of Noc is at its lowest. This typically corresponds to the location where the two terminus regions of the forming chromosomes segregate. Some bacteria, such as *C. crescentus*, utilize different nucleoid occlusion strategies by using proteins that directly interact with the ParB partition complex. Such is a protein MipZ (Mid-cell positioning of FtsZ), which forms a gradient from the origin to the terminus, allowing the division ring to form only nearby terminus regions of the chromosomes[115].

Some systems ensure that the division ring is located in the middle of the cell. The MinCDE system in *E. coli* is an example of this, as it oscillates between the cell poles[116,117] and dismantles the division ring formation at the poles[116]. As the cell grows, a depletion region emerges at its center,[116,117] and this is where the division ring formation can occur most efficiently. It is also the region where the chromosomal termini are most likely to segregate, allowing the division ring to form between two chromosomes. Although not present in its entirety in all bacterial species, individual components of this system are present in many bacteria and work in conjunction with other nucleoid occlusion systems or polar protein anchor systems[118].

These and many other undiscovered mechanisms ensure that the cell division occurs such that the nascent chromosomes are partitioned to daughter cells, irrespective or the number and the position of the chromosomes.

1.5 Final thoughts

It is worth noting that each bacterial species adapted to specific environmental needs and conditions and, employs slightly modified systems that differ from that described above. Moreover, many of these systems do not assume a singular role in the complex milieu of the cellular environment. For example, ParA protein is highly involved in the

regulation of the initiation DNA replication[119]. ParB protein is involved in the recruitment of SMC proteins[120-122], nucleoid occlusion by interacting with MipZ[123], nucleoid positioning to the cell pole by interacting with PadC-Bactofilin complex[124,125], or even gene expression[126]. SMC proteins interact with XerCD and modulate each other's activity[127], and FtsK is involved in cell wall synthesis[128] and its regulation[129]. Min proteins are also diverse in their interactions with other proteins such as DivIVA[130], FtsZ[116], MinJ[131,132], et cetera. Interestingly, and likely not serendipitously, MinD is ParA-like protein[133] while Noc is ParB-like protein[113] sharing many similar domains and even enzymatic specificity for ATP[133] and CTP[134] nucleotides, respectively.

This is all testament to the very diverse set of mechanisms that bacteria use to properly organize, replicate and segregate their chromosomes in each division cycle. The focus of this thesis will be investigating the fundamental principles of chromosome organization by detailed investigation of supercoiling, ParABS system (most specifically ParB protein) and SMC effects on the global genome organization. It focuses on *in vitro* or *in vivo* approaches to studying these mechanisms in the model system *B. subtilis* but invokes that future studies should extend to other systems and organisms.

1.6 References

1. Nakabachi, A. et al. The 160-kilobase genome of the bacterial endosymbiont Carsonella. *Science* **314**, 267 (2006).
2. Han, K. et al. Extraordinary expansion of a Sorangium cellulosum genome from an alkaline milieu. *Scientific Reports* **3**, 2101 (2013).
3. Kunst, F. et al. The complete genome sequence of the gram-positive bacterium *Bacillus subtilis*. *Nature* **390**, 249-56 (1997).
4. Piekarski, G. Cytologische Untersuchungen an Paratyphus-und Colibakterien. *Archiv für Mikrobiologie* **8**, 428-439 (1937).
5. Ellis, R.J. Macromolecular crowding: obvious but underappreciated. *Trends Biochem Sci* **26**, 597-604 (2001).
6. Richter, K., Nessling, M. & Lichter, P. Experimental evidence for the influence of molecular crowding on nuclear architecture. *J Cell Sci* **120**, 1673-80 (2007).
7. Holub, M. et al. Extracting and characterizing protein-free megabase-pair DNA for in vitro experiments. *Cell Rep Methods* **2**, 100366 (2022).
8. Boccard, F., Esnault, E. & Valens, M. Spatial arrangement and macrodomain organization of bacterial chromosomes. *Mol Microbiol* **57**, 9-16 (2005).
9. Niki, H., Yamaichi, Y. & Hiraga, S. Dynamic organization of chromosomal DNA in Escherichia coli. *Genes Dev* **14**, 212-23 (2000).
10. Valens, M., Penaud, S., Rossignol, M., Cornet, F. & Boccard, F. Macrodomain organization of the Escherichia coli chromosome. *Embo j* **23**, 4330-41 (2004).
11. Espeli, O., Mercier, R. & Boccard, F. DNA dynamics vary according to macrodomain topography in the E. coli chromosome. *Mol Microbiol* **68**, 1418-27 (2008).
12. O'Donnell, M., Langston, L. & Stillman, B. Principles and concepts of DNA replication in bacteria, archaea, and eukarya. *Cold Spring Harb Perspect Biol* **5**(2013).
13. Dimude, J.U., Midgley-Smith, S.L., Stein, M. & Rudolph, C.J. Replication Termination: Containing Fork Fusion-Mediated Pathologies in Escherichia coli. *Genes (Basel)* **7**(2016).
14. Rudolph, C.J., Upton, A.L., Stockum, A., Nieduszynski, C.A. & Lloyd, R.G. Avoiding chromosome pathology when replication forks collide. *Nature* **500**, 608-11 (2013).
15. Wu, F. et al. Direct imaging of the circular chromosome in a live bacterium. *Nature Communications* **10**, 2194 (2019).
16. Marbouty, M. et al. Condensin- and Replication-Mediated Bacterial Chromosome Folding and Origin Condensation Revealed by Hi-C and Super-resolution Imaging. *Molecular Cell* **59**, 588-602 (2015).

17. Gilbert, N. & Allan, J. Supercoiling in DNA and chromatin. *Curr Opin Genet Dev* **25**, 15-21 (2014).

18. Burns, H. & Minchin, S. Thermal energy requirement for strand separation during transcription initiation: the effect of supercoiling and extended protein DNA contacts. *Nucleic Acids Res* **22**, 3840-5 (1994).

19. Kim, S., Beltran, B., Irnov, I. & Jacobs-Wagner, C. Long-Distance Cooperative and Antagonistic RNA Polymerase Dynamics via DNA Supercoiling. *Cell* **179**, 106-119.e16 (2019).

20. Drlica, K. Control of bacterial DNA supercoiling. *Mol Microbiol* **6**, 425-33 (1992).

21. Lodge, J.K., Kazic, T. & Berg, D.E. Formation of supercoiling domains in plasmid pBR322. *J Bacteriol* **171**, 2181-7 (1989).

22. Pruss, G.J. & Drlica, K. Topoisomerase I mutants: the gene on pBR322 that encodes resistance to tetracycline affects plasmid DNA supercoiling. *Proc Natl Acad Sci U S A* **83**, 8952-6 (1986).

23. Altan-Bonnet, G., Libchaber, A. & Krichevsky, O. Bubble Dynamics in Double-Stranded DNA. *Physical Review Letters* **90**, 138101 (2003).

24. Jeon, J.H., Adamcik, J., Dietler, G. & Metzler, R. Supercoiling induces denaturation bubbles in circular DNA. *Phys Rev Lett* **105**, 208101 (2010).

25. Strick, T.R., Allemand, J.F., Bensimon, D., Bensimon, A. & Croquette, V. The elasticity of a single supercoiled DNA molecule. *Science* **271**, 1835-7 (1996).

26. Peter, B.J., Ullsperger, C., Hiasa, H., Marians, K.J. & Cozzarelli, N.R. The structure of supercoiled intermediates in DNA replication. *Cell* **94**, 819-27 (1998).

27. Hirose, S., Hiraga, S. & Okazaki, T. Initiation site of deoxyribonucleotide polymerization at the replication origin of the Escherichia coli chromosome. *Mol Gen Genet* **189**, 422-31 (1983).

28. Gotta, S.L., Miller, O.L., Jr. & French, S.L. rRNA transcription rate in Escherichia coli. *J Bacteriol* **173**, 6647-9 (1991).

29. Baker, T.A. & Bell, S.P. Polymerases and the replisome: machines within machines. *Cell* **92**, 295-305 (1998).

30. Liu, L.F. & Wang, J.C. Supercoiling of the DNA template during transcription. *Proc Natl Acad Sci U S A* **84**, 7024-7 (1987).

31. Dwyer, D.J., Kohanski, M.A., Hayete, B. & Collins, J.J. Gyrase inhibitors induce an oxidative damage cellular death pathway in Escherichia coli. *Mol Syst Biol* **3**, 91 (2007).

32. Champoux, J.J. DNA topoisomerases: structure, function, and mechanism. *Annu Rev Biochem* **70**, 369-413 (2001).

33. Cheng, B., Zhu, C.X., Ji, C., Ahumada, A. & Tse-Dinh, Y.C. Direct interaction between Escherichia coli RNA polymerase and the zinc ribbon domains of DNA topoisomerase I. *J Biol Chem* **278**, 30705-10 (2003).

34. Cozzarelli, N.R. DNA gyrase and the supercoiling of DNA. *Science* **207**, 953-60 (1980).

35. Gellert, M., Mizuuchi, K., O'Dea, M.H. & Nash, H.A. DNA gyrase: an enzyme that introduces superhelical turns into DNA. *Proc Natl Acad Sci U S A* **73**, 3872-6 (1976).

36. Bates, A.D. & Maxwell, A. Energy coupling in type II topoisomerases: why do they hydrolyze ATP? *Biochemistry* **46**, 7929-41 (2007).

37. Nöllmann, M., Crisona, N.J. & Arimondo, P.B. Thirty years of Escherichia coli DNA gyrase: from in vivo function to single-molecule mechanism. *Biochimie* **89**, 490-9 (2007).

38. Dillon, S.C. & Dorman, C.J. Bacterial nucleoid-associated proteins, nucleoid structure and gene expression. *Nat Rev Microbiol* **8**, 185-95 (2010).

39. Peter, B.J. et al. Genomic transcriptional response to loss of chromosomal supercoiling in Escherichia coli. *Genome Biol* **5**, R87 (2004).

40. Cheung, K.J., Badarinarayana, V., Selinger, D.W., Janse, D. & Church, G.M. A microarray-based antibiotic screen identifies a regulatory role for supercoiling in the osmotic stress response of Escherichia coli. *Genome Res* **13**, 206-15 (2003).

41. Arold, S.T., Leonard, P.G., Parkinson, G.N. & Ladbury, J.E. H-NS forms a superhelical protein scaffold for DNA condensation. *Proceedings of the National Academy of Sciences* **107**, 15728-15732 (2010).

42. Bouffartigues, E., Buckle, M., Badaut, C., Travers, A. & Rimsky, S. H-NS cooperative binding to high-affinity sites in a regulatory element results in transcriptional silencing. *Nat Struct Mol Biol* **14**, 441-8 (2007).

43. Dorman, C.J. H-NS: a universal regulator for a dynamic genome. *Nat Rev Microbiol* **2**, 391-400 (2004).

44. Postow, L., Hardy, C.D., Arsuaga, J. & Cozzarelli, N.R. Topological domain structure of the Escherichia coli chromosome. *Genes Dev* **18**, 1766-79 (2004).

45. Deng, S., Stein, R.A. & Higgins, N.P. Organization of supercoil domains and their reorganization by transcription. *Mol Microbiol* **57**, 1511-21 (2005).

46. Ohniwa, R.L., Ushijima, Y., Saito, S. & Morikawa, K. Proteomic analyses of nucleoid-associated proteins in Escherichia coli, Pseudomonas aeruginosa, Bacillus subtilis, and Staphylococcus aureus. *PLoS One* **6**, e19172 (2011).

47. Rouvière-Yaniv, J. & Gros, F. Characterization of a novel, low-molecular-weight DNA-binding protein from Escherichia coli. *Proc Natl Acad Sci U S A* **72**, 3428-32 (1975).

48. Rouvière-Yaniv, J. & Kjeldgaard, N.O. Native Escherichia coli HU protein is a heterotypic dimer. *FEBS Lett* **106**, 297-300 (1979).

49. Oppenheim, A.B., Rudd, K.E., Mendelson, I. & Teff, D. Integration host factor binds to a unique class of complex repetitive extragenic DNA sequences in Escherichia coli. *Mol Microbiol* **10**, 113-22 (1993).

50. Koch, C. & Kahmann, R. Purification and properties of the Escherichia coli host factor required for inversion of the G segment in bacteriophage Mu. *J Biol Chem* **261**, 15673-8 (1986).

51. Hulton, C.S. et al. Histone-like protein H1 (H-NS), DNA supercoiling, and gene expression in bacteria. *Cell* **63**, 631-42 (1990).

52. Almirón, M., Link, A.J., Furlong, D. & Kolter, R. A novel DNA-binding protein with regulatory and protective roles in starved Escherichia coli. *Genes Dev* **6**, 2646-54 (1992).

53. Hołówka, J. & Zakrzewska-Czerwińska, J. Nucleoid Associated Proteins: The Small Organizers That Help to Cope With Stress. *Front Microbiol* **11**, 590 (2020).

54. Grainger, D.C., Goldberg, M.D., Lee, D.J. & Busby, S.J. Selective repression by Fis and H-NS at the Escherichia coli dps promoter. *Mol Microbiol* **68**, 1366-77 (2008).

55. Ali Azam, T., Iwata, A., Nishimura, A., Ueda, S. & Ishihama, A. Growth phase-dependent variation in protein composition of the Escherichia coli nucleoid. *J Bacteriol* **181**, 6361-70 (1999).

56. Claret, L. & Rouviere-Yaniv, J. Variation in HU composition during growth of Escherichia coli: the heterodimer is required for long term survival. *J Mol Biol* **273**, 93-104 (1997).

57. Claret, L. & Rouviere-Yaniv, J. Regulation of HU alpha and HU beta by CRP and FIS in Escherichia coli. *J Mol Biol* **263**, 126-39 (1996).

58. Tanaka, H., Goshima, N., Kohno, K., Kano, Y. & Imamoto, F. Properties of DNA-binding of HU heterotypic and homotypic dimers from Escherichia coli. *J Biochem* **113**, 568-72 (1993).

59. Jalal, A.S.B. & Le, T.B.K. Bacterial chromosome segregation by the ParABS system. *Open Biology* **10:200097**(2020).

60. Breier, A.M. & Grossman, A.D. Whole-genome analysis of the chromosome partitioning and sporulation protein Spo0J (ParB) reveals spreading and origin-distal sites on the Bacillus subtilis chromosome. *Molecular Microbiology* **64:703-18**(2007).

61. Dame, R.T., Wyman, C. & Goosen, N. H-NS mediated compaction of DNA visualised by atomic force microscopy. *Nucleic Acids Res* **28**, 3504-10 (2000).

62. Navarre, W.W. et al. Selective silencing of foreign DNA with low GC content by the H-NS protein in Salmonella. *Science* **313**, 236-8 (2006).

63. Lang, B. et al. High-affinity DNA binding sites for H-NS provide a molecular basis for selective silencing within proteobacterial genomes. *Nucleic Acids Res* **35**, 6330-7 (2007).

64. Mäkelä, J. & Sherratt, D.J. Organization of the Escherichia coli Chromosome by a MukBEF Axial Core. *Molecular Cell* **78**, 250-260.e5 (2020).

65. Wang, X., Brandão, H.B., Le, T.B.K., Laub, M.T. & Rudner, D.Z. Bacillus subtilis SMC complexes juxtapose chromosome arms as they travel from origin to terminus. *Science* **355**, 524-527 (2017).

66. Wang, X. et al. In Vivo Evidence for ATPase-Dependent DNA Translocation by the Bacillus subtilis SMC Condensin Complex. *Mol Cell* **71**, 841-847.e5 (2018).

67. Kim, E., Barth, R. & Dekker, C. Looping the Genome with SMC Complexes. *Annu Rev Biochem* **92**, 15-41 (2023).

68. Wang, X. et al. Condensin promotes the juxtaposition of dna flanking its loading site in Bacillus subtilis. *Genes and Development* **29**, 1661-1675 (2015).

69. Onn, I., Heidinger-Pauli, J.M., Guacci, V., Unal, E. & Koshland, D.E. Sister chromatid cohesion: a simple concept with a complex reality. *Annu Rev Cell Dev Biol* **24**, 105-29 (2008).

70. Wu, N. & Yu, H. The Smc complexes in DNA damage response. *Cell Biosci* **2**, 5 (2012).

71. Bickel, J.S. et al. Structural maintenance of chromosomes (SMC) proteins promote homolog-independent recombination repair in meiosis crucial for germ cell genomic stability. *PLoS Genet* **6**, e1001028 (2010).

72. Lin, D.C., Levin, P.A. & Grossman, A.D. Bipolar localization of a chromosome partition protein in Bacillus subtilis. *Proc Natl Acad Sci U S A* **94**, 4721-6 (1997).

73. Webb, C.D. et al. Bipolar localization of the replication origin regions of chromosomes in vegetative and sporulating cells of B. subtilis. *Cell* **88**, 667-74 (1997).

74. Le, T.B., Imakaev, M.V., Mirny, L.A. & Laub, M.T. High-resolution mapping of the spatial organization of a bacterial chromosome. *Science* **342**, 731-4 (2013).

75. Tran, N.T., Laub, M.T. & Le, T.B.K. SMC Progressively Aligns Chromosomal Arms in Caulobacter crescentus but Is Antagonized by Convergent Transcription. *Cell Reports* **20**, 2057-2071 (2017).

76. Wang, X., Liu, X., Possoz, C. & Sherratt, D.J. The two Escherichia coli chromosome arms locate to separate cell halves. *Genes Dev* **20**, 1727-31 (2006).

77. Bates, D. & Kleckner, N. Chromosome and replisome dynamics in E. coli: loss of sister cohesion triggers global chromosome movement and mediates chromosome segregation. *Cell* **121**, 899-911 (2005).

78. Wang, X., Llopis, P.M. & Rudner, D.Z. *Bacillus subtilis* chromosome organization oscillates between two distinct patterns. *Proceedings of the National Academy of Sciences of the United States of America* **111**, 12877-12882 (2014).

79. Rowlett, V.W. & Margolin, W. The Min system and other nucleoid-independent regulators of Z ring positioning. *Front Microbiol* **6**, 478 (2015).

80. Angert, E.R. Alternatives to binary fission in bacteria. *Nat Rev Microbiol* **3**, 214-24 (2005).

81. Kaljević, J. et al. Chromosome choreography during the non-binary cell cycle of a predatory bacterium. *Current Biology* **31**, 3707-3720.e5 (2021).

82. Reyes-Lamothe, R., Nicolas, E. & Sherratt, D.J. Chromosome replication and segregation in bacteria. *Annu Rev Genet* **46**, 121-43 (2012).

83. Livny, J., Yamaichi, Y. & Waldor, M.K. Distribution of centromere-like parS sites in bacteria: Insights from comparative genomics. *Journal of Bacteriology* **189:8693-703**(2007).

84. Graham, T.G.W. et al. ParB spreading requires DNA bridging. *Genes and Development* **28:1228–1238**(2014).

85. Murray, H., Ferreira, H. & Errington, J. The bacterial chromosome segregation protein Spo0J spreads along DNA from parS nucleation sites. *Molecular Microbiology* **61**, 1352-61 (2006).

86. Vecchiarelli, A.G. et al. ATP control of dynamic P1 ParA-DNA interactions: a key role for the nucleoid in plasmid partition. *Mol Microbiol* **78**, 78-91 (2010).

87. Marston, A.L. & Errington, J. Dynamic movement of the ParA-like Soj protein of B. subtilis and its dual role in nucleoid organization and developmental regulation. *Molecular Cell* **4:673-82**(1999).

88. Lim, H.C. et al. Evidence for a DNA-relay mechanism in ParABS-mediated chromosome segregation. *eLife* **3:e02758**, e02758 (2014).

89. Glaser, P. et al. Dynamic, mitotic-like behavior of a bacterial protein required for accurate chromosome partitioning. *Genes Dev* **11**, 1160-8 (1997).

90. Lewis, P.J. & Errington, J. Direct evidence for active segregation of oriC regions of the Bacillus subtilis chromosome and co-localization with the SpoOJ partitioning protein. *Mol Microbiol* **25**, 945-54 (1997).

91. Rybenkov, V.V., Herrera, V., Petrushenko, Z.M. & Zhao, H. MukBEF, a chromosomal organizer. *J Mol Microbiol Biotechnol* **24**, 371-83 (2014).

92. Japaridze, A. et al. MukBEF-dependent chromosomal organization in widened Escherichia coli. *Frontiers in Microbiology* **14**, 1107093 (2023).

93. Jun, S. & Mulder, B. Entropy-driven spatial organization of highly confined polymers: Lessons for the bacterial chromosome. *Proceedings of the National Academy of Sciences* **103**, 12388-12393 (2006).

94. Rothfield, L.I. & Justice, S.S. Bacterial cell division: the cycle of the ring. *Cell* **88**, 581-4 (1997).

95. Lesterlin, C., Barre, F.X. & Cornet, F. Genetic recombination and the cell cycle: what we have learned from chromosome dimers. *Mol Microbiol* **54**, 1151-60 (2004).

96. Dillingham, M.S. & Kowalczykowski, S.C. RecBCD enzyme and the repair of double-stranded DNA breaks. *Microbiol Mol Biol Rev* **72**, 642-71, Table of Contents (2008).

97. Smith, G.R. How RecBCD enzyme and Chi promote DNA break repair and recombination: a molecular biologist's view. *Microbiol Mol Biol Rev* **76**, 217-28 (2012).

98. Kuempel, P.L., Henson, J.M., Dircks, L., Tecklenburg, M. & Lim, D.F. dif, a recA-independent recombination site in the terminus region of the chromosome of Escherichia coli. *New Biol* **3**, 799-811 (1991).

99. Steiner, W.W. & Kuempel, P.L. Cell division is required for resolution of dimer chromosomes at the dif locus of Escherichia coli. *Mol Microbiol* **27**, 257-68 (1998).

100. Cornet, F., Louarn, J., Patte, J. & Louarn, J.M. Restriction of the activity of the recombination site dif to a small zone of the Escherichia coli chromosome. *Genes Dev* **10**, 1152-61 (1996).

101. Pérals, K. et al. Interplay between recombination, cell division and chromosome structure during chromosome dimer resolution in Escherichia coli. *Mol Microbiol* **39**, 904-13 (2001).

102. Aussel, L. et al. FtsK Is a DNA motor protein that activates chromosome dimer resolution by switching the catalytic state of the XerC and XerD recombinases. *Cell* **108**, 195-205 (2002).

103. Steiner, W., Liu, G., Donachie, W.D. & Kuempel, P. The cytoplasmic domain of FtsK protein is required for resolution of chromosome dimers. *Mol Microbiol* **31**, 579-83 (1999).

104. Wang, L. & Lutkenhaus, J. FtsK is an essential cell division protein that is localized to the septum and induced as part of the SOS response. *Mol Microbiol* **29**, 731-40 (1998).

105. Yu, X.C., Tran, A.H., Sun, Q. & Margolin, W. Localization of cell division protein FtsK to the Escherichia coli septum and identification of a potential N-terminal targeting domain. *J Bacteriol* **180**, 1296-304 (1998).

106. Bigot, S., Saleh, O.A., Cornet, F., Allemand, J.F. & Barre, F.X. Oriented loading of FtsK on KOPS. *Nat Struct Mol Biol* **13**, 1026-8 (2006).

107. Bigot, S. et al. KOPS: DNA motifs that control E. coli chromosome segregation by orienting the FtsK translocase. *Embo j* **24**, 3770-80 (2005).

108. Blakely, G., Colloms, S., May, G., Burke, M. & Sherratt, D. Escherichia coli XerC recombinase is required for chromosomal segregation at cell division. *New Biol* **3**, 789-98 (1991).

109. Blakely, G. et al. Two related recombinases are required for site-specific recombination at dif and cer in E. coli K12. *Cell* **75**, 351-61 (1993).

110. Castillo, F., Benmohamed, A. & Szatmari, G. Xer Site Specific Recombination: Double and Single Recombinase Systems. *Front Microbiol* **8**, 453 (2017).

111. Wu, L.J. & Errington, J. Nucleoid occlusion and bacterial cell division. *Nat Rev Microbiol* **10**, 8-12 (2011).

112. Bernhardt, T.G. & de Boer, P.A. SlmA, a nucleoid-associated, FtsZ binding protein required for blocking septal ring assembly over Chromosomes in E. coli. *Mol Cell* **18**, 555-64 (2005).

113. Wu, L.J. & Errington, J. Coordination of cell division and chromosome segregation by a nucleoid occlusion protein in Bacillus subtilis. *Cell* **117**, 915-25 (2004).

114. Wu, L.J. et al. Noc protein binds to specific DNA sequences to coordinate cell division with chromosome segregation. *Embo j* **28**, 1940-52 (2009).

115. Thanbichler, M. & Shapiro, L. MipZ, a spatial regulator coordinating chromosome segregation with cell division in Caulobacter. *Cell* **126**, 147-62 (2006).

116. Hu, Z. & Lutkenhaus, J. Topological regulation of cell division in Escherichia coli involves rapid pole to pole oscillation of the division inhibitor MinC under the control of MinD and MinE. *Mol Microbiol* **34**, 82-90 (1999).

117. Raskin, D.M. & de Boer, P.A. Rapid pole-to-pole oscillation of a protein required for directing division to the middle of Escherichia coli. *Proc Natl Acad Sci U S A* **96**, 4971-6 (1999).

118. Barák, I. Open questions about the function and evolution of bacterial Min systems. *Front Microbiol* **4**, 378 (2013).

119. Scholefield, G., Errington, J. & Murray, H. Soj/ParA stalls DNA replication by inhibiting helix formation of the initiator protein DnaA. *Embo j* **31**, 1542-55 (2012).

120. Bock, F.P., Liu, H.W., Anchimiuk, A., Diebold-Durand, M.-L. & Gruber, S. A joint-ParB interface promotes Smc DNA recruitment. *Cell reports* **40**, 111273 (2022).

121. Gruber, S. & Errington, J. Recruitment of Condensin to Replication Origin Regions by ParB/SpoOJ Promotes Chromosome Segregation in B. subtilis. *Cell* **137**, 685-96 (2009).

122. Sullivan, N.L., Marquis, K.A. & Rudner, D.Z. Recruitment of SMC by ParB-parS Organizes the Origin Region and Promotes Efficient Chromosome Segregation. *Cell* **137**, 697–707 (2009).

123. Dubarry, N., Willis, C.R., Ball, G., Lesterlin, C. & Armitage, J.P. In Vivo Imaging of the Segregation of the 2 Chromosomes and the Cell Division Proteins of Rhodobacter sphaeroides Reveals an Unexpected Role for MipZ. *mBio* **10**(2019).

124. Anand, D., Schumacher, D. & Søgaard-Andersen, L. SMC and the bactofilin/PadC scaffold have distinct yet redundant functions in chromosome segregation and organization in Myxococcus xanthus. *Mol Microbiol* **114**, 839-856 (2020).

125. Lin, L., Osorio Valeriano, M., Harms, A., Søgaard-Andersen, L. & Thanbichler, M. Bactofilin-mediated organization of the ParABS chromosome segregation system in Myxococcus xanthus. *Nat Commun* **8**, 1817 (2017).

126. Rodionov, O., ŁObocka, M. & Yarmolinsky, M. Silencing of genes flanking the P1 plasmid centromere. *Science* **283:546–549**(1999).

127. Karaboja, X. et al. XerD unloads bacterial SMC complexes at the replication terminus. *Molecular Cell* **81**, 756-766.e8 (2021).

128. Park, K.-T., Pichoff, S., Du, S. & Lutkenhaus, J. FtsA acts through FtsW to promote cell wall synthesis during cell division in Escherichia coli. *Proceedings of the National Academy of Sciences* **118**, e2107210118 (2021).

129. Veiga, H. et al. Cell division protein FtsK coordinates bacterial chromosome segregation and daughter cell separation in Staphylococcus aureus. *Embo j* **42**, e112140 (2023).

130. Edwards, D.H. & Errington, J. The Bacillus subtilis DivIVA protein targets to the division septum and controls the site specificity of cell division. *Mol Microbiol* **24**, 905-15 (1997).

131. Patrick, J.E. & Kearns, D.B. MinJ (YvjD) is a topological determinant of cell division in Bacillus subtilis. *Mol Microbiol* **70**, 1166-79 (2008).

132. Valenčíková, R., Krascsenitsová, E., Labajová, N., Makroczyová, J. & Barák, I. Clostridial DivIVA and MinD interact in the absence of MinJ. *Anaerobe* **50**, 22-31 (2018).

133. de Boer, P.A., Crossley, R.E., Hand, A.R. & Rothfield, L.I. The MinD protein is a membrane ATPase required for the correct placement of the Escherichia coli division site. *Embo j* **10**, 4371-80 (1991).

134. Jalal, A.S.B. et al. CTP regulates membrane-binding activity of the nucleoid occlusion protein Noc. *Mol Cell* **81**, 3623-3636.e6 (2021).

1

2

CONNECTING THE DOTS: KEY INSIGHTS INTO THE PARB PROTEIN FOR CHROMOSOME SEGREGATION FROM SINGLE-MOLECULE STUDIES

Bacterial cells require highly coordinated DNA segregation machinery to accommodate the division during their life cycle. The most notable system involved in chromosome and plasmid segregation in most bacteria is the ParABS system. A core protein of this system – partition protein B (ParB)- regulates chromosome organization and chromosome segregation during the bacterial cell cycle. Over the past three decades, research has greatly improved our knowledge of the ParABS system. However, many intricate details of the mechanism of ParB proteins have only been uncovered within the last decade using single molecule in vitro approaches. These approaches have served as invaluable tools, allowing exploration of the molecular dynamics of ParB proteins in precisely controlled environments, free from complexities within the cellular milieu. This review covers the early developments but emphasizes recent advances in our knowledge of ParB proteins and their mechanism, as entangled by means of in vitro single-molecule methods. Furthermore, we provide an outlook on future endeavors in investigating ParB, ParB-like proteins, and potentially their interaction partners using powerful in vitro and single-molecule techniques.

This chapter was published as Tišma M, Kaljević J, Gruber S, Le T, Dekker C. *Connecting the dots: key insights into the ParB protein for chromosome segregation from single-molecule studies*. FEMS Microbiology Reviews (2023)

2.1 Introduction

To ensure that both chromosomal and plasmid DNA content is equally distributed to offspring, bacteria utilize partition systems (Par) that maintain the fidelity and precision of DNA segregation. Initially identified in plasmids nearly 40 years ago, partition systems have been shown to be crucial in securing the proper segregation of plasmids during cell division, maintaining their integrity and genes within the bacterial population [1,2]. With the rise of DNA sequencing and comparative genomics, it has become apparent that certain chromosomal regions carry genes with high homology to the plasmid partition systems [3]. The fact that these genes were shown to affect the chromosome dynamics [4,5] suggested that a system once thought to be unique to plasmids could also be integral to segregating chromosomes, primary carriers of genetic information. Phylogenetic lineages of plasmid and chromosomal Par systems showed that these systems likely originated from plasmids via horizontal gene transfer [6], and were later repurposed for chromosomal segregation. Concluding evidence of the similarity between plasmid and chromosomal Par systems came as an essential partition site – *parS* site, was found on the chromosomal DNA [7], which is necessary for loading Par proteins to the DNA. Today, we recognize that the ParABS system is essential for proper functioning of many bacteria. Deletion of this system leads to severe defects and decreased fitness in many species (reviewed by [8]).

The chromosomal ParABS system consists of three key players, ParA and ParB proteins, and a ParB loading site - *parS.* The *parS* sites are typically short (~16 bp), inverted repeats located proximal to the origin of replication [9]. Most bacterial species have between one and four repeats of putative *parS* sites, although this number can rise to 20 or more in some species [10-12].

ParB proteins are relatively small proteins with three distinct domains (Fig. 2.1A). This domain organization is conserved across species. The C-terminal domain (CTD) contains a dimerization surface, whereby two ParB monomers are brought together and reside in a dimeric state in the cells (Fig. 2.1B) [13,14]. The CTD also plays a crucial role in non-specific DNA-binding activities, facilitating ParB spreading and the formation of a nucleoprotein complex [14-16]. This domain is connected via a disordered linker to the Helix-Turn-Helix motif (HTH) that allows for flexibility between the CTD domain and the rest of the protein and that provides for a DNA-storing lumen (Fig. 2.1B). The HTH domain enables ParB to bind specifically to the *parS* sequence [17]. Finally, the N-terminal part of the protein (NTD) is the most highly conserved amongst ParB and ParB-like proteins The N-terminal domain (NTD) has a highly conserved ParA-binding motif (LG-R/K-GL) [18]. Positively charged residues in this motif are crucial for interaction with

ParA and stimulation of ParA ATPase activity [18,19]. Additionally, the NTD features an arginine-rich motif (GERRxRA) (Fig. 2.1A-B). Mutations in this motif significantly impair the protein's function and the overall survival of bacterial cells [12,13,17,20-22].

It was the recent integration of both *in vitro* and *in vivo* research that brought a surprising and transformative insight to light, namely that ParB [23] and ParB-like [24] proteins are CTP hydrolases (unlike the common ATPases and GTPases). These groundbreaking studies demonstrated that the amino acids in the GERRxRA motif directly interact with the CTP nucleotide, which turns out to be a crucial cofactor of ParB protein [23-28]. In fact, the importance of CTP binding has been shown to be a vital functional characteristic across all investigated ParB proteins to date.

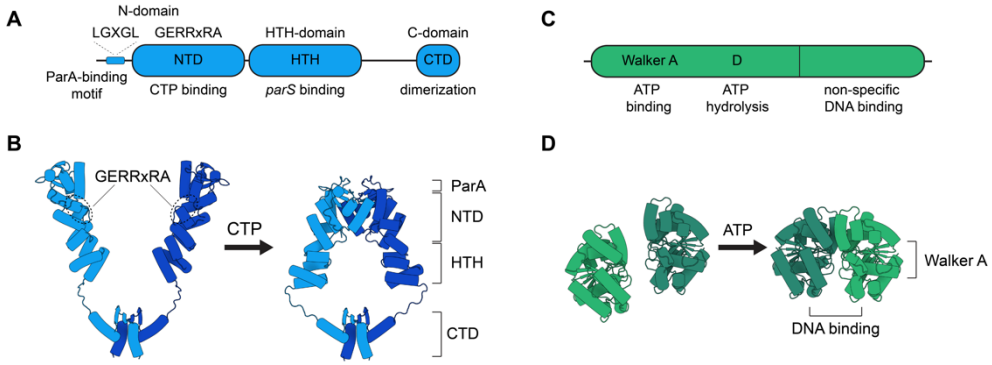


Figure 2.1. Domain architecture and conformational states of ParB and ParA proteins. ***A)*** *The ParB protein is depicted with its three distinct domains: the N-terminal domain, the domain containing the HTH motif, and the C-terminal domain. Functions associated with each domain are noted. The disordered ParA-binding motif containing the LGXGL consensus sequence is represented as a smaller blue box.* ***B)*** *ParB monomers dimerize through CTDs, forming an open clamp configuration. The dashed region represents the CTP-binding pocket containing conserved GERRxRA residues. Upon binding to CTP and parS (not shown), the ParB clamp adopts a closed conformation. Corresponding domains are marked.* ***C)*** *Representation of the ParA protein highlighting its characteristic Walker A motif and a conserved aspartate residue essential for ATP hydrolysis.* ***D)*** *Representation of two ParA monomers that dimerize in the presence of ATP, highlighting the specific motifs involved in this process. The protein part responsible for DNA binding is marked. All structures were obtained using AlphaFold2 [29,30] on UniProt entries P26497 (Spo0J/ParB) and P37522 (Soj/ParA).*

Most importantly, CTP-bound N-terminal domains of two ParB monomers will undergo dimerization, resulting in a clamp formation (Fig. 2.1B) [23,26-28]. Once attached, the clamp enables ParB to be rapidly released from the *parS* site but not disengage from the DNA. Instead, ParB spreads to the neighboring DNA through one-dimensional diffusion while remaining topologically trapped by embracing DNA within the lumen of the clamp. Disengaging from the *parS* site frees this loading site up for new ParB dimers to load, resulting in concentrated ParB localization near the *parS* site. Another important feature of the NTD is a target interface that allows interactions with the SMC (Structural Maintenance of Chromosomes) proteins [31]. This interaction is essential for recruiting SMCs to the *ori* region [32,33], where they initiate the process of macroscale chromosome organization and segregation [34].

ParA proteins are members of the ParA/MinD family of ATPases, as reviewed in [35]. They are identified by a distinct Walker A motif essential for ATP binding. Importantly, ParA proteins often carry basic residues at their C-terminal end, which are pivotal for non-specific DNA binding [36] (Fig. 2.1C). In the presence of ATP, ParA dimerizes, resulting in the entrapment of two ATP molecules at the dimer interface [18]. This dimerization results in the formation of a composite interface for DNA contact, which allows ParA dimers to bind across the entire chromosome non-specifically (Fig. 2.1D). ParA dimer formation and ParA-DNA interaction are modulated by ATP hydrolysis, with the hydrolyzed state causing ParA to revert to a monomeric form and dissociate from DNA into the cytoplasm [37]. While ParA proteins have a basal ATPase activity, ATP hydrolysis is strongly increased via direct interaction with their partners - ParB proteins [38], which is essential for efficient origin segregation to the new cell pole. In some bacteria, ParA proteins are essential for the proper segregation of DNA during cell division, while in others, they may be non-essential while still playing a role in various cellular processes. For instance, in *Bacillus subtilis*, they also affect sporulation [39], DNA replication [40,41], and the organization of DNA through interactions with SMC proteins [42]. These additional roles of ParA are dependent on its ATP/ADP state, indicating that the ParB-ParA interaction orchestrates a broader spectrum of cellular processes than previously understood.

In cells, the core function of ParB protein centers around binding to *parS* sites and achieving a high local concentration (~10 mM [43]) which culminates in the formation of a dense nucleoprotein complex - known as the “partition complex” or “segrosome” (Fig. 2.2) [7,16,21,44,45].

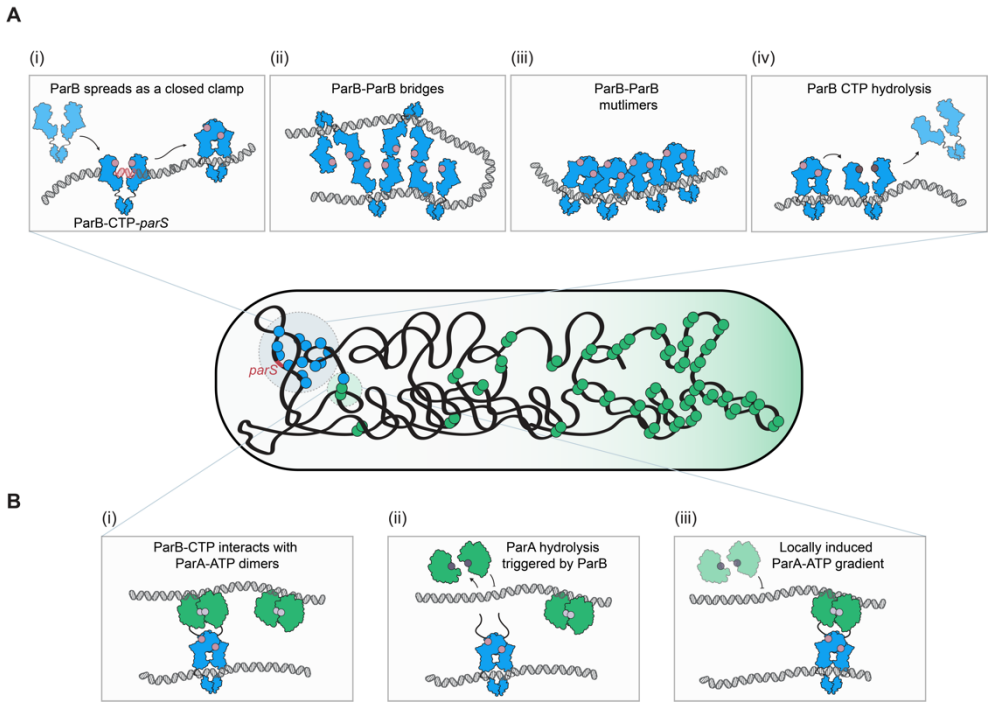


Figure 2.2. Overview of the ParABS system mechanism in chromosome segregation. ***A)*** *Interaction of ParB protein with the parS sequence and formation of the partitioning complex. (i) ParB binds CTP in an "open clamp" configuration and recognizes the parS sequence. A conformational change causes the clamp to close around the DNA upon binding. Once closed, ParB detaches from parS and spreads along the DNA. (ii) Adjacent ParB-CTP molecules bridge using their N-terminal domains, enabling interactions between these DNA-bound ParB dimers. (iii) ParB-CTP further enhance DNA compaction through multimerization. (iv) ParB eventually hydrolyzes CTP to CDP. This action prompts the clamp to revert to its "open" state, leading to ParB's release from the DNA.* ***B)*** *Dynamics of the ParB-parS complex's intracellular movement mediated by the ParA gradient. (i) ParA-ATP dimers bind to the DNA in a non-specific manner. The ParB clamp interacts with the ParA-ATP dimers through its N-terminus. (ii) ParB induces the ATPase activity of ParA-ATP, leading to the hydrolysis of ATP to ADP. Post ATP hydrolysis, the ParA-ADP monomers release from the DNA. (iii) Following the detachment of some ParA dimers, a local gradient of ParA on the DNA is established. This causes the ParB clamp to move on the DNA, interacting with the next available ParA-ATP dimer.*

Recent insights from *in vitro* and *in vivo* studies have underscored the critical role of the CTPase activity of ParB in the formation of this complex [23,25-28,46]. Aside from promoting more efficient binding to the *parS* site and spreading to adjacent DNA (Fig. 2.2A-i), CTP is also involved in ParB multimerization and ParB bridging (Fig. 2.2A-ii, iii), which are essential for the partition complex formation. Several recent studies even postulate that ParB undergoes liquid-liquid phase separation (LLPS), where CTP binding acts as a regulating step for the formation of phase-separated droplets [43,47]. Further, CTP hydrolysis favors the dissociation of ParB from the DNA. This step is important as it recycles ParB proteins, allowing them to repeatedly bind to *parS* sites. This continuous cycle of binding and release maintains a steady presence of ParB near *parS* sites, not allowing the ParB clamps to diffuse too far away from the loading site which is essential for effective chromosome segregation [23,25,28] (Fig. 2.2A-iv).

The partition complex initially forms near the origin of replication. When the origin is duplicated during DNA replication, partition complexes assemble on both origins of the nascent chromosomes. The bidirectional movement required for this separation is driven by the interaction between the ParB-*parS* partition complex and a gradient of ParA proteins (Fig. 2.2) [48]. The ParB-*parS* partition complex interacts with adjacent ParA-ATP, stimulating ParA's ATPase activity (Fig. 2.2B-i). This catalytic activity leads to the hydrolysis of ATP to ADP, causing ParA-ADP monomers to detach from the DNA (Fig. 2.2B-ii) [49-51]. The ParA-ADP monomers are temporarily inhibited from DNA binding due to a kinetic time delay, providing a time window before they can rebind ATP and, subsequently bind the DNA [52,53]. Together with ParB-stimulated ATP hydrolysis, this delay establishes a local gradient of ATP-bound ParA, with regions of higher concentration distant from the ParB-*parS* complex. ParB-*parS* complex starts directionally moving towards areas of higher ParA concentration (Fig. 2.2B-iii). This ParB directional movement has been explained by several models: diffusion-ratchet model [48], DNA relay model [54], and the hitch-hiking model [55]. In all models, as the complex moves, it continues to engage with ParA, ensuring consistent ATP hydrolysis and the maintenance of local gradient ParA-ATP [54,56,57]. This intricate mechanism drives the replicated chromosome directionally across the cell, ensuring effective chromosome segregation before the cell divides.

2.2 Single-molecule techniques to study ParB-DNA interactions

The *in vivo* studies provided a foundational understanding of the ParABS system and its effects on chromosome integrity in various bacterial species. Research on ParB in living cells spotlighted critical steps of its action: binding to a specific DNA sequence (*parS*),

forming a partition complex (seen as a bright foci under the microscope), and a directional movement towards the new cell pole following replication [58-60]. Subsequent efforts from biochemical studies further increased our understanding of ParB mechanism by unveiling its CTPase activity [23-25] and the detailed mechanics of clamp closure upon interaction with the *parS* site [26-28]. These studies posed new questions on the mechanistic details of these proteins in the presence of their indispensable co-factors.

In this context, *in vitro* single-molecule studies have emerged as a vital complementary approach to address mechanistic questions on the ParABS system, offering highly controlled conditions that can shed light onto the ParB behavior and its interaction with associated proteins. The primary objective of this review is to cover the new insights into the ParB mode of action that was recently obtained from single-molecule *in vitro* studies. We discuss the results on the ParABS system from a range of methodologies, paving the way for future experiments that may address open questions in ParB research.

2.2.1 Magnetic tweezers: DNA condensation

Initial observations of ParB proteins localizing at a very small area of the chromosome raised hypotheses of the protein inducing local condensation of the DNA [61]. Magnetic tweezers (MT) proved instrumental in investigating these phenomena due to their real-time ability to observe DNA condensation. In a typical MT experiment, a DNA molecule of interest is tethered between a glass surface with one of its ends and a micron-size magnetic bead at its other end (Fig. 2.3A). Using magnets positioned above the bead, one applies a constant force on the molecule, and thus MT function as a force clamp where DNA is stretched to a certain length. If a DNA-binding protein affects the conformation of the DNA, the length change can be precisely measured (Fig. 2.3A). This is done by observing the size and the pattern of the diffraction rings around the magnetic bead as it moves downwards, out of the z-plane. These patterns can be converted very precisely (with a resolution of a few nm) to the position of the bead [62]. MT is a label-free technique that offers a way to study protein-DNA interaction devoid of any extra modifications on the protein, which potentially might cause a change in its physiological behavior. MT can be highly parallelized, allowing measurements of thousands of beads in parallel [63,64]. While direct visualization of protein binding or clustering is challenging due to the absence of protein labels, it is possible to visualize protein in MT by combining fluorescence microscopy and MT, but this involves rather complex setups [65].

First studies of ParB proteins in MT [66], done in the absence of CTP, showed that very high concentrations (1 μM) of ParB proteins were required to promote DNA condensation both in the presence and absence of a *parS* site on the DNA (Fig. 2.3B). Further studies with truncated and mutated proteins showed that some *B. subtilis* ParB

proteins employ specific Lys residues at the C-terminal dimerization domain of the protein, which are necessary for non-specific DNA binding and condensation [14]. Mutations of these residues caused severe defects in partition complex formation *in vivo*, just as proposed by the MT results, underscoring the potent synergy achieved when combining *in vivo* and *in vitro* approaches in understanding complex biological processes [14].

Following the discovery of the CTP binding and hydrolase activity of ParB proteins [23,24], MT were again used for studying the real-time DNA condensation by ParB proteins at single-molecule level. These experiments showed that DNA condensation can occur at much lower concentrations of ParB (10 nM) in the presence of CTP nucleotide, and they also showed a strong dependence on the presence of a *parS* site [67,68] (Fig. 2.3C). The stark contrast to the previous findings [14,66] likely was due to the larger loading rate of ParB proteins onto the DNA in the presence of CTP and *parS* [23-25]. MT also allowed fast screening of different buffer conditions, which showed the necessity of the presence of Mg^{2+} ions and a high specificity for DNA condensation only in the presence of CTP and not other nucleotides (GTP, ATP, UTP) [67].

With a precise measurement of DNA length and forces in the MT setup, it was shown that ParB proteins could effectively condense DNA molecules only when the forces on the DNA were reduced to the range of 0.2-0.6 pN [67,69]. This is a low force range compared to the forces exerted by single motor proteins such as RNA polymerases (25 pN, [70], DNA translocases (29 pN, [71]) or helicases (50 pN, [72]). This shows that the ParB-DNA cluster involves weak interactions that are easily disrupted by external forces. Indeed, subjecting the condensed ParB-DNA cluster to external forces of 5 pN resulted in gradual de-condensation of the cluster over the course of 1-1.5min [68]. Interestingly, de-condensation was also shown to be highly dependent on the presence of CTP, whereby in the absence of the nucleotide, ParB-DNA clusters decondensed even faster, within 5s [68]. Similar effects were also observed in bulk assays, whereby the presence of CTP or non-hydrolyzable CTP analog (CTPγS) significantly extended the release time of ParB proteins from the DNA [26,28].

Further MT experiments showed that a single *parS* site is sufficient for ParB molecules to condense the DNA [69]. Conformational changes in ParB proteins were found to be necessary to condense the DNA efficiently: by using crosslinking mutants that prevent clamp opening (such as Fig. 2.2A-iv), it was shown that ParB proteins cannot condense DNA efficiently when N-terminal domains are crosslinked after loading onto the DNA [69]. Conversely, when the C-terminus of the ParB protein was crosslinked, there was no effect on the condensation dynamics. Using non-hydrolyzable CTPγS or a non-

hydrolyzing mutant protein (ParB^{E111Q} in *B. subtilis* that forces the ParB clamp into a prolonged closed state [26]) failed to promote an efficient DNA condensation (akin to Fig. 2.2A–ii) [69].A modified version of MT where the magnetic bead is not directly attached to the DNA, but rather to RNAP which was loaded onto the DNA [73], was used to test the effect of a ParB:DNA cluster on a transcribing RNAP [69]. Interestingly, the presence of the ParB condensate did not affect the RNAP processivity and only had a slightly reducing effect on the average transcription speed.

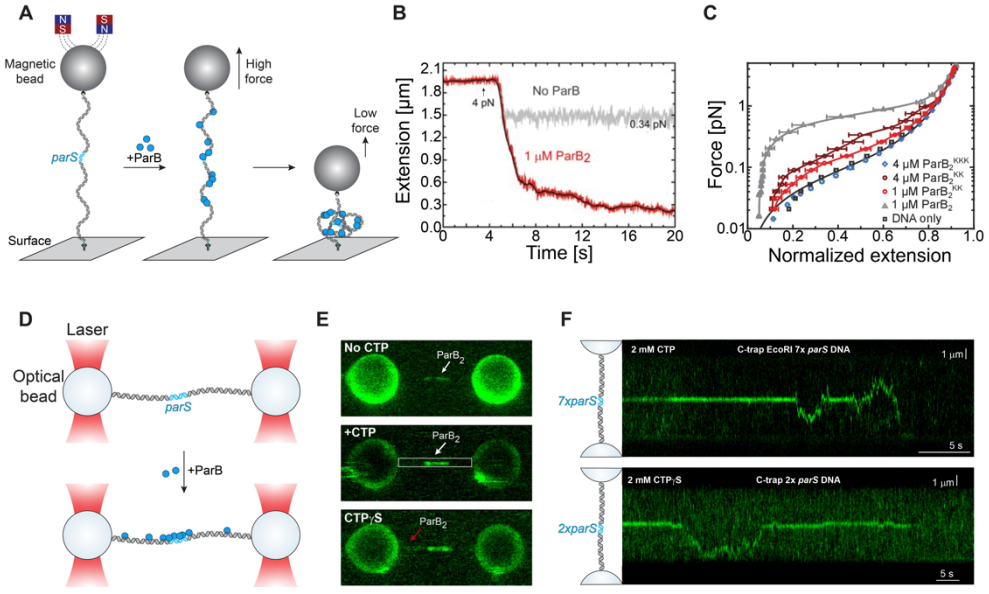


Figure 2.3. Force spectroscopy tweezers techniques for investigating ParB proteins. ***A)*** *Magnetic tweezers setup. Schematics of a typical experiment where the DNA is held stretched at high force (~5 pN) during the addition of ParB proteins, and then released to low forces, whereupon condensation occurs.* ***B)*** *A MT setup was used measure the DNA-condensation in the presence of ParB in real-time. Adapted from [66].* ***C)*** *Force extension measurements of wild type ParB$_{Bsub}$ in comparison to different Lys mutants at the C-terminal domain interface. Adapter from [14].* ***D)*** *Optical tweezers setup. Two optical beads are trapped using focused laser beams, with a DNA molecule stretched between them. Upon moving these beads to another channel with ParB proteins, coverage of the loading site and adjacent regions will occur.* ***E)*** *OT was used for visualization of ParB binding to parS proximal region in the absence and presence of CTP/CTPgS nucleotides. F) Single-particle tracking of one-dimensional diffusion by ParB proteins. E,F adapted from [67].*

This suggests that the gene repression effects of ParB that were reported previously [74-80] likely act on access of the RNAP to the promotor, rather than being due to halting or blocking a transcribing RNAP.

Taken together, MT provided valuable knowledge of the underlying mechanism and requirements for DNA condensation by ParB proteins, which were inaccessible (or laborious to test) in *vivo*. There are many options to expand this type of experiment. Its capacity for swiftly testing various conditions (like nucleotides, salts, and loading site numbers) makes it an easily accessible and useful technique. MT can for example be utilized to test the interaction of ParB with supercoiled DNA molecules [68], or multiple DNA molecules can be tethered to the bead. Cross-testing chromosomal or plasmid ParB proteins from different species and ParB-like proteins would be the next step in learning about the generality of the DNA-condensation process in chromosome segregation and plasmid partitioning.

2.2.2 Optical tweezers: *parS* binding and spreading

Optical tweezers (OT) also stand out as a useful tool, offering a complementary approach to magnetic tweezers (MT) for studying ParB proteins, as they enable direct visualization of ParB protein on the DNA while also allowing for adjustable forces to be applied to the DNA. In OT, functionalized micron-size beads are trapped using a highly focused laser, thus providing a position clamp. A typical OT experiment starts by trapping two beads within a microfluidic channel and ensuring the attachment of a single DNA molecule between them (Fig. 2.3D). These beads connected by DNA are moved within the microfluidic channels where, through laminar flow and multiple wells, a constant supply of various buffers and conditions can be maintained. Individual beads can be moved independently allowing the application of a stretching force to the tethered DNA molecule. Importantly both the DNA and the proteins can be labelled using fluorescent dyes, which allows visualization of both components using confocal microscopy. This enables direct, single-molecule observation and timelapse tracking of all phenomena exhibited by the investigated proteins (Fig. 2.3E). While OT is beneficial for direct visualization, it also faces challenges. Notably, its low throughput poses a significant constraint for testing many molecules. A typical experiment involves recording one molecule at a time under distinct conditions. Furthermore, extended exposure to laser illumination can induce DNA breakage, hindering extended data acquisition. Moreover, OTs typically operate at higher forces (1-100 pN) and will have a low signal-to noise ratio for conditions under which ParB proteins can efficiently condense the DNA (0.01 - 0.5 pN).

Yet, OT has been used to study the binding and spreading of ParB proteins in the presence of CTP and *parS* sites. In fact, it allowed the first single-molecule traces of diffusing ParB proteins to be visualized [67] (Fig. 2.3F). Due to CTP hydrolysis and dissociation of ParB proteins from the DNA, many traces could be acquired using a single DNA molecule. This allowed the quantification of the diffusion coefficient for *B. subtilis* ParB protein (0.41±0.02 $\mu m^2/s$), which showed that these proteins, experience similar dynamics as common DNA-binding proteins during their target search phase when they are non-specifically attached to the DNA [81,82]. Guo et al. reported that ParB proteins can connect and traverse as multimers – a previously undescribed mode of movement, especially in the presence of CTP [83]. Additionally, OT experiments allowed the quantification of ParB spreading on the DNA in real time. By incorporating multiple *parS* sites in a linear DNA construct, Balaguer et al. observed a substantial increase in the signal near the *parS* sites and the neighboring regions, offering one of the first visualizations of ParB spreading [67]. Moreover, they reported that ParB diffusion on stretched DNA molecules can be blocked by a strongly attached DNA-binding protein (an inactive $EcoRI^{E111Q}$).

Several recent studies have postulated that plasmid and chromosomal ParB proteins undergo LLPS on DNA [43,47], whereby the *parS* site would initiate the binding by ParB proteins, which would attract multiple new ParB proteins to that position and locally induce droplet formation. OT represents a suitable system for testing this, as it potentially may distinguish between the two most prominent types of phase separation – liquid-liquid phase separation and bridging-induced phase separation. With the ability to stretch the DNA and thus vary the force, the necessity for a DNA scaffold in the phase-separated droplet can be tested and quantified.

2.2.3 Single-molecule stretching assays: ParB spreading, recruitment, and DNA condensation

Single-molecule stretching assays allow scientists to directly visualize interactions and dynamics of ParB proteins on DNA. These techniques rely on DNA molecules that are stretched along a PEGylated or lipid-coated surface, where they covalently attach either with one [84] or with both DNA ends [85] to the surface (Fig. 2.4). In single-end tethering with typically many DNA molecules in parallel ("DNA curtains" [86], or "PIFE" – protein-induced fluorescence enhancement [87]), molecules have one loose end and are maintained in the stretched state by a continuous flow (Fig. 2.4A). When the DNA is tethered with both ends to the surface [85], the effect of proteins on the DNA can be observed without an applied flow. In these setups, DNA and proteins can simultaneously be labeled and tracked with a high signal-to-noise ratio using TIRF or HILO microscopy. A strong

advantage of these techniques is that many DNA molecules can be imaged simultaneously. A disadvantage, however, is low spatial resolution (~300 nm) and the inability to control the force on the DNA with a knob, such as in MT or OT.

Early experiments with single-end tethered DNA molecules in OTs provided direct confirmations of DNA condensation by ParB proteins [21]. These data showed the intriguing propensity of ParB proteins to progressively condense DNA molecules across a spectrum of chromosomal (*B. subtilis, S. pneumoniae, P. aeruginosa, V. cholerae*) and plasmid ParB proteins [21] (Fig. 2.4B-C). Interestingly, the condensation occurred only from the free DNA end, where the stretching force approximated zero (or very low values), rather than continuously over the DNA molecule. This raised hypotheses that ParB proteins condense the DNA by stabilizing large DNA loops since the regions stretched at higher forces, close to the tether point, were condensed last. Subsequently, the same assay was used for detailed screening of the amino-acid residues involved in bridging interactions and condensation [20]. Many residues present in the N-terminal domain of ParB from *B. subtilis* were shown to be crucial for DNA condensation as when mutated (R39A, H57E, L60E, R79A, R80A, R82A, R105E), this ability was entirely lost even at very high protein concentrations (300 nM). The lack of *in vitro* condensation was consistent with *in vivo* data that showed a complete absence of a fluorescent focus or diffuse protein signal in most cases [20]. While these results were obtained before discovering a CTP requirement for the clamping mode of DNA loading by ParB proteins [23,24], they were helpful to identify residues that may play a role in bridging interactions in the post-hydrolysis open protein state. Following the discovery of the CTP hydrolase activity of ParB and increased interest in single-molecule studies, the same DNA curtains assay was used to test the effects of common protein tags on the ParB function by screening a high number of conditions and mutants [88].

A different type of DNA stretching assay features single DNA molecules that are tethered to the surface at both ends [85] (Fig. 2.4D). This assay can use torsionally constrained DNA molecules that contain supercoiling within the molecule, thus allowing the study of ParB proteins on supercoiled DNA, although most experiments are done on torsionally relaxed (i.e. nicked) DNA. This assay was initially used to demonstrate the ParB loading and spreading from *parS* sites in the presence of CTP molecules [23]. Adding roadblocks ($EcoRI^{E111Q}$) flanking the *parS* site was shown to efficiently block the diffusion of ParB proteins and restrict the localization to within the region between the two roadblocks.

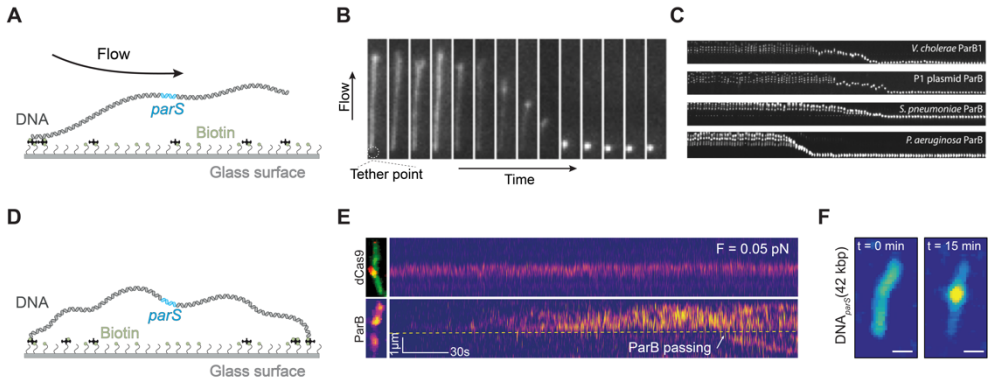


Figure 2.4. Single-molecule stretching assays for real-time observation of DNA condensation by ParB. A) *DNA stretching assay using single-tethered molecules with high flow.* ***B-C)*** *This assay was used for initial real-time imaging of DNA condensation in multiple ParB variants. Adapted from* [21]. ***D)*** *DNA stretching assay using double-tethered molecules without flow.* ***E)*** *This assay was used to show ParB-ParB recruitment over a DNA-roadblock in real-time* [46] *and* ***F)*** *DNA condensation in the presence of CTP* [89].

A similar assay, but with a longer (42 kbp) DNA molecule, was used to show single diffusing ParB molecules and quantify the diffusion coefficient (0.06 ± 0.01 $\mu m^2/s$ for $ParB_{Bsub}$ [46], which matched the *in vivo* single particle tracking of ParB proteins within the partition complex [43]. This assay enabled measuring the residence times of ParB molecules (~76 s) [46]. Interestingly, the residence times showed a non-exponential distribution, unlike standard protein-DNA interactions, which pointed to the hypothesis that a loaded ParB dimer needs to hydrolyze both CTP molecules before dissociating from the DNA [46]. This result is an example of the power of the single-molecule technique to reveal intricate mechanistic details of the ParB mechanism. Using direct visualization, Tišma et al. observed that ParB dimers loaded on *parS* can additionally recruit new ParB dimers to a genomic location distant from *parS* by *in-trans* recruitment [46] (Fig. 2.4E), which was an unexpected finding that went beyond the common wisdom that ParB only loads at the *parS* site. This allowed ParB proteins to efficiently spread on the linear DNA molecules even in the presence of firmly bound DNA roadblocks, since, at low forces, spatial fluctuations in the DNA allow ParB to recruit new ParB at a faraway genomic location beyond the roadblock.

The double-tethered DNA molecules also provided a robust framework for probing the DNA condensation process (Fig. 2.4F). Weakly stretched molecules allowed observation

of the high dynamics of DNA condensation whereby the ParB-DNA cluster showed continuous fluctuations in the amount of DNA contained within it [69]. These data also allowed quantification of the stalling force of the growing ParB-DNA cluster (0.2 pN)[69].

Summing up, single-molecule stretching assays have emerged as a powerful tool for visualizing the behavior of a single (or low number of) ParB protein(s) on a single DNA molecule. It allows observing behaviors that cannot be measured *in vivo* or in bulk biochemical assays. Looking forward, these assays can for example be used for a variety of ParB-related proteins on DNA, or to study the interaction of ParB with supercoiled DNA, which is highly abundant in *in vivo* settings both near the chromosome origin and plasmid DNA.

2.2.4 Atomic Force Microscopy: ParB-ParB bridging

Atomic Force Microscopy (AFM) is a single-molecule technique that offers the highest spatial resolution for studying ParB-DNA interactions. The method deploys a cantilever with a pointed tip to scan the surface where the tip deflections are translated into a 3D image of the surface at a nanometer resolution (Fig. 2.5A). In addition to nanometer resolution, AFM allows studying ParB and DNA interactions without additional labeling of the molecules. AFM can either capture static images of the molecules on the surface (dry AFM) or dynamic behavior in liquid where the molecules are weakly attached to the surface (high-speed AFM – hsAFM). Interpreting AFM images demands caution due to the potential impact of surface interactions on the process of DNA binding by ParB proteins. While hsAFM, with its swiftly scanning tip, can compile high-resolution images, the tip interactions with the molecules of interest can also influence the dynamics. Finally, in the case of dry AFM, deposited molecules can adopt artificial conformations during surface attachment and sample drying.

In exploring the structure of the ParB:DNA condensate, Balaguer et al. used AFM to show that the *parS* site and CTP significantly increased ParB binding to the DNA [67] (Fig. 2.5B). ParB-DNA structures showed condensed conformations with a high density of proteins around the plasmid DNA [67]. This was confirmed in the subsequent study [69] and extended to study the initiation of the ParB-DNA condensate formation using hsAFM. ParB loading and bridging dynamics were imaged at high spatial and temporal resolution. It was shown that ParB proteins initiate complex formation by forming transient loops which persist for ~50 s, slightly less than the proteins' residence time on the DNA [46] (Fig. 2.5C).

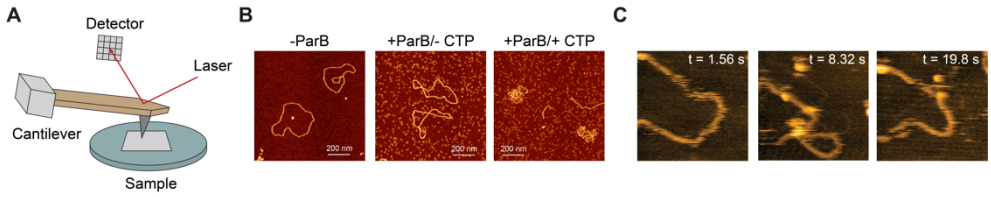


Figure 2.5. Atomic force microscopy allows high-resolution imaging of ParB-DNA complexes. A) *Atomic force microscopy setup.* ***B)*** *AFM was used to obtain high-resolution images of the ParB-DNA complex in the presence of the parS site and CTP nucleotide. Adapted from* [67]. ***C)*** *High-speed liquid-cell AFM was used for real-time visualization of the transient loop formation by DNA-bound ParB proteins* [89].

Further insight into the early and late stages of ParB:DNA condensate formation would benefit from using high-resolution techniques. HsAFM has the spatial and temporal resolving power for studying highly dynamic DNA-protein interactions, capturing transient and short-lived states that conventional techniques might miss. This is especially important when investigating processes like DNA binding, looping, and condensation mediated by ParB. Observing the condensation process in its entirety, from ParB loading to fully condensed ParB-DNA cluster could further shed light on the mechanics of this process.

2.2.5 Cargo transport assay: ParB-ParA interactions

While the previously described techniques offered great progress in studying ParB proteins, the ParABS system in its entirety has been less explored. However, visualization of all the components of the system has been done using a "cargo transport assay" [56,57,90]. Here, a standard TIRF setup images a glass surface that is covered by a 'DNA carpet', where, in the presence of ATP, ParA proteins efficiently bind non-specifically to the DNA-carpet (Fig. 2.6A) [56]. This ParA-DNA surface can now be used as a mimic of the bacterial nucleoid to study the interaction of ParB-plasmid complexes [56,57]. A caveat of such systems is that the plasmids or beads will only briefly interact with the surface before diffusing away. Also, when investigating ParB-plasmid complexes, inadvertently large plasmid clusters form which are dissimilar to a controlled single molecule setup or *in vivo* scenario. In an attempt to circumvent these issues, magnetic beads were used which could be attracted to the surface for a long time at very low force (~5 fN) and do not show large aggregates seen when using a plasmid substrate [90].

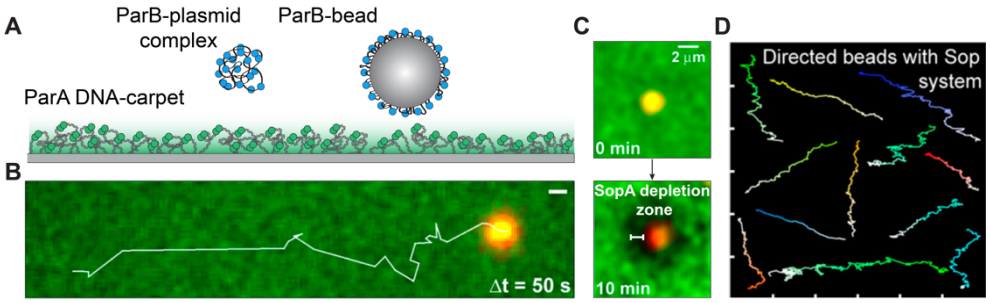


Figure 2.6. Cargo transport assay achieves studying of all components of ParABS system in real-time. A) *Schematic representation of cargo transport assay. The surface is covered with DNA molecules which are bound by ParA-ATP proteins. Condensed plasmids containing a parS site, or magnetic beads carrying parS-DNA are covered with ParB proteins and observed via fluorescent TIRF microscopy.* ***B)*** *ParB-plasmid complex (from P1 plasmid) directionally moving on the ParA-DNA carpet. Adapted from* [57]. ***C)*** *ParB-covered magnetic bead held at the surface via weak magnetic force (~5 fN), creates a ParA depletion zone around it. Adapted from* [90]. ***D)*** *Multiple trajectories of the ParB-covered beads in the presence of ParA on the DNA carpet. ParA induces directional movement of the ParB-covered beads. Adapted from* [90].

This assay was initially used to test the interactions between plasmid ParA and ParB proteins (from P1 and F-plasmid) [56]. The dynamics of these proteins were obtained using fluorescent recovery after photobleaching (FRAP), whereby ParA proteins were shown to dynamically exchange on the DNA much faster than their ATP hydrolysis rate (hydrolysis rate - r_{ATP} = 0.2 min^{-1}, dissociation rate – r_{SopA} = 8 min^{-1} [56]). Upon addition of ParB proteins DNA-bound ParA-ATP was stabilized from dissociating from the DNA, but its ATP hydrolysis rate increased. This resulted in the formation of a ParA-depletion zone in the local vicinity of the ParB-plasmid. This depletion zone caused a persistent and directional movement of both ParB-plasmid complexes (Fig. 2.6B) [56,57] and ParB-covered beads (Fig. 2.6C-D) [90]. In some cases, large plasmid complexes would split and directionally move away from each other, akin to plasmid segregation in cells [56]. Measurements of the directed super-diffusive behavior of particles [90], and further insights from *in silico* simulations of the same system [91] pointed to a general mechanism of the segregation of ParB-DNA complex based on a diffusion-ratchet model.

The cargo transport assay provided an important step toward a single-molecule investigation of the complete ParABS system. While dating back to the days before the CTPase activity of ParB proteins was discovered, these cargo transport experiments provided important insight into the mechanisms of plasmid segregation [48] and a baseline

for further investigations on chromosomal segregation systems using a slightly modified diffusion-ratchet model [54]. Looking forward, this system could be applied to study the dynamics of chromosomal ParA and ParB proteins, in the presence of both essential nucleotides (ATP/CTP), as well as to explore differences between different ParABS systems (as initial studies already showed differences between P1- and F-plasmid) [56,57].

2.3 Future perspectives: ParB interaction partners, ParB variants, and ParB-like proteins

While our understanding of the mechanism of ParB has deepened, it represents just a piece of the larger puzzle. Its function and interactions within the broader ParABS system, especially with proteins like ParA, still faces questions. Despite its significant role in chromosome or plasmid segregation, the ParA protein remains relatively underexplored in single-molecule experiments [57]. Understanding how ParA protein coats the DNA and promotes the directional movement of ParB-CTP-*parS* will aid in creating a comprehensive picture of the individual factors in the ParABS system. The interaction between a CTPase ParB and the ATPase ParA may also change the respective dynamics in the presence of both actors [68]. More single-molecule experiments with both ParA and ParB could bring us closer to resolving the ParABS system. Furthermore, ParA proteins can transport cargo different from the ParB-*parS* complex using a diffusion ratchet mechanism [92]. Therefore, studying chromosomal ParA in single-molecule studies will open up a range of possibilities that can be applied to different systems.

A second prominent interaction partner of ParB is the SMC protein complex [31-33], which is essential in organizing the bacterial chromosome in a distinct overall shape where both chromosomal arms are juxtaposed [34,93-95]. ParB proteins seem to be the sole recruiter of SMC proteins near the origin of replication, presumably at *parS* [31]. In fact, Antar *et al.* reported that ParB mutants ($ParB^{E78Q}$ / $ParB^{E111Q}$ in *B. subtilis*) which are rendered non-functional for partition complex formation in cells, can still efficiently recruit SMC proteins to the origin of replication [26]. How this interaction occurs at a single-molecule level remains entirely unclear. While *B. subtilis* SMC (at very high concentrations) was shown to condense the DNA in a DNA curtains assay [96], no single-molecule work has explored ParB and SMC in tandem, despite their known vital interaction within cells. The single-molecule stretching assay covered in this review poses an ideal platform [97-99] for such a study of DNA condensation [100] by SMCs. However, so far, *in vitro* reconstitution of loop extrusion by bacterial SMCs has not been successful.

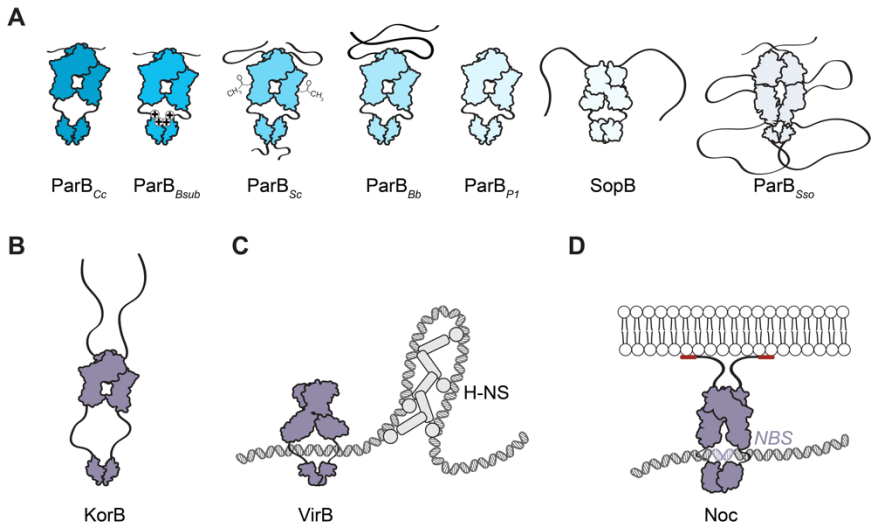


Figure 2.7. Schematic representations of various ParB and ParB-like proteins. A) *From left to right (Cc, Caulobacter crescentus; Bsub, Bacillus subtilis; Sc, Streptomyces coelicolor; Bb, Bdellovibrio bacteriovorus; P1, plasmid P1; SopB, plasmid F; Sso, Sulfolobus solfataricus). ParB$_{Cc}$ lacks the positively charged lysines at its C-terminus in contrast to ParB$_{Bsub}$, which is important for non-specific DNA contact during spreading and bridging [14]. ParB$_{Sc}$ is characterized by HTH-domain acetylation that impacts its parS binding [101]. ParB$_{Bb}$ binds parS in a growth-phase-dependent manner [102]. ParB$_{P1}$ and SopB (UniProt: P62558) are plasmid-borne and show potential differences in interaction with ParA [57], which could be compared to chromosomal ParB proteins. ParB$_{Sso}$ originating from archaea [103], showcases long disordered domains between the NTD, HTH, and CTD domains (UniProt: O93707).* ***B)*** *ParB-like proteins that harbor unique roles beyond chromosome or plasmid segregation. From left to right: KorB, which functions as a transcriptional regulator for plasmid genes [104,105] (UniProt: P07674). Noc binds CTP and DNA but also to the cell membrane, orchestrating the cell division process [106] (UniProt: P37524). VirB is a ParB-like protein with CTP binding, that modulates the transcription of virulence genes in Shigella [107-109] (UniProt: P0A247). All schematic representations are based on AlphaFold2 predictions of the dimeric state[29,30].*

In many organisms, chromosomal ParB proteins interact with species-specific protein factors such as DivIVA [110], MipZ [111] , PopZ [112,113], FtsZ [114], and many others - signalling the prominent role of ParB proteins. These interactions can significantly change the ParB behavior (binding, spreading, DNA condensation, dynamics). These interactions remain

largely unexplored in single-molecule studies, presenting an intriguing avenue for future research.

ParB proteins manifest subtle species-specific variations shaped by evolutionary pressures and specific requirements of their host (Fig. 2.7A). Current single-molecule studies have so far explored ParB proteins from a limited number of species, i.e., mostly *B. subtilis* and *C. crescentus*. Expanding single-molecule investigations to ParABS systems from other organisms may provide a comprehensive picture of the spectrum of ParB behaviors [17,102,115] and interactions [8].

Finally, there is also a broad range of ParB-like proteins. These are related in structure (often exhibiting CTPase activity [24,106,116]) but vary significantly in their functional roles within the cell (Fig. 2.7B). An intriguing example is the KorB protein found in the RK2 plasmid of *Pseudomonas*, which maintains a partitioning role but also modulates transcriptional regulation with its interaction partner, KorA [117]. A single-molecule study on the KorAB system, their binding, potential spreading, and dynamics, would provide a powerful complement to current *in vivo* or biochemical studies. Other interesting ParB-like candidates are VirB [108,109,116], a key transcriptional factor of *Shigella* virulence genes, and Noc (Nucleoid occlusion protein [106]) from *Firmicutes*, which is involved in cell division and interacts with the cell membrane.

2.4 Concluding remarks

Single-molecule techniques have illuminated mechanistic intricacies of ParB proteins, revealing nuanced details of their role in initiating and maintaining the formation of the partition complex. Single-molecule techniques have equipped us with the capacity to measure ParB binding to *parS* quantitatively [46,67], observe real-time DNA condensation [20,21,69], and even ParA-ParB interactions [118], thus enlightening our understanding of the assembly of the partition complex. Further, new phenomena such as ParB-ParB recruitment [46] and ParB interaction with an RNA polymerase [69] could be resolved on a single protein level. Moving forward, a major frontier lies in reconciling *in vitro* data with *in vivo* contexts, to ensure that mechanistic insights garnered from single-molecule experiments are validated within the multifaceted environment of the living cell. Expanding single-molecule techniques to other ParB and ParB-like proteins will not only provide insights into their mechanism but also address foundational questions: How are the dynamics affected in the presence of different interaction partners? How do evolutionary differences affect the binding, spreading, or DNA condensation by ParB/ParB-like proteins? What are common behaviors of ParB proteins?

Expanding the pool of single-molecule techniques to study the dynamic behavior of ParB and ParB-like proteins can further add to our understanding of these systems. Fluorescence Correlation Spectroscopy (FCS) and Förster Resonance Energy Transfer (FRET) studies could further inform us on the precise dynamics of two monomers assembling into a typical "open" dimer state, as well as the detailed dynamics of clamp closure, which is essential in all ParB proteins to date [25,26,28]. TIRF microscopy, in combination with surface-bound Noc proteins (akin to microtubule motility assays [119]), could be useful for studying the dynamics of Noc binding to the chromosomal DNA.

Finally, in addition to experimental work, *in silico* studies have greatly contributed to the insights into the ParB mechanism of action on a single molecule level [46,120] and within the cellular context [28,120-123]. A holistic approach, starting from detailed insights from single-molecule studies and testing these insights in an *in vivo* context, is essential for a robust and complete understanding of molecular mechanisms like that of ParB proteins in their natural cellular environments. By unraveling the complexities and subtle variations of ParB proteins across different organisms, we further inch closer to fully decoding the mechanisms that underpin bacterial chromosome segregation.

2.5 References

1. Austin, S. & Abeles, A. Partition of unit-copy miniplasmids to daughter cells. II. The partition region of miniplasmid P1 encodes an essential protein and a centromere-like site at which it acts. *Journal of Molecular Biology* **169**, 373-87 (1983).
2. Austin, S. & Abeles, A. Partition of unit-copy miniplasmids to daughter cells. I. P1 and F miniplasmids contain discrete, interchangeable sequences sufficient to promote equipartition. *Journal of Molecular Biology* **169**, 353-72 (1983).
3. Ogasawara, N. & Yoshikawa, H. Genes and their organization in the replication origin region of the bacterial chromosome. *Mol Microbiol* **6**, 629-34 (1992).
4. Mysliwiec, T.H., Errington, J., Vaidya, A.B. & Bramucci, M.G. The Bacillus subtilis spo0J gene: evidence for involvement in catabolite repression of sporulation. *J Bacteriol* **173**, 1911-9 (1991).
5. Ireton, K., Gunther, N.W.t. & Grossman, A.D. spo0J is required for normal chromosome segregation as well as the initiation of sporulation in Bacillus subtilis. *J Bacteriol* **176**, 5320-9 (1994).
6. Gerdes, K., Møller-Jensen, J. & Bugge Jensen, R. Plasmid and chromosome partitioning: surprises from phylogeny. *Mol Microbiol* **37**, 455-66 (2000).
7. Lin, D.C.H. & Grossman, A.D. Identification and characterization of a bacterial chromosome partitioning site. *Cell* **92**, 675–685 (1998).
8. Kawalek, A., Wawrzyniak, P., Bartosik, A.A. & Jagura-Burdzy, G. Rules and Exceptions: The Role of Chromosomal ParB in DNA Segregation and Other Cellular Processes. *Microorganisms* **8**(2020).
9. Livny, J., Yamaichi, Y. & Waldor, M.K. Distribution of centromere-like parS sites in bacteria: Insights from comparative genomics. *Journal of Bacteriology* **189**, 8693-703 (2007).
10. Jakimowicz, D., Chater, K. & Zakrzewska-Czerwínska, J. The ParB protein of Streptomyces coelicolor A3(2) recognizes a cluster of parS sequences within the origin-proximal region of the linear chromosome. *Molecular Microbiology* **45**, 1365-77 (2002).
11. Jung, A. et al. Two-step chromosome segregation in the stalked budding bacterium Hyphomonas neptunium. *Nature Communications* **10**, 3290 (2019).
12. Tran, N.T. et al. Permissive zones for the centromere-binding protein ParB on the Caulobacter crescentus chromosome. *Nucleic Acids Research* **46**, 1196-1209 (2018).
13. Leonard, T.A., Butler, P.J. & Löwe, J. Structural analysis of the chromosome segregation protein Spo0J from Thermus thermophilus. *Molecular Microbiology* **53**, 419-32 (2004).
14. Fisher, G.L.M. et al. The structural basis for dynamic DNA binding and bridging interactions which condense the bacterial centromere. *eLife* **6**, e28086 (2017).

15. Chen, B.W., Lin, M.H., Chu, C.H., Hsu, C.E. & Sun, Y.J. Insights into ParB spreading from the complex structure of Spo0J and parS. *Proceedings of the National Academy of Sciences of the United States of America* **112**, 6613-8 (2015).

16. Hayes, F. & Barillà, D. The bacterial segrosome: a dynamic nucleoprotein machine for DNA trafficking and segregation. *Nature Reviews Microbiology* **4**, 133-43 (2006).

17. Jalal, A.S.B. et al. Diversification of DNA-Binding Specificity by Permissive and Specificity-Switching Mutations in the ParB/Noc Protein Family. *Cell Reports* **32**, 107928 (2020).

18. Leonard, T.A., Butler, P.J. & Löwe, J. Bacterial chromosome segregation: structure and DNA binding of the Soj dimer — a conserved biological switch. *Embo j* **24**, 270-82 (2005).

19. Barillà, D., Carmelo, E. & Hayes, F. The tail of the ParG DNA segregation protein remodels ParF polymers and enhances ATP hydrolysis via an arginine finger-like motif. *Proceedings of the National Academy of Sciences* **104**, 1811-1816 (2007).

20. Song, D., Rodrigues, K., Graham, T.G.W. & Loparo, J.J. A network of cis and trans interactions is required for ParB spreading. *Nucleic Acids Research* **45**, 7106-7117 (2017).

21. Graham, T.G.W. et al. ParB spreading requires DNA bridging. *Genes and Development* **28**, 1228–1238 (2014).

22. Schumacher, M.A. & Funnell, B.E. Structures of ParB bound to DNA reveal mechanism of partition complex formation. *Nature* **438**, 516-9 (2005).

23. Soh, Y.M. et al. Self-organization of parS centromeres by the ParB CTP hydrolase. *Science* **366**, 1129–1133 (2019).

24. Osorio-Valeriano, M. et al. ParB-type DNA Segregation Proteins Are CTP-Dependent Molecular Switches. *Cell* **179**, 1512–1524 (2019).

25. Jalal, A.S., Tran, N.T. & Le, T.B. ParB spreading on DNA requires cytidine triphosphate in vitro. *eLife* **9**, e53515 (2020).

26. Antar, H. et al. Relief of ParB autoinhibition by parS DNA catalysis and ParB recycling by CTP hydrolysis promote bacterial centromere assembly. *Science Advances* **7**, eabj2854 (2021).

27. Jalal, A.S.B. et al. A CTP-dependent gating mechanism enables ParB spreading on DNA. *eLife* **10**, e69676 (2021).

28. Osorio-Valeriano, M. et al. The CTPase activity of ParB determines the size and dynamics of prokaryotic DNA partition complexes. *Molecular Cell* **81**, 3992–4007 (2021).

29. Jumper, J. et al. Highly accurate protein structure prediction with AlphaFold. *Nature* **596**, 583-589 (2021).

30. Mirdita, M. et al. ColabFold: making protein folding accessible to all. *Nat Methods* **19**, 679-682 (2022).

31. Bock, F.P., Liu, H.W., Anchimiuk, A., Diebold-Durand, M.-L. & Gruber, S. A joint-ParB interface promotes Smc DNA recruitment. *Cell reports* **40**, 111273 (2022).

32. Gruber, S. & Errington, J. Recruitment of Condensin to Replication Origin Regions by ParB/SpoOJ Promotes Chromosome Segregation in B. subtilis. *Cell* **137**, 685-96 (2009).

33. Sullivan, N.L., Marquis, K.A. & Rudner, D.Z. Recruitment of SMC by ParB-parS Organizes the Origin Region and Promotes Efficient Chromosome Segregation. *Cell* **137**, 697–707 (2009).

34. Wang, X., Brandão, H.B., Le, T.B., Laub, M.T. & Rudner, D.Z. Bacillus subtilis SMC complexes juxtapose chromosome arms as they travel from origin to terminus. *Science* **355**, 524-527 (2017).

35. Vecchiarelli, A.G., Mizuuchi, K. & Funnell, B.E. Surfing biological surfaces: exploiting the nucleoid for partition and transport in bacteria. *Molecular Microbiology* **86**, 513-23 (2012).

36. Hester, C.M. & Lutkenhaus, J. Soj (ParA) DNA binding is mediated by conserved arginines and is essential for plasmid segregation. *Proc Natl Acad Sci U S A* **104**, 20326-31 (2007).

37. Scholefield, G., Whiting, R., Errington, J. & Murray, H. Spo0J regulates the oligomeric state of Soj to trigger its switch from an activator to an inhibitor of DNA replication initiation. *Mol Microbiol* **79**, 1089-100 (2011).

38. Davis, M.A., Martin, K.A. & Austin, S.J. Biochemical activities of the parA partition protein of the P1 plasmid. *Molecular Microbiology* **6**, 1141-7 (1992).

39. Wu, L.J. & Errington, J. RacA and the Soj-Spo0J system combine to effect polar chromosome segregation in sporulating Bacillus subtilis. *Mol Microbiol* **49**, 1463-75 (2003).

40. Murray, H. & Errington, J. Dynamic control of the DNA replication initiation protein DnaA by Soj/ParA. *Cell* **135**, 74-84 (2008).

41. Scholefield, G., Errington, J. & Murray, H. Soj/ParA stalls DNA replication by inhibiting helix formation of the initiator protein DnaA. *Embo j* **31**, 1542-55 (2012).

42. Roberts, D.M. et al. Chromosome remodelling by SMC/Condensin in *B. subtilis* is regulated by monomeric Soj/ParA during growth and sporulation. *Proceedings of the National Academy of Sciences* **119**, e2204042119 (2022).

43. Guilhas, B. et al. ATP-Driven Separation of Liquid Phase Condensates in Bacteria. *Molecular Cell* **79**, 293–303 (2019).

44. Jalal, A.S.B. & Le, T.B.K. Bacterial chromosome segregation by the ParABS system. *Open Biology* **10**, 200097 (2020).

45. McLean, T.C. & Le, T.B. CTP switches in ParABS-mediated bacterial chromosome segregation and beyond. *Curr Opin Microbiol* **73**, 102289 (2023).

46. Tišma, M. et al. ParB proteins can bypass DNA-bound roadblocks via dimer-dimer recruitment. *Science Advances* **8**, eabn3299 (2022).

47. Babl, L. et al. CTP-controlled liquid–liquid phase separation of ParB. *Journal of Molecular Biology* **434**, 167401 (2022).

48. Hu, L., Vecchiarelli, A.G., Mizuuchi, K., Neuman, K.C. & Liu, J. Brownian ratchet mechanisms of ParA-mediated partitioning. *Plasmid* **92**, 12-16 (2017).

49. Bouet, J.Y. & Funnell, B.E. P1 ParA interacts with the P1 partition complex at parS and an ATP-ADP switch controls ParA activities. *Embo j* **18**, 1415-24 (1999).

50. Chu, C.H. et al. Crystal structures of HpSoj-DNA complexes and the nucleoid-adaptor complex formation in chromosome segregation. *Nucleic Acids Research* **47**, 2113-2129 (2019).

51. Zhang, H. & Schumacher, M.A. Structures of partition protein ParA with nonspecific DNA and ParB effector reveal molecular insights into principles governing Walker-box DNA segregation. *Genes and Development* **31**, 481-492 (2017).

52. Vecchiarelli, A.G. et al. ATP control of dynamic P1 ParA-DNA interactions: a key role for the nucleoid in plasmid partition. *Molecular Microbiology* **78**, 78-91 (2010).

53. Vecchiarelli, A.G., Neuman, K.C. & Mizuuchi, K. A propagating ATPase gradient drives transport of surface-confined cellular cargo. *Proceedings of the National Academy of Sciences* **111**, 4880-4885 (2014).

54. Lim, H.C. et al. Evidence for a DNA-relay mechanism in ParABS-mediated chromosome segregation. *eLife* **3**, e02758 (2014).

55. Le Gall, A. et al. Bacterial partition complexes segregate within the volume of the nucleoid. *Nature Communications* **7**, 12107 (2016).

56. Hwang, L.C. et al. ParA-mediated plasmid partition driven by protein pattern self-organization. *Embo j* **32**, 1238-49 (2013).

57. Vecchiarelli, A.G., Hwang, L.C. & Mizuuchi, K. Cell-free study of F plasmid partition provides evidence for cargo transport by a diffusion-ratchet mechanism. *Proceedings of the National Academy of Sciences of the United States of America* **110**, E1390-7 (2013).

58. Webb, C.D. et al. Bipolar localization of the replication origin regions of chromosomes in vegetative and sporulating cells of B. subtilis. *Cell* **88**, 667-74 (1997).

59. Glaser, P. et al. Dynamic, mitotic-like behavior of a bacterial protein required for accurate chromosome partitioning. *Genes and Development* **11**, 1160-8 (1997).

60. Lin, D.C., Levin, P.A. & Grossman, A.D. Bipolar localization of a chromosome partition protein in Bacillus subtilis. *Proceedings of the National Academy of Sciences of the United States of America* **94**, 4721-6 (1997).

61. Murray, H., Ferreira, H. & Errington, J. The bacterial chromosome segregation protein Spo0J spreads along DNA from parS nucleation sites. *Molecular Microbiology* **61**, 1352-1361 (2006).

62. van Loenhout, M.T., Kerssemakers, J.W., De Vlaminck, I. & Dekker, C. Non-bias-limited tracking of spherical particles, enabling nanometer resolution at low magnification. *Biophys J* **102**, 2362-71 (2012).

63. De Vlaminck, I. & Dekker, C. Recent advances in magnetic tweezers. *Annu Rev Biophys* **41**, 453-72 (2012).

64. De Vlaminck, I. et al. Highly parallel magnetic tweezers by targeted DNA tethering. *Nano Lett* **11**, 5489-93 (2011).

65. Madariaga-Marcos, J., Pastrana, C.L., Fisher, G.L.M., Dillingham, M.S. & Moreno-Herrero, F. ParB dynamics and the critical role of the CTD in DNA condensation unveiled by combined force-fluorescence measurements. *eLife* **8**, e43812 (2019).

66. Taylor, J.A. et al. Specific and non-specific interactions of ParB with DNA: Implications for chromosome segregation. *Nucleic Acids Research* **43**, 719-31 (2015).

67. Balaguer, F.d.A. et al. CTP promotes efficient ParB-dependent DNA condensation by facilitating one-dimensional diffusion from parS. *eLife* **10**, e67554 (2021).

68. Taylor, J.A., Seol, Y., Budhathoki, J., Neuman, K.C. & Mizuuchi, K. CTP and parS coordinate ParB partition complex dynamics and ParA-ATPase activation for ParABS-mediated DNA partitioning. *eLife* **10**, e65651 (2021).

69. Tišma, M. et al. Dynamic ParB–DNA interactions initiate and maintain a partition condensate for bacterial chromosome segregation. *Nucleic Acids Research* (2023).

70. Wang, M.D. et al. Force and velocity measured for single molecules of RNA polymerase. *Science* **282:902-7**(1998).

71. Saleh, O.A., Pérals, C., Barre, F.X. & Allemand, J.F. Fast, DNA-sequence independent translocation by FtsK in a single-molecule experiment. *Embo j* **23**, 2430-9 (2004).

72. Liu, N., Chistol, G., Cui, Y. & Bustamante, C. Mechanochemical coupling and bi-phasic force-velocity dependence in the ultra-fast ring ATPase SpoIIIE. *eLife* **7**(2018).

73. Janissen, R. et al. Global DNA Compaction in Stationary-Phase Bacteria Does Not Affect Transcription. *Cell* **174**, 1188-1199 (2018).

74. Bartosik, A.A., Lasocki, K., Mierzejewska, J., Thomas, C.M. & Jagura-Burdzy, G. ParB of Pseudomonas aeruginosa: interactions with its partner ParA and its target parS and specific effects on bacterial growth. *Journal of Bacteriology* **186**, 6983-98 (2004).

75. Jakimowicz, D., Chater, K. & Zakrzewska-Czerwinska, J. The ParB protein of Streptomyces coelicolor A3(2) recognizes a cluster of parS sequences within the origin-proximal region of the linear chromosome. *Mol Microbiol* **45:1365-77**(2002).

76. Kawalek, A., Glabski, K., Bartosik, A.A., Fogtman, A. & Jagura-Burdzy, G. Increased ParB level affects expression of stress response, adaptation and virulence operons and potentiates repression

of promoters adjacent to the high affinity binding sites parS3 and parS4 in Pseudomonas aeruginosa. *PLoS One* **12**, e0181726 (2017).

77. Kusiak, M., Gapczynska, A., Plochocka, D., Thomas, C.M. & Jagura-Burdzy, G. Binding and spreading of ParB on DNA determine its biological function in Pseudomonas aeruginosa. *J Bacteriol* **193**, 3342-55 (2011).

78. Lynch, A.S. & Wang, J.C. SopB protein-mediated silencing of genes linked to the sopC locus of Escherichia coli F plasmid. *Proceedings of the National Academy of Sciences of the United States of America* **92**, 1896–1900 (1995).

79. Rodionov, O., ŁObocka, M. & Yarmolinsky, M. Silencing of genes flanking the P1 plasmid centromere. *Science* **283**, 546–549 (1999).

80. Venkova-Canova, T., Baek, J.H., Fitzgerald, P.C., Blokesch, M. & Chattoraj, D.K. Evidence for two different regulatory mechanisms linking replication and segregation of vibrio cholerae chromosome II. *PLOS Genetics* **9**, e1003579 (2013).

81. Stracy, M. et al. Live-cell superresolution microscopy reveals the organization of RNA polymerase in the bacterial nucleoid. *Proc Natl Acad Sci U S A* **112**, E4390-9 (2015).

82. Stracy, M. et al. Transient non-specific DNA binding dominates the target search of bacterial DNA-binding proteins. *Mol Cell* **81**, 1499-1514.e6 (2021).

83. Guo, L. et al. Stochastically multimerized ParB orchestrates DNA assembly as unveiled by single-molecule analysis. *Nucleic Acids Research* **50**, 9294-9305 (2022).

84. Greene, E.C., Wind, S., Fazio, T., Gorman, J. & Visnapuu, M.L. DNA curtains for high-throughput single-molecule optical imaging. *Methods Enzymol* **472**, 293-315 (2010).

85. Ganji, M., Kim, S.H., van der Torre, J., Abbondanzieri, E. & Dekker, C. Intercalation-Based Single-Molecule Fluorescence Assay To Study DNA Supercoil Dynamics. *Nano Letters* **16**, 4699-707 (2016).

86. Granéli, A., Yeykal, C.C., Prasad, T.K. & Greene, E.C. Organized arrays of individual DNA molecules tethered to supported lipid bilayers. *Langmuir* **22**, 292-9 (2006).

87. Song, D., Graham, T.G. & Loparo, J.J. A general approach to visualize protein binding and DNA conformation without protein labelling. *Nature Communications* **7**, 10976 (2016).

88. Molina, M. et al. A framework to validate fluorescently labeled DNA-binding proteins for single-molecule experiments. *Cell Reports Methods*, 100614 (2023).

89. Tišma, M. et al. Dynamic ParB-DNA interactions initiate and maintain a partition condensate for bacterial chromosome segregation. *bioRxiv*, 2023.06.25.546419 (2023).

90. Vecchiarelli, A.G., Neuman, K.C. & Mizuuchi, K. A propagating ATPase gradient drives transport of surface-confined cellular cargo. *Proceedings of the National Academy of Sciences of the United States of America* **111**, 4880-5 (2014).

91. Hu, L., Vecchiarelli, A.G., Mizuuchi, K., Neuman, K.C. & Liu, J. Directed and persistent movement arises from mechanochemistry of the ParA/ParB system. *Proceedings of the National Academy of Sciences of the United States of America* **112**, E7055-64 (2015).

92. Pulianmackal, L.T. et al. Multiple ParA/MinD ATPases coordinate the positioning of disparate cargos in a bacterial cell. *Nature Communications* **14**, 3255 (2023).

93. Le, T.B.K., Imakaev, M.V., Mirny, L.A. & Laub, M.T. High-resolution mapping of the spatial organization of a bacterial chromosome. *Science* (2013).

94. Tran, N.T., Laub, M.T. & Le, T.B.K. SMC Progressively Aligns Chromosomal Arms in Caulobacter crescentus but Is Antagonized by Convergent Transcription. *Cell Reports* **20**, 2057-2071 (2017).

95. Wang, X. et al. Condensin promotes the juxtaposition of dna flanking its loading site in Bacillus subtilis. *Genes and Development* **29**, 1661-1675 (2015).

96. Kim, H. & Loparo, J.J. Multistep assembly of DNA condensation clusters by SMC. *Nature Communications* **7**, 10200 (2016).

97. Davidson, I.F. et al. DNA loop extrusion by human cohesin. *Science* **366**, 1338-1345 (2019).

98. Ganji, M. et al. Real-time imaging of DNA loop extrusion by condensin. *Science* **360**, 102-105 (2018).

99. Pradhan, B. et al. The Smc5/6 complex is a DNA loop-extruding motor. *Nature* **616**, 843-848 (2023).

100. Ryu, J.-K. et al. Bridging-induced phase separation induced by cohesin SMC protein complexes. *Science Advances* **7**, eabe5905 (2021).

101. Li, P., Zhang, H., Zhao, G.P. & Zhao, W. Deacetylation enhances ParB-DNA interactions affecting chromosome segregation in Streptomyces coelicolor. *Nucleic Acids Res* **48**, 4902-4914 (2020).

102. Kaljević, J., Tesseur, C., Le, T.B.K. & Laloux, G. Cell cycle-dependent organization of a bacterial centromere through multi-layered regulation of the ParABS system. *PLOS Genetics* **19**, e1010951 (2023).

103. Schumacher, M.A. et al. Structures of archaeal DNA segregation machinery reveal bacterial and eukaryotic linkages. *Science* **349**, 1120-4 (2015).

104. Kornacki, J.A., Burlage, R.S. & Figurski, D.H. The kil-kor regulon of broad-host-range plasmid RK2: nucleotide sequence, polypeptide product, and expression of regulatory gene korC. *J Bacteriol* **172**, 3040-50 (1990).

105. Thomas, C.M. & Hussain, A.A. The korB gene of broad host range plasmid RK2 is a major copy number control element which may act together with trfB by limiting trfA expression. *Embo j* **3**, 1513-9 (1984).

106. Jalal, A.S.B. et al. CTP regulates membrane-binding activity of the nucleoid occlusion protein Noc. *Molecular Cell* **81**, 3623-3636.e6 (2021).

107. Antar, H. & Gruber, S. VirB, a transcriptional activator of virulence in Shigella flexneri, uses CTP as a cofactor. *bioRxiv*, 2023.05.19.541425 (2023).

108. Gerson, T.M. et al. VirB, a key transcriptional regulator of Shigella virulence, requires a CTP ligand for its regulatory activities. *mBio* **0**, e01519-23 (2023).

109. Jakob, S. et al. The virulence regulator VirB from Shigella flexneri uses a CTP-dependent switch mechanism to activate gene expression. *bioRxiv*, 2023.06.01.543266 (2023).

110. Perry, S.E. & Edwards, D.H. The Bacillus subtilis DivIVA protein has a sporulation-specific proximity to Spo0J. *J Bacteriol* **188**, 6039-43 (2006).

111. Thanbichler, M. & Shapiro, L. MipZ, a spatial regulator coordinating chromosome segregation with cell division in Caulobacter. *Cell* **126**, 147-62 (2006).

112. Ebersbach, G., Briegel, A., Jensen, G.J. & Jacobs-Wagner, C. A self-associating protein critical for chromosome attachment, division, and polar organization in caulobacter. *Cell* **134**, 956-68 (2008).

113. Bowman, G.R. et al. A polymeric protein anchors the chromosomal origin/ParB complex at a bacterial cell pole. *Cell* **134**, 945-55 (2008).

114. Donovan, C., Schwaiger, A., Krämer, R. & Bramkamp, M. Subcellular localization and characterization of the ParAB system from Corynebacterium glutamicum. *Journal of Bacteriology* **192**, 3441-51 (2010).

115. Kaljević, J. et al. Chromosome choreography during the non-binary cell cycle of a predatory bacterium. *Curr Biol* **31**, 3707-3720.e5 (2021).

116. Antar, H. & Gruber, S. VirB, a transcriptional activator of virulence in Shigella flexneri, uses CTP as a cofactor. *Communications Biology* **6**, 1204 (2023).

117. Kolatka, K., Kubik, S., Rajewska, M. & Konieczny, I. Replication and partitioning of the broad-host-range plasmid RK2. *Plasmid* **64**, 119-34 (2010).

118. Vecchiarelli, A.G., Seol, Y., Neuman, K.C. & Mizuuchi, K. A moving ParA gradient on the nucleoid directs subcellular cargo transport via a chemophoresis force. *Bioarchitecture* **4**, 154-9 (2014).

119. Howard, J., Hudspeth, A.J. & Vale, R.D. Movement of microtubules by single kinesin molecules. *Nature* **342**, 154-8 (1989).

120. Connolley, L., Schnabel, L., Thanbichler, M. & Murray, S.M. Partition complex structure can arise from sliding and bridging of ParB dimers. *Nature Communications* **14**, 4567 (2023).

121. Broedersz, C.P. et al. Condensation and localization of the partitioning protein ParB on the bacterial chromosome. *Proceedings of the National Academy of Sciences of the United States of America* **111**, 8809-8814 (2014).

122. Walter, J.C. et al. Supercoiled DNA and non-equilibrium formation of protein complexes: A quantitative model of the nucleoprotein ParBS partition complex. *PLoS Comput Biol* **17**, e1008869 (2021).

123. Walter, J.C. et al. Physical Modeling of a Sliding Clamp Mechanism for the Spreading of ParB at Short Genomic Distance from Bacterial Centromere Sites. *iScience* **23**(2020).

3

SUPERCOILING-DEPENDENT DNA BINDING: QUANTITATIVE MODELING AND APPLICATIONS TO BULK AND SINGLE-MOLECULE EXPERIMENTS

DNA stores our genetic information and is ubiquitous in applications, where it interacts with binding partners ranging from small molecules to large macromolecular complexes. Binding is modulated by mechanical strains in the molecule and, in turn, can change local DNA structure. Frequently, DNA occurs in closed topological forms where topology and supercoiling add a global constraint to the interplay of binding-induced deformations and strain-modulated binding. Here, we present a quantitative model with a straight-forward numerical implementation of how the global constraints introduced by DNA topology modulate binding. We focus on fluorescent intercalators, which unwind DNA and enable direct quantification via fluorescence detection. Our model correctly describes bulk experiments using plasmids with different starting topologies, different intercalators, and over a broad range of intercalator and DNA concentrations. We demonstrate and quantitatively model supercoiling-dependent binding in a single-molecule assay, where we directly observe the different intercalator densities going from supercoiled to nicked DNA. The single-molecule assay provides direct access to binding kinetics and DNA supercoil dynamics. Our model has broad implications for the detection and quantification of DNA, including the use of psoralen for UV-induced DNA crosslinking to quantify torsional tension in vivo, and for the modulation of DNA binding in cellular contexts.

This chapter was published as Kolbeck P. J, Tišma M, Analikwu B. T, Vanderlinden W, Dekker C, Lipfert J. *Supercoiling-dependent DNA binding: quantitative modeling and applications to bulk and single-molecule experiments*. Nucleic Acids Res (2023)

3.1 Introduction

DNA is the carrier of genetic information in all cellular life. *In vivo*, double-stranded DNA is often present in circular and, therefore, topological closed form. In particular, bacterial chromosomes and plasmids are circular DNA molecules, whose degree of supercoiling is tightly regulated *in vivo* [1-3]. In eukaryotes, DNA topology and supercoiling similarly play important roles in the context of a chromatinized genome, e.g., in the compaction, processing, and regulation of genetic information [4-12].

Both in its biological role and in many biotechnological applications, DNA interacts with a broad range of binding partners that range from small molecules to large proteins complexes. In particular, the detection and quantification of DNA often rely on staining with fluorescent small molecules that frequently bind in an intercalative binding mode [13-19]. Ligand binding to DNA can, in general, locally alter the DNA structure and introduce strains away from the equilibrium B-form DNA conformation [20-25]. In turn, stretching forces and torsional strains have been shown to systematically affect binding equilibria [20,26-33]. Having a defined DNA topology, e.g., in a plasmid or other topological domains, imposes a global constraint on the interplay between strain-dependent binding and binding-induced conformational changes, as described in seminal work by Bauer and Vinograd [26,27,33] and subsequently shown for both small molecule [4,26,27,33,34] and protein binding to DNA [10,35,36].

Here we present a quantitative model for DNA-ligand binding for various degrees of supercoiling under a global topological constraint and apply it to both bulk experiments and to a single-molecule assay that enables us to study DNA supercoil dynamics in real time. Our model for ligand binding to topologically closed DNA combines and integrates aspects of previous work. In particular we take into account the constraints of binding to a linear molecule [37], both the finite DNA and intercalator concentrations [19], the conformational changes induced by the ligand [13,14,19,27,31], the influence of strains on binding equilibria [26,33], a physical model of plasmid mechanics [38,39], and the global constraint introduced by having a defined linking number due to the defined topology [27,40,41]. Importantly, the parameters of our model have a direct physical interpretation and can be determined from other assays. Therefore, our model can provide quantitative predictions without free parameters.

We focus on commonly used intercalators that are well-characterized by previous studies: Ethidium bromide (EtBr), SYBR Gold, and SYTOX Orange (Fig. S3.1). EtBr is a very widely used stain for DNA visualization in gels and other applications [14,30-32,42-46]. SYBR Gold is a more recently developed DNA stain, which has very high quantum efficiency and brightness [19,47-49].

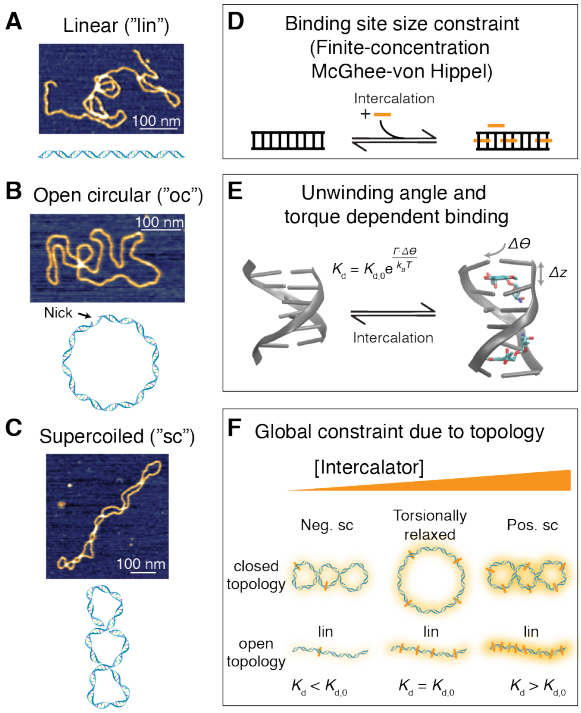


Figure 3.1. Overview of different topological conformations of plasmid DNA and outline of the binding model under global constraint. A) *Schematic and an AFM height image of linear DNA.* ***B)*** *Schematic and an AFM height image of open circular DNA, i.e., of plasmid DNA that is nicked at a single site.* ***C)*** *Schematic and an AFM height image of a negatively supercoiled DNA plasmid. AFM images in panels A-C are of pBR322 plasmid DNA (4,361 bp; see Methods).* ***D)*** *Schematic of the McGhee-von Hippel binding model for ligand binding to DNA, whereby the binding site size modulates the binding equilibrium.* ***E)*** *Illustration of how intercalation into DNA lengthens and underwinds the B-form helix. Left: B-form DNA, rendered from PDB entry 4C64* [50]*. Right: DNA in the presence of an intercalator, here daunomycin rendered from PDB entry 1D11* [1]*.* ***F)*** *Schematic of how the global constraint due to topology leads to increased binding as long as the topologically closed DNA is negatively supercoiled (left), but will decrease binding when the DNA is positively supercoiled (right), compared to the torsionally relaxed form (center). Intercalation, in turn, locally underwinds the DNA and, therefore, leads to an increase in Wr with increasing intercalation in topologically closed DNA. For comparison, a topologically open DNA is shown below.*

SYTOX Orange is frequently used to stain and supercoil DNA in single-molecule experiments [49,51-54]. Finally, we extend our analysis to the intercaltor 4,5',8-trimethylpsoralen (TMP; also known as trioxsalen) that is used as a photo-crosslinking agent, both for phototherapy [55] and to detect supercoiling and chromatin structure *in vivo* [7,8,10,56-59].

We first perform experiments in bulk using native topologically constrained plasmid DNA, i.e., circular DNA with both strands fully intact (referred to as the supercoiled species, "sc"; Fig. 3.1A) and, for comparison, topologically open DNA (nicked, open circular, "oc", or linearized, "lin"; Fig. 3.1B,C). We use fluorescence detection to quantify the amount of binding and find quantitative agreement with our model. We then apply our model to a single-molecule DNA assay [51,54], where DNA is supercoiled *in situ* by intercalation. We monitor the fluorescence change upon nicking of the DNA molecule, which induces an abrupt transition from a closed topology to a topology unconstrained, nicked form and again find excellent agreement with our model. The single-molecule assay enables us to observe the re-adjustment of the binding equilibrium upon change in topology in real time, which enables us to probe the dynamics of torque release, intercalation, and supercoil relaxation.

Our findings have direct practical applications since gel-based assays for the discrimination and detection of topoisomers are widely used to study the properties of circular DNA and of various enzymes that alter DNA topology, including topoisomerases, gyrase, reverse gyrase, and recombinases [60-62]. An unbiased quantification of the different topoisomers using fluorescence staining, which is increasingly used to replace radiolabelling due to the hazards associated with handling, storing, and disposing of radioactive materials, must take into account the observed topology dependencies. Furthermore, our model is directly applicable to single-molecule fluorescence studies of supercoiled DNA, and we demonstrate real-time monitoring of supercoiling-dependent binding dynamics. Finally, we provide practical guidelines for unbiased detection of different topoisomers and discuss consequences of topology-dependent binding more broadly.

3.2 Results

3.2.1 Model for ligand binding under topological constraint

We develop a model for ligand binding to topologically closed supercoiled (e.g. plasmid) DNA, where the topology imposes a global constraint (Fig. 3.1D-F). Binding to plasmid DNA is different from a standard bimolecular binding equilibrium for several reasons that we take into account in our model. First, the linear structure of DNA imposes local constraints for ligand binding, if bound ligands occupy a binding size of *n* bases (Fig.

3.1D). Binding of ligands with binding site size *n* can be modeled using the McGhee-von Hippel model [31,37] in cases where the DNA concentration is much lower than the ligand concentration, such that the free and total ligand concentrations are approximately equal. For bulk measurements, however, the concentration of DNA bases can be similar to or even larger than the ligand concentration and needs to be considered [19]. Therefore, we use an extension of the McGhee-von Hippel model that explicitly takes into account both the ligand (c_{total}) and DNA (c_{DNA}) concentration that was derived in Ref. [19]. The fractional binding γ is given by

$$\gamma = \frac{c_{bound}}{c_{DNA}} = \frac{(c_{total} - c_{bound})}{K_d} \cdot \frac{\left(1 - n \cdot \frac{c_{bound}}{c_{total}}\right)^n}{\left(1 - n \cdot \frac{c_{bound}}{c_{DNA}} + \frac{c_{bound}}{c_{DNA}}\right)^{n-1}} \quad (1)$$

Here $\boldsymbol{c_{bound}}$ is the bound ligand concentration, c_{free} is the free ligand concentration, $c_{total} = c_{free} + c_{bound}$ the total ligand concentration, K_d is the dissociation constant (in M), and $\boldsymbol{n}$ is the binding site size (in base pairs). Typical values of the binding site size for intercalators are $n \approx 2$, corresponding to binding every other base pair.

Intercalation affects the local geometry of the DNA helix, by locally unwinding and lengthening the helix [14,16,27,30,31,49,63,64] (Fig. 3.1E). Here we assume that each intercalation event locally lengthens the DNA by Δz and unwinds it by $\Delta\theta$. Typical values for intercalators are in the range $\Delta z \approx 0.34$ nm and $\Delta\theta \approx 15°$-$30°$. The fact that intercalation lengthens and unwinds the DNA helix suggests, by Le Chatelier's principle, that applying a stretching force or unwinding torque, respectively, will increase intercalative binding. Conversely, overwinding the helix will hinder intercalation. We assume an Arrhenius-like exponential dependence of the binding constant [30,45,49,65] on applied force F and torque Γ:

$$K_d(F,\Gamma) = K_{d,0} \cdot e^{-\frac{\Gamma \cdot \Delta\Theta}{k_B T}} \cdot e^{-\frac{F \cdot \Delta z}{k_B T}} \quad (2)$$

Here $K_{d,0}$ is the dissociation constant for the relaxed molecule, i.e., in the absence of forces or torques, k_B Boltzmann's constant and T the absolute temperature. For plasmids in free solution, the force is zero (or at least small, specifically $F \ll k_B T / \Delta z \approx 10$ pN) and the second exponential factor in Equation 2 can be neglected. Values for n, K_d, Δz, and $\Delta\theta$ for selected dyes are summarized in Table 1.

For linear or open circular DNA molecules, there is no torsional constraint, and the torque will be zero in equilibrium; consequently, binding will simply be determined by Equation 1. In contrast, for topologically closed plasmids, the topology imposes a global constraint. For a closed plasmid, the linking number Lk is a topological invariant and

partitions into twist *Tw* and writhe *Wr* by White's formula (also known as Calugareanu's theorem or Calugareanu-White-Fuller theorem) [27,40,41,66,67]:

$$Lk = Tw + Wr \tag{3}$$

Tw is a measure for the local winding of the helix and directly related to the torsional strain in the molecule. Conversely, *Wr* corresponds to the coiling of the double helix axis in 3D space and in a plasmid is related to the number of plectonemic supercoils (and other writhed configurations, such as toroidal supercoils and curls). We express the linking number balance relative to the torsionally relaxed double-stranded DNA, for which we define $\Delta Lk = Lk - Lk_0 = 0$, and where Lk_0 ($=Tw_0 + Wr_0$) is the natural linking number of torsionally relaxed DNA, $\Delta Tw = Tw - Tw_0 = 0$, where Tw_0 is the natural twist of DNA, equal to the number of base pairs divided by the helical turn (≈ 10.5 bp per turn for bare DNA), and $\Delta Wr = Wr$, i.e. the torsionally relaxed conformation has an average *Wr* of zero. DNA is defined to be supercoiled if ΔLk is different from zero.

Intercalation changes the intrinsic twist of the helix and, therefore, shifts the linking number difference at which the molecule is torsionally relaxed by $N_{\text{bound}} \cdot \Delta\theta/360°$ where N_{bound} is the number of dye molecules bound. For a given plasmid, the linking number difference relative to the torsionally relaxed state is, therefore, given by

$$\Delta Lk = \Delta Lk_0 + N_{\text{bound}} \cdot \Delta\theta/360° \tag{4}$$

where ΔLk_0 is the linking number difference of the plasmid in the absence of intercalation. In general, excess linking number will partition into twist and writhe (Equation 3). For plasmids, it has been shown that the partitioning is independent of the magnitude [38] and sign [68] of the linking difference and is approximately 20% *Tw* and 80% *Wr*. We assume that this partitioning between twist and writhe also holds in the presence of intercalators and for molecules with attached ends at low forces, such that

$$\Delta Tw = 0.2 \cdot \Delta Lk \tag{5}$$

where ΔLk is given by Equation 4. In order to compute the torsional strain for a given initial linking difference ΔLk_0 and given number of intercalated molecules N_{bound}, we convert the excess twist (Equation 5) to torque by taking into account the torsional stiffness of DNA:

$$\Gamma = \frac{C \cdot k_B T \cdot 2\pi}{L_C} \cdot \Delta Tw \tag{6}$$

where *C* is the torsional stiffness of DNA in nm and L_C the contour length, which in turn depends on the number of molecules bound as $L_C = L_{C,0} + N_{\text{bound}} \cdot \Delta z$, where $L_{C,0}$ is the contour length in the absence of intercalation, ≈ 0.34 nm per bp. The torsional stiffness

of DNA has been measured using single-molecule methods [69-71], is independent of ionic strength [71], and reported values are in the range of $C \approx 100$ nm [70,72,73]. However, it is not well known whether or how C is altered by intercalation. Previous measurements using DNA in free solution using EtBr [42,74,75] have found lower values of the torsional stiffness in the range $C \approx 50$ nm, which we take as a starting point for the EtBr data. For all other conditions we use $C = 100$ nm.

To determine the number of intercalated molecules per plasmid as a function of total ligand concentration c_{total} and DNA concentration c_{DNA} (typically expressed as the base pair concentration), we numerically solve the coupled Equations 1-6 using an iterative approach (Materials and Methods). The main output of the model is N_{bound}. Assuming a linear relationship between the number of intercalated molecules and the fluorescence intensity, which we have previously found to hold for a large range of dye concentrations [19], the observed fluorescence intensity I is given by

$$I = \alpha \cdot c_{\text{DNA}} \cdot N_{\text{bound}} \tag{7}$$

where α is a proportionality factor that depends on the quantum efficiency of the dye and the details of the experiments but is constant for a given intercalator and instrumental set up. We note that the proportionality factor α cancels for our predictions of the *relative* binding of closed vs. open topology.

3.2.2 DNA supercoiling modulates intercalation

Intercalation into topologically closed DNA can increase or decrease binding due to the by the global constraint, relatively to a torsionally relaxed (or linearized) plasmid [26,27,33]. Starting with a negatively supercoiled plasmid, which is the form typically found *in vivo*, intercalation at low ligand concentration is increased relative to the nicked DNA, due to the negative torsional strain in the molecule (Fig. 3.1F). As more and more molecules intercalate, the negative linking difference is compensated until the plasmid becomes torsionally relaxed, at which point binding to the topologically closed and open forms is the same. Finally, as the intercalator concentration is increased further, the closed plasmid becomes overwound, and the positive torsional strain hinders further intercalation. Therefore, at high intercalator concentration fewer molecules bind to the closed compared to the open plasmid (Fig. 3.1F).

To experimentally test the predictions of the model outlined in the previous section, we used plasmid DNA in both topologically constrained, negatively supercoiled form and in open circular and linear topologies (Fig. 3.1A-C; Materials and Methods). We prepared mixtures with equal amounts of the three different DNA topologies to facilitate direct comparison on a gel. We then separated the mixtures on a gel (Fig. 3.2A), imaged

the gel, and quantified the band intensities to monitor the amount of intercalation (Fig. S3.3). While the open circular and linear topologies exhibit similar intensities, the topologically constrained species in comparison appears less bright on the gel for high EtBr concentrations (Fig. S3.4A). In contrast, for the lowest EtBr concentration, the supercoiled species exhibits a higher intensity than the other two species (Fig. S3.4B). We use our model to quantitatively account for the topology dependent intensities (Fig. 3.2B, Fig. S3.5A). We find that for the experimental parameters used here, the number of intercalated molecules per plasmid is approximately independent of DNA concentration (Fig. S3.5A). Consequently, the fluorescent intensity increases with DNA concentration (Fig. 3.2B). At the lowest EtBr concentration (Fig. 3.2B, black lines and symbols), more molecules bind to the supercoiled species (Fig. 3.2B, lines and symbols with red highlighting) as compared to open circular and linear, while at the highest concentration (Fig. 3.2B, light brown lines and symbols) intercalation is reduced for supercoiled compared to the other species. At the intermediate EtBr concentration (Fig. 3.2B, brown lines and symbols) the topologically open and closed species bind EtBr similarly. The differences in binding between the different topologies are a consequence of the negative torsional strain at the lowest EtBr concentration and the positive strain for the highest concentration (Fig. S3.5B). Averaging over the different DNA concentrations, we can quantitatively compare the relative enhancement or reduction of interaction for the topologically closed species compared to the open circular and linear species (Fig. 3.2C) and find excellent agreement between our model and the experimental data. We note that for low EtBr concentrations, the error bars are larger and the fit of our model appears less well than at higher concentrations, which might be in part due to i) some presence of alternative (non-B form) DNA structures, ii) a distribution of topoisomers for negatively coiled DNA, and iii) the lower fluorescence signal at lower EtBr concentrations. Nonetheless, we achieve reasonable agreement within experimental error for all conditions tested.

3.2.3 Topology dependent binding depends on initial topology and intercalator affinity

Having demonstrated that our model can quantitatively account for how DNA topology alters DNA binding starting with a negatively supercoiled plasmid ($\Delta Lk_0 < 0$), where intercalation is increased at low intercalator concentrations and suppressed at high concentrations compared to an open topology (Fig. 3.2C), we turn to initially torsionally relaxed plasmids. A clear prediction of our model is that if the DNA is initially torsionally relaxed (or even positively supercoiled), intercalation should always be reduced for the closed topology compared to an open topology.

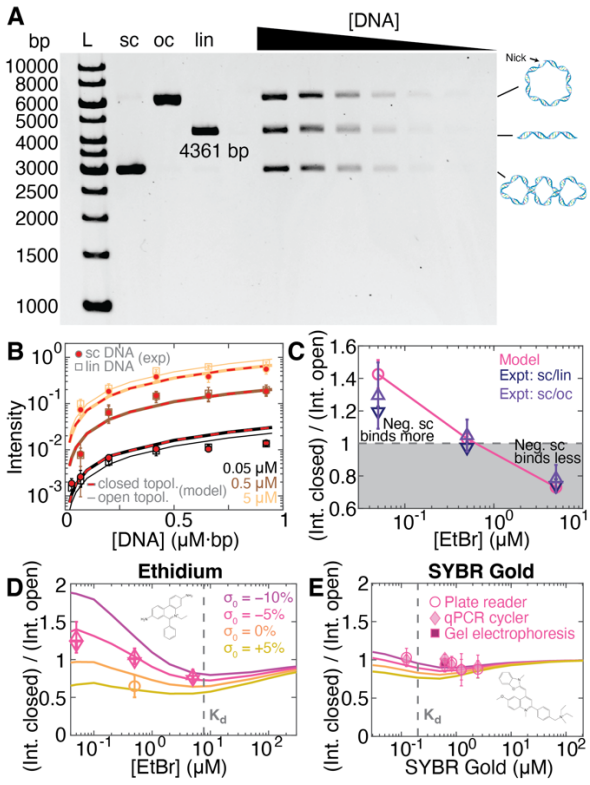


Figure 3.2. DNA topology dependent intercalation. A) *Agarose gel stained with EtBr at a final concentration of 0.5 μM. Different DNA topologies are separated on the gel. L: DNA size ladders (1 kb gene ruler, Thermo Scientific, 5 μL). Lanes 2-4 are the stock solutions of negatively supercoiled, linear, and open circular DNA, respectively. Lanes 5-11 are equimolar mixtures of the three topologies, at different total DNA concentrations.* ***B)*** *Experimentally determined fluorescence intensity for supercoiled DNA (circles with red highlight) and linear DNA (squares) as a function EtBr and DNA concentration for pBR322 DNA (4361 bp). Thin lines are for topologically open DNA (linear and open circular); thick lines with red highlights are for topologically closed DNA (supercoiled, here with supercoiling density* $\sigma \approx -5\%$*, corresponding to* $\Delta Lk_0 \approx -20$ *turns). Symbols are the mean and std from at least two gels. Lines are predictions of our binding model (Equation 7).* ***C)*** *Relative fluorescence intensity of a topologically closed DNA relative to the topologically open constructs. Data points are obtained by averaging the different DNA concentration at the same EtBr condition..* ***D)*** *Relative binding to topologically closed:open DNA. Colored lines are the predictions of our model. Symbols are the data from Figure 3.2E. Further analyses are shown in Supplementary Figure S3.5.* ***E)*** *Same as in panel D for SYBR Gold.*

We test this prediction experimentally by again preparing and separating DNA plasmids with different topologies, but now using a sample where the plasmid has been relaxed by topoisomerase treatment (Methods), such as that $\Delta Lk_0 \approx 0$ (Fig. S3.6 and S3.7). As predicted, we find that EtBr intercalation is reduced for the closed topology (Fig. S3.7A-C), in excellent agreement with our model. More broadly, the relative effect of DNA topology depends both in the initial linking number ΔLk_0 and on the intercalator concentration (Fig. 3.2D).

Our model predicts that topology dependent binding is most pronounced at ligand concentration below the K_d (Fig. 3.2D, the K_d value is indicated as a vertical line). At concentrations greater than the K_d, binding saturates and the modulation by the torsional strain in the topologically closed plasmid is predicted to only lead to small or negligible changes in binding compared to the torsionally relaxed forms. To test this prediction, we carried out measurements using the intercalator SYBR Gold [19,47,48], which has a much lower K_d (i.e. higher affinity) compared to EtBr (Table 1, Fig. 3.2E, and Fig. S3.8). Performing measurements with initially negatively supercoiled or relaxed plasmids at different SYBR Gold concentrations around and above its K_d, we find that indeed the topologically closed and open constructs bind similar amounts of SYBR Gold, in quantitative agreement with our model (Fig. 3.2E). To show the broad range of applications, we used three different assays to obtain fluorescence intensity data for SYBR Gold, namely gel electrophoresis, a well plate reader, and a qPCR cycler (see Methods for details). In addition, we performed control measurement with different plasmids, notably a shorter (2.7 kbp) and longer (7.2 kbp) construct, compared to the pBR322 plasmid with 4361 bp. We find similar results, within experimental error, for the different plasmids (Fig. S3.9), suggesting that the results do not strongly depend on DNA sequence or length. We note that our model predicts that there is no dependence of the topology effects on DNA length, which is born out experimentally in the length range investigated (Fig. S3.9). Importantly, the almost topology-independent binding of DNA intercalators above their K_d is advantageous for assays that aim to quantitatively compare different DNA topologies, e.g., to monitor the products of integration or topoisomerization reactions [62,76-78]. In particular, for SYBR Gold DNA staining is essentially unbiased by topology for dye concentrations in the range of 1-2 μM, which is the concentration range that we previously identified as optimal for achieving a linear relationship between the fluorescence signal and the amount of DNA present [19].

3.2.4 Psoralen-based DNA crosslinking to detect DNA torsional tension

Intercalators of the psoralen family can crosslink DNA upon irradiation with UV light (Fig. 3.3A). They have been widely used in phototherapy [55] and to detect chromatin

structure and the degree of DNA supercoiling *in vivo* [8,56-59]. Often it is assumed as a simplification that the amount of DNA crosslinking varies linearly with the supercoiling density σ [57,59]. Our model for intercalation under the global constraint induced by topology accurately captures the relative binding of the psoralen compound TMP to supercoiled DNA vs. nicked DNA, determined from a radioactivity assay using ^{3}H-labeled TMP [57] (Fig. 3.3B). Similarly, our model correctly predicts the degree of crosslinking induced by TMP for different supercoiling densities [59] (Fig. 3.3C and Fig. S3.10A). Importantly, the crosslinking conditions are chosen such that at most one crosslinking event per plasmid is induced, which means that only a small fraction of the intercalated TMP molecules reacts.

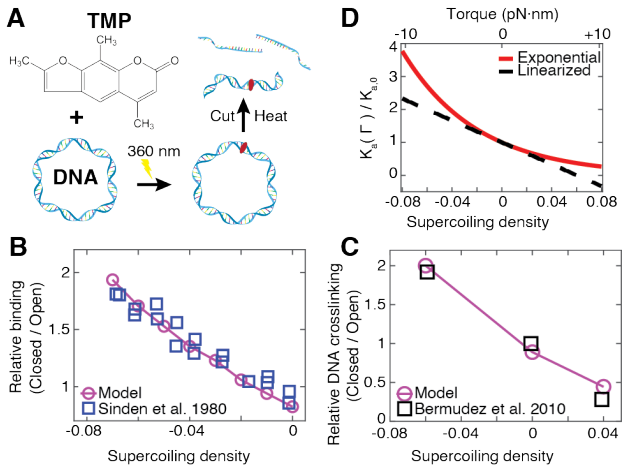


Figure 3.3. Topology-dependent DNA crosslinking by trimethylpsoralen. A) *4,5',8-trimethylpsoralen (TMP) intercalates into DNA and causes DNA crosslinking upon UV irradiation. DNA supercoiling-dependent crosslinking is widely used to probe DNA supercoiling and chromatin conformations in vivo.* ***B)*** *Binding of TMP to supercoiled DNA plasmids with different initial supercoiling densities relative to open circular DNA. Experimental binding data are from Ref. [57] and were determined using the radioactivity of ^{3}H-labeled TMP.* ***C)*** *Binding of TMP to supercoiled DNA plasmids. Experimental data are from Ref. [59] and were obtained by quantifying the amount of DNA crosslinking after irradiation. Experimental data are normalized to the data point at zero supercoiling density. The model in panels B and C uses the parameters in Table 1 and quantified binding to supercoiled relative to topologically open DNA.* ***D)*** *Dependence of the torque-dependent association constant (the inverse of the dissociation constant) on supercoiling density using Equations 2-6 (red solid line). The black dashed line shows the linearization of Equation 2, i.e., the approximation $\exp(-x) \approx 1 - x$, with $x = \Gamma \cdot \Delta\theta / k_B T$.*

For example, under the conditions of the data in Fig. 3.3C, there are > 10 TMP molecules bound (Fig. S3.10B), but < 1 on average react. However, the fact that the crosslinking signal is well approximated by our binding model using a proportionality constant analogous to Equation 7, suggests that crosslinking is directly proportional to binding. While TMP binding is at least approximately linear with supercoiling density in the range investigated in Fig. 3.3B and C, a linear relationship is only an approximation to the intrinsic exponential dependence on torque [26,27,33] and its validity is limited to relatively small supercoiling densities (Fig. 3.3D).

3.2.5 Single-molecule assay monitors supercoiling-dependent binding in real time

To explore consequences of supercoiling dependent binding at the single-molecule level, we investigated ligand binding to DNA under a topological constraint via single-molecule fluorescence imaging. In our assay, we attached DNA via multiple biotin-streptavidin bonds at each end to a surface (Fig. 3.4A), ensuring that the molecule is topologically constrained. While the surface attachment stretches the molecules, the effective stretching forces are very low and are estimated to be ≤ 0.1 pN under the conditions of our experiments (Fig. S3.11).

Adding the intercalator SYTOX Orange enables us both to induce supercoiling in the DNA and to visualize the molecules using fluorescence imaging [51,54]. To systematically study the effect of topology, we performed two different types of experiments (Materials and Methods). In the first case, we prepared negatively supercoiled DNA by first staining with the intercalative dye SYTOX Orange at a high concentration (250 nM), then attaching the DNA to the surface to topologically constrain it, and subsequently imaging at a lower concentration (50 nM). Following the reduction of SYTOX Orange concentration, plectonemic supercoils are clearly visible as bright spots that diffuse along the length of the DNA molecules, as has been observed previously [51,54,79,80] (Fig. 3.4B,C).

During continuous observation and laser exposure, DNA molecule will nick at some point, likely due to radicals generated by photochemical processes [81,82], which is usually an undesirable feature. However, here we use nicking upon illumination to our advantage since it enables us to observe both the supercoiled (closed) and subsequently the nicked (open) and finally torsionally relaxed state of the same DNA molecule. Upon nicking, the fluorescence intensity suddenly decreases significantly (Fig. 3.4D) and the bright spots indicative of plectonemic supercoils disappear (Fig. 3.4B,C). This is in line with our previous observations: The negative supercoiling helps intercalation, consequently,

once the molecule nicks, less SYTOX Orange binds and the fluorescence intensity decreases.

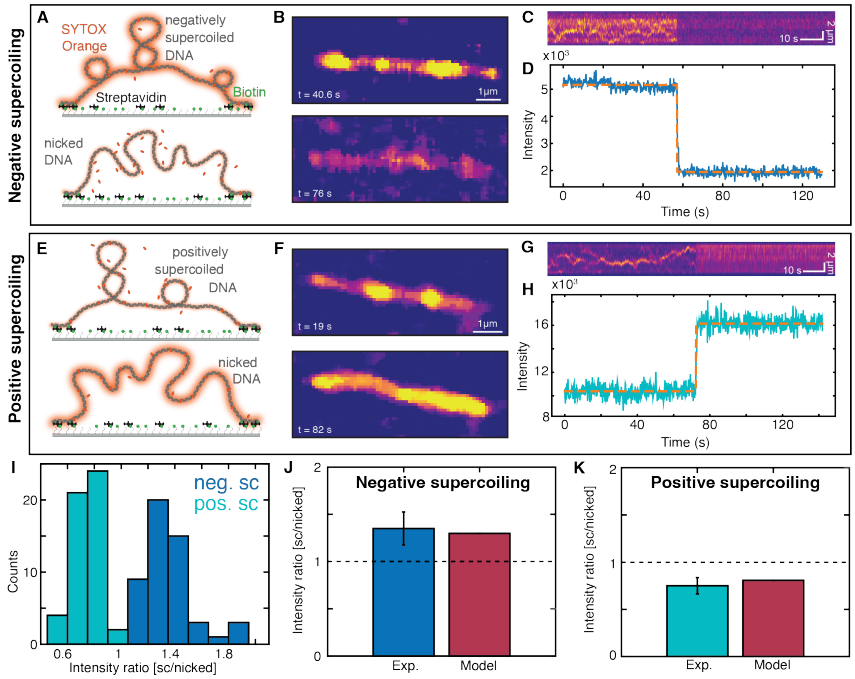


Figure 3.4. Single-molecule fluorescence assay to quantify topology dependent binding. A) *Schematic representation of the experimental set up. The SYTOX Orange-stained DNA is tethered at both its ends via multible biotin-streptavidin bonds to the surface. Top: negatively supercoiled DNA; bottom: nicked DNA.* ***B)*** *Fluorescence image snapshots at 40.6 s when the DNA is still negatively supercoiled and at 76 s after the DNA was nicked.* ***C)*** *Kymograph of SYTOX-Orange stained-DNA. When the DNA is nicked, the intensity decreases abruptly.* ***D)*** *Integrated fluorescence intensity of the kymograph shown in panel C. The dotted orange line is a fit of a two-state hidden Markov model to the data* [83]. ***E)-H)*** *Same as A-D) for positively supercoiled DNA.* ***I)*** *Intensity ratios before and after nicking for originally negatively supercoiled DNA (blue) and for originally positively supercoiled DNA (turquoise). Averaging gives 1.35 ± 0.18 (N= 51, mean ± std; ratio sc/nicked) for originally negatively supercoiled DNA and 0.75 ± 0.09 (N= 51, mean ± std; ratio supercoiled/nicked) for originally positively supercoiled DNA.* ***J)*** *Comparison of the experimental intensity ratio to the value from theoretical modeling for originally negatively supercoiled DNA from N = 51 molecules.* ***K)*** *Comparison of the experimental intensity ratio to the value from theoretical modelling for originally positively supercoiled DNA from N = 51 molecules.*

For the second type of experiment, we prepared positively supercoiled DNA by attaching the DNA to the surface in the presence of a low SYTOX Orange concentration (25 nM; Fig. 3.4E). We then increased the dye concentration (to 250 nM), but since positive supercoiling hinders intercalative binding to the DNA, the fluorescence intensity stays relatively low. Again, plectonemic supercoils appear as bright spots that diffuse along the DNA molecule (Fig. 3.4F,G). After the positively supercoiled molecule is nicked, we observe that the fluorescence intensity increases (Fig. 3.4H). Importantly, our assay enables us to quantify the change in fluorescence intensity upon changes in topology by integrating the intensity over the entire molecule, before and after nicking (Fig. 3.4D and H). We find a decrease in fluorescence intensity upon nicking for initially negatively supercoiled DNA of 1.35 ± 0.18 (mean ± std; ratio supercoiled/nicked) and an increase in fluorescence intensity upon nicking for initially positively supercoiled DNA of 0.75 ± 0.09 (mean ± std; ratio supercoiled/nicked) (Fig. 3.4I).

To quantitatively model the changes in fluorescence upon nicking observed *in situ*, we used our model with the parameters reported by Biebricher *et al.* [49] for the binding site size n, elongation per dye Δz, and binding constant K taken in 100 mM NaCl, which approximately corresponds to the ionic strength in our experiments (40 mM Tris-HCl, 2.5 mM $MgCl_2$, 65 mM KCl). The unwinding angle per intercalation event $\Delta\theta$ is not known for SYTOX Orange; we assume $\Delta\theta = 19.1°$, which is the value for SYBR Gold [19] since the dyes are relatively similar dyes and also generally values in the range of about 20° are typical [19,31,84]. Importantly, the model is applied here in two stages: We first compute the supercoiling density, relatively to relaxed, bare DNA and in the absence of intercalator, induced by attaching the DNA in the presence of 25 and 250 nM SYTOX Orange, which are $\sigma = 2.7\%$ and $\sigma = 9.7\%$, respectively. We then compute binding to DNA and re-adjustment of the supercoiling level at the new SYTOX Orange concentrations used for imaging (250 and 50 nM, for which we find $\sigma = +5.2\%$ and $\sigma = -3.9\%$), using the levels of supercoiling obtained in the first step as an input. For comparison, we compute binding to topologically open DNA, which enables us to calculate the changes in fluorescence upon nicking (Fig. 3.4J,K). Here, we observe an excellent agreement between the predictions of our computed model and the experimentally observed changes in fluorescence intensity upon torsional relaxation in our single molecule experiments (Fig. 3.4J,K).

3.2.6 High-speed fluorescence tracking reveals binding dynamics

To quantitatively study the dynamics of intercalation into DNA under topological constraint, we performed single-molecule fluorescence imaging at a 20 ms frame rate

(Fig. 3.5), ten times faster than the data shown in Fig. 3.4. By fitting a simple kinetic model to the fluorescence intensity traces (Fig. 3.5A,B and E,F) at the transition between supercoiled and nicked DNA, we are able to determine the on- and off-rate of SYTOX Orange.

Our kinetic model for the total fluorescence intensity of the initially supercoiled molecules, reads as follows:

$$I(t) = I_{initial} \text{ for } t < t_0 \text{ and } I(t) = I_{initial} + (I_{final} - I_{initial}) \cdot (1 - \exp[-k \cdot (t - t_0)]) \qquad (8)$$

Where the initial intensity $I_{initial}$, the final intensity I_{final}, the rate k, and the time at which the intensity begins to change t_0 are fitting parameters. For the DNA molecules that are negatively supercoiled prior to nicking, we find a reduction in fluorescence intensity with overall rate $k = (2.16 \pm 0.38)\ s^{-1}$ (mean ± sem from 32 traces; Fig. 3.5D), which is close to the off-rate extrapolated to zero force reported by Biebricher *et al.* of $(3.2 \pm 0.8)\ s^{-1}$ using a single-molecule stretching assay [49]. Conversely, starting with positively supercoiled DNA prior to nicking, we find an increase in intensity with an overall rate $k = (1.92 \pm 0.26)\ s^{-1}$ (mean ± sem from 22 traces; Fig. 3.5H). Assuming that this increase is due to binding with a simple bimolecular association rate, we find an on-rate of $(7.68 \pm 1.3) \cdot 10^6\ M^{-1}s^{-1}$ (since the SYTOX Orange concentration is constant at 250 nM in this case), again in agreement to the on-rate reported by Biebricher *et al.* of $(7.9 \pm 2.6) \cdot 10^6\ M^{-1}s^{-1}$ [49]. The very good agreement of our fitted overall rates with previously published on- and off-rates for SYTOX Orange suggests that binding and dissociation of the dyes and not the relaxation of torsional strain is rate limiting for the observed changes in fluorescence intensity. This is consistent with estimates from simulations that suggest that relaxation of torsional strain in DNA occurs on ~µs time scales for ~kbp DNA segments [85]. The disappearance of the fluorescent spots (Fig. 3.5C and G) allows us to estimate the dynamics of the writhe relaxation upon nicking, i.e., the time scale over which the plectonemic supercoils are resolved. We observe the disappearance of fluorescent spots over at least 3-4 frames (Fig. S3.12), suggesting that writhe relaxation occurs over ≥ 80 ms in our assay. The observed time scale for plectoneme disappearance is very similar to the lifetime of plectonemes before "hopping" events that have previously been detected by fluorescence imaging [79], suggesting that writhe relaxation occurs via "hopping" relaxation to a nick. Conversely, our measurements suggest that writhe relaxation does not occur predominantly by diffusion of plectonemes along the DNA to the nicking site, which would take on the order of $\tau \approx L^2/D \geq 3$ s, where L is the length over which diffusion occurs ($L \geq 1$ µm) and D the diffusion coefficient, which is $\leq 0.3\ \mu m^2/s$ [79].

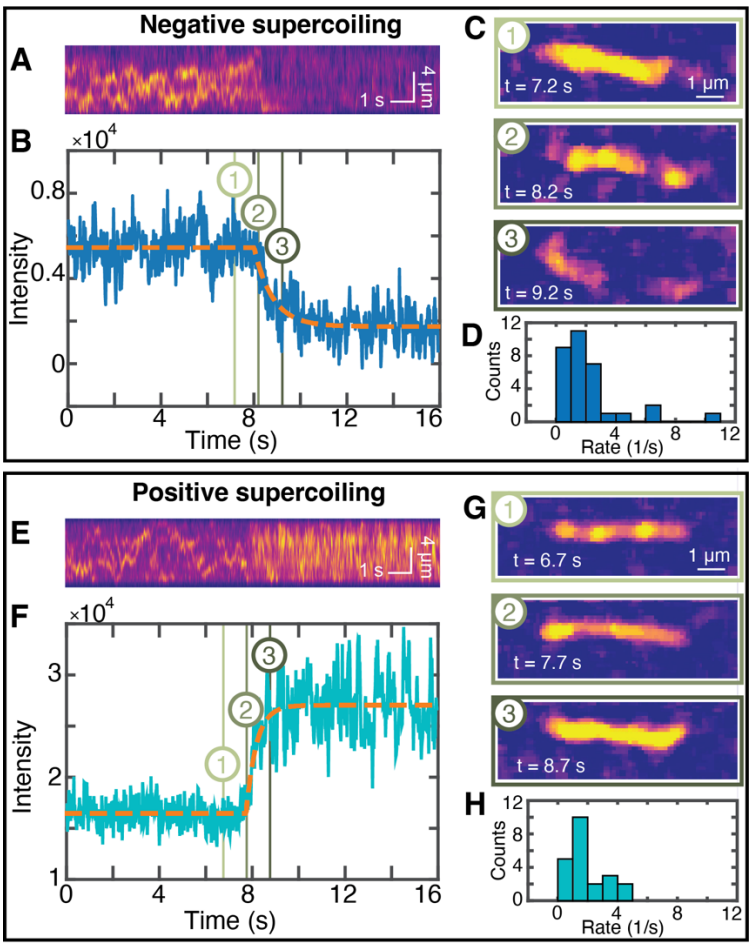


Figure 3.5. Probing the interplay of dye and supercoil dynamics. A)-D): Negatively supercoiled DNA. A) *Kymograph of SYTOX-Orange stained-DNA. When the DNA is nicked, the intensity decreases abruptly.* ***B)*** *Integrated fluorescence intensity of the kymograph shown in panel A. The dotted orange line is a fit of the model shown in Equation 8 to the data.* ***C)*** *Fluorescence image snapshots at 7.2 s when the DNA is still negatively supercoiled, at 8.2 s when the nick occurs, and at 9.2 s after the DNA was nicked. Time points are indicated by matching numbers in panel B.* ***D)*** *Experimentally determined rates k for fluorescence decrease from the fits of Equation 8 to time traces from N = 32 independent measurements. The mean ± sem are (2.16 ± 0.38) s^{-1}.* ***E-G)*** *Same as A-C) for positively supercoiled DNA molecules.* ***H)*** *Experimentally determined rates k for the increase in fluorescence after nicking from N = 22 independent measurements. The mean ± sem are (1.92 ± 0.26) s^{-1}.*

3.3 Discussion

We have developed a quantitative model to describe DNA binding under supercoiling constraints that integrates aspects of previous models [26,27,33]. Importantly, all parameters in our model have clear physical interpretations and can be determined independently (see e.g. Table 1), enabling quantitative predictions. Intriguingly, supercoiling DNA with a global topological constraint can increase or decrease binding, depending on the concentration and binding regimes [27]. Fig. 3.1F and 3.2C). This is an important difference to applied stretching forces, which similarly can modulate binding in an Arrhenius-like exponential dependence [30,45,49], but will bias binding in only one direction.

Using the well-characterized and widely used intercalators, SYBR Gold and ethidium bromide, we could show that topology-dependent binding depends on initial topology and intercalator affinity. In particular, we demonstrate that binding of DNA intercalators above their K_d is almost supercoiling independent. With this, we can provide recommendations for optimal use of intercalative dyes to visualize DNA under a topological constraint: To avoid biases due to torque-dependent binding, a dye with a low K_d should be used, ideally at concentrations well above the K_d. Specifically, SYBR Gold at a concentration of 1-2 µM satisfies this criterion. Importantly, SYBR Gold at 1-2 µM concentration is also the optimal concentration range to obtain a high signal as well as a linear relation between DNA amount and fluorescence intensity [19]. In general, the choice of intercalator type and concentration range is crucial for reliably topology-unbiased DNA staining and quantification and to obtain consistent results with other approaches of DNA quantification.

Moreover, our model can quantitatively account for observations made with the widely-used intercalator psoralen for UV-induced DNA crosslinking. Importantly, in applications where intercalation is used to detect supercoiling, a dye with a high K_d (i.e. low affinity) and large unwinding angle is desirable.

We present a single-molecule assay to observe supercoiling dependent binding of SYTOX Orange to DNA in real time. We find good agreement between the theoretical predictions of our model and the experimentally observed changes in fluorescence intensity upon torsional relaxation. High-speed tracking allows us to infer information about the binding dynamics of SYTOX Orange to DNA. We find overall on- and off-rates in good agreement with previously published rates for SYTOX Orange, suggesting that binding and dissociation of the dyes, rather than torsional relaxation, is rate limiting for the observed changes in fluorescence intensity.

Taken together, our work shows how combining theoretical modeling and multiple complementary experimental techniques can provide a highly quantitative and comprehensive view of DNA-ligand interactions under a global topological constraint. As future directions, our modeling approach could be extended to take into account topoisomer distributions, non-canonical DNA structures (e.g. flipped bases or melting bubbles), or sequence dependencies [54,86-88]. We anticipate our approach to be broadly applicable to other DNA binding agents and allow for reliable and unbiased detection and quantification of different topological states of DNA. In addition, the interplay of DNA binding and topology has important implications for the processing and regulation of genetic information *in vivo*. In the cell, DNA forms topological domains and e.g. advancing polymerases introduce torsional strains of different handedness [1,2,89-92]. Together, these factors are expected to modulate binding to DNA, e.g. by nucleosomes and transcription factors, also in a cellular context. Our results provide a baseline to quantitatively investigate these complex processes in the future.

3.4 Materials and methods

3.4.1 Plasmid DNA preparation

We used the commonly used plasmid pBR322 (NEB, catalogue number N3033S) as the DNA substrate for bulk measurements of intercalation. We prepared different topological states of the DNA by cutting (i.e. introducing a double-strand break) or nicking (i.e. a DNA single-strand break) the original supercoiled DNA to obtain linear and open circular DNA, respectively. Reactions were performed in NEBuffer 3.1 (NEB) using the enzymes EcoRV (NEB; incubation temperature 37 °C) to prepare linear DNA and Nt.BspQI (NEB; incubation temperature 50 °C) to create open circular DNA. The reactions were stopped after one hour by heat inactivation at 80 °C for 20 minutes. The products were purified with a PCR clean-up kit (Qiagen). For the topologically closed and initially negatively supercoiled condition, the plasmid was only cleaned with a PCR clean-up kit (Qiagen) and we assume an initial supercoiling density of $\sigma \cong -5\%$, as previously reported [76,93-96]. Additionally, we prepared topologically closed but initially relaxed plasmids by incubation with Wheat Germ Topoisomerase I. For a total volume of 100 µl, 16.2 µl assay buffer (50 mM Tris HCl, 1 mM EDTA, 1 mM DTT, 20% (v/v) glycerol, 50 mM NaCl, pH 7.9), 82.12 µl RNase-free water, 2.16 µl topoisomerase I, 0.52 µl pBR322 (c = 1000 ng/µl) were combined in a reaction tube and incubated for 1 h at 37 °C.

Control measurements used natively negatively supercoiled plasmids of different lengths and different sequences: pUC19 (2.686 kbp) and M13mp18 (7.249 kbp), both obtained similar from NEB (catalogue numbers N3041S and N4040S, respectively) and purified with a PCR clean-up kit (Qiagen). DNA concentrations were determined using a nanodrop UV/vis photospectrometer (ThermoFisher Scientific). To every 100 µl reaction volume, we added 20 µl Gel Loading Dye Purple (6x) (NEB, catalogue number B7024S) prior to running the gel. For the plate reader and qPCR cycler experiments, no gel loading dye was added.

3.4.2 DNA dilution series

For the DNA dilution series with negatively supercoiled DNA, the different topologies were combined to an equimolar mixture and diluted with Tris-acetate-EDTA (TAE) buffer (40 mM Tris, 20 mM acetic acid, and 1 mM EDTA, pH 8.6) and gel loading dye in a serial dilution to obtain 7 different DNA concentrations (Table S1). For the experiments using topoisomerase relaxed DNA, only the linear and the relaxed topologies were combined to an equimolar mixture and diluted with TAE buffer and gel

loading dye, again in a serial dilution to obtain 7 different DNA concentrations (Table S1).

3.4.3 AFM imaging of DNA plasmids

AFM imaging of plasmid DNA was performed as described previously [97-99]. In brief, for the AFM imaging, we deposited 20 µl of DNA at different topological states in TE buffer at a final concentration of 1 ng/µl on freshly cleaved poly-L-lysine (Sigma Aldrich, diluted to 0.01% in milliQ water; PLL)-coated muscovite mica. The sample was incubated 30 s before washing with 20 ml MilliQ water and drying with a gentle stream of filtered argon gas. After drying, the AFM images were recorded in tapping mode at room temperature using a Nanowizard Ultraspeed 2 (JPK, Berlin, Germany) AFM with silicon tips (FASTSCAN-A, drive frequency 1400 kHz, tip radius 5 nm, Bruker, Billerica, Massachusetts, USA). Images were scanned over different fields of view with a scanning speed of 5 Hz. The free amplitude was set to 10 nm. The amplitude setpoint was set to 80% of the free amplitude and adjusted to maintain a good image resolution. AFM image post-processing was performed in the software SPIP (v.6.4, Image Metrology, Hørsholm, Denmark) to flatten and line-wise correct the images (Fig. S3.2).

3.4.4 Gel electrophoresis

For gel electrophoresis we used 1%-broad-range-agarose (Carl Roth) gels and TAE buffer. We used the 1 kb gene ruler (Thermo Scientific; 5 µl) as a size standard. The gels were run for 120 min at 75 V at 4 °C. Subsequently, the gels were removed from the gel box and placed for 20 minutes in 100 ml of 0.5 µM (1:100000 dilution of the stock; 2 independent gels), 5 µM (1:10000 dilution of the stock; 7 independent gels), or 50 µM (1:1000 dilution of the stock; 2 independent gels) EtBr in TAE buffer, respectively, for staining. Subsequently, the gel was de-stained in TAE buffer for 15 min. The gels were visualized using a Gel Doc XR+ system (Biorad). The same procedure was employed for SYBR Gold staining, except that the gels were stained for 20 minutes in 100 ml of 3 (1:4000 dilution of the stock; 2 gels in total) or 6 µM (1:2000 dilution of the stock; 2 gels in total). Since the dye concentration used in staining is reduced by the agarose gel matrix and the de-staining step, we used a staining correction factor of 0.1 as determined previously [19], which we use to correct all gel data.

3.4.5 Gel electrophoresis image analysis

We saved the images from the Gel Doc system in scn format to allow for quantitative fluorescence intensity analysis. The software SPIP (v.6.4, Image Metrology, Hørsholm, Denmark) was used to remove spikes from the image (without changing the intensity of the bands) and to generate average intensity profiles along each lane of the gel. In a next

step, we used Origin (OriginLab, Northampton, Massachusetts, USA) to flatten the background of the profiles and to convert the peaks into fractions of supercoiled, open-circular, linear, and/or relaxed DNA respectively, by calculating the area under the lane profiles (Supplemenary Fig. S3.3).

3.4.6 Bulk fluorescence experiments

For the SYBR Gold bulk fluorescence measurements, we used a well plate reader (Tecan Infinite M1000 PRO; well plates: corning black polystyrene 384 well microplate with a flat bottom, Sigma-Aldrich, catalogue number: CLS3821) and a qPCR cycler (CFX96 Touch Real-Time PCR Detection System, BioRad). In the well-plate reader, the DNA mix including various SYBR Gold concentrations was filled in the wells and the fluorescence was read out from the bottom of the wells. The excitation and emission bandwidths were set to 5 nm, the gain to 100, the flash frequency to 400 Hz, and the integration time to 20 s. We chose the excitation and emission wavelengths - according to the excitation and emission maxima for SYBR Gold provided by Invitrogen - to be 495 nm and 537 nm.

In the fluorescence bulk experiments using a qPCR cycler, the DNA was filled into low-profile PCR tubes (Bio Rad, Nucleic Acids Research, 2021 5, product ID: TLS-0851), closed with flat, optical, ultra-clear caps (Bio Rad, product ID: TCS-0803) since the fluorescence was read out from the top of the tubes (at 24 °C). As read-out channels, channels with absorption and emission wavelengths of 494 and 518 nm, respectively, were chosen because these were the closest match to those of SYBR Gold.

3.4.7 Single-molecule fluorescence experiments

Supercoiled DNA were prepared and imaged at the single-molecule level essentially as described previously [51,54]. Experiments were performed in custom-made flow cells built by connecting a surface-passivated glass slide and a glass coverslip using double-sided tape [51]. The surface of the glass slides was prepared as previously described [100] with slight modifications. In brief, after extensive cleaning, the surface was silanized using APTES (10% v/v) and acetic acid (5% v/v) methanol solution. The surface was passivated with NHS-ester PEG (5,000 Da) and biotinylated NHS-ester PEG (5,000 Da) in relation 40:1. The biotinylated NHS-ester PEG allowed us to tether the DNA molecules to the surface via biotin-streptavidin interactions.

The DNA used for intercalation with SYTOX Orange was prepared as described in Ref. [101] with the exception of introducing multiple-biotin handles at the DNA ends to allow the torsional constrain on the DNA rotation. To introduce multiple biotins on the DNA handles we performed a PCR on pBluescript SK+ (Stratagene) with GoTaq G2 DNA

polymerase (Promega, M7845), in the presence of biotin-16-dUTP (Jena Bioscience, NU-803-BIO16-L) and dTTP (Thermo Fisher Scientific, 10520651) in molar ratio of 1:4, respectively. The PCR was done using primers: ACCGAGATAGGGTTGAGTG and CAGGGTCGGAACAGGAGAGC, resulting in a 1,238 bp DNA fragment that contained multiple biotins randomly incorporated due to the presence of biotin-16-dUTP modified nucleotides. The PCR products were cleaned up using a standard purification kit (Promega, A9282) and we digested both the biotin handle and large 42 kb DNA plasmid with SpeI-HF (New England Biolabs, R3133L) for 2 h at 37 °C. The reaction was stopped by subsequent heat-inactivation for 20 min at 80 °C. This resulted in linear 42 kbp DNA and ~600-bp biotin handles. The digested products were mixed, using a 10:1 molar excess of the biotin handle to linear plasmid. We then added T4 DNA ligase (New England Biolabs, M0202L) in the presence of 1 mM ATP overnight at 16 °C and subsequently heat-inactivated for 20 min at 65 °C. The resulting coilable 42 kbp DNA construct was cleaned up by size exclusion chromatography on an ÄKTA pure system, with a homemade gel filtration column containing approximately 46 ml of Sephacryl S-1000 SF gel filtration media (Cytiva), run with TE + 150 mM NaCl buffer. The sample was run at 0.2 ml·min^{-1}, and we collected 0.5 ml fractions.

For immobilization of the 42 kbp biotinylated-DNA, we introduced 100 µl of ~0.5 pM DNA molecules at a flow rate of 4.2 µl/min in imaging buffer with no oxygen scavenging system components (40 mM Tris-HCl, 2 mM Trolox, 2.5 mM $MgCl_2$, 65 mM KCl). The buffer during the DNA immobilization step contained either a low SYTOX Orange concentration (25 nM; to allow introducing positive supercoiling in a later step, see below), or high concentration of SYTOX Orange (250 nM; to allow introducing negative supercoiling in a later step, see below) during initial immobilization.

Immediately after the introduction of DNA molecules into the flow cell, we further flowed 100 µl of the same buffer without the DNA at the same flow rate to ensure stretching and tethering of the other end of the DNA to the surface (which introduces the topological constraint) as well as to remove unbound DNA molecules. To introduce plectonemic supercoils into the bound DNA molecules that are torsionally constrained, we change the SYTOX Orange concentration by introducing imaging buffer with the same salt concentration but with varying SYTOX Orange concentration and an oxygen scavenging system for imaging (40 mM Tris-HCl, 2 mM Trolox, 2.5 mM $MgCl_2$, 65 mM KCl, 2.5 mM protocatechuic acid (PCA), 50 nM protocatechuate-3,4-dioxygenase (PCD)) [102]. For positive supercoiling we increased the concentration from 25 nM during immobilization to 250 nM SYTOX Orange, while for the negative supercoiling we reduced the concentration from the initial binding at 250 nM to a final concentration of 50 nM for imaging. In both cases we checked for a visible presence of supercoiling on

the DNA by observing moving foci appearing along the DNA molecules (Supplementary Movies S1 and S2 – in original publicaiton). Thus, supercoiling was introduced by differential SYTOX Orange concentrations between the DNA-binding step (where torsional constraint is ensured via multiple biotin molecules) and the imaging step where SYTOX Orange concentration is increased or reduced in order to generate positive or negative supercoils, respectively. For the direct visualization of plectonemic DNA extruded to the side we used a second outlet connected to a syringe. After initial imaging of supercoiled DNA without flow, we applied a strong outflow through the side outlet to extrude the plectonemic DNA sideways. We performed the side flow experiments using the same imaging buffer as the measurements without flow, to maintain the same level of supercoiling and environmental conditions.

For fluorescence imaging, we used a home-built objective-TIRF microscope. We employed continuous excitation with a 561 nm (15-20 mW) laser in Highly Inclined and Laminated Optical sheet (HiLo) microscopy mode, to image SYTOX Orange-stained DNA as well as to introduce DNA nicking. All images were acquired with an PrimeBSI sCMOS camera at an exposure time of 20-200 ms, depending on the experiment, with a 60x oil immersion, 1.49 NA CFI APO TIRF (Nikon). For DNA visualization, and kymograph generation, we used a custom written python software published in Ref. [103].

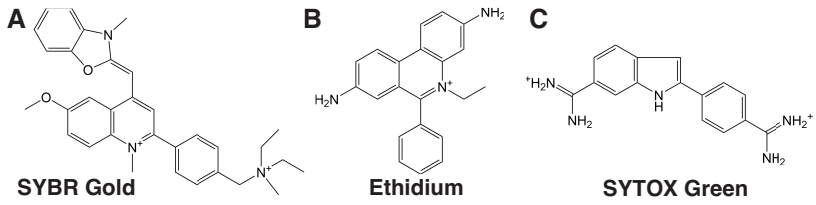
3.4.8 Numerical implementation of the binding model under topological constraint

To model the effects of the global constraint imposed by DNA topology on binding, we developed a model that takes into account changes in linking number due to intercalation and, conversely, torque-dependent binding (see the section “Model for ligand binding under topological constraint” in Results). The model comprises coupled Equations 1-6 that are solved iteratively using a custom routine written in Matlab (Mathworks). Input parameters are the temperature T and for DNA the number of base pairs N_{bp}, the torsional stiffness C, the initial linking difference ΔLk_0, and the DNA concentration c_{DNA}. N_{bp}, ΔLk_0, and c_{DNA} are typically known from how the DNA was prepared and we used a value $C = 100$ nm, unless otherwise noted [70,72,73]. For the single-molecule assay, the DNA concentration is poorly defined, but low, much lower than the intercalator concentration used. In this case, we used concentrations in the range of 1-100 pM·bp, which are much lower than the intercalator concentration used, but high enough to ensure numerical stability of the calculation. We found that the calculated results are insensitive to the concentration used in this regime.

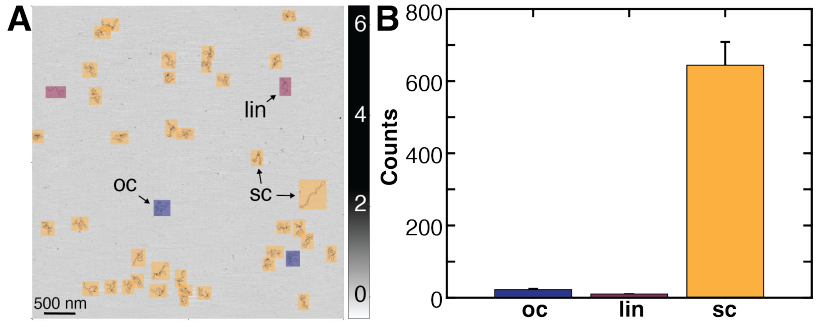
Input parameters for the intercalator are the binding site size n, the dissociation constant K_{d}, the length increase per intercalator bound Δz, the change in DNA helical twist per

intercalator bound $\Delta\theta$, and the intercalator concentration c_{total}. Values for n, K_d, Δz, and $\Delta\theta$ used in this work are provided in Table 1. The outputs of the model are the number of intercalator molecules bound per DNA molecule, the torque in the DNA, and the total fluorescence intensity expected, which contains an overall scaling factor α defined in Equation 7. Our numerical implementation uses the numerical solutions to the McGhee-von Hippel described previously [19,104] and a successive over-relaxation type approach [105] to speed up convergence. The code implementing out model is available in the public repository YODA at https://doi.org/10.24416/UU01-YDNOBO.

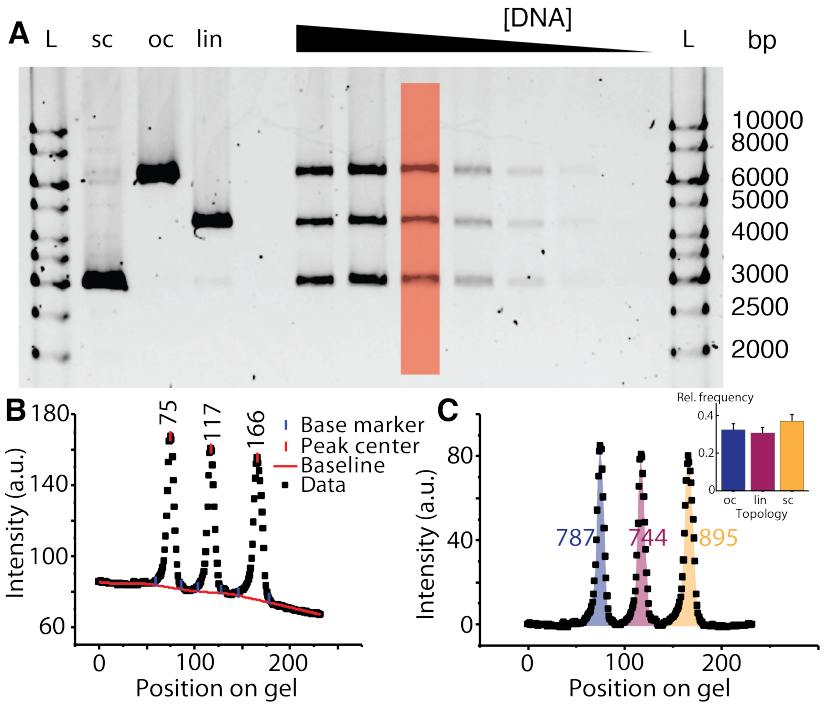
3.5 Supplementary data



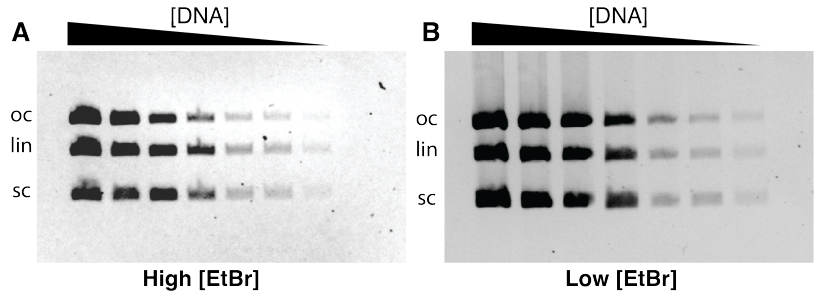
Supplementary Figure S3.1. Molecular structure of the three intercalators (A) SYBR Gold, (B) Ethidium, (C) SYTOX Green. *The SYBR Gold structure was taken from Reference [19], the Ethidium structure from reference [31]. Since the structure of SYTOX Orange, the dye used for the single-molecule fluorescence assay in this work, is unknown, we show the structure of the related dye SYTOX Green (taken from reference [106]) here.*



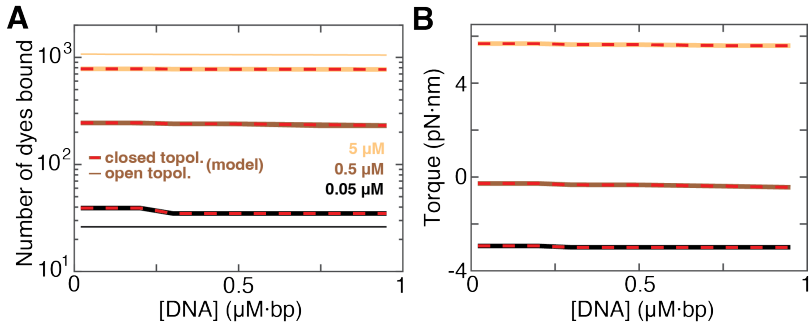
Supplementary Figure S3.2. DNA topology analysis and quality control via AFM imaging. A) *AFM height image of supercoiled pBR322 DNA at a concentration of 1 ng/μL deposited on PLL mica after drying in air. The different topologies are indicated with different colors, open circular DNA (oc) in blue, linear DNA (lin) in red, and supercoiled DNA (sc) in yellow. Z-ranges are indicated in nm by the scale bar on the right.* ***B)*** *Topology analysis from AFM experiments of pBR322 DNA that was also used as supercoiled DNA for gel experiments. From a total of 676 molecules, 95% are supercoiled, 3% open circular, and 2% linear. Error bars are from counting statistics.*



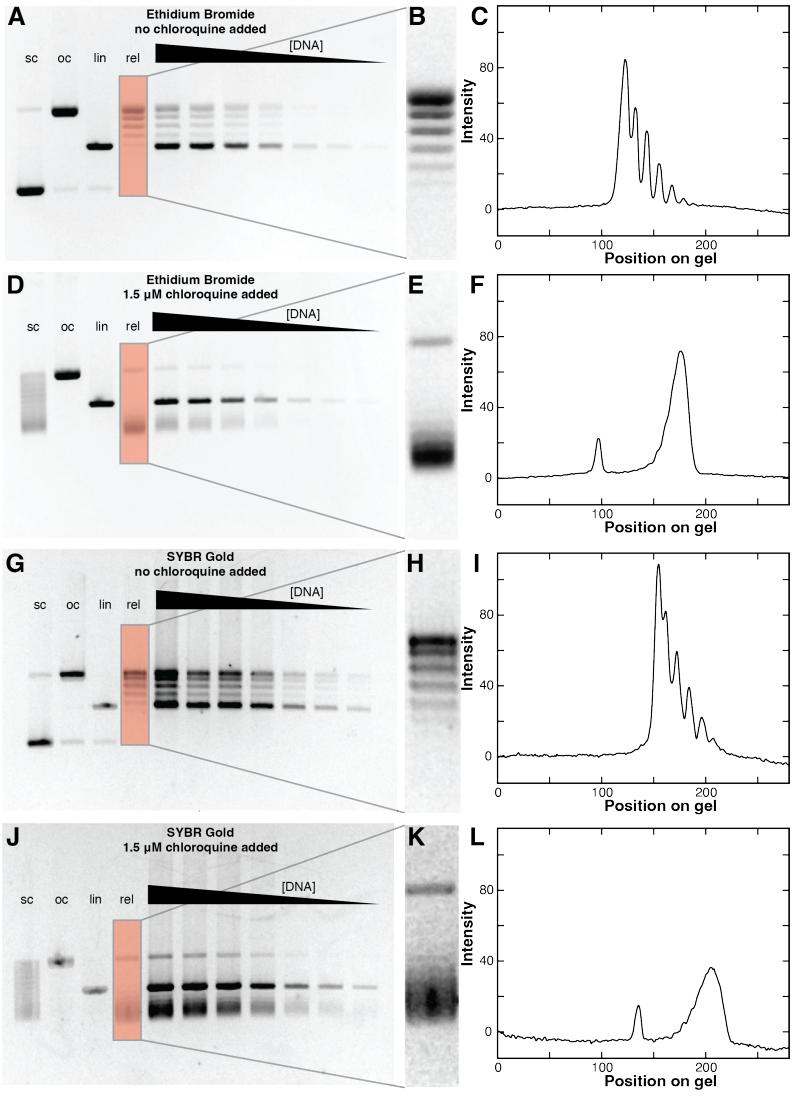
Supplementary Figure S3.3. Analysis of gel electrophoresis data. A) *Agarose gel stained with SYBR Gold at a final concentration of 0.3 μM. Different DNA topologies are separated on the gel. L: DNA size ladders (1 kb gene ruler, Thermo Scientific, 5 μL). Lanes 2-4 are the stock solutions of the supercoiled, linear, and open circular DNA, respectively. Lanes 6-12 are equimolar mixtures of the three topologies, at different total DNA concentrations. For quantitative analysis, individual lanes are selected (as highlighted in red) to create intensity profiles.* ***B)*** *Line profile of the area highlighted in red in panel A. Using the software Origin, a baseline is set and the peaks corresponding to the three topologies ("oc", "lin", "sc") are detected automatically.* ***C)*** *Same data as in panel B, only baseline corrected. The area under the peaks (which corresponds to the fluorescence intensity of the individual topologies) is calculated and used to determine the intensity ratios of the three topological states. Inset: integrated and normalized intensities of the individual peaks shown in panel C.*



Supplementary Figure S3.4. Agarose gel stained with EtBr at a final concentration of 5 µM (A) and 0.05 µM (B), respectively. *Different DNA topologies are separated on the gel. Lanes 1-7 are equimolar mixtures of the three topologies, at different total DNA concentrations, using the pBR322 plasmid, similar to Figure 2A.*

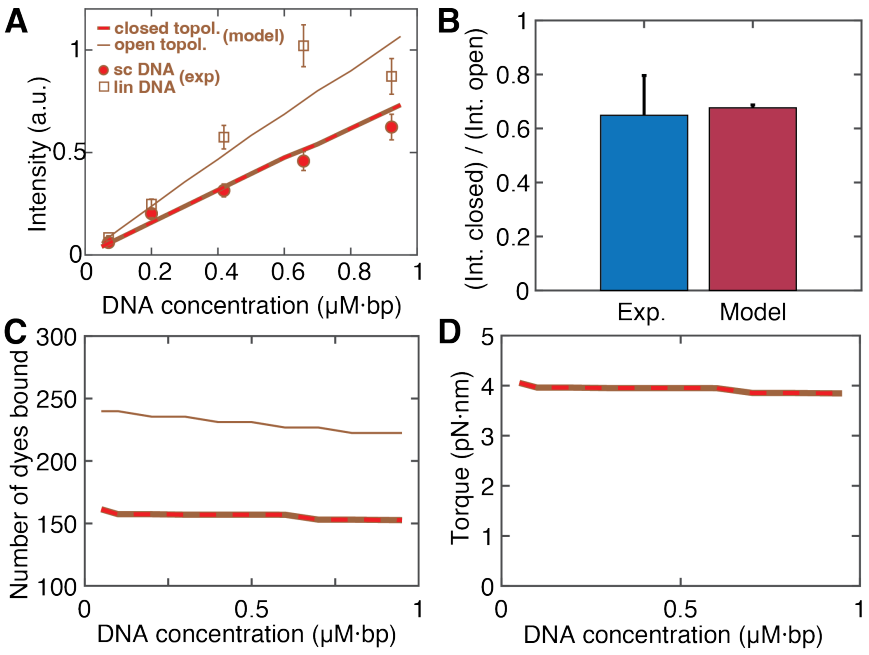


Supplementary Figure S3.5. Topology dependent binding of EtBr. A) *Predicted number of intercalated molecules N_{bound} as function of DNA concentration for pBR322 DNA (4361 bp). Different colors correspond to different EtBr concentrations: from dark to light 0.05, 0.5, and 5 µM. Thin lines are for topologically open DNA (linear and open circular); thick lines with red highlights are for topologically closed DNA (supercoiled, here with initial supercoiling density $\sigma \approx -5\%$, corresponding to $\Delta Lk_0 \approx -20$ turns). The number of molecules bound is approximately independent of DNA concentration under the conditions investigated, but clearly dependents on EtBr concentration and DNA topology.* ***B)*** *Predicted torque in the plasmid from our model, same color code as in panel A. The torque in the topologically open conformations is zero and not shown for clarity.*

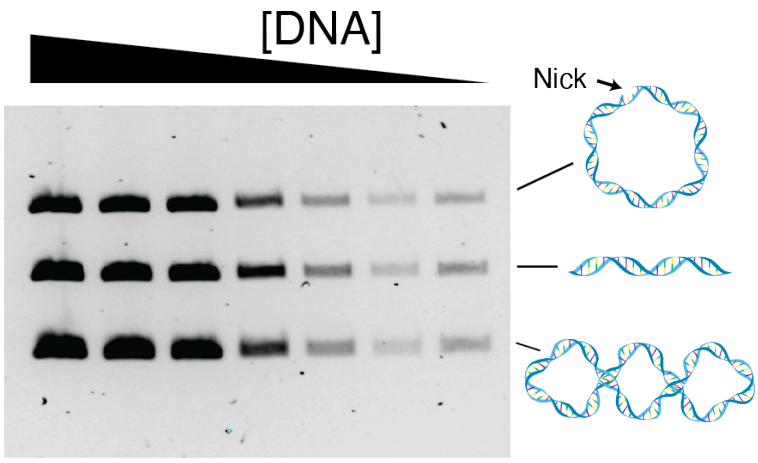


Supplementary Figure S3.6. Characterization of initially torsionally relaxed plasmids. *pBR322 plasmids where relaxed with Wheat Germ Topoisomerase I (Inspiralis) at 37 ºC in a assay buffer containing 50 mM Tris HCl, 1 mM DTT, 20% (v/v) Glycerol, 50 mM NaCl. Subsequently, gel electrophoresis was performed at 22 ºC in a running buffer containing 40 mM Tris, 20 mM NaAc, 1 mM EDTA.* ***A, D, G, J)*** *Gels were stained either using EtBr (A,D) or SYBR Gold (G,J). All gels contained the untreated supercoiled, open circular, and linear DNA for comparisons (lanes 1-3). Lane 4 contains the topoisomerase relaxed plasmid ("rel"). Lanes 5-11 contain equimolar mixtures of relaxed and linear plasmids and are further analyzed in Figure 2 and Supplementary*

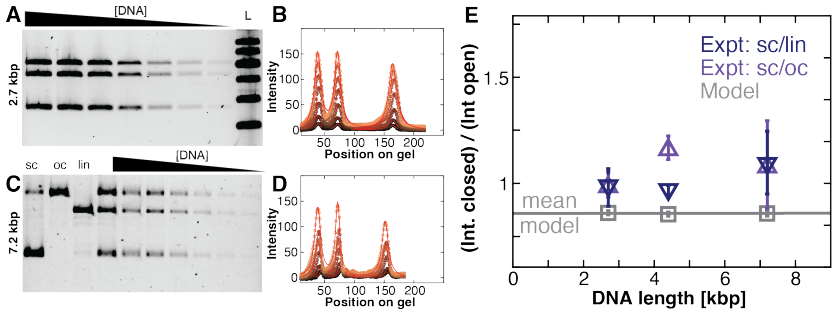
Figure S3.7. Gels in panels A and G used the regular running buffer. Gels in panel D and J used running buffer supplement with 1.5 μM chloroquine, an intercalator, which will unwind DNA and therefore introduce positive Wr. ***B, E, H, K)*** *Zoom into the gel images from panels A, D, G, and J, focusing on the lanes that have the relaxed plasmids only (lane 4).* ***C, F, I, L)*** *Lane intensity profile for the lanes that contain the relaxed plasmid only (lane 4). Lane profiles were obtained using the software SPIP (v.6.4, Image Metrology, Hørsholm, Denmark). Electrophoretic analysis of the relaxed plasmid in the absence of chloroquine (A and G) clearly shows individual bands that migrate close to and slightly faster than the oc species, i.e. are close to zero Wr. This is expected, since relaxation with topoisomerase I has been show to yield a Gaussian distribution of topoisomers centered on ΔLk = 0 [107,108]. We note that the ΔLk = 0 topoisomer will have a Wr slightly shifted from zero in our gels, since the relaxation reaction and gels used slightly different temperatures and salt conditions and since the DNA twist is temperature [107,109] and salt dependent [65,110]. However, we estimate this shift to be only about ΔWr ~ −1 turn. In the presence of chloroquine (D and J), the topoisomer distribution is shifted to positive Wr. Under the condition of our gels, the individual topoisomer bands are not well enough resolved to analyze them using the Depew and Wang approach [108]. Nonetheless, it is clear that the relaxed plasmid is close to ΔLk = 0, with a topoisomer distribution with a standard deviation of at most two ΔLk units, consistent with previous reports [111]. For simplicity, we model the "relaxed" plasmid condition using an initial value ΔLk = 0. Using initial linking numbers in the range ΔLk = ± 2 does not significantly change the results in Figure 3.2D and Figure S3.7B, within experimental error.*



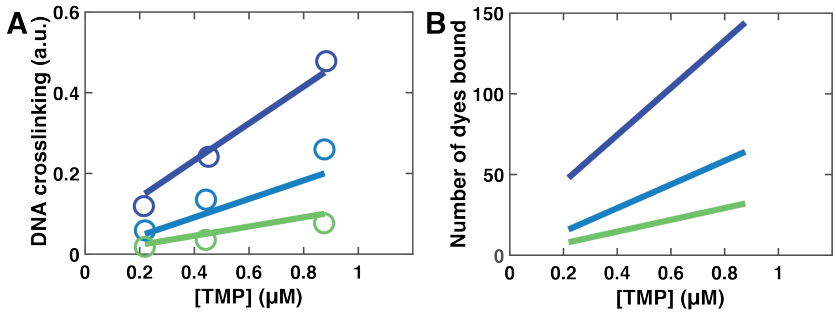
Supplementary Figure S3.7. Topology dependent binding of EtBr to initially relaxed plasmids. A) *Experimentally determined fluorescence intensity for topologically closed DNA (circles with red highlight) and linear DNA (squares) as a function of DNA concentration. The data are taken from the gel shown in Supplementray Figure S3.6A. Lines are predictions of our binding model (same color code as in Figure 2), with the scale factor α as the only fitting parameter (Equation 7). The EtBr concentration is 0.5 μM.* ***B)*** *Relative fluorescence intensity of a topologically closed DNA with* $\Delta Lk_0 \approx 0$ *relative to the topologically open DNA. The experimental data are the mean and std over different DNA concentration.* ***C)*** *Predicted number of intercalated molecules* N_{bound} *as function of DNA concentration for pBR322 DNA (4361 bp) with* $\Delta Lk_0 \approx 0$*. The thin line is for the topologically open DNA, the solid thick line with red highlighting for the topologically closed DNA. The number of molecules bound depends only weakly on DNA concentration under the conditions investigated but is clearly reduced for the closed DNA topology compared to linear DNA.* ***D)*** *Predicted torque in the plasmid from our model, same color code as in panel A,C.*



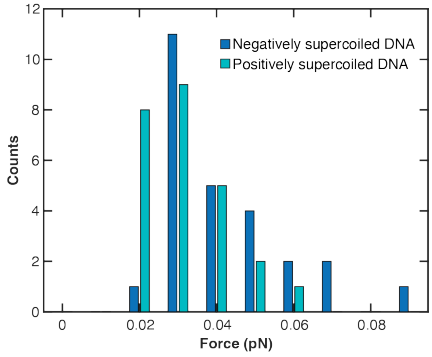
Supplementary Figure S3.8. Gel electrophoresis with SYBR Gold staining. *Agarose gel with equimolar mixtures of open-circular, linear, and supercoiled pBR322 plasmid DNA, stained with SYBR Gold at a final concentration of 0.6 μM.*



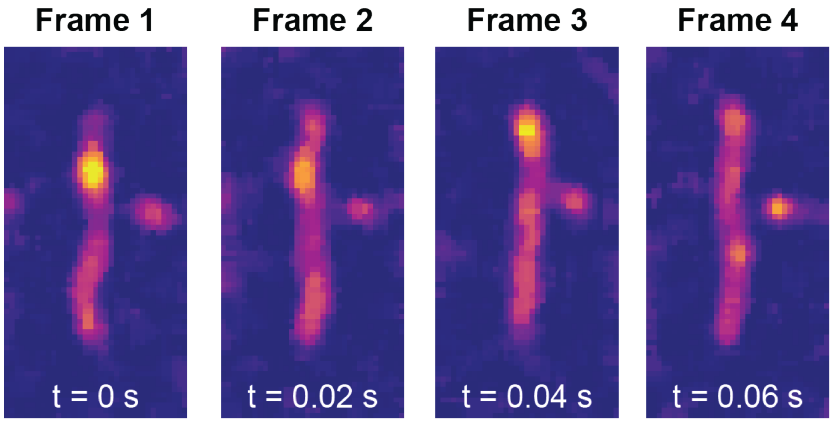
Supplementary Figure S3.9. Topology dependent intercalation of SYBR Gold for plasmids of different length. A,C) *Agarose gels stained with SYBR Gold at a final concentration of 0.6 μM for a 2.7 kbp DNA plasmid (A) and a 7.2 kbp DNA plasmid (C), see Methods for details. Plasmids are natively supercoiled and we assume a supercoiling density of $\sigma \approx -5\%$. The analysis of topology dependent intercalation of SYBR Gold is similar to what is shown in Figure 2A, except for the different DNA length. Lanes with different total DNA concentrations (lanes 1-7 in A and 4-10 in C) contain equimolar mixtures of supercoiled (bottom bands), linear (middle bands), and open circular (top bands) DNA. The ladder in the rightmost lane of panel A is a 1 kb gene ruler (Thermo Scientific) molecular mass standard.* ***B, D)*** *Lane intensity profiles of the lanes containing the different topoisomers in A and C, respectively, used for quantification of the intensity for each topological species and DNA concentration.* ***E)*** *Relative fluorescence intensity of the topologically closed DNA relative to the topologically open constructs. Experimental data points are obtained by averaging the different DNA concentration and indicate mean ± standard deviation. Gray symbols are the prediction of or model; the gray horizontal line is the mean for the three data points of the model, indicating that the model predicts the binding ratio to be independent of DNA length.*



Supplementary Figure S3.10. Model prediction for TMP binding to plasmid DNA. A) *Number of DNA crosslinks as a function of TMP concentration for DNA plasmids with different initial supercoiling density (from blue to green, top to bottom: σ = −0.06, 0, +0.04). Circles are the experimental data from Ref. [59]. Solid lines are the prediction of our model using the parameters in Table 1. B) Number of dyes bound as a function of TMP concentration. Same colour code as in panel A.*



Supplementary Figure S3.11. Estimate of the stretching forces acting on surface attached DNA molecules in our single-molecule assay. *Stretching forces for the surface tethered DNA molecules are estimated from the end-to-end distance [53] using the worm-like chain model [112-114]. Despite being stretched due to the surface attachment, the forces are very low, < 0.1 pN. The estimates shown are for nicked molecules, i.e. the effect of supercoiling is not taking into account. However, similar estimates taking into the reduction of the effective contour length due to plectonemic supercoiling still give low forces, < 0.2 pN.*



Supplementary Figure S3.12. Subsequent fluorescence image snapshots at the transition between negatively supercoiled and nicked DNA. *We observe that the fluorescent spots disappear over 4 frames (20 ms frame rate), suggesting that writhe relaxation occurs within approximately 80 ms.*

3.6 References

1. Liu, L.F. & Wang, J.C. Supercoiling of the DNA template during transcription. *Proc Natl Acad Sci U S A* **84**, 7024-7 (1987).

2. Koster, D.A., Crut, A., Shuman, S., Bjornsti, M.A. & Dekker, N.H. Cellular strategies for regulating DNA supercoiling: a single-molecule perspective. *Cell* **142**, 519-30 (2010).

3. Vologodskii, A.V. & Cozzarelli, N.R. Conformational and thermodynamic properties of supercoiled DNA. *Annual Review of Biophysics and Biomolecular Structure* **23**, 609-643 (1994).

4. Cook, P.R. & Brazell, I.A. Spectrofluorometric Measurement of the Binding of Ethidium to Superhelical DNA from Cell Nuclei. *European Journal of Biochemistry* **84**, 465-477 (1978).

5. Kouzine, F., Sanford, S., Elisha-Feil, Z. & Levens, D. The functional response of upstream DNA to dynamic supercoiling in vivo. *Nat Struct Mol Biol* **15**, 146-54 (2008).

6. Kouzine, F., Liu, J., Sanford, S., Chung, H.J. & Levens, D. The dynamic response of upstream DNA to transcription-generated torsional stress. *Nat Struct Mol Biol* **11**, 1092-100 (2004).

7. Kouzine, F. et al. Transcription-dependent dynamic supercoiling is a short-range genomic force. *Nature Structural & Molecular Biology* **20**, 396-403 (2013).

8. Naughton, C. et al. Transcription forms and remodels supercoiling domains unfolding large-scale chromatin structures. *Nature Structural & Molecular Biology* **20**, 387-395 (2013).

9. Gilbert, N. & Allan, J. Supercoiling in DNA and chromatin. *Current Opinion in Genetics & Development* **25**, 15-21 (2014).

10. Teves, S.S. & Henikoff, S. Transcription-generated torsional stress destabilizes nucleosomes. *Nature Structural & Molecular Biology* **21**, 88-94 (2014).

11. Corless, S. & Gilbert, N. Effects of DNA supercoiling on chromatin architecture. *Biophysical Reviews* **8**, 245-258 (2016).

12. Achar, Y.J., Adhil, M., Choudhary, R., Gilbert, N. & Foiani, M. Negative supercoil at gene boundaries modulates gene topology. *Nature* **577**, 701-705 (2020).

13. Lerman, L.S. Structural considerations in the interaction of DNA and acridines. *J Mol Biol* **3**, 18-30 (1961).

14. Wang, J.G. The degree of unwinding of the DNA helix by ethidium: I. Titration of twisted PM2 DNA molecules in alkaline cesium chloride density gradients. *Journal of Molecular Biology* **89**, 783-801 (1974).

15. Le Pecq, J.-B. Ethidium Bromide: A Fluorescent Probe of Nucleic Acid Structure and Its Potential for in-Vivo Studies. in *Fluorescence Techniques in Cell Biology* (eds. Thaer, A.A. & Sernetz, M.) 301-309 (Springer Berlin Heidelberg, Berlin, Heidelberg, 1973).

16. Long, E.C. & Barton, J.K. On demonstrating DNA intercalation. *Accounts of Chemical Research* **23**, 271-273 (1990).

17. Baguley, B. DNA intercalating anti-tumour agents. *Anti-cancer drug design* **6**, 1-35 (1991).

18. Langner, K.M., Kedzierski, P., Sokalski, W.A. & Leszczynski, J. Physical Nature of Ethidium and Proflavine Interactions with Nucleic Acid Bases in the Intercalation Plane. *The Journal of Physical Chemistry B* **110**, 9720-9727 (2006).

19. Kolbeck, P.J. et al. Molecular structure, DNA binding mode, photophysical properties and recommendations for use of SYBR Gold. *Nucleic Acids Research* **49**, 5143-5158 (2021).

20. Wu, P.G. et al. Interaction of chloroquine with linear and supercoiled DNAs. Effect on the torsional dynamics, rigidity, and twist energy parameter. *Biochemistry* **27**, 8128-44 (1988).

21. Olson, W.K., Gorin, A.A., Lu, X.J., Hock, L.M. & Zhurkin, V.B. DNA sequence-dependent deformability deduced from protein-DNA crystal complexes. *Proc Natl Acad Sci U S A* **95**, 11163-8 (1998).

22. Chou, F.C., Lipfert, J. & Das, R. Blind predictions of DNA and RNA tweezers experiments with force and torque. *PLoS Comput Biol* **10**, e1003756 (2014).

23. Skoruppa, E., Nomidis, S.K., Marko, J.F. & Carlon, E. Bend-Induced Twist Waves and the Structure of Nucleosomal DNA. *Physical Review Letters* **121**, 088101 (2018).

24. Vanderlinden, W., Lipfert, J., Demeulemeester, J., Debyser, Z. & De Feyter, S. Structure, mechanics, and binding mode heterogeneity of LEDGF/p75–DNA nucleoprotein complexes revealed by scanning force microscopy. *Nanoscale* **6**, 4611-4619 (2014).

25. Seol, Y. & Neuman, K.C. The Dynamic Interplay Between DNA Topoisomerases and DNA Topology. *Biophys Rev* **8**, 221-231 (2016).

26. Bauer, W. & Vinograd, J. Interaction of closed circular DNA with intercalative dyes. II. The free energy of superhelix formation in SV40 DNA. *J Mol Biol* **47**, 419-35 (1970).

27. Bauer, W. & Vinograd, J. The interaction of closed circular DNA with intercalative dyes. I. The superhelix density of SV40 DNA in the presence and absence of dye. *J Mol Biol* **33**, 141-71 (1968).

28. Bell, G.I. Models for the specific adhesion of cells to cells. *Science* **200**, 618-27 (1978).

29. Evans, E. & Ritchie, K. Dynamic strength of molecular adhesion bonds. *Biophys J* **72**, 1541-55 (1997).

30. Vladescu, I.D., McCauley, M.J., Nuñez, M.E., Rouzina, I. & Williams, M.C. Quantifying force-dependent and zero-force DNA intercalation by single-molecule stretching. *Nature Methods* **4**, 517-522 (2007).

31. Lipfert, J., Klijnhout, S. & Dekker, N.H. Torsional sensing of small-molecule binding using magnetic tweezers. *Nucleic acids research* **38**, 7122-7132 (2010).

32. Salerno, D. et al. Magnetic tweezers measurements of the nanomechanical properties of DNA in the presence of drugs. *Nucleic Acids Research* **38**, 7089-7099 (2010).

33. Bauer, W. & Vinograd, J. The interaction of closed circular DNA with intercalative dyes: III. Dependence of the buoyant density upon superhelix density and base composition. *Journal of Molecular Biology* **54**, 281-298 (1970).

34. Hinton, D.M. & Bode, V.C. Ethidium binding affinity of circular lambda deoxyribonucleic acid determined fluorometrically. *Journal of Biological Chemistry* **250**, 1061-1070 (1975).

35. Wei, J., Czapla, L., Grosner, M.A., Swigon, D. & Olson, W.K. DNA topology confers sequence specificity to nonspecific architectural proteins. *Proceedings of the National Academy of Sciences* **111**, 16742-16747 (2014).

36. Watson, G.D., Chan, E.W., Leake, M.C. & Noy, A. Structural interplay between DNA-shape protein recognition and supercoiling: The case of IHF. *Computational and Structural Biotechnology Journal* **20**, 5264-5274 (2022).

37. McGhee, J.D. & Hippel, P.H.v. Theoretical Aspects of DNA-Protein Interactions :Co-operative and Non-co-operative Binding of Large Ligands to a One-dimensional Homogeneous Lattice. *J. Mol. Biol.* **86**, 469-489 (1974).

38. Boles, T.C., White, J.H. & Cozzarelli, N.R. Structure of plectonemically supercoiled DNA. *J Mol Biol* **213**, 931-51 (1990).

39. Ubbink, J. & Odijk, T. Electrostatic-undulatory theory of plectonemically supercoiled DNA. *Biophys J* **76**, 2502-19 (1999).

40. Calugareanu, G. L'intégrale de Gauss et l'analyse des nœuds tridimensionnels. *Rev. Math. pures appl* **4**(1959).

41. White, J.H. Self-Linking and Gauss-Integral in higher dimensions. *American Journal of Mathematics* **91**, 693-& (1969).

42. Selvin, P.R. et al. Torsional rigidity of positively and negatively supercoiled DNA. *Science* **255**, 82-5 (1992).

43. Sischka, A. et al. Molecular Mechanisms and Kinetics between DNA and DNA Binding Ligands. *Biophysical Journal* **88**, 404-411 (2005).

44. Hayashi, M. & Harada, Y. Direct observation of the reversible unwinding of a single DNA molecule caused by the intercalation of ethidium bromide. *Nucleic Acids Res* **35**, e125 (2007).

45. Celedon, A., Wirtz, D. & Sun, S. Torsional Mechanics of DNA Are Regulated by Small-Molecule Intercalation. *The Journal of Physical Chemistry B* **114**, 16929-16935 (2010).

46. Dikic, J. & Seidel, R. Anticooperative Binding Governs the Mechanics of Ethidium-Complexed DNA. *Biophys J* **116**, 1394-1405 (2019).

47. Tuma, R.S. et al. Characterization of SYBR Gold Nucleic Acid Gel Stain: A Dye Optimized for Use with 300-nm Ultraviolet Transilluminators. *Analytical Biochemistry* **268**, 278-288 (1999).

48. Cosa, G., Focsaneanu, K.S., McLean, J.R.N., McNamee, J.P. & Scaiano, J.C. Photophysical Properties of Fluorescent DNA-dyes Bound to Single- and Double-stranded DNA in Aqueous Buffered Solution¶. *Photochemistry and Photobiology* **73**, 585-599 (2001).

49. Biebricher, A.S. et al. The impact of DNA intercalators on DNA and DNA-processing enzymes elucidated through force-dependent binding kinetics. *Nat Commun* **6**, 7304 (2015).

50. Lercher, L. et al. Structural insights into how 5-hydroxymethylation influences transcription factor binding. *Chemical Communications* **50**, 1794-1796 (2014).

51. Ganji, M., Kim, S.H., van der Torre, J., Abbondanzieri, E. & Dekker, C. Intercalation-Based Single-Molecule Fluorescence Assay To Study DNA Supercoil Dynamics. *Nano Letters* **16**, 4699-4707 (2016).

52. King, G.A., Biebricher, A.S., Heller, I., Peterman, E.J.G. & Wuite, G.J.L. Quantifying Local Molecular Tension Using Intercalated DNA Fluorescence. *Nano Letters* **18**, 2274-2281 (2018).

53. Ganji, M. et al. Real-time imaging of DNA loop extrusion by condensin. *Science* **360**, 102-105 (2018).

54. Kim, S.H. et al. DNA sequence encodes the position of DNA supercoils. *eLife* **7**, e36557 (2018).

55. Lapolla, W., Yentzer, B.A., Bagel, J., Halvorson, C.R. & Feldman, S.R. A review of phototherapy protocols for psoriasis treatment. *Journal of the American Academy of Dermatology* **64**, 936-949 (2011).

56. Cech, T. & Pardue, M.L. Cross-linking of DNA with trimethylpsoralen is a probe for chromatin structure. *Cell* **11**, 631-640 (1977).

57. Sinden, R.R., Carlson, J.O. & Pettijohn, D.E. Torsional tension in the DNA double helix measured with trimethylpsoralen in living E. coli cells: Analogous measurements in insect and human cells. *Cell* **21**, 773-783 (1980).

58. Cimino, G.D., Gamper, H.B., Isaacs, S.T. & Hearst, J.E. Psoralens as photoactive probes of nucleic acid structure and function: organic chemistry, photochemistry, and biochemistry. *Annual Review of Biochemistry* **54**, 1151-1193 (1985).

59. Bermúdez, I., García-Martínez, J., Pérez-Ortín, J.E. & Roca, J. A method for genome-wide analysis of DNA helical tension by means of psoralen–DNA photobinding. *Nucleic Acids Research* **38**, e182-e182 (2010).

60. Yamashita, Y. et al. Induction of mammalian DNA topoisomerase I mediated DNA cleavage by antitumor indolocarbazole derivatives. *Biochemistry* **31**, 12069-12075 (1992).

61. Webb, M.R. & Ebeler, S.E. A gel electrophoresis assay for the simultaneous determination of topoisomerase I inhibition and DNA intercalation. *Analytical Biochemistry* **321**, 22-30 (2003).

62. Maxwell, A., Burton, N.P. & O'Hagan, N. High-throughput assays for DNA gyrase and other topoisomerases. *Nucleic Acids Research* **34**, e104-e104 (2006).

63. Wang, J.C. Variation of the average rotation angle of the DNA helix and the superhelical turns of covalently closed cyclic λ DNA. *Journal of Molecular Biology* **43**, 25-39 (1969).

64. Bauer, W.R. Structure and reactions of closed duplex DNA. *Annual review of biophysics and bioengineering* **7**, 287-313 (1978).

65. Anderson, P. & Bauer, W. Supercoiling in closed circular DNA: dependence upon ion type and concentration. *Biochemistry* **17**, 594-601 (1978).

66. Călugăreanu, G. Sur les classes d'isotopie des noeuds tridimensionnels et leurs invariants. *Czechoslovak Mathematical Journal* **11**, 588-625 (1961).

67. Fuller, F.B. The Writhing Number of a Space Curve. *Proceedings of the National Academy of Sciences* **68**, 815-819 (1971).

68. Brouns, T. et al. Free Energy Landscape and Dynamics of Supercoiled DNA by High-Speed Atomic Force Microscopy. *ACS Nano* **12**, 11907-11916 (2018).

69. Moroz, J.D. & Nelson, P. Torsional directed walks, entropic elasticity, and DNA twist stiffness. *Proc Natl Acad Sci U S A* **94**, 14418-22 (1997).

70. Lipfert, J., Kerssemakers, J.W., Jager, T. & Dekker, N.H. Magnetic torque tweezers: measuring torsional stiffness in DNA and RecA-DNA filaments. *Nat Methods* **7**, 977-80 (2010).

71. Kriegel, F. et al. Probing the salt dependence of the torsional stiffness of DNA by multiplexed magnetic torque tweezers. *Nucleic Acids Research* **45**, 5920-5929 (2017).

72. Bryant, Z. et al. Structural transitions and elasticity from torque measurements on DNA. *Nature* **424**, 338-41 (2003).

73. Mosconi, F., Allemand, J.F., Bensimon, D. & Croquette, V. Measurement of the torque on a single stretched and twisted DNA using magnetic tweezers. *Phys Rev Lett* **102**, 078301 (2009).

74. Fujimoto, B.S. & Schurr, J.M. Dependence of the torsional rigidity of DNA on base composition. *Nature* **344**, 175-7 (1990).

75. Heath, P.J., Clendenning, J.B., Fujimoto, B.S. & Schurr, J.M. Effect of bending strain on the torsion elastic constant of DNA. *J Mol Biol* **260**, 718-30 (1996).

76. Vanderlinden, W. et al. The free energy landscape of retroviral integration. *Nature Communications* **10**, 4738 (2019).

77. Molloy, M.J. et al. Effective and robust plasmid topology analysis and the subsequent characterization of the plasmid isoforms thereby observed. *Nucleic Acids Research* **32**, e129-e129 (2004).

78. Wang, M. et al. A platform method for plasmid isoforms analysis by capillary gel electrophoresis. *Electrophoresis* **43**, 1174-1182 (2022).

79. van Loenhout, M.T., de Grunt, M.V. & Dekker, C. Dynamics of DNA supercoils. *Science* **338**, 94-7 (2012).

80. Kim, E., Gonzalez, A.M., Pradhan, B., van der Torre, J. & Dekker, C. Condensin-driven loop extrusion on supercoiled DNA. *Nature Structural & Molecular Biology* **29**, 719-727 (2022).

81. Tycon, M.A., Dial, C.F., Faison, K., Melvin, W. & Fecko, C.J. Quantification of dye-mediated photodamage during single-molecule DNA imaging. *Analytical Biochemistry* **426**, 13-21 (2012).

82. Paillous, N. & Vicendo, P. Mechanisms of photosensitized DNA cleavage. *Journal of Photochemistry and Photobiology B: Biology* **20**, 203-209 (1993).

83. Liu, H. & Shima, T. A fast and objective hidden Markov modeling for accurate analysis of biophysical data with numerous states. *bioRxiv*, 2021.05.30.446337 (2021).

84. Vanderlinden, W. et al. Ru(TAP)32+ uses multivalent binding to accelerate and constrain photo-adduct formation on DNA. *Chemical Communications* **55**, 8764-8767 (2019).

85. Fosado, Y.A.G., Michieletto, D., Brackley, C.A. & Marenduzzo, D. Nonequilibrium dynamics and action at a distance in transcriptionally driven DNA supercoiling. *Proceedings of the National Academy of Sciences* **118**, e1905215118 (2021).

86. Benham, C.J. Torsional stress and local denaturation in supercoiled DNA. *Proceedings of the National Academy of Sciences* **76**, 3870-3874 (1979).

87. Dittmore, A., Brahmachari, S., Takagi, Y., Marko, J.F. & Neuman, K.C. Supercoiling DNA Locates Mismatches. *Physical Review Letters* **119**, 147801 (2017).

88. Liebl, K. & Zacharias, M. How global DNA unwinding causes non-uniform stress distribution and melting of DNA. *PLOS ONE* **15**, e0232976 (2020).

89. Finzi, L. & Dunlap, D. Supercoiling biases the formation of loops involved in gene regulation. *Biophys Rev* **8**, 65-74 (2016).

90. Lipfert, J., van Oene, M.M., Lee, M., Pedaci, F. & Dekker, N.H. Torque spectroscopy for the study of rotary motion in biological systems. *Chem Rev* **115**, 1449-74 (2015).

91. Naumova, N. et al. Organization of the mitotic chromosome. *Science* **342**, 948-53 (2013).

92. Postow, L., Hardy, C.D., Arsuaga, J. & Cozzarelli, N.R. Topological domain structure of the Escherichia coli chromosome. *Genes Dev* **18**, 1766-79 (2004).

93. Naimushin, A.N. et al. Effect of ethidium binding and superhelix density on the apparent supercoiling free energy and torsion constant of pBR322 DNA. *Biophysical Chemistry* **52**, 219-226 (1994).

94. Constant, J.F., O'Connor, T.R., Lhomme, J. & Laval, J. 9-[(10-(aden-9-yl)-4,8-diazadecyl)amino]-6-chloro-2-methoxy-acridine incises DNA at apurinic sites. *Nucleic Acids Research* **16**, 2691-2703 (1988).

95. Litwin, T.R., Solà, M., Holt, I.J. & Neuman, K.C. A robust assay to measure DNA topology-dependent protein binding affinity. *Nucleic Acids Research* **43**, e43-e43 (2014).

96. Bates, A.D. & Maxwell, A. *DNA Topology*, (Oxford University Press, 2005).

97. Kolbeck, P.J. et al. DNA Origami Fiducial for Accurate 3D Atomic Force Microscopy Imaging. *Nano Letters* (2023).

98. Konrad, S.F., Vanderlinden, W. & Lipfert, J. A High-throughput Pipeline to Determine DNA and Nucleosome Conformations by AFM Imaging. *Bio-protocol* **11**, e4180 (2021).

99. Bussiek, M., Mücke, N. & Langowski, J. Polylysine-coated mica can be used to observe systematic changes in the supercoiled DNA conformation by scanning force microscopy in solution. *Nucleic Acids Research* **31**, e137-e137 (2003).

100. Chandradoss, S.D. et al. Surface Passivation for Single-molecule Protein Studies. *JoVE*, e50549 (2014).

101. Tišma, M. et al. ParB proteins can bypass DNA-bound roadblocks via dimer-dimer recruitment. *Science Advances* **8**, eabn3299 (2022).

102. Aitken, C.E., Marshall, R.A. & Puglisi, J.D. An Oxygen Scavenging System for Improvement of Dye Stability in Single-Molecule Fluorescence Experiments. *Biophysical Journal* **94**, 1826-1835 (2008).

103. Pradhan, B. et al. The Smc5/6 complex is a DNA loop-extruding motor. *Nature* **616**, 843-848 (2023).

104. Ali, M., Lipfert, J., Seifert, S., Herschlag, D. & Doniach, S. The ligand-free state of the TPP riboswitch: a partially folded RNA structure. *J Mol Biol* **396**, 153-65 (2010).

105. Golub, G.H. & Van Loan, C.F. *Matrix computations*, (JHU press, 2013).

106. Wright, D.A. & Welschmeyer, N.A. Establishing benchmarks in compliance assessment for the ballast water management convention by port state control. *Journal of Marine Engineering & Technology* **14**, 9-18 (2015).

107. Duguet, M. The helical repeat of DNA at high temperature. *Nucleic Acids Research* **21**, 463-468 (1993).

108. Depew, D. & Wang, J.C. Conformational fluctuations of DNA helix. *Proceedings of the National Academy of Sciences* **72**, 4275-4279 (1975).

109. Kriegel, F. et al. The temperature dependence of the helical twist of DNA. *Nucleic Acids Res* **46**, 7998-8009 (2018).

110. Cruz-León, S. et al. Twisting DNA by salt. *Nucleic Acids Research* **50**, 5726-5738 (2022).

111. Geggier, S., Kotlyar, A. & Vologodskii, A. Temperature dependence of DNA persistence length. *Nucleic Acids Research* **39**, 1419-1426 (2011).

112. Bustamante, C., Marko, J.F., Siggia, E.D. & Smith, S. Entropic elasticity of lambda-phage DNA. *Science* **265**, 1599-600 (1994).

113. Bouchiat, C. et al. Estimating the Persistence Length of a Worm-Like Chain Molecule from Force-Extension Measurements. *Biophysical Journal* **76**, 409-413 (1999).

114. Davidson, I.F. et al. CTCF is a DNA-tension-dependent barrier to cohesin-mediated loop extrusion. *Nature* **616**, 822-827 (2023).

4

PARB PROTEINS CAN BYPASS DNA-BOUND ROADBLOCKS VIA DIMER-DIMER RECRUITMENT

The ParABS system plays an essential role in prokaryotic chromosome segregation. After loading at the parS site on the genome, ParB proteins rapidly redistribute to distances of ~15 kb away from the loading site. It has remained puzzling how this large-distance spreading can occur along DNA that is loaded with hundreds of proteins. Using in vitro single-molecule fluorescence imaging, we here show that ParB from Bacillus subtilis can load onto DNA distantly of parS, whereby loaded ParB molecules are themselves able to recruit additional ParB proteins from bulk. Strikingly, this recruitment can occur in-cis but also in-trans whereby, at low tensions within the DNA, newly recruited ParB can bypass roadblocks as it gets loaded to spatially proximal but genomically distant DNA regions. The data are supported by Molecular Dynamics simulations which show that cooperative ParB-ParB recruitment can enhance spreading. ParS-independent recruitment explains how ParB can cover substantial genomic distance during chromosome segregation which is vital for the bacterial cell cycle.

This chapter was published as Tišma M, Panoukidou M, Antar H, Soh YM, Barth R, Pradhan B, Barth A, van der Torre J, Michieletto D, Gruber S, Dekker C. *ParB proteins can bypass DNA-bound roadblocks via dimer-dimer recruitment*. Science Advances. (2022)

4.1 Introduction

Accurate chromosome segregation is crucial for a stable transmission of genetic material through each cell cycle. To actively segregate origins of replication, most prokaryotes rely on the ParAB*S* system[1,2], which consists of a *parS* binding sequence, the ATPase partition protein A (ParA), and the CTPase partition protein B (ParB) [3-6]. ParB dimers bind to the *parS* sequence, located near the origin of replication, spread laterally and ultimately form ParB-DNA partition complexes that are imperative for DNA segregation[7-13]. A ParA gradient along the cell axis subsequently segregates these complexes to effectively administer the nascent genomes to the daughter cells[14,15]. Proper partitioning of the ParB complexes is vital for bacterial cell survival and has been studied intensively in recent years[16], especially since it was recently discovered that ParB proteins from several model organisms utilize CTP to load onto a *parS* sequence[4,5,17].

A necessary feature for correct chromosome partitioning comes from a particular ability of ParB proteins to clamp the *parS*-DNA as a dimer[4,5] and to subsequently slide along the DNA by diffusion, effectively freeing the *parS* site for new ParB proteins to load. Indeed, ParB has been found to laterally spread over large genomic regions surrounding the *parS* sites *in vivo* (10-15 kb; [18-22]), which was reported to be essential for partition complex formation[9,10,16,18,19,23-25]. However, *in vitro* studies showed that single DNA-bound proteins block the diffusion of ParB along DNA very efficiently[4,7,17], raising the question how spreading can occur in a dense cellular environment, where, with ~1 gene and ~20-50 Nucleoid Associated Proteins (NAPs) per kb[26,27], sliding ParB dimers will continuously run into 'roadblocks' that will stall their movement. Indeed, theoretical modelling of a ParB 'clamping and sliding' model indicated that such roadblocks dramatically limit the spreading distance on F-plasmids[28]. Yet, *in vivo* ChIP-seq data do not show strong changes in the ParB occupancy in the vicinity of genes and operons[18-22,29].

4.2 Results

Here, we examine the mechanism of ParB spreading using a controlled DNA-stretching assay that allows *in vitro* visualization at the single-molecule level[30]. First, we verified that CTP and the *parS* site are essential for the loading and diffusion of *Bacillus subtilis* ParB on the DNA. We tethered 42 kb long DNA molecules with a single *parS* site close to the middle (DNA_{parS}) to a streptavidin-functionalized surface via their 5'-biotin ends (Fig. 4.1A, S4.1A). Highly Inclined and Laminated Optical sheet (HiLo) microscopy was used to observe DNA and proteins labelled with different fluorescent dyes (see *Supplementary info,* Fig. S4.1B-F).

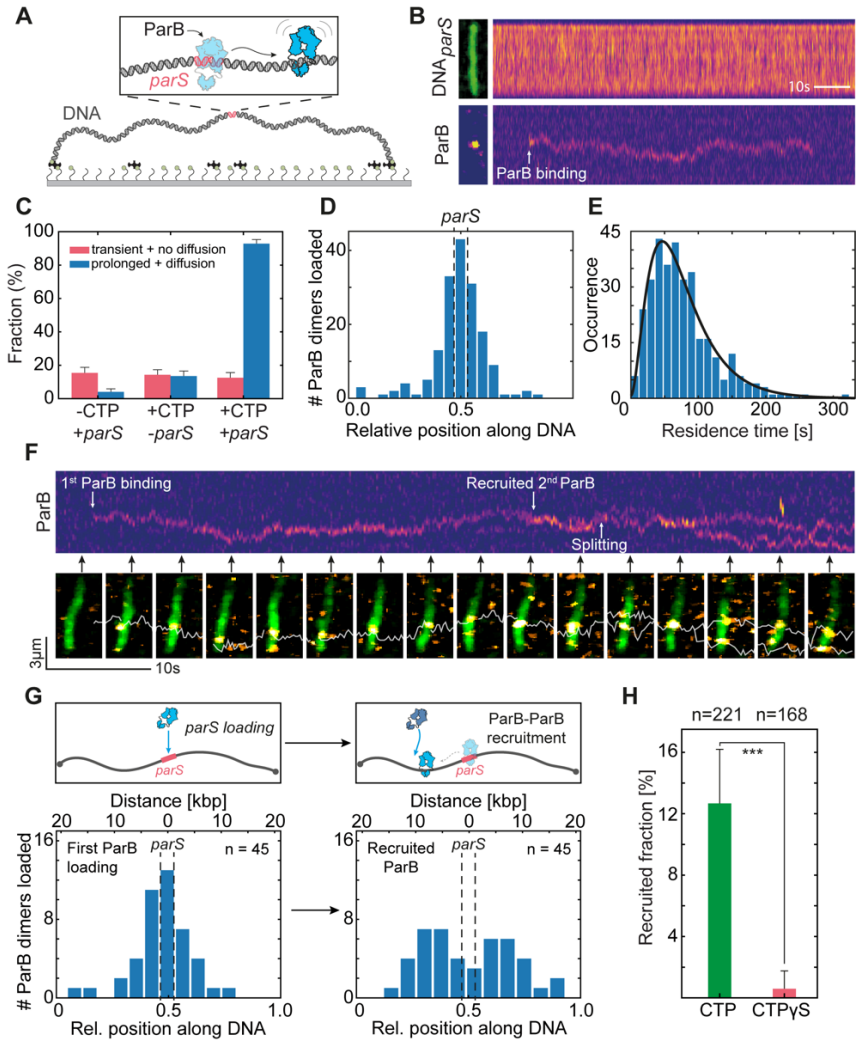


Figure 4.1. DNA-bound ParB dimers can recruit new ParB dimers independently of parS. A) *Schematic representation of DNA_{parS} that is tethered at both its ends to a surface, see also Fig. S1.* ***B)*** *Kymographs for DNA_{parS} stained with SytoxGreen (top) and $ParB^{alexa647}$ (bottom). Left images show single-frame snapshots of the DNA and ParB at the moment of binding. White arrow indicates ParB loading.* ***C)*** *Fraction of DNA tethers with transient binding with no diffusion and the fraction showing prolonged binding with diffusion of ParB molecules, for various conditions (n = 123, 133, 112 from left to right). Error bars represent binomial proportion confidence intervals.* ***D)*** *Histogram showing loading position of ParB dimers along DNA_{parS}. The position of parS site is represented by dashed lines, n=168.* ***E)*** *Residence times of diffusing ParB dimer molecules after binding DNA_{parS} (n=332). The data were fitted to a model assuming a delayed*

dissociation of ParB from the DNA after CTP hydrolysis (black line, see Methods, Figure S4.3B-C). ***F)*** *Top: kymograph for $ParB^{alexa647}$. White arrows indicate first ParB-dimer binding, second ParB-dimer binding, and splitting. Bottom: Snapshot images, taken at time points indicated by black arrows. White line indicates the single-particle-tracking trace.* ***G)*** *Distributions of ParB dimer loading positions. Left: First ParB dimer loading at parS site. Right: loading position of the recruited second ParB dimer. Top panels are illustrative schemes.* ***H)*** *Recruitment rate in presence of CTP (green) or CTPγS (red). Error bars represent binominal confidence intervals. Statistical significance calculated using chi-squared test for a binomial distribution, χ^2 (n=389) = 20.196, p<0.0001.*

4.2.1 CTP-hydrolysis determines residence of ParB on DNA

ParB was found to exhibit two different types of behaviors, viz., transient non-diffusive binding at various locations (Fig. S4.2A-C), as well as binding at the *parS* site followed by diffusion (Fig. 4.1B and S2D-E). Transient binding was short (~5-20 s), independent of the presence of CTP in the medium, and only weakly correlated to the *parS* sequence (Fig 4.1C, S4.2B-C). In the presence of both the *parS* sequence and CTP, however, binding initiated predominantly at the location of the *parS* sequence (Fig. 4.1D and Fig. S4.2D-H). Both the transient binding and binding at the *parS* site were dependent on the C-terminal domain, and the previously described mutant ($ParB^{KKK}$, see Methods) that is disabled in non-specific DNA binding[31], did not show either of these binding types in our fluorescence assay and in a biolayer interferometry assay (Fig. S4.2I) [4,19,32]. Surprisingly, the $ParB^{KKK}$ mutant still showed DNA_{parS}-stimulated CTP hydrolysis, despite its poor DNA binding (Fig. S4.2J).

When ParB dimers were specifically loaded at *parS* site, they remained bound to the DNA for an average time of 76 ± 2 seconds (average ± SEM; Fig. 4.1E), during which time the ParB diffused away from the *parS* site. Taking into account slight effects of the dyes on the CTP hydrolysis rate (Fig. S4.1F), this residence time is in line with the previously determined CTP hydrolysis rate of 1 CTP per 100 s for $ParB_{BSu}$[4], where the hydrolysis of CTP would cause the ParB clamp to destabilize and open, allowing dissociation from the DNA[4,5,19]. Interestingly, we observed a non-exponential distribution of ParB residence times, indicating that CTP hydrolysis is rate-limiting for dissociation (Fig. S4.3). A model assuming immediate dissociation of ParB after the independent hydrolysis of the two CTP molecules was unable to fully describe the data (see *Methods*, Fig. S4.3B-C, Table S4.2), suggesting that ParB may remain weakly bound to the DNA after CTP hydrolysis. Indeed, accounting for a delayed dissociation of ParB provided a significantly improved description of the experimental data with an average dwell time of ~15 seconds after CTP hydrolysis (Fig. 4.1E, S4.3B-C, Table

S4.2). The delayed dissociation may originate from nonspecific interaction of the open ParB clamp with the DNA via its positive residue patch at the C-terminus[31,33].

4.2.2 Diffusing ParB proteins can recruit new dimers onto the DNA

Strikingly, the data also revealed an unexpected behavior that was different from mere loading and diffusion of ParB dimers: a ParB dimer that was previously loaded onto the DNA_{parS}, was observed to be able to load a new ParB dimer onto the DNA (Fig. 4.1F, G and S4.4A-E). This behavior was characterized by the recruitment of a second ParB dimer at the site of an existing one (as evidenced from an increase of the fluorescent intensity), a brief colocalization and conjunct diffusion of the two ParB dimers (for 8.2 ± 3.5 s, average ± SD; Fig. S4.4D), after which the two dimers split into two independently diffusing ParB dimers (Fig. S4.4A-C). This intriguing behavior occurred in about 12% of the observed ParB molecules that loaded onto the *parS* site (Fig. 4.1H), which is significantly higher than accidental co-localization by off-site loading (Fig. S4.4D). We refer to this type of loading behavior as "ParB-ParB recruitment". We can distinguish ParB-ParB recruitment from simple subsequent loading of ParB proteins at the *parS* site by evaluating the position along DNA where events occur. As expected, the first ParB dimer loaded at the *parS* site near the middle of the DNA_{parS} (Fig. 4.1F, 4.1G-left), but the loading of the second, recruited ParB dimer occurred later at a position that was, on average, 5.2 ± 3.8 kb (average ± SD, n=46) away from the *parS* site (Fig. 4.1F, 4.1G -right). Accordingly, the first ParB loaded at *parS* site and already diffused a significant distance before recruiting a new ParB dimer at a distant location (Fig. 4.1G-right). Interestingly, after ParB-ParB recruitment, we observed that *both* ParB dimers resided on the DNA for ~72 s, i.e., for a similar amount of time as single diffusing ParB before recruitment (~66 s, Fig. S4.4C). The recruitment thus approximately doubled the residence time of the initially loaded ParB dimer to ~138 s (Fig. S4.4C). Notably, the ParB-ParB recruitment process was highly dependent on the presence of CTP, and occurred significantly less at lower CTP concentrations (see below), and hardly at all in the presence of the slowly hydrolysable nucleotide variant CTPγS (Fig. 4.1H)[25]. Hereafter, we refer to these recruitment events where the second ParB loaded at a DNA position adjacent to the first one, as '*in-cis'* (Fig. 4.2A-left), akin to what was previously proposed for ParB-bridges[10].

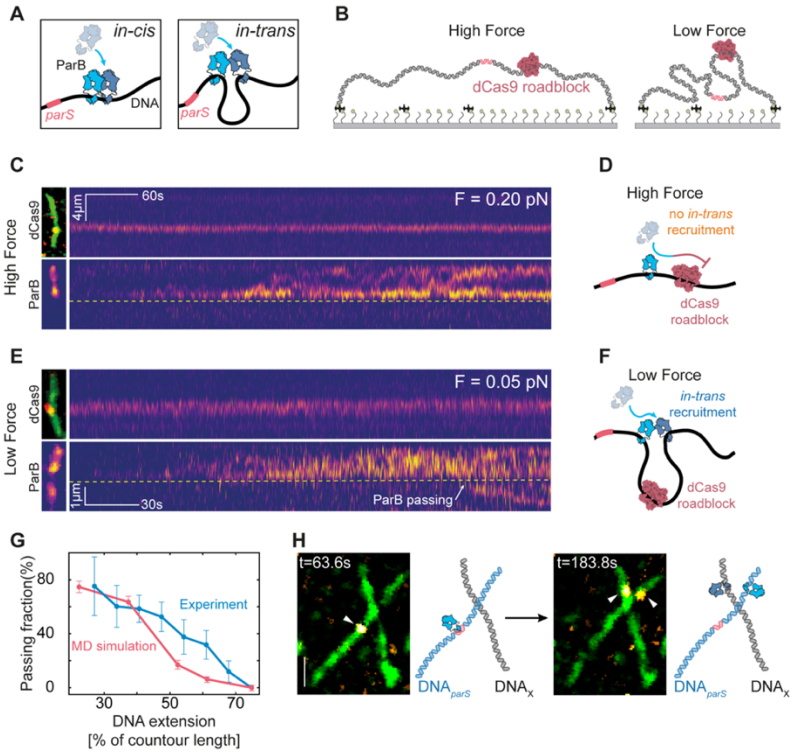


Figure 4.2. ParB can bypass roadblocks by in-trans ParB-ParB recruitment. A) *Illustration of in-cis (left) and in-trans (right) recruitment events.* ***B)*** *Schematic of the roadblock experiment for a large (left, high force) and small DNA_{parS} end-to-end distance (right, low force).* ***C)*** *Kymograph for $dCas9^{alexa549}$ (top), and $ParB^{alexa647}$ (bottom) for DNA_{parS} at 0.20 pN. Snapshots of $dCas9^{alexa549}$/$^{SytoxGreen}DNA_{parS}$ overlay and $ParB^{alexa647}$ signal are provided on the left. Yellow dashed line indicates the position of the $dCas9^{alexa549}$.* ***D)*** *Cartoon of the DNA_{parS} at high force where ParB molecules cannot be recruited across the roadblock.* ***E)*** *Same as panel C but data at a force of 0.05 pN. White arrow denotes a passing event.* ***F)*** *Same as panel D but for low force where ParB molecules can be recruited in-trans across the dCas9–roadblock.* ***G)*** *Fraction of DNA molecules that exhibit ParB dimers passing the dCas9-roadblock, displayed versus stretching length of the DNA. Error bars represent binomial proportion confidence intervals (blue, n = 122), and standard deviation from simulation cycles (pink, n=128).* ***H)*** *Left: Snapshot of the DNA_{parS}-DNA_X crossing at the time of the first ParB binding to parS site, t=105s. Right: Snapshot of the same field of view at time t=306s, where a second ParB was recruited onto the DNA_X by in trans recruitment. White arrows indicate the positions of ParB dimers. Cartoon representations are provided on the right of the snapshot frames. Scale bar = 2 µm.*

4.2.3 *In-trans* ParB-ParB recruitment can overcome DNA-bound roadblocks

Interestingly, we observed that ParB-ParB recruitment events can also happen '*in-trans*', where the second ParB got loaded onto a DNA position that is genomically distant, but transiently proximal in 3D space via DNA looping (Fig. 4.2A-right). Since these types of *in-trans* events could potentially allow for the passage of DNA-bound roadblocks in the crowded *in vivo* environment, we designed an experiment to test for *in-trans* recruitment in the presence of DNA-bound roadblocks. We placed a firmly bound dCas9 protein on one side of the *parS* sequence on the DNA (Fig. 4.2B) and tuned the end-to-end distance of the DNA to 65% of its total contour length (corresponding to a stretching force of 0.20 pN within the DNA[34]). In these conditions, we observed that the dCas9 roadblock efficiently prevented the diffusion of ParB proteins (Fig. 4.2C, D and Fig. S4.5A-E), in line with findings with other DNA-bound roadblocks[4,7,17]. However, when repeating the same experiment for a lower end-to-end distance (27% of the DNA_{parS} contour length; $F = 0.05$ pN[34]), we observed events where ParB proteins would cross the roadblock and continue one-dimensional diffusion along the DNA on the other side of dCas9 (Fig. 4.2E, F and S4.6A-E). We attribute this behavior to *in-trans* ParB-ParB recruitment. The bypassing of the Cas9 roadblock was also visibly apparent in the cumulated ParB fluorescence intensity signal, that rapidly increased on the *parS* side, while the non-*parS* side displayed discrete increases in intensity only for the non-stretched DNA_{parS} (Fig. S4.5C, E and S4.6B, D).

The tension within the DNA appeared to have a significant effect on the success rate of crossing the roadblock. As Fig. 4.2G displays, the fraction of DNA molecules where ParB successfully passed the dCas9 roadblock decreased from ~80% at 0.05 pN (27% of the total DNA contour length) to zero at 0.35 pN (75% contour length [34]). These data are consistent with *in-trans* ParB-ParB recruitment, where at low stretching forces, regions that are distant in DNA sequence can come into physical contact through bending and looping of the DNA via thermal fluctuations. We further corroborated these findings by observing the ParB-mediated *in-trans* loading of a new ParB dimer onto a *different* DNA molecule that was spatially nearby, where this DNA did not contain an endogenous *parS* site (Fig. 4.2H, S7). Here, as previously, we bound the DNA_{parS} to the surface but then subsequently bound a new DNA molecule lacking the *parS* site (DNA_X), perpendicular to the originally bound DNA_{parS} (Fig. S4.7A-B). In this assay, we observed events where ParB first specifically bound the DNA_{parS}, then reached the crossing point by random diffusion, where it recruited a new ParB molecule onto the DNA_X (Fig. S4.7C, dashed line), yielding a transfer and subsequent independent one-dimensional diffusion of the newly recruited ParB dimer on the DNA_X molecule (Fig. 4.2H, S4.7C).

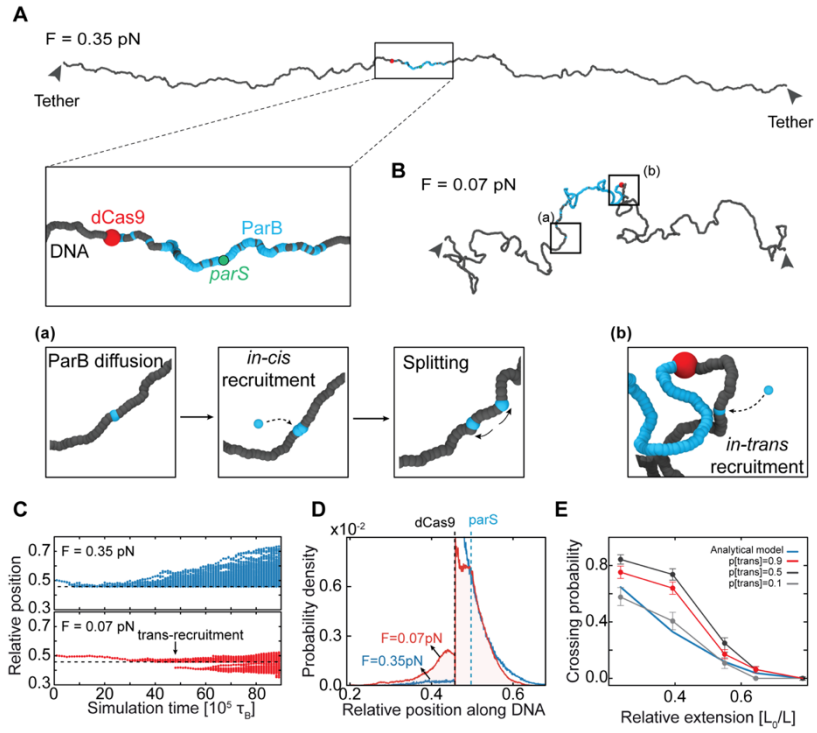


Figure 4.3. DNA looping via thermal fluctuations allows in-trans ParB-ParB recruitment and spreading across roadblocks. A) *Single frame snapshot of the DNA tethers in the MD simulations. DNA tether end-to-end length 11μm (i.e., 75% contour length, force of 0.35pN). Zoomed region highlights the region proximal to parS site. Tether has a parS site in the middle (green), and simulated dCas9-roadblock on one side (red). ParB represented in yellow.* ***B)*** *Single frame snapshot of low-force DNA molecule in MD simulations. DNA tether end-to-end length 5.5μm (i.e., 35% contour length, force of 0.07pN). Highlighted regions (a) and (b) show in-cis and in-trans recruitment events, respectively. Color-coding same as in panel A.* ***C)*** *Simulated kymographs representing distributions of ParB positions during the simulation. Top: kymograph for DNA tether at 0.35pN; bottom: same at F=0.07pN. Black arrow indicates an in-trans recruitment event.* ***D)*** *Probability density of ParB position from MD simulations at different tether lengths (blue 11μm, red 5.5μm) averaged over n=64 simulations. Dashed line indicates the position of dCas9 roadblock.* ***E)*** *Fraction of simulated DNA tethers that exhibit ParB dimers passing the dCas9-roadblock at different cis/trans ratios. The theoretical bypassing rate (integral of the polymer looping probability, see Fig. S8E) is shown in blue. Error bars represent standard deviation across independent simulations (n=128).*

Using coarse-grained molecular dynamics simulations, we modeled the passage of DNA-bound roadblocks by *in-trans* binding, and found a similar strong force dependence of the passing fraction of roadblocks. We simulated DNA tethers containing a blocking particle which strictly prohibited ParB diffusion through it (Fig. 4.3A), whereas concurrently ParB could exhibit *in-cis* or *in-trans* recruitment with an inbuilt rate (Fig. 4.3B, see *Methods*). While in the absence of a roadblock, both *in-cis* and *in-trans* recruitment increased the lateral spreading of ParB on the DNA (Fig. S4.8A), the presence of a roadblock allowed ParB to spread beyond it only through *in-trans* recruitment (Fig. 4.3C-D, S4.8B-D). Upon quantifying the passing fractions at different DNA end-to-end lengths and *cis/trans* recruitment ratios, we obtained the closest comparison with the experimental data at *cis/trans* ratio of ~0.1 (Fig. 4.2G, 4.3E). Hence, the best agreement with the experimental data was obtained when *in-trans* recruitment was assumed to lead to more successful events compared to *in-cis* recruitment (Fig. 4.2G). Overall, the modeling at low forces verified the notion that contacts between regions on opposing sides of the roadblock occur sufficiently often to allow for ParB to overcome roadblocks via ParB-ParB recruitment.

4.2.4 CTP hydrolysis in ParB-ParB recruitment

We found CTP hydrolysis to be crucial for the occurrence of ParB-ParB recruitment (Fig. 4.1H, S4.9). After repeating the experiments at low CTP concentration of 10 μM, close to the K_D of ParB-CTP[19], we observed a lower recruitment rate per loaded ParB dimer (Fig. S4.9A), indicating that an exchange of CTP molecules may occur during the ParB-ParB recruitment process or that the recruited ParB needs to have CTP bound to be effectively recruited. To examine the role of CTP further, we replaced CTP by the poorly hydrolysable CTPγS (Fig. S4.9B), which allows for the initial loading (clamp closing) but reduces opening of the ParB clamp upon hydrolysis (Fig. S4.9C-F) [4,7,19,25]. This resulted in a low and length-independent passing fraction, indicating an essential role of CTP hydrolysis in the *in-trans* ParB-ParB recruitment (Fig. S4.9G-I). As CTP hydrolysis is tightly connected with ParB clamp re-opening and dissociation from the DNA, it is likely that the N-terminal domain of ParB plays a role in the recruitment process. Recent work on ParB bridging interactions showed that a $ParB^{R80A}$ mutant, deficient in CTP binding, does not efficiently form ParB-ParB bridges [4,7,10]. As we hypothesize that ParB-ParB recruitment involves a transient bridge between the dimer proteins, the absence of open forms of ParB could explain the lack of recruitment with CTPγS in our experiments, because CTPγS binding keeps ParB proteins in a closed-clamp configuration. Furthermore, ParB mutants defective in CTP hydrolysis previously showed an altered distribution around *parS* in *B. subtilis,* with a reduced spreading against the orientation of highly expressed rRNA operons, genes encoding for ribosomal

proteins, and tRNA operons, as well as an increased spreading in the opposite direction[19]. We suggest that this distribution for the mutant ParB arises from one-dimensional diffusion only (equivalent to the clamping and spreading model), while the spreading of the wild-type protein additionally relies on ParB-ParB recruitment that can overcome head-on encounters with protein machineries such as RNA polymerases or replication forks. Similar observations were made for ParB in *C. crescentus*[25], whereas by contrast, *Myxococcus* ParB mutants showed extensive spreading in both directions[32], possibly by unhindered 1D diffusion due to the differences in life cycles (i.e., lower gene transcription and replication rates - see[35,36])

4.3 Discussion

4.3.1 Model of ParB spreading in presence of DNA-bound roadblocks

Based on our findings, we propose a model for ParB spreading (Fig. 4.4) that expands the well-known clamping and sliding model. First, ParB loads onto the *parS* site and spreads away by one-dimensional diffusion (Fig. 4.4A), until it hydrolyzes the bound CTP. In our model, however, unlike commonly assumed, the hydrolysis does not necessarily imply the immediate dissociation of ParB from the DNA. Instead, we hypothesize that the ParB dimer may briefly reside in an intermediary state after hydrolyzing CTP, where one of the monomers is not fully engaged in N-terminal dimerization[19]. Given abundant CTP in the surrounding buffer, the CDP can now exchange to a new CTP molecule, which leaves the CTP-bound free N-terminal part of the protein with two possibilities: (1) either re-connect with the N-terminus on the adjacent monomer of the ParB to re-close the clamp and continue diffusion (Fig. 4.4B) [19], or (2) connect to the N-terminus of a different ParB dimer that is nearby in the solution. The second scenario can lead to recruitment of a second ParB dimer to the nearby DNA, which can occur either *in-cis* or *in-trans* (Fig. 4.4C). This would involve a transient loop formation between two distal segments on the DNA molecule. Previous work on ParB indicated that long loops may underlie ParB-DNA condensation[37], particularly at very low forces exerted in magnetic tweezer experiments [7,31,33] or DNA curtains [10,13]. In our case, a loop would form *transiently* and the ParB-ParB dimer-dimer connection would break following the recruitment event. In this way, *in-trans* recruitment, can result in DNA-roadblock passing and free diffusion on the other side. The precise molecular mechanism of how the recruited ParB releases the dimer-dimer connection and whether it re-adopts a clamped conformation remain unknown (Fig. 4.4C and 4.4D).

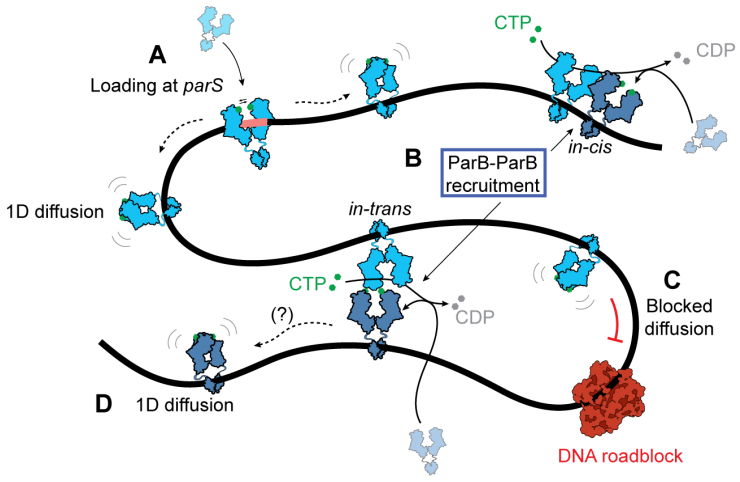


Figure 4.4. Model of ParB spreading and recruitment. *Cartoon of the various ParB modalities on DNA:* ***(A)*** *ParB dimer loads at the parS site, dimerizes upon closing its N-termini, losing its affinity to the parS-site, and diffusing away as a closed clamp. Subsequently* ***(B)****, ParB hydrolyzes CTP and enters an intermediary state where it can bind and recruit another ParB dimer to a nearby DNA, which can occur in-cis or in-trans. While one-dimensional diffusion is blocked by DNA-roadblocks* ***(C)****, ParB dimers that are recruited in-trans across the roadblock can continue diffusion along the DNA* ***(D)****, yielding an expanded spreading of ParB along DNA. Whether ParB re-forms a closed clamp structure after ParB-ParB recruitment (D) or not remains unknown.*

Overall, *in-trans* ParB-ParB recruitment is consistent with the extensive spreading of ParB along genomic DNA that contains many roadblock proteins. Furthermore, it offers an alternative mechanism to the 'stochastic binding' that was proposed previously[28] and expands on the combination of 1D and 3D interactions between ParB molecules in former models[37] to include the role of CTP and explain the presence of ParB at large distances from *parS* sites in *in vivo* ChIP-seq data. We speculate that ideal hotspots for ParB *in-trans* recruitment events may additionally be found in regions that are brought into close proximity of a *parS* site by the action of an SMC complex[38,39]. Indeed, recent reports on Hi-C maps detected in strains that were constructed for testing SMC collisions *in vivo*, showed the co-alignment of DNA flanking a *parS*-free region which is characteristically only found at *parS* sites. Physical contact of DNA with a genomically-distant *parS*-containing region may lead to *in-trans* ParB-ParB recruitment and create *parS*-free ParB-DNA structures suitable for further off-site SMC recruitment[40]. In line with our model, when the ParB-*parS* system was used for spot labelling in yeast or

human cells, it would still spread (up to 3 kb) and form a bright fluorescent locus, despite the ubiquitous abundance of histones on the eukaryotic DNA molecule[41,42]. This could be facilitated via recruitment of new ParB proteins to nearby DNA overcoming the nucleosomes bound in between.

Our findings uncover a new pathway for ParB proteins to cooperatively cover large distances on DNA that is loaded with DNA-binding proteins. It involves the combination of lateral 1D diffusion along the DNA and a new type of CTP-hydrolysis-dependent ParB loading (ParB-ParB recruitment) which can occur irrespective of the *parS* site. Both our experimental and simulation data showed that *in-trans* ParB-ParB recruitment can account for overcoming DNA-bound roadblocks at low forces where DNA forms a fluctuating polymer blob that facilitates frequent DNA-DNA encounters. Since both the ParB concentration and the DNA-contact frequency are higher in the tightly packed genome within a bacterial cell compared to our single-molecule experiments, we expect ParB-ParB recruitment to be a common mechanism *in vivo*, where it may facilitate the collective spreading distance of ParB proteins on the protein-bound DNA.

4.4 Materials and methods

4.4.1 ParB purification and fluorescent labelling

We prepared *Bacillus subtilis* ParB expression constructs using pET-28a derived plasmids through Golden-gate cloning. We expressed untagged recombinant proteins in *E. coli* BL21-Gold (DE3) for 24 h in ZYM-5052 autoinduction medium at 24°C. Purification of $ParB^{L5C}$ variants was performed as described before[19]. Briefly, we pelleted the cells by centrifugation and subjected them to lysis by sonication in buffer A (1 mM EDTA pH 8, 500 mM NaCl, 50 mM Tris-HCl (pH 7.5), 5 mM β-mercaptoethanol, 5 % (v/v) glycerol, and protease inhibitor cocktail (PIC, SigmaAldrich). We then added ammonium sulfate to the supernatant to 40% (w/v) saturation and kept stirring at 4°C for 30 min. We centrifuged the sample and collected the supernatant, and subsequently added ammonium sulfate to 50% (w/v) saturation and kept stirring at 4°C for 30 min. We collected the pellet (containing ParB) and dissolved it in buffer B (50 mM Tris-HCl (pH 7.5), 1 mM EDTA pH 8 and 2 mM β-mercaptoethanol). The sample was also diluted with buffer B to achieve a conductivity of 18 mS/cm before loading onto a Heparin column (GE healthcare). We used a linear gradient of buffer B containing 1 M NaCl to elute the protein. After collecting the peak fractions, we diluted them in buffer B to 18 mS/cm conductivity, and loaded onto HiTrap SP columns (GE healthcare). For elution, we used a linear gradient of buffer B containing 1 M NaCl. Collected peak fractions were loaded directly onto a Superdex 200-16/600 pg column (GE healthcare) preequilibrated in 300 mM NaCl, 50 mM Tris-HCl (pH 7.5), and 1 mM TCEP. For fluorescent labeling, we incubated purified $ParB^{L5C}$ variant with either TMR-maleimide or Alexa647-C_2-malemeide at a 1:1.2 or 1:10 (protein:dye) molar ratio, respectively. We incubated the mixture for 15 min on ice, centrifuged for 10 min and then eluted from a spin desalting column (Zeba) and flash frozen in liquid nitrogen. We estimated the fluorophore labelling efficiency at 74% for $ParB^{alexa647}$ and 69% for $ParB^{TMR}$ (resulting in 93% and 90% dimers labelled, respectively) by an inbuilt function on Nanodrop using extinction coefficients of $\varepsilon = 270\,000\ cm^{-1}M^{-1}$ for Alexa647 and $\varepsilon = 60\,000\ cm^{-1}M^{-1}$ for TMR.

4.4.2 ParBs CTP-hydrolysis assays

We test for the activity of the labelled-$ParB^{L5C}$, as well as $ParB^{KKK}$ mutant by their ability to hydrolyze CTP in the presence of DNA_{parS}. For this reason, we measured the hydrolysis rate by Malachite Green colorimetric detection. In brief, we prepared a mixture of 2x[CTP] and 2x 40bp DNA_{parS} concentration in reaction buffer (150 mM NaCl, 50 mM Tris-HCl (pH 7.5), 5 mM $MgCl_2$) and placed it on ice. We added an equal volume of 2x solution, containing the purified protein to the 2xCTP/DNA mixture and

left to incubate at 25°C for 1 h in a PCR machine. In parallel, we prepared phosphate blanks. The samples were then diluted 4-fold with deionized water, and subsequently mixed with 20 µl working reagent (SigmaAldrich) and transferred to a flat bottom 96-well plate. The plate was left to incubate at 25°C for 30 min, and we measured the absorbance at a wavelength of 620 nm. We used the absorbance values from the phosphate standard samples to plot an OD_{620} versus phosphate concentration standard curve. Using the standard curve, we converted raw values to rate values, and calculate the absolute rates by normalizing for protein concentration.

4.4.3 Biolayer interferometry

Measurements were performed in a buffer containing 150 mM NaCl, 50 mM Tris-HCl (pH 7.5), and 5 mM $MgCl_2$ on BLItz machine (FortéBio Sartorius), similar to described previously in Antar *et al*[19]. Final protein concentrations in the association step (Fig. S4.2I, (c)) were fixed at 1 µM for both ParB and the $ParB^{KKK}$ mutant. All measurements were analyzed on the BLItz analysis software.

4.4.4 Construction and purification of 42kb DNA_{parS} construct

For the construction of a long linear DNA_{parS}, we used a large 42kb cosmid-i95 reported previously[43] and a synthetic construct containing the *parS* site (Integrated DNA Technologies, Table. S4.1, underlined sequence). First, we linearized the i95 cosmid using the PsiI-v2 restriction enzyme (New England Biolabs). Next, we dephosphorylated the remaining 5'-phosphate groups using Calf Intestinal Alkaline Phosphatase for 10 min at 37°C, followed by heat inactivation for 20 min at 80°C (Quick CIP, New England Biolabs). We added the 5'-phospho group on the synthetic *parS* fragment by adding a T4 kinase for 30 min at 37°C and heat-inactivated 20 min 65°C in 1x PNK buffer supplemented with 1 mM ATP (T4 PNK, New England Biolabs). Next, we ligated the two fragments together using a T4 DNA ligase in T4 ligase buffer (New England Biolabs), containing 1 mM ATP overnight at 16°C. The final cosmid construct was transformed into *E. coli* NEB10beta cells (New England Biolabs), and we verified the presence of insert by sequencing using JT138 and JT139 (Table S4.1). To prepare a linear fragment adapted for flow cell experiments, we isolated cosmid-i95 via a midiprep using a Qiafilater plasmid midi kit (Qiagen). The cosmid-i95 was then digested for 2 h at 37°C and heat-inactivated for 20 min at 80°C using AjuI restriction enzyme (ThermoFischer Scientific). Linear DNA constructs for three-color experiments with roadblocks were constructed in the same way using the SpeI-HF restriction enzyme (New England Biolabs). Next, we constructed the 5'-biotin handles by a PCR from a pBluescript SK+ (Stratagene) using 5'-biotin primers JT337 and JT338 (Table S4.1), to get a final 1245 bp fragment. The PCR fragment was digested using the same procedure

described for cosmid-i95, resulting in ~600 bp 5'-biotin-handles. Finally, we mixed the digested cosmid-i95 and handles in a 1:10 molar ratio and ligated them together using T4 DNA ligase in T4 ligase buffer (New England Biolabs) at 16°C overnight, which was subsequently heat-inactivated for 25 min at 65°C. We cleaned up the resulting linear (42 +1.2) kb DNA$_{parS}$ construct from the access handles using an ÄKTA Pure (Cytiva), with a homemade gel filtration column containing 46 ml of Sephacryl S-1000 SF gel filtration media, run with TE + 150 mM NaCl buffer at 0.2ml/min. We stored the collected fractions as aliquots after snap-freezing them by submerging them in liquid nitrogen.

4.4.5 Preparation and binding dCas9 roadblock to DNAparS

To form the dCas9-alexa549 roadblock complex, we initially prepared a tr-crRNA duplex by mixing universal 67mer trRNA and a custom-designed crRNA (Table S4.1), in a duplex buffer (Integrated DNA Technologies), to a final concentration of 10 µM each. The mixture was incubated at 95°C for 5 min, and then slowly cooled to 4°C by decreasing the temperature for 5°C every 5 min over the course of 1.5 hours. We next incubated the tr-crRNA solution with the dCas9 in the "binding buffer" (2 µM tr-crRNA complex, 1 µM dCas9-SNAP (New England Biolabs), 1x NEB3.1 buffer) for 10 min at 37°C, before placing it on ice. Following the tr-crRNA-dCas9 complex formation, we bound it to the DNA$_{parS}$ by incubating the DNA$_{parS}$:tr-crRNA-dCas9 in molar ratio 1:50 for 60 min at 37°C. We labelled the dCas9-SNAP by adding alexa546-BG (or alexa647-BG for photobleaching estimation) to a final concentration of 1 µM for 30 min at room temperature before flowing it into the flow cell.

4.4.6 Single-molecule visualization assay

The surface of imaging coverslips was prepared as previously described[44], with the addition of surfaces being pegylated 5x24h. For immobilization of 42kb DNA$_{parS}$, we introduced 50 µl of ~1 pM of 5'-biotinylated-DNA$_{parS}$ molecules at a flow rate of 3 – 14 µl/min, depending on the desired end-to-end length in the experiment, in T20 buffer (40 mM Tris-HCl (pH 8.0), 20 mM NaCl, 25 nM SytoxGreen (SxG, ThermoFisher Scientific)). Immediately after the flow, we further flowed 100 µl of the wash buffer (40 mM Tris–HCl, pH 8.0, 20 mM NaCl, 65mM KCl, 25 nM SxG) at the same flow rate to ensure stretching and tethering of the other end of the DNA to the surface. By adjusting the flow, we obtained a stretch of around 25−80% of the contour length of DNA. Next, we flowed in the imaging buffer (40 mM Tris-HCl, 2 mM Trolox, 1 mM TCEP, 10 nM Catalase, 18.75 nM Glucose Oxidase, 30 mM Glucose, 2.5 mM $MgCl_2$, 65 mM KCl, 0.25 µg/ml BSA, 1 mM CTP, 25 nM SxG) without ParB protein at the same flow rate to maintain identical conditions before and after protein addition. Experiments were performed in the same conditions with exception of replacing 1 mM CTP with 10 µM

CTP or 1 mM CTPγS where mentioned. Real-time observation of ParB diffusion was carried out by introducing ParB (0.05-1 nM) in the imaging buffer. We used a home-built objective-TIRF microscope to achieve fluorescence imaging. We used alternating excitation of 488-nm and 646-nm, 561-nm lasers in Highly Inclined and Laminated Optical sheet (HiLo) microscopy mode, to image SxG-stained DNA and Alexa647- or TMR-labelled ParB using. When imaging Alexa488-ParB, we used continuous 488 nm excitation in the absence of SxG. All images were acquired with an PrimeBSI sCMOS camera at an exposure time of 100 ms for dual-color experiments and 60 ms for three-color experiments, with a 60x oil immersion, 1.49NA CFI APO TIRF (Nikon).

4.4.7 Crossed DNA_{parS}-DNA_X assay

The surface was prepared, and binding of the DNA_{parS} was done the same as described above. The flow cell was then blocked at the primary inlet (Fig. S4.7) and resumed from a secondary inlet to establish a cross flow that was oriented under a substantial angle with the flow that stretched DNA_{parS} on the surface. In this second flush, DNA that contained no *parS* site was stretched onto the surface, until sufficient number of crossed DNA_{parS}-DNA_X events was observed. We performed the remainder of the experiment identically to the previously described protocol with a fixed concentration of 500 pM ParB.

4.4.8 Image processing

The areas with single DNA molecules were cropped from the raw image sequences and analyzed separately with a custom-written interactive python software. The images were smoothened using a median filter with a window size of 10 pixels, and the background was subtracted with the "white_tophat" operation provided in the *scipy* python module. The contrast of the images were further adjusted manually for visualization only (i.e. Fig. 4.1F, bottom). The ends of a DNA were manually marked. Total fluorescence intensity of 11 pixels across the axis of the DNA was obtained for each time point and was stacked to get a kymograph (i.e., Fig. 4.1B). The same DNA axis was chosen to obtain kymograph of the ParB fluorescence channel.

4.4.9 Data analysis of single-molecule imaging traces

We resolved the initial loading positions of ParB by calculating the mean pixel position over the first full second of the ParB traces from the kymograph, and then determining that value relative to the DNA ends, i.e.,

$$Relative\ loading\ position = \frac{(x_{end} - x_{load\ avg.})}{(x_{end} - x_{start})} \quad (1)$$

All loading positions obtained like this were pulled together and represented in a histogram using a custom-written python script (Fig. 4.1D, S4.2B, H, S4.9). We determined the residence time of ParB molecules by measuring the length of traces of single ParB proteins by their fluorescence (Fig. 4.1E, S4.3B-D, S4.4C, D, S4.9F). We fitted the histogram with 2- or 3-parameter model and computed the Bayesian Information Criterion (BIC, Fig. S4.3B-C) for each fit in order to determine the optimal model underlying the data. The mean was obtained via bootstrapping of all data ($n_{iterations}$ = 5000, Fig 4.1E). The standard error of the mean was computed using the following formula:

$$Standard\ Error\ of\ Mean\ (SEM) = \frac{Standard\ deviation}{\sqrt{Sample\ size}} \qquad (2)$$

Similarly, we obtained the ParB residence time before and after recruitment (Fig. S4.4C, E).

We obtained the *parS* and non-*parS* arm intensities in dCas9-roadblock experiments (Fig. 4.2C, E) by selecting the corresponding regions in the kymograph before (~100 frames) and after (~2000 frames) the observable binding of the first ParB molecule to the DNA. Pixel values before the initial binding, representing noise, were averaged over the 100 frames and subtracted from each frame in the region after the initial molecule bound. The roadblock position was determined as the maximum value over the time-averaged kymograph in the 561 nm channel after applying the Savitzky–Golay filter implemented from the *scipy* python module, with a window length of 11 frames, and order 1. ParB signal intensity was obtained by applying a median filter the kymograph from 647 nm channel with a kernel size of 21 frames to account for the signal noise and the noise from the wiggling of the DNA molecule. We discarded intensity data from a window of 5 pixels above and below the dCas9 position to account for "leaking" fluorescence due to fixed pixel position of dCas9 (at the peak of Savitzky–Golay curve) and simultaneous wiggling DNA and ParB signal with it. The raw data was plotted on the same graph as the median filter curves, in the background.

To determine the fluorescence intensity of ParB proteins before, during, and after recruitment events, single discernable ParB proteins were tracked on kymographs as described above. We then integrated the fluorescence from the three surrounding pixels of the track position for 20 frames before, during and after the recruitment event. For visualization of example recruitment events (Fig. S4.4B) we temporally averaged 20 frames of kymographs to obtain a profile across the DNA length and identified one or two peaks (before/during and after recruitment, respectively) by calling a Gaussian

Mixture Model from the python *sklearn* module with the respective number of components.

4.4.10 Modeling the distribution of residence times

To model the distribution of residence times of ParB on DNA in saturating concentration of CTP of 1 mM, we consider the pathway depicted in Fig. S4.3A. Starting with the saturated ParB dimer on the DNA, we assume that the CTP hydrolysis in the two monomers occurs independently with rate constant k_{CTP}. Once both CTP molecules are hydrolyzed, ParB is released from the DNA with rate k_{off}. To model the independent hydrolysis of the two CTP molecules, we assume that the CTP hydrolysis follows single exponential kinetics:

$$P(t) = k_{\mathrm{CTP}} e^{-k_{\mathrm{CTP}} t}. \tag{3}$$

The time until both CTP molecules are hydrolyzed (t_{CTP}) then corresponds to the maximum of two exponential random variables with rate k_{CTP}. The distribution of t_{CTP} is given by the probability that either one of the two CTP molecules is hydrolyzed at time point t_{CTP}, multiplied by the probability that the other CTP molecule was already hydrolyzed at an earlier time point, i.e.

$$P(t_{\mathrm{CTP}}) = 2P(t = t_{\mathrm{CTP}})P(t \leq t_{\mathrm{CTP}}), \tag{4}$$

where the factor 2 accounts for the fact that either of the ParB monomers might hydrolyze at first, from which we obtain:

$$P(t_{\mathrm{CTP}}) = 2k_{\mathrm{CTP}} e^{-k_{\mathrm{CTP}} t}(1 - e^{-k_{\mathrm{CTP}} t}). \tag{5}$$

We assume that the release of the ParB dimer from the DNA after hydrolysis of both CTP molecules occurs with a constant rate k_{off},

$$P(t_{\mathrm{off}}) = k_{\mathrm{off}} e^{-k_{\mathrm{off}} t}. \tag{6}$$

The total dwell time of ParB on the DNA is then given by $T = t_{\mathrm{CTP}} + t_{\mathrm{off}}$. The distribution of the dwell time T is obtained from the convolution of $P(t_{\mathrm{CTP}})$ and $P(t_{\mathrm{off}})$:

$$P(T) = \int_0^T P(t_{\mathrm{CTP}} = t)\, P(t_{\mathrm{off}} = T - t) dt, \tag{7}$$

which evaluates to

$$P(T) = 2k_{\mathrm{CTP}} k_{\mathrm{off}} e^{-k_{\mathrm{off}} T} \cdot \left[(k_{\mathrm{CTP}} - k_{\mathrm{off}})^{-1}\left(1 - e^{-(k_{\mathrm{CTP}} - k_{\mathrm{off}})T}\right) - (2k_{\mathrm{CTP}} - k_{\mathrm{off}})^{-1}\left(1 - e^{-(2k_{\mathrm{CTP}} - k_{\mathrm{off}})T}\right)\right]. \tag{8}$$

To account for the photobleaching of the fluorophore, we consider the apparent dwell time $T' = \min(T, t_{\mathrm{bl}})$ as the minimum of the dwell time T and the exponentially distributed bleaching time t_{bl}

$$P(t_{\mathrm{bl}}) = k_{\mathrm{bl}} e^{-k_{\mathrm{bl}} t_{\mathrm{bl}}}, \tag{9}$$

where k_{bl} is the bleaching rate. The distribution of the apparent dwell time is then obtained as

$$P(T' = \min(T, t_{\mathrm{bl}})) = P(T = T')P(t_{bl} > T') + P(t_{\mathrm{bl}} = T')P(T > T'). \tag{10}$$

Here, $P(T = T')P(t_{bl} > T')$ is the probability that ParB dissociates from the DNA before photobleaching occurs, and $P(t_{\mathrm{bl}} = T')P(T > T')$ is the probability that photobleaching occurs during the dwell time of ParB on the DNA, with:

$$P(t_{\mathrm{bl}} > T') = 1 - P(t_{\mathrm{bl}} \leq T') = 1 - \int_0^{T'} P(t_{\mathrm{bl}} = t)dt = e^{-k_{\mathrm{bl}} T'}, \tag{11}$$

and accordingly

$$P(T > T') = 1 - \frac{2k_{\mathrm{CTP}} k_{\mathrm{off}}}{(2k_{\mathrm{CTP}} - k_{\mathrm{off}})(k_{\mathrm{CTP}} - k_{\mathrm{off}})} \cdot$$

$$\left[\frac{k_{\mathrm{CTP}}}{k_{\mathrm{off}}}(1 - e^{-k_{\mathrm{off}} T}) - \frac{2k_{\mathrm{CTP}} - k_{\mathrm{off}}}{k_{\mathrm{CTP}}}(1 - e^{-k_{\mathrm{CTP}} T}) + \frac{k_{\mathrm{CTP}} - k_{\mathrm{off}}}{2k_{\mathrm{CTP}}}(1 - e^{-2k_{\mathrm{CTP}} T})\right]. \tag{12}$$

The same procedure was applied account for bleaching in the case of immediate release of ParB from the DNA according to eq. 5.

4.4.11 Fitting of the dwell time distributions

To avoid artifacts related to the binning of the data, we applied a maximum likelihood approach to fit the experimentally obtained apparent dwell times t'. The log-likelihood of the data given the model function as given by eq. 10 is given by

$$\log \mathcal{L} = \sum \log P(T' = t_i') \,. \tag{13}$$

Optimization of the log-likelihood with respect to the rates of CTP hydrolysis (k_{CTP}) and release (k_{off}) was performed using the interior point algorithm as implemented in the *fmincon* function in MATLAB. The bleaching rate k_{bl} was fixed ($k_{\mathrm{bl}} = 1.75 \cdot 10^{-4}$ s^{-1} for Alexa647, extracted from our experimental data, for TMR this rate was fixed to $k_{\mathrm{bl}} =$ 0 s^{-1}). Confidence intervals (68%) were determined from the Hessian at the solution. To compare different model functions with varying parameters (i.e., immediate vs. delayed release from the DNA), we employed the Bayesian information criterion defined as

$$BIC = \nu \log N - 2 \log \mathcal{L}, \quad (14)$$

where ν is the number of fit parameters ($\nu = 1$ for immediate release, $\nu = 2$ for delayed release) and N is the number of data points. The model with the lowest value for the BIC was preferred.

4.4.12 CTP hydrolysis rates and ParB dissociation rates

We fitted the experimental residence time distributions for ParB^{TMR} and ParB^{alexa647} to the immediate-release (eq. 5) and delayed-release (eq. 8) models (Table S4.2 and Fig. S4.3B-C). For both dyes, the delayed release model was clearly preferred, based on the lower value for the BIC. The CTP hydrolysis rates for the delayed release model were consistent between ParB^{TMR} (k_{CTP} = 0.022 ± 0.003 s^{-1}) and ParB^{alexa647} (k_{CTP} = 0.025 ± 0.003 s^{-1}) but faster compared to the bulk rates of ~0.007 s^{-1} that we measured (Fig. S4.1F) and previous reports of ~0.01 s^{-1} [4]. On the other hand, we obtained different dissociation rates k_{off} for ParB^{TMR} (0.025 ± 0.005 s^{-1}) and ParB^{alexa647} (0.06 ± 0.02 s^{-1}), corresponding to dwell times of the ParB dimer on DNA after CTP hydrolysis of 40 ± 8 s for ParB^{TMR} and 17 ± 5 s for ParB^{alexa647}. While the CTPase activity remained unaffected by the dye labeling (Fig. S4.1F), this suggests that the organic dye could promote the DNA binding affinity of the ParB dimer after clamp opening. Taken together, we estimate a dissociation rate of k_{off} = 0.04 ± 0.02 s^{-1} (dwell time: 25 ± 13 s).

4.4.13 Accidental recruitment co-localization simulations

Since the recruitment of ParB molecules is visually indistinguishable from a co-localization of a newly recruited ParB dimer onto the location of an already bound ParB, we analysed if a random co-localization of ParB's might give rise to the experimentally observed recruitment frequency. To this end, we simulated kymographs mimicking DNA being tethered at an end-to-end length which was used for experiments. A molecule was allowed to bind at the *parS* site (at a relative DNA position of 0.5) and undergo one-dimensional diffusion with an experimentally determined diffusion constant $D = 0.066\,\mu m^2/s$ (Fig. S4.2E) and an average residence time of 76 s (Fig. 4.1E), drawn from a normal distribution with $\sigma = 50\,s$. The number of *parS*-loaded ParB's and non-specifically bound ParB's per kymograph of 7500 frames (equivalent to 1500 sec) was drawn from a normal distribution with mean 4 and standard deviation 1 molecule, in line with the experimentally observed value. Non-specifically bound molecules were allowed to bind anywhere along the DNA with equal probability. Such scenarios were simulated a 1000 times (Fig. S4.4D shows an example) and co-localization of *parS*-loaded and non-specifically bound ParB molecules were counted if the two molecules came closer than 300 nm from each other within 3 frames in time,

accounting for our diffraction limit during experiments, below which the two molecules cannot be distinguished (we estimate that the point spread function of our microscope is roughly 300 nm wide).

4.4.14 Modelling and molecular dynamics simulations

We modelled the DNA as a coarse-grained semiflexible polymer made of 1400 spherical beads of size $\sigma = 5.5\,nm = 16bp$. We placed the *parS* recruitment sequence in the middle of the chain. In addition, at 2/3 of the DNA chain, we placed a roadblock that stopped the diffusion of ParB, representing the dCas9 enzyme. The beads interact purely by excluded volume following the shifted and truncated Lennard-Jones (LJ) force field

$$U_{LJ}(r,\sigma) = \begin{cases} 4\varepsilon\left[\left(\frac{\sigma}{r}\right)^{12} - \left(\frac{\sigma}{r}\right)^{6} + \frac{1}{4}\right] \;\; for\; r \le r_c \\ 0 \;\; otherwise \end{cases} \tag{15}$$

where r denotes the distance between any two beads and $r_c = 2^{\frac{1}{6}}\sigma$ is the cut-off. We defined the bonds between two monomers along the DNA contour length by the finite extensible nonlinear elastic (FENE) potential, given by

$$U_{FENE}(r) = -0.5kR_o^2 \log\left(1 - \left(\frac{r}{R_o}\right)^2\right) \;\; for\; r \le R_o \tag{16}$$

with $k = 30\varepsilon/\sigma^2$ the spring constant, ε is thermal energy, and $R_o = 1.5\sigma$ the maximum length of the bond. We introduced the persistence length of the DNA chain as a bending potential energy between three consecutive beads given by

$$U_{bend}(\theta) = k_\theta(1 - cos\theta) \tag{17}$$

where θ is the angle between two consecutive bonds and $k_\theta = 10\; k_B T$ is the bending stiffness, corresponding to a persistence length of about 10 beads or ~55 nm. We modelled ParB by calling, within the LAMMPS engine, an external program that modifies the types of the beads along the DNA over time and thereby mimics the diffusion/recruitment of ParB. Specifically, at $t = 0$, we loaded a ParB protein onto the *parS* site and allowed to diffuse with a constant $D = 0.05\frac{\mu m^2}{s} = 0.05\left(\frac{182^2\sigma^2}{2.8\;10^8 dt}\right) = 0.062\frac{\sigma^2}{10^4 dt}$. This is done by updating the position of a loaded ParB protein either to the left or to the right with probability 0.125 every $10^4 dt = 10^2 \tau_B$ timesteps (recall that MSD = 2 Dt in a 1D system, hence why the jump probability is twice the diffusion coefficient D). The diffusion cannot happen (the move is rejected) if the attempt brings a ParB protein either on top of another ParB or on top of dCas9.

On top of diffusion, we add a recruitment process at a rate of $10^{-6}\tau_B^{-1}$, i.e., on average every $10^6\tau_B$ timesteps (0.35 seconds), in which another ParB is recruited by a loaded ParB. When this happens, the recruitment can stochastically happen *in-cis* (with probability p_c) or *in-trans* (with probability $p_T = 1 - p_C$). If the former is selected, one of the two adjacent beads is selected at random and, if unoccupied and not the dCas9 bead, a new ParB is added onto the chain. Otherwise, if the latter '*in-trans*' mechanism is selected, we compute the list of 3D proximal neighbors which must be 1) within an Euclidean cutoff distance of 11 nm (roughly the size of a two ParB dimers) and 2) farther than the second-nearest neighbor in 1D (i.e. the first and second nearest neighbors cannot be picked to avoid *in-trans* events that are in practice *in-cis*). The "theoretical" bypass probability is given by the integral of the looping probability (e.g., Yamakawa-Shimada J factor) (Fig. S4.8E) as:

$$P_{bypass} \propto \int_2^\infty P_{loop}(x)dx \tag{18}$$

Once the list of 3D neighbors is compiled, we randomly pick one of these from the list (if not empty), load a new ParB protein and resume the Langevin simulation.

4.5 Supplementary data

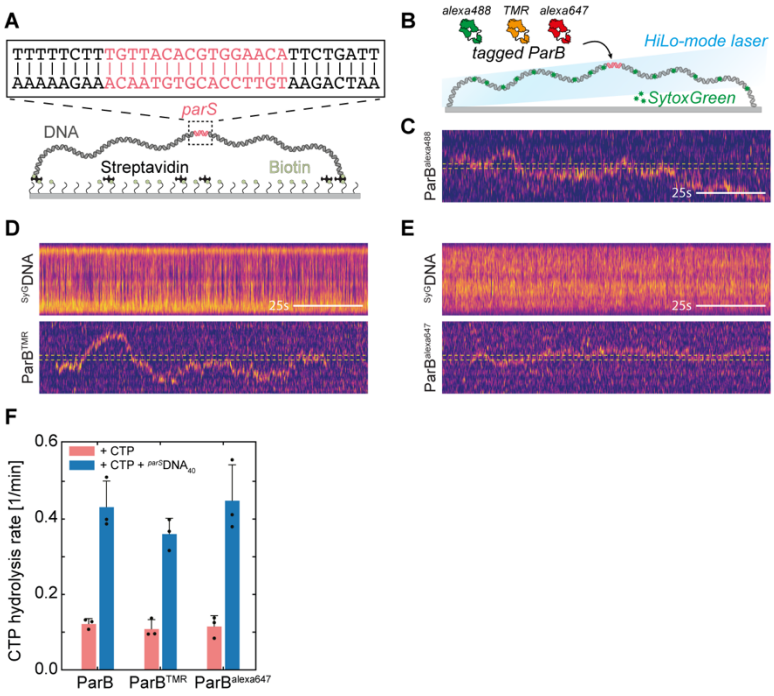


Figure S4.1. ParB exhibits one-dimensional diffusion irrespective of the fluorescent tag. A) *Schematic representation of the DNA_{parS} that is tethered at both its ends to a surface. Zoomed region shows parS sequence.* ***B)*** *Schematic representation of HiLo imaging setup using different fluorescent tags on ParB as well as SytoxGreen for DNA_{parS} staining.* ***C)*** *Kymograph showing ParB diffusion using $ParB^{alexa488}$. Scale bar = 25s. yellow line - parS position (mirrored)* ***D)*** *and* ***E)*** *Kymographs for DNA_{parS} stained with SytoxGreen (top) and $ParB^{TMR}$ (bottom) or $ParB^{alexa647}$ (bottom), respectively. Scale bar = 25s. yellow line - parS position (mirrored)* ***F)*** *CTP hydrolysis assay with Malachite Green for unlabelled, TMR- and Alexa647-labelled ParB proteins. The rates were normalized to the blank phosphate controls (see Methods). Error bars represent standard deviation from a triplicate (presented as black circles).*

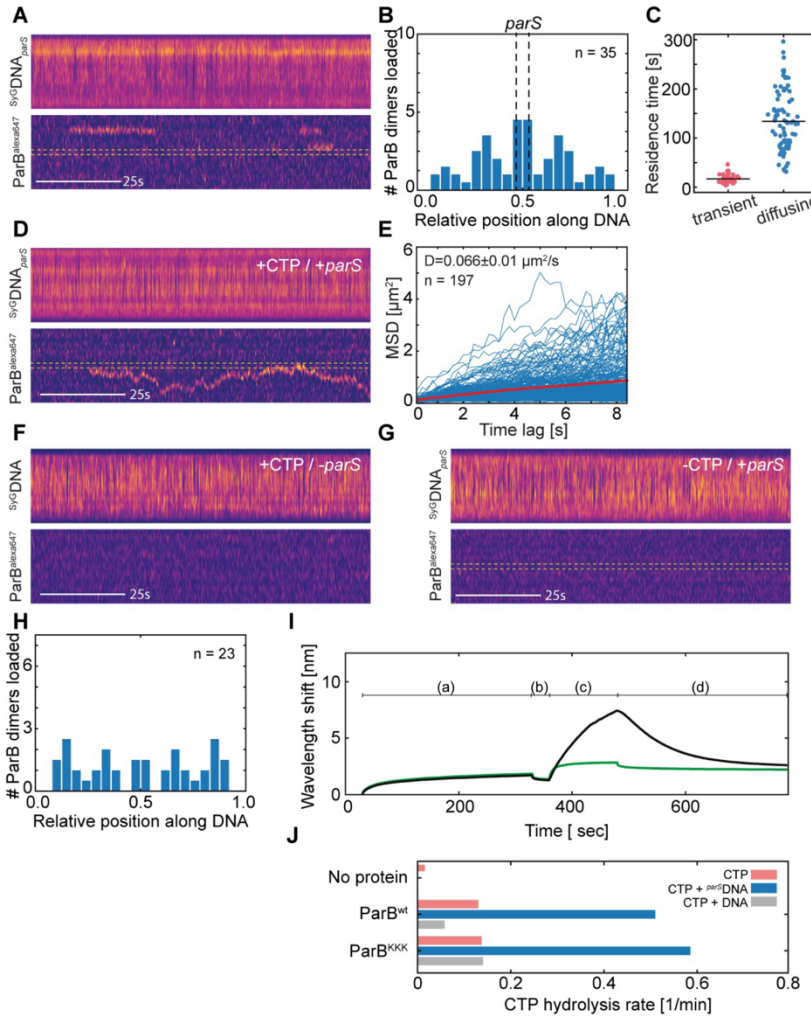


Figure S4.2. ParB spreading by diffusion occurs in the presence of parS sequence and CTP. A) *Kymographs for DNA_{parS} stained with SytoxGreen (top) and $ParB^{alexa647}$ (bottom). Yellow dashed line indicates the parS site (mirrored).* ***B)*** *Mirrored histogram representing transient binding position of ParB dimer molecules relative to the DNA_{parS} ends. The events are double counted and hence display a symmetrical distribution as the head-to-tail orientation of the DNA is unknown. The position of parS site is represented by dashed lines. n=35.* ***C)*** *Residence times of transiently bound non-diffusing (pink) and parS-bound and diffusing ParB dimers (blue).* ***D)*** *Kymographs for DNA_{parS} stained with SytoxGreen (top) and ParB-alexa647 (bottom) in the presence of both CTP and parS site. Yellow dashed line indicates the parS site (mirrored).* ***E)*** *Mean square displacement of the diffusing ParB molecules loaded at parS site. Red line represents a linear fit to the*

MSD curves. Apparent diffusion coefficient is on average D= 0.066±0.01 μm²/s, n= 197. ***F)*** *Kymographs for DNA_{parS} stained with SytoxGreen (top) and $ParB^{alexa647}$ (bottom) in the absence of parS-site.* ***G)*** *Kymographs for DNA_{parS} stained with SytoxGreen (top) and $ParB^{alexa647}$ (bottom) in the absence of CTP. Yellow dashed line indicates the parS site.* ***H)*** *Mirrored histogram for the binding position on non-specifically bound ParB dimers (+CTP/-parS) relative to the DNA_{parS} ends. The events are double counted and hence display a symmetrical distribution as the head-to-tail orientation of the DNA is unknown.* ***I)*** *Biolayer interference showing DNA_{parS} binding of ParB (black) and $ParB^{KKK}$ mutant (green). (a) Binding of biotin-immobilized 169bp DNA_{parS}; (b) buffer only; (c) protein association step as 1 μM protein and 1 mM CTP was added to buffer; and finally, during dissociation (d), an equivalent buffer lacking ParB protein and nucleotide was applied (see Methods and Antar et al[19]).* ***J)*** *CTP hydrolysis assay with Malachite Green for ParB and $ParB^{KKK}$ mutant.*

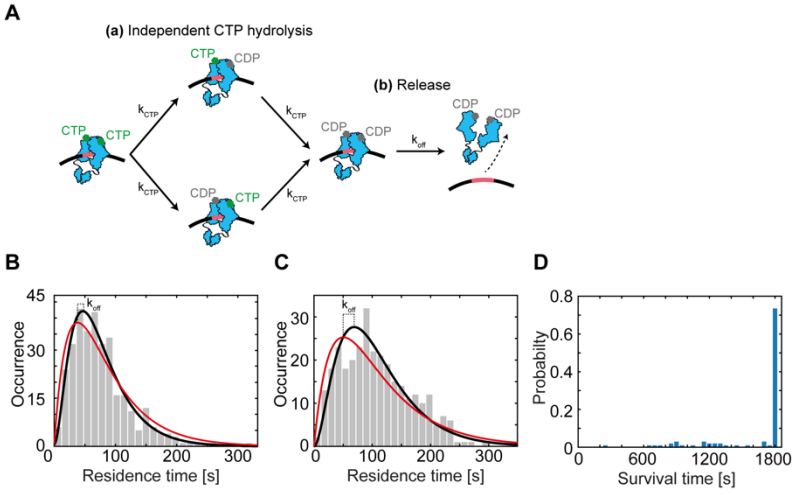


Figure S4.3. Model for the release of the ParB dimer from DNA after CTP hydrolysis. ***A)*** *Following hydrolysis of both CTP molecules with equal rates k_{CTP}, the ParB dimer releases from the DNA with rate k_{off}.* ***B)*** *Fit to the experimental residence time distribution for $ParB^{alexa647}$ to the model in A) assuming immediate (red, BIC=3493) or delayed (black, BIC=3418) dissociation of ParB from the DNA after CTP hydrolysis.* ***C)*** *Same as in B) for $ParB^{TMR}$. For immediate release (red) the BIC is 3382, while for delayed release BIC = 3363. The results of the fits are given in Table S2.* ***D)*** *Survival rates of dCas9-alexa647 proteins undergone the same imaging procedure as ParB proteins. Bleaching rate was very low, k_{bl} = 0.00018 s^{-1}.*

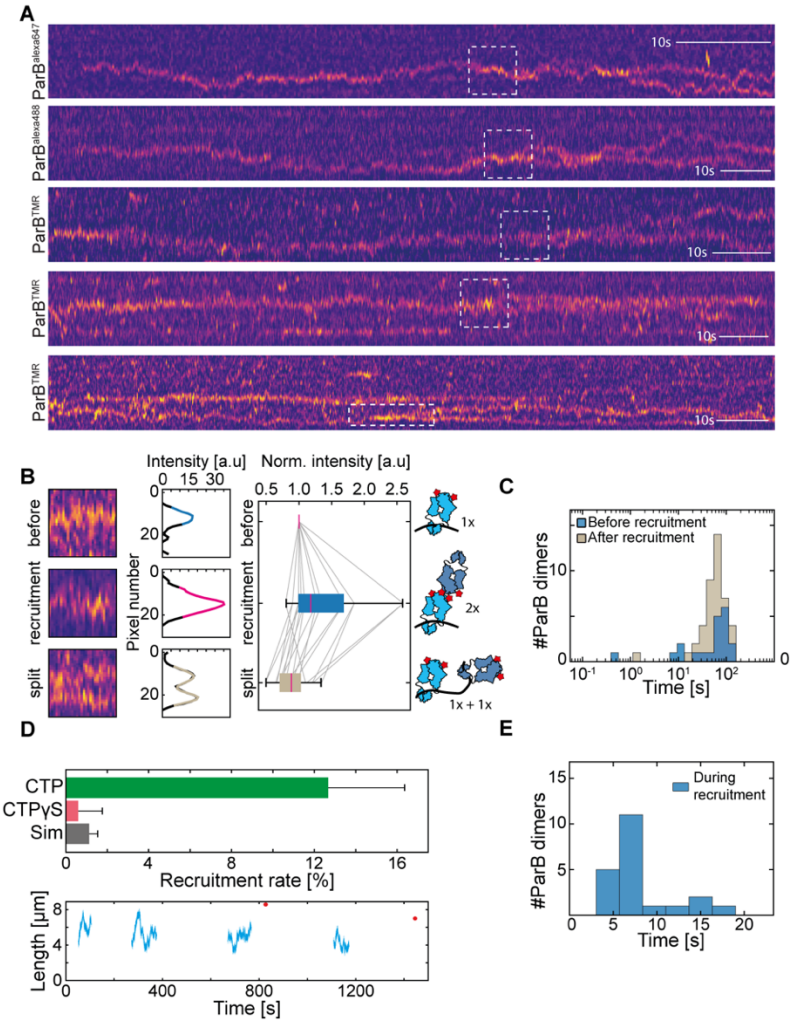


Figure S4.4. ParB-ParB recruitment is marked by short conjunct diffusion followed by a split and two individually diffusing ParB dimers. A) *Kymographs for ParB-ParB recruitment using ParB proteins with different tags. Top-to-bottom: ParB-alexa647, ParB-alexa488, 3xParB-TMR. Scale bar = 10s. Dashed boxes represent ParB-ParB recruitment event.* ***B)*** *Left: exemplary parts of the kymographs "before recruitment", "during recruitment" and "split after recruitment" from traces such in panel A). Window size is 25px*25 frames. Middle: Mean intensity projection from the windows on the left. Right: Relative intensity "during recruitment" and "split after recruitment", as normalized to the "before recruitment" of the same kymograph. n=25 before and n=50*

after splitting. Cartoon representations on the right represent the ParB dimerization that explains the increased signals during recruitment. ***C)*** *Residence time of single ParB dimers before (blue) and after (cream) recruitment events.* ***D)*** *Simulated traces with experimental parameters to estimate the "accidental colocalization" probability. Top – colocalization events occurred in presence of CTP, CTPγS and in our in-silico experiment. Bottom – exemplary trace of our colocalization simulations* ***E)*** *Time duration of the conjunct diffusion period during the recruitment event.*

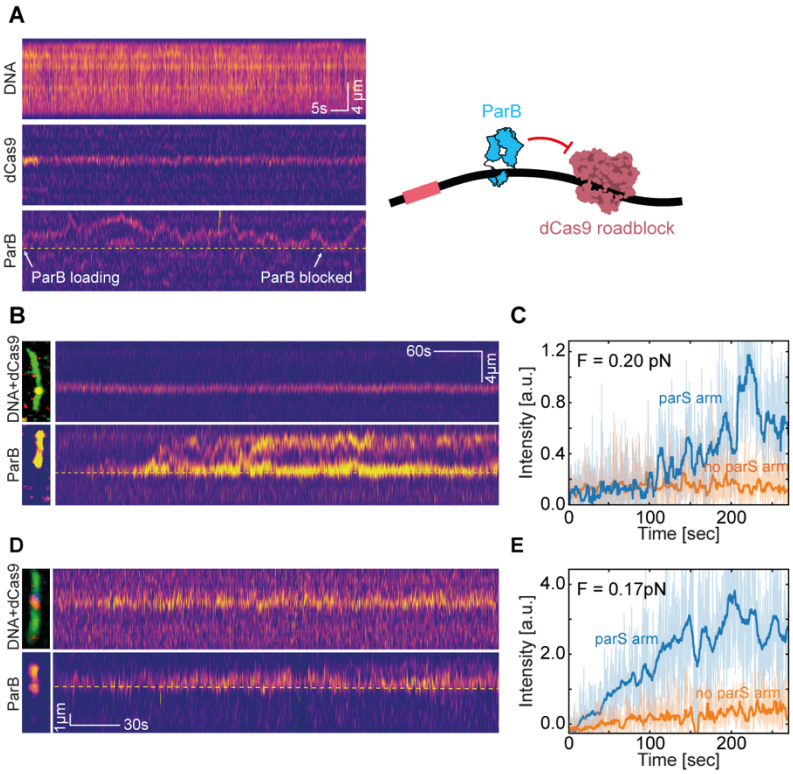


Figure S4.5. DNA-bound dCas9 roadblocks efficiently block diffusion of ParB dimers. ***A)*** *Kymographs for DNA_{parS} stained with SytoxGreen (top) and $dCas^{alexa549}$ (middle) and $ParB^{TMR}$ (bottom) at low concentration [0.1nM]. White arrows indicate the loading position (left) and the moment of dCas9 blocking ParB diffusion (right). Cartoon representation shown on the right. Scale bars: spatial 4µm, temporal 5s.* ***B)*** *Kymographs for $dCas^{alexa549}$ (top) and $ParB^{alexa647}$ (bottom) at 10x higher ParB concentration [1nM]. Left images are snapshots of $dCas9^{alexa549}$ & $^{SytoxGreen}DNA_{parS}$ overlay, and $ParB^{alexa647}$ signal at the end of the trace. Yellow dashed line indicates the position of the $dCas9^{alexa549}$. Scale bars: spatial 4µm, temporal 60s.* ***C)*** *Quantification of the kymograph data of panel B, that displays the ParB signal in the top (blue, raw data – light blue) and bottom (orange, raw data – light orange) part of the DNA, i.e., above and below the Cas9 (dashed yellow line), respectively, at F = 0.20 pN.* ***D)*** *Same as panel B.* ***E)*** *Same as panel C.*

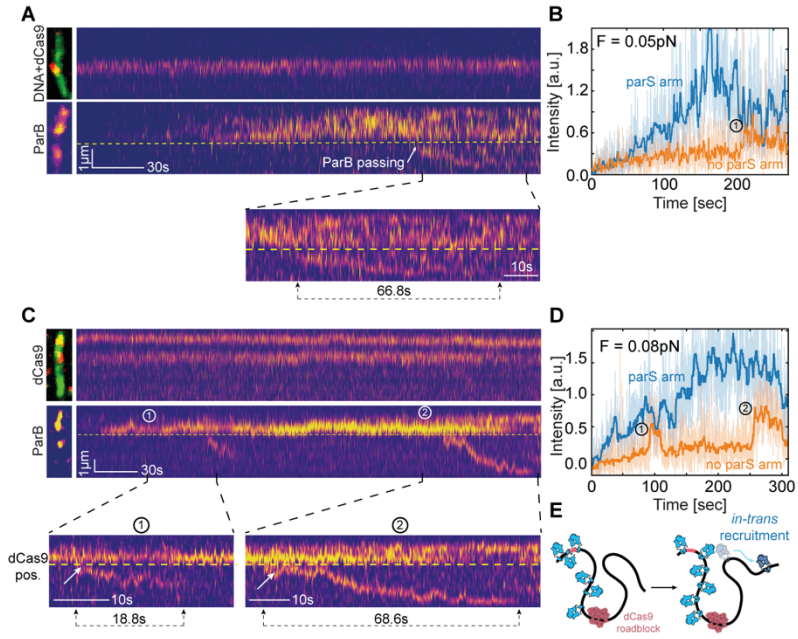


Figure S4.6. ParB-ParB in-trans recruitment allows for bypassing DNA-roadblocks at low forces. A) *Kymograph for dCas9^{alexa549} (top), and ParB^{alexa647} (bottom) for DNA$_{parS}$ (same as Fig.S5B) at F= 0.05 pN. Left images are snapshots of dCas9^{alexa549} &* ^{SytoxGreen}*DNA$_{parS}$ overlay and ParB^{alexa647} signal at time of recruitment (2). Yellow dashed line indicates the position of the dCas9^{alexa549}. Scale bar 30s. Zoomed region (1) represents event where ParB is recruited over the dCas9-roadblock, and continues diffusion over it. The total length of the trace is denoted below.* ***B)*** *Quantification of the kymograph data of panel A, that displays the ParB signal in the top (blue, raw data – light blue) and bottom (orange raw data – light orange) part of the DNA, i.e., above and below the Cas9 (dashed yellow line), respectively. (1) represents a crossing event where the intensity increases on the 'no parS side'.* ***C)*** *Same as in panel A. Zoomed regions (1) and (2) represent two events where ParB is recruited over the dCas9-roadblock, and continues diffusion over it. The total length of the traces are denoted below.* ***D)*** *Same as panel B. (1) and (2) represent crossing events that are marked by an intensity increase on the 'no-parS side'.* ***E)*** *Cartoon representation of the hypothesized ParB-ParB in-trans recruitment event.*

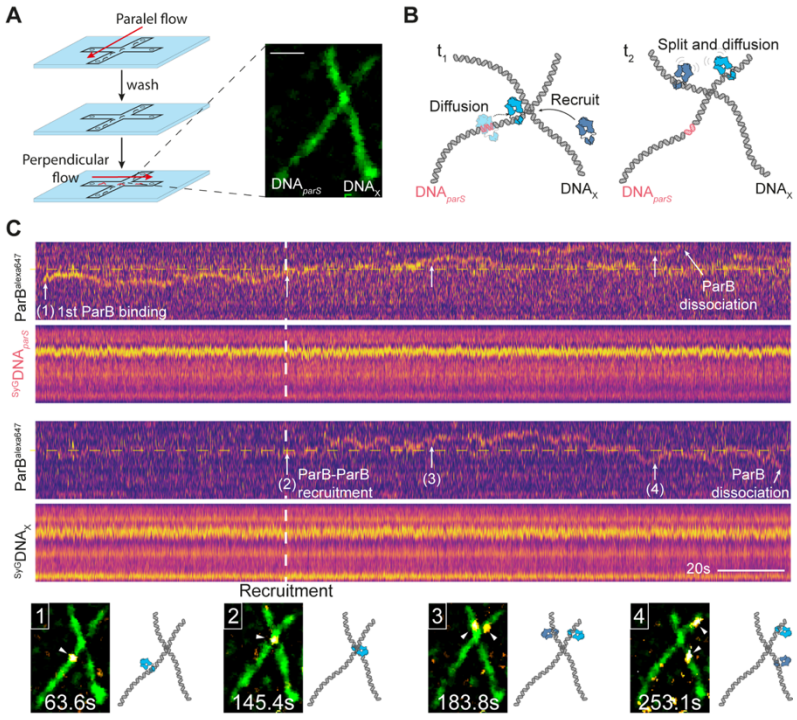


Figure S4.7. A new ParB dimer can be recruited by a ParB dimer on a different DNA molecule. ***A)*** *Schematic representation of the experimental setup flow cell and simplified experimental procedure (see Methods). Parallel flow is applied to bind a DNA_{parS} molecule to the surface. After washing, perpendicular flow is applied to bind DNA_X molecules at a large angle compared to the initially bound DNA_{parS}. Right: single frame snapshot of the final arrangement of DNA_{parS}-DNA_X. Scale bar: 2 µm* ***B)*** *Cartoon representation of the experiment. parS-sequence is indicated in pink* ***C)*** *Kymographs for $ParB^{alexa647}$ (top) and DNA stained with SytoxGreen (bottom). Top two kymographs represent the DNA_{parS} signal taken from intensity profiles along the DNA_{parS} molecule. Bottom two kymographs represent DNA_X signal taken from intensity profiles along the DNA_X molecule. Dashed yellow line indicates the approximate junction point. Dashed white vertical line indicates the time when the event occurred where ParB on the DNA_{parS} molecule met the junction point and a new ParB dimer was loaded onto the DNA_X molecule. Bottom row shows single frame snapshots (with corresponding cartoon representations on the side) of the DNA_{parS}-DNA_X molecules at timepoints indicated by (1)-(4).*

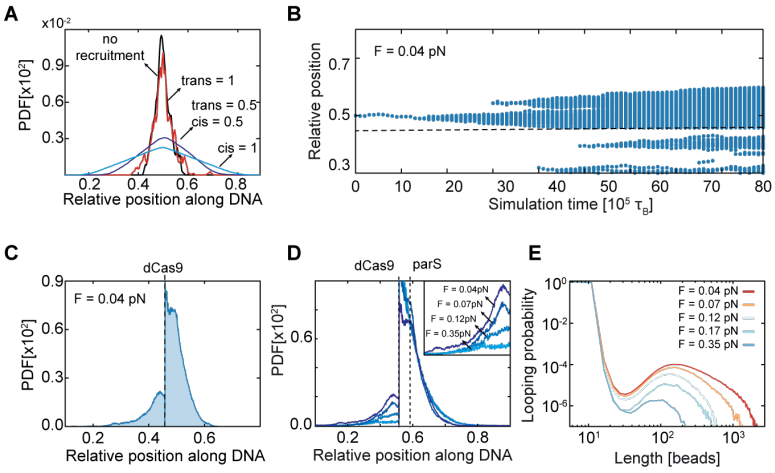


Figure S4.8. In-trans recruitment leads to roadblock-passing via DNA looping. A) *ParB spreading with different in-built recruitment ratios (in all cases: cis+trans = 1, see Methods) compared to "no recruitment" scenario, equivalent to clamping and spreading model.* ***B)*** *Histogram of ParB positions during simulation experiments (F = 0.04 pN). Dashed line indicates the position of the roadblock particle.* ***C)*** *Histogram of cumulated ParB probability density from MD simulations averaged over n=64 simulations represented in panel B. Dashed line indicates the position of the roadblock particle.* ***D)*** *Same as C, with overlaid histograms at different forces (tether lengths).* ***E)*** *Polymer looping probability as the function of tether length (force to length conversion based on WLC model*[34]***.***

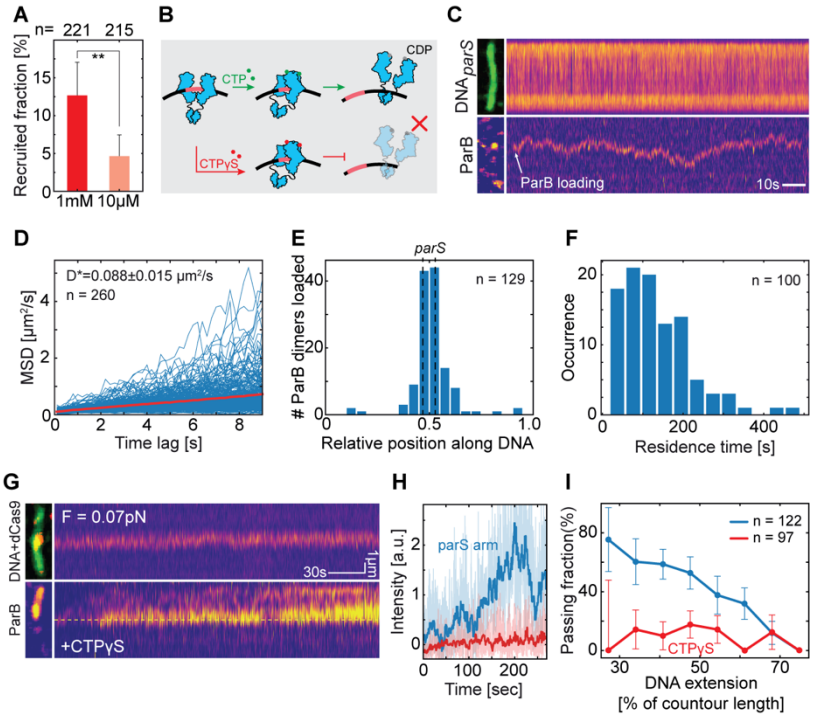


Figure S4.9. CTPase activity is not required for spreading but is required for ParB-ParB recruitment. ***A)*** *Recruitment rate in presence of CTP at 1 mM (red) or 10 μM (pink). Error bars represent binominal confidence intervals. Statistical significance calculated using chi-squared test for a binomial distribution,* $\chi^2(n=405) = 8.8072$, $p<0.003$. ***B)*** *Cartoon representation of ParB in the presence of CTP and CTPγS. While CTP allows for hydrolysis and clamp opening, CTPγS largely prevents that and retains ParB in a closed conformation*[4,5]. ***C)*** *Kymographs for* DNA_{parS} *stained with SytoxGreen (top) and* $ParB^{alexa647}$ *(bottom). Single frame snapshots of the DNA and ParB at the moment of binding, are provided on the left. White arrow indicates ParB loading. Scale bar = 10s.* ***D)*** *Mean square displacement of the diffusing ParB molecules loaded at parS site in the presence of CTPγS. Apparent diffusion coefficient is* $D = 0.088\pm0.015\ \mu m^2/s$, *n= 260.* ***E)*** *Mirrored histogram representing loading position of ParB dimer molecules in the presence of CTPγS relative to the* DNA_{parS} *ends. parS site position is represented by dashed lines. n=129.* ***F)*** *Residence times of diffusing ParB molecules after binding the* DNA_{parS} *in presence of CTPγS (n=100).* ***G)*** *Kymograph for* $dCas9^{alexa549}$ *(top), and* $ParB^{alexa647}$ *(bottom) for* DNA_{parS} *at F= 0.07 pN in the presence of CTPγS. Snapshots of* $dCas9^{alexa549}$ *and* $^{SytoxGreen}DNA_{parS}$ *overlay and* $ParB^{alexa647}$ *signal are provided on the left. Yellow dashed line indicates the position of the* $dCas9^{alexa549}$. ***H)*** *Quantification of the kymograph data of panel F, that displays the ParB signal in the top (blue) and bottom*

(red) part of the DNA, i.e. above and below the Cas9 (dashed yellow line), respectively. F = 0.07 pN. ***I)*** *Fraction of DNA molecules that exhibit ParB dimers passing the dCas9-roadblock. Blue and red data are for CTP (blue, n=122) and slowly-hydrolysable CTPγS (red, n=97), respectively*[17]*. Error bars represent binomial proportion confidence intervals.*

4.6 References

1. Bean, G.J. et al. A22 disrupts the bacterial actin cytoskeleton by directly binding and inducing a low-affinity state in MreB. *Biochemistry* (2009).

2. Livny, J., Yamaichi, Y. & Waldor, M.K. Distribution of centromere-like parS sites in bacteria: Insights from comparative genomics. *Journal of Bacteriology* **189**(2007).

3. Lin, D.C.H. & Grossman, A.D. Identification and characterization of a bacterial chromosome partitioning site. *Cell* (1998).

4. Soh, Y.M. et al. Self-organization of parS centromeres by the ParB CTP hydrolase. *Science* **366**, 1129-1133 (2019).

5. Osorio-Valeriano, M. et al. ParB-type DNA Segregation Proteins Are CTP-Dependent Molecular Switches. *Cell* (2019).

6. Surovtsev, I.V. & Jacobs-Wagner, C. Subcellular Organization: A Critical Feature of Bacterial Cell Replication. in *Cell* Vol. 172 (2018).

7. Balaguer, F.d.A. et al. Ctp promotes efficient parb-dependent dna condensation by facilitating onedimensional diffusion from pars. *eLife* **10**(2021).

8. Chen, B.W., Lin, M.H., Chu, C.H., Hsu, C.E. & Sun, Y.J. Insights into ParB spreading from the complex structure of Spo0J and parS. *Proceedings of the National Academy of Sciences of the United States of America* **112**(2015).

9. Sanchez, A. et al. Stochastic Self-Assembly of ParB Proteins Builds the Bacterial DNA Segregation Apparatus. *Cell Systems* **1**(2015).

10. Song, D., Rodrigues, K., Graham, T.G.W. & Loparo, J.J. A network of cis and trans interactions is required for ParB spreading. *Nucleic Acids Research* **45**(2017).

11. Funnell, B.E. ParB partition proteins: Complex formation and spreading at bacterial and plasmid centromeres. in *Frontiers in Molecular Biosciences* (2016).

12. Guilhas, B. et al. ATP-Driven Separation of Liquid Phase Condensates in Bacteria. *SSRN Electronic Journal* (2019).

13. Graham, T.G.W. et al. ParB spreading requires DNA bridging. *Genes and Development* **28**(2014).

14. Lim, H.C. et al. Evidence for a DNA-relay mechanism in ParABS-mediated chromosome segregation. *eLife* (2014).

15. Vecchiarelli, A.G., Neuman, K.C. & Mizuuchi, K. A propagating ATPase gradient drives transport of surface-confined cellular cargo. *Proceedings of the National Academy of Sciences of the United States of America* **111**(2014).

16. Jalal, A.S.B. & Le, T.B.K. Bacterial chromosome segregation by the ParABS system. *Open Biology* **10:200097**(2020).

17. Jalal, A.S., Tran, N.T. & Le, T.B. ParB spreading on DNA requires cytidine triphosphate in vitro. *eLife* **9:e53515**(2020).

18. Breier, A.M. & Grossman, A.D. Whole-genome analysis of the chromosome partitioning and sporulation protein Spo0J (ParB) reveals spreading and origin-distal sites on the Bacillus subtilis chromosome. *Molecular Microbiology* **64**(2007).

19. Antar, H. et al. Relief of ParB autoinhibition by parS DNA catalysis and ParB recycling by CTP hydrolysis promote bacterial centromere assembly. *Science Advances* (2021).

20. Lagage, V., Boccard, F. & Vallet-Gely, I. Regional Control of Chromosome Segregation in Pseudomonas aeruginosa. *PLoS Genetics* **12**(2016).

21. Böhm, K. et al. Chromosome organization by a conserved condensin-ParB system in the actinobacterium Corynebacterium glutamicum. *Nature Communications* **11**(2020).

22. Baek, J.H., Rajagopala, S.V. & Chattoraj, D.K. Chromosome segregation proteins of vibrio cholerae as transcription regulators. *mBio* **5**(2014).

23. Murray, H., Ferreira, H. & Errington, J. The bacterial chromosome segregation protein Spo0J spreads along DNA from parS nucleation sites. *Molecular Microbiology* **61**(2006).

24. Rodionov, O., ŁObocka, M. & Yarmolinsky, M. Silencing of genes flanking the P1 plasmid centromere. *Science* **283**(1999).

25. Jalal, A.S.B. et al. A CTP-dependent gating mechanism enables ParB spreading on DNA. *eLife* **10**(2021).

26. Kunst, F. et al. The complete genome sequence of the gram-positive bacterium Bacillus subtilis. *Nature* **390**(1997).

27. Ohniwa, R.L., Ushijima, Y., Saito, S. & Morikawa, K. Proteomic analyses of nucleoid-associated proteins in escherichia coli, pseudomonas aeruginosa, bacillus subtilis, and staphylococcus aureus. *PLoS ONE* **6**(2011).

28. Walter, J.C. et al. Physical Modeling of a Sliding Clamp Mechanism for the Spreading of ParB at Short Genomic Distance from Bacterial Centromere Sites. *iScience* **23**(2020).

29. Debaugny, R.E. et al. A conserved mechanism drives partition complex assembly on bacterial chromosomes and plasmids. *Molecular Systems Biology* **14**(2018).

30. Ganji, M. et al. Real-time imaging of DNA loop extrusion by condensin. *Science* **360**, 102-105 (2018).

31. Fisher, G.L.M. et al. The structural basis for dynamic DNA binding and bridging interactions which condense the bacterial centromere. *eLife* **6**, e28086 (2017).

32. Osorio-Valeriano, M. et al. The CTPase activity of ParB determines the size and dynamics of prokaryotic DNA partition complexes. *Molecular Cell* **81**, 3992-4007.e10 (2021).

33. Taylor, J.A. et al. Specific and non-specific interactions of ParB with DNA: Implications for chromosome segregation. *Nucleic Acids Research* **43**(2015).

34. Bouchiat, C. et al. Estimating the persistence length of a worm-like chain molecule from force-extension measurements. *Biophysical Journal* **76**(1999).

35. Muñoz-Dorado, J. et al. Transcriptome dynamics of the myxococcus xanthus multicellular developmental program. *eLife* **8**(2019).

36. Thiery, S. & Kaimer, C. The Predation Strategy of Myxococcus xanthus. *Front Microbiol* **11**, 2 (2020).

37. Broedersz, C.P. et al. Condensation and localization of the partitioning protein ParB on the bacterial chromosome. *Proceedings of the National Academy of Sciences of the United States of America* **111**(2014).

38. Wang, X., Brandão, H.B., Le, T.B.K., Laub, M.T. & Rudner, D.Z. Bacillus subtilis SMC complexes juxtapose chromosome arms as they travel from origin to terminus. *Science* (2017).

39. Wang, X. et al. Condensin promotes the juxtaposition of dna flanking its loading site in Bacillus subtilis. *Genes and Development* **29**, 1661-1675 (2015).

40. Brandão, H.B., Ren, Z., Karaboja, X., Mirny, L.A. & Wang, X. DNA-loop-extruding SMC complexes can traverse one another in vivo. *Nature Structural and Molecular Biology* **28**(2021).

41. Germier, T. et al. Real-Time Imaging of a Single Gene Reveals Transcription-Initiated Local Confinement. *Biophysical Journal* **113**(2017).

42. Saad, H. et al. DNA Dynamics during Early Double-Strand Break Processing Revealed by Non-Intrusive Imaging of Living Cells. *PLoS Genetics* **10**(2014).

43. Pradhan, B. et al. SMC complexes can traverse physical roadblocks bigger than their ring size. *bioRxiv* (2021).

44. Kim, E., Kerssemakers, J., Shaltiel, I.A., Haering, C.H. & Dekker, C. DNA-loop extruding condensin complexes can traverse one another. *Nature* (2020).

5

DYNAMIC PARB-DNA INTERACTIONS INITIATE AND MAINTAIN A PARTITION CONDENSATE FOR BACTERIAL CHROMOSOME SEGREGATION

In most bacteria, chromosome segregation is driven by the ParABS system where the CTPase protein ParB loads at the parS site to trigger the formation of a large partition complex. Here, we present in vitro studies of the partition complex for Bacillus subtilis ParB, using single-molecule fluorescence microscopy and AFM imaging to show that transient ParB-ParB bridges are essential for forming DNA condensates. Molecular Dynamics simulations confirm that condensation occurs abruptly at a critical concentration of ParB and show that multimerization is a prerequisite for forming the partition complex. Magnetic tweezer force spectroscopy on mutant ParB proteins demonstrates that CTP hydrolysis at the N-terminal domain is essential for DNA condensation. Finally, we show that transcribing RNA polymerases can steadily traverse the ParB-DNA partition complex. These findings uncover how ParB forms a stable yet dynamic partition complex for chromosome segregation that induces DNA condensation and segregation while enabling replication and transcription.

This chapter was published as Tišma M, Janissen R, Antar H, Martin-Gonzalez A, Barth R, Beekman T, van der Torre J, Michieletto D, Gruber S, Dekker C. *Dynamic ParB-DNA interactions initiate and maintain a partition condensate for bacterial chromosome segregation*. Nucleic Acids Res, (2023)

5.1 Introduction

Precise chromosome segregation at each cell cycle is important for the stable propagation of all life forms. In most bacteria, the ParAB*S* system is the main component ensuring such faithful segregation of chromosomes[1]. This system consists of an ATP-hydrolase partition protein A (ParA), a CTP-hydrolase partition protein B (ParB), and a 16-bp centromeric sequence *parS* that is typically located near the replication origin on the genome [2-5]. ParB proteins can load at the *parS* sequence and subsequently assemble into a higher-order nucleoprotein complex that is referred to as 'the partition complex' [6-9]. Following replication, the two partition complexes interact with a ParA gradient along the cylindrical cell axis to segregate the nascent origins of bacterial chromosomes [10,11]. Bacterial SMC proteins are recruited to the partition complex [12-14] to further increase the fidelity of the segregation process [14-18]. The formation of a functional partition complex is essential to ensure a correct distribution of chromosomes during cell division.

Several models have been proposed for the molecular structure of the partition complex (reviewed in detail by Jalal and Le [19]), including 'bridging and condensing' [8,20,21], 'nucleation and caging' [22,23], and recent work indicating liquid-liquid phase-separated droplets [24,25]. In essence, all these models rely on the initial nucleation of ParB proteins at the *parS* site followed by some 'self-self' interactions by ParB proteins to bring distal DNA elements together to form a partition complex. Many older models that relied on *in vitro* insights required revision after it was shown that ParB proteins utilize CTP to load at a *parS*-site and able to spread over multiple kilobases [3,4,26]. ParB proteins were shown to condense DNA in the presence of CTP, and a new model combining one-dimensional sliding and ParB-ParB bridging has been proposed w, in which ParB dimers form a clamp that binds two CTP molecules upon loading at the *parS* site, whereupon they lose the affinity to *parS* and slide along the DNA to spread to adjacent DNA regions [4,27,28]. After some time, the ParB clamp is hypothesized to open either at the C- or N-terminus, which enables to bring two distant DNA segments into proximity through *in-trans* bridging interactions [29]. This model integrates the DNA 'clamping and sliding' hypothesis in the presence of CTP with previous models that considered 'caging' or 'bridging' of ParB proteins [8,9,20,21,30].

Many questions remain, however, on the formation and maintenance of the partition complex. For example, what is the structure and dynamics of the partition complex? How is the condensation of the complex initiated? How does CTP hydrolysis regulate both the DNA binding and clamping, and the self-self interactions needed for bridge formation? Which protein domains are involved in bridge formation? While the necessity of both C- and N-terminal domains is clear [20,31], it remains to be determined

which conformational changes need to occur prior to bridge formation and DNA condensation [4,27,28]. Moreover, partition complex formation via DNA condensation has never been reconstituted *in vitro* using a single *parS* site, while a single *parS* site was found to be sufficient for *in vivo* partition complex function[18,32].
To address these questions, we investigated the mechanism of ParB-DNA complex formation *in vitro* at the single-molecule level using purified *Bacillus subtilis* ParB proteins in Atomic Force Microscopy (AFM), Magnetic Tweezers (MT), and visualization by TIRF microscopy in a DNA-stretching assay [33]. Furthermore, we performed Molecular Dynamics (MD) simulations using a coarse-grained DNA polymer and ParB models. Finally, we used *in vitro* transcription to clarify the debate if a ParB:DNA cluster affects transcription, and we observed that, remarkably, transcription by bacterial DNA-dependent RNA polymerase (RNAP) is not affected by ParB or condensed ParB:DNA clusters.

5.2 Results

5.2.1 ParB proteins condense DNA with a single *parS* site

The recent discovery that ParB proteins require CTP nucleotide to specifically load onto a DNA with a *parS* site (DNA_{parS}) and perform their cellular function challenged many established models of ParB function [3,4,34]. Most previous condensation studies used very high protein concentrations in order to show the occurrence of ParB condensation or DNA binding [2,8,20,21,31], and often no differences were found in the presence or absence of a *parS* site on the DNA substrate [8,20,21]. Recent work on chromosome and plasmid ParB proteins[29,35], however, showed that in the presence of CTP nucleotide, ParB proteins could induce condensation of a ~6 kbp DNA at nanomolar concentrations, in line with the efficient loading of ParB. This study reported that at least 7 *parS* sites were necessary on the DNA for condensation to occur [29], which was unexpected given that *B. subtilis* mutants carrying a single *parS* site showed no defective phenotype in growth or ParB loading in vivo [18,32].

To quantify the ability of ParB to drive condensation, we first used MT to study the interaction of *B. subtilis* ParB proteins with a long DNA substrate (~14 kbp) that contained only a single *parS* site in the middle of the construct. Chemical groups attached to opposite ends of this DNA_{parS} were used to tether one end of the DNA to a streptavidin-coated magnetic bead (through a biotin group) and the other end to an anti-DIG antibody-coated surface (through a digoxigenin group) (Fig. 5.1A, S1A, see Methods). We incrementally lowered the force that was applied to the magnetic bead

from 7 to 0.05 pN (Fig. 5.1B – blue line) and recorded the change in end-to-end length of the attached DNA molecule.

Strikingly, in the presence of ParB and CTP, a single *parS* site on the DNA was found to be sufficient for DNA condensation, as evidenced by the abrupt reduction of the DNA end-to-end length (i.e., a rapid lowering of the bead height) when lowering the force below ~0.3 pN (Fig. 5.1B - red line). This was not observed when ParB protein was not present (Fig. 5.1B - black line). Similarly, we did not observe any DNA condensation in the absence of CTP or in the absence of a *parS* site (Fig. S5.1B-C). We quantified the force-extension curves for different concentrations of ParB and observed an abrupt transition at a critical concentration between 5 and 20 nM, where condensation was observed only above this critical value (Fig. 5.1C). Condensation was observed for a wide range of ParB concentrations (20-200 nM) and always yielded the same degree of DNA condensation, irrespective of the ParB concentration.

Next, we optically visualized the DNA condensation in a fluorescence-based DNA-stretching assay [36] using a TMR-labelled *B. subtilis* ParB protein and SYTOXGreen (SxG) intercalator to label the DNA molecules. Here, the DNA_{parS} was 42 kbp long, loosely tethered onto the surface via biotin-streptavidin interaction at both DNA ends, and it contained a single *parS* site in the middle of the DNA_{parS} [36] (see Methods for details, Fig. S5.1D). Upon incubation with 25 nM ParB, we observed strong fluorescent DNA loci arising over time on the DNA_{parS}, which colocalized with the fluorescent ParB signal (Fig. 5.1D, Fig. S5.1E). From the fluorescence intensity of the ParB:DNA condensate, we quantified the amount of DNA within the condensate as well as the force that the condensation exerted on the DNA fragments outside of the condensate [37,38]. Strikingly, we observed that DNA condensate sizes reached up to 25 kbp, i.e., it could contain over 60% of the total DNA content (see Fig. S5.1F). Furthermore, we observed that condensate sizes varied by a factor of >2 as the end-to-end length of the tethered DNA varied between 20% and 50% of the DNA contour length (maximal contour length was ~14 μm; Fig. 5.1E). While the condensate size thus could vary significantly, we found, by contrast, that the pulling force that it exerted on the DNA was rather constant, at a value of $F = 0.08 \pm 0.03$ pN (mean ± SD., Fig. 5.1F).

Finally, we used AFM to image the ParB:DNA condensates at single-molecule resolution. The AFM images showed protein-bound DNA structures that are locally bridged and entangled, where higher local structures (>4 nm) indicated the presence of ParB molecules on the DNA (Fig. 5.1G-H). In contrast, we did not observe such higher-order DNA:ParB structures in the absence of either ParB, a *parS* site on the DNA, or CTP molecules (Fig. S5.1G-I).

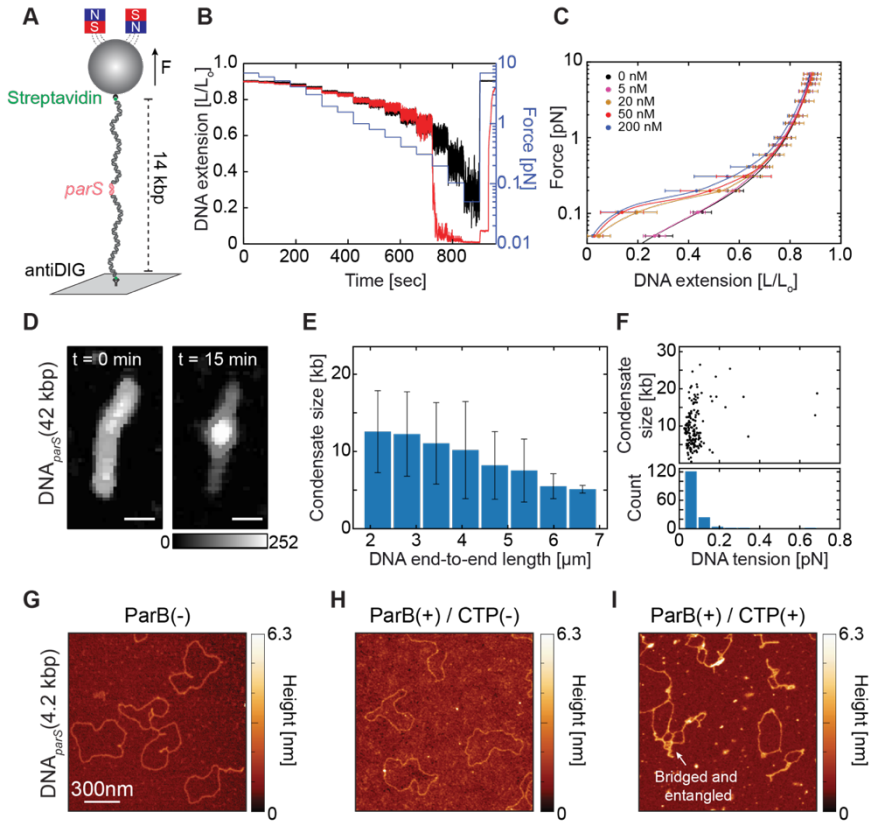


Figure 5.1. ParB proteins efficiently condense DNA in the presence of a single parS site. ***(A)*** *Schematic representation of experimental MT assay, using a single parS site at the DNA_{parS} molecule (see Methods).* ***(B)*** *DNA extension in the absence (black) and the presence (red) of 50 nM ParB protein at different forces applied to the magnetic bead (blue) over time.* ***C)*** *Average DNA_{parS} extension (mean±SD) when lowering force (N = 35 for each ParB concentration) in the presence of different ParB concentrations. Black line represents a WLC fit to the 0 nM ParB control data.* ***(D)*** *Snapshot fluorescence images of a DNA_{parS} molecule before and after 15 min incubation with 25 nM ParB.* ***(E)*** *The effect of DNA tethering length on final condensate size (mean±SD; N = 153), represented as kilobase pairs of the DNA that it contains. r = - 0.64 (Pearson correlation coefficient).* ***(F)*** *Tension that the formed ParB clusters of different sizes exert on the DNA fragments outside the cluster. N = 153.* ***(G)*** *Dry AFM image of 4.2 kbp circular DNA_{parS} molecule in the absence of ParB proteins.* ***(H)*** *Same as in (G) but in the presence of 5 nM ParB proteins.* ***(I)*** *Same as (G) but in the presence of both 1 mM CTP and 5 nM ParB.*

5.2.2 DNA condensation by ParB proteins is dynamic and reversible

Previous work on ParB proteins hinted at a dynamic exchange of the proteins with DNA_{parS} [24,25]. Here, using our DNA-stretching assay and fluorescence recovery after photobleaching (FRAP), we tested the binding and unbinding of ParB within condensed ParB:DNA clusters. In a similar setup as described previously (Fig. 5.1D) [39], we stretched the DNA_{parS} on the surface and incubated it in the presence of a high concentration of ParB proteins until most DNA molecules were condensed (15 min). After this time, most of the molecules reached a stable equilibrium between loading and dissociating ParB proteins. To study the recovery dynamics of ParB:DNA complexes, we co-imaged the DNA and ParB proteins within the condensates over time, after photobleaching with a strong laser power (Fig. 5.2A-B, see Methods). Following bleaching, the FRAP experiments showed a quick recovery (~1 min) of the ParB fluorescence signal within the condensate (Fig. 5.2B). The recovery time and dynamics is in line with the date previously obtained for plasmids and chromosomal ParB proteins [25,28,40], and it points to a fast exchange of ParB proteins with the soluble pool of ParB in the buffer, while maintaining a condensed ParB:DNA structure.

Interestingly, the ParB signal in the condensate did not exhibit a steady plateau but instead showed significant and sustained dynamic fluctuations of up to 40% in its intensity on the minute timescale (Fig. S5.2A). We quantified the total amount of DNA within a single condensate and as well as the amount of total ParB proteins on the DNA over time and observed that both the DNA and ParB intensities displayed substantial fluctuations (Fig.S2B-G). The DNA and ParB signals were not strongly correlated, showing that, in steady state, the DNA can dynamically reorganize while the amount of ParB proteins does not change much. We additionally observed that the ParB:DNA condensate varied in size over time, although the condensate was stably maintained throughout time (Fig. 5.2A-B and S5.2B-G). We recorded timelapses of the initial steps of condensation to monitor the beginning of the entire process from the ParB loading to the spreading on DNA_{parS} and the condensation. As Fig. 5.2C-D shows, we observed loading of ParB, whereupon its subsequent spreading led to a covering of basically the entire DNA within minutes after flushing in the protein, after which DNA-condensation was established through the formation of a local cluster (Fig. 5.2D, S5.3A, C). The DNA_{parS} within the resulting ParB:DNA condensates exhibited sizeable fluctuations of the order of ~10 kbp within minutes (Fig. S5.3B, D). In complementary MT experiments similar high fluctuations of ParB:DNA condensates were observed (Fig. S5.3E, G, H). If ParB molecules would form permanent protein-protein bridges to bring distant parts of the DNA together, a continuously increasing condensation into a single static ParB:DNA condensate would occur. On the contrary, our data suggested that ParB-ParB

bridges are transient, continuously reforming and breaking, thus establishing a condensate whose components are quickly turning over.

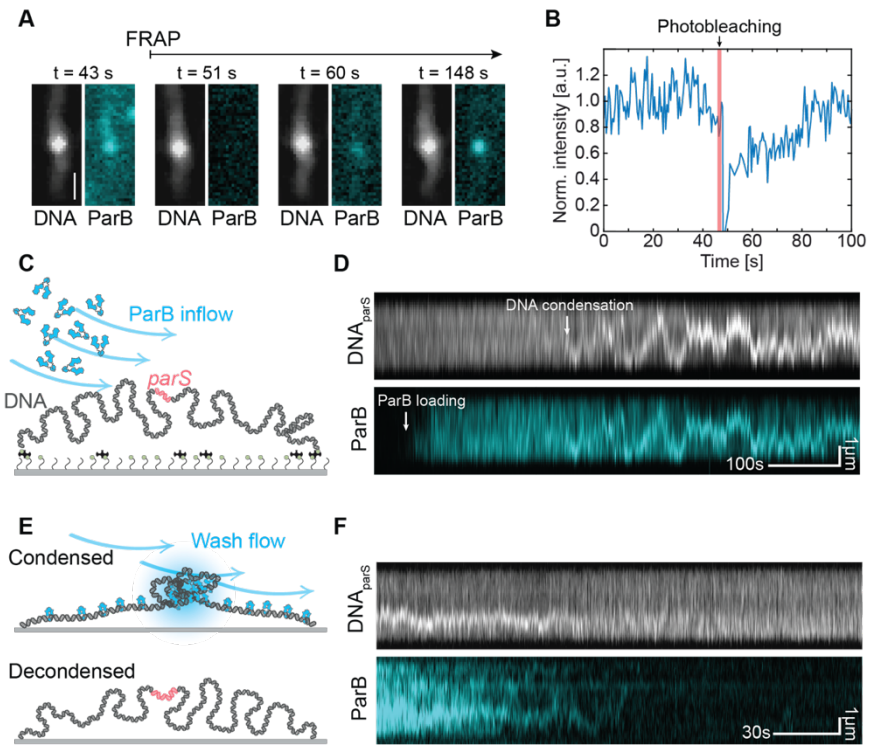


Figure 5.2. DNA condensation is dynamic. ***(A)*** *Snapshots of DNA signal stained with SxG (greyscale) and ParB^{Alexa647} signal (cyan) shown at different time points before photobleaching and during fluorescence recovery. t = 0 s represents the imaging start time after the protein incubation step (at 25 nM) of 15 min.* ***(B)*** *Fluorescence intensity of the ParB:DNA condensate before photobleaching and during fluorescence recovery of the condensate, integrated over the full length of the DNA molecule (full trace Fig. S2A).* ***(C)*** *Schematic representation of the single-molecule fluorescence DNA-stretching assay used for probing DNA condensation.* ***(D)*** *Kymographs of DNA$_{parS}$, stained with SxG (top) and ParB^{TMR} (bottom, 25nM). White arrow indicates ParB loading to DNA.* ***(E)*** *Same as in C but for washing experiments.* ***(F)*** *Same as in D but for washing experiments.*

The dynamic nature of the ParB:DNA condensates was confirmed by washing experiments where we washed the condensates with a buffer that did not contain ParB proteins (Fig. 5.2E). Our data showed that most ParB:DNA condensates slowly washed out within a time of ~1-2 minutes, wherein the DNA molecules returned to their initial non-condensed state (Fig. 5.2F, S5.4A,B). This occurred similarly with or without the presence of CTP molecules (Fig. S5.4A and S5.4C, respectively).

Altogether, FRAP experiments showed the dynamic exchange of the ParB proteins with the DNA condensate, and washing experiments pointed to the transiency of the ParB-ParB bridges that allowed for proteins to be washed away and decondense the DNA. Our data showed that the ParB:DNA condensates are dynamic entities that continuously rearrange, consistent with ParB-ParB bridges that are transient and continuously breaking and reforming while maintaining the overall condensate intact.

5.2.3 DNA condensation starts with loop formation

To explore the very initial stages of the ParB-DNA condensate formation, we strongly lowered the concentration of the ParB protein to 0.3 nM and observed their behavior at the single-molecule level in real-time. Using our fluorescence DNA-stretching assay, we observed that two ParB dimers loaded on the DNA$_{parS}$ could spontaneously meet and connect, forming a DNA loop between them. By tracking the higher-intensity region of the DNA (the loop), we observed that it is dynamic in its position (as it diffused along the DNA) and transient (as it disrupted after some time) (Fig. 5.3A-B). As we kept the protein concentration very low, there were typically only a few ParB proteins on the DNA, and such loop formation was rare.

To observe the initial loop formation by ParB proteins more accurately, we turned to high-speed AFM (see Methods), where we examined a shorter circular DNA$_{parS}$ molecule (4.2 kbp). We observed that ParB dimers bound to different spots on the DNA could form a transient loop of DNA by bridging these distant segments together (Fig. 5.3C, S5.4D-G). We quantified the loop residence times and observed that loops persisted much longer in the presence of ParB proteins than loops observed in a control without ParB (Fig. 5.3D, S5.4H). On average, the DNA loops resided for 50 ± 25 s (mean ± SD) before disrupting. We reasoned that the observed loop formation was the precursor of the condensation of more extended DNA:ParB structures, as proposed for ParB proteins from F-plasmid recently[35]. Specifically, at larger ParB concentrations, the amount of binding ParB became larger than set by its unbinding rate, triggering a non-linear cooperative binding and spreading on the DNA substrate, leading to condensation.

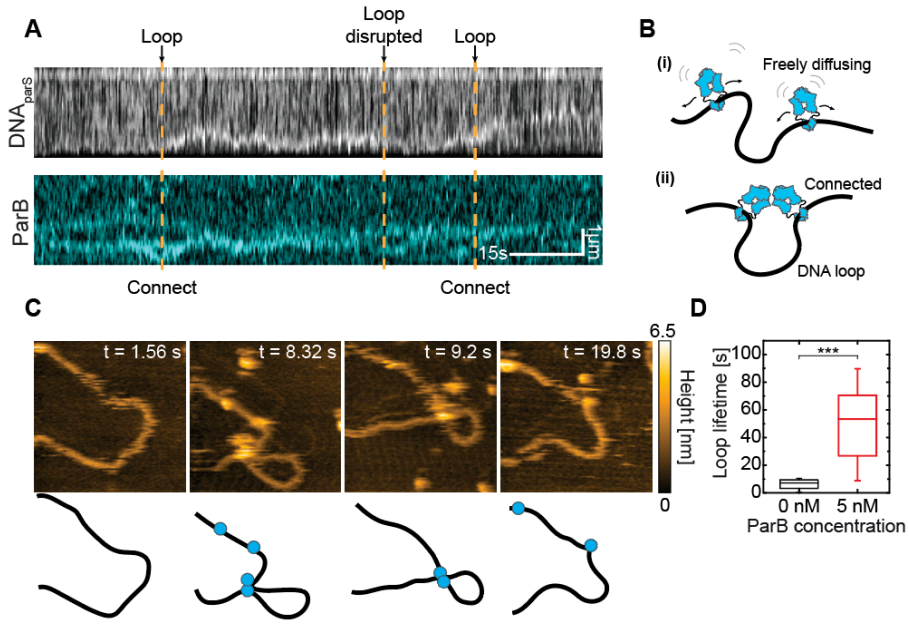


Figure 5.3. DNA condensation is initiated via the ParB-ParB bridge and a transient loop formation. (A) *Kymographs for DNA_{parS} stained with SxG (top) and $ParB^{TMR}$ (bottom, 0.3 nM). Orange dashed lines show the initiation and breaking points of the DNA loop held by ParB connection points.* ***(B)*** *Schematic representation of DNA loop formation induced by ParB-ParB bridging.* ***(C)*** *High-speed AFM topography images of a transient loop formation induced by ParB-ParB bridging..* ***(D)*** *Box-whisker plot of DNA loop lifetime in the absence (black; mean±SD 5.6 ± 3.3 s; N = 15) and the presence (red; mean±SD 50 ± 25 s; N = 16) of 1 nM ParB. Significance value by 2-tailed, unpaired t-test: $p = 1.29 * 10^{-4}$.*

5

5.2.4 CTP hydrolysis at the ParB N-terminal is required for partition complex formation

Previous work[6,8,9,22,23,29,30] hypothesized that DNA bridging induced by ParB dimers involves the interaction between two monomers of different ParB dimers. However, current models cannot distinguish whether ParB proteins need to be opened at the N- or C-terminal domain (Fig. 5.4A) prior to DNA condensation[29]. Balaguer *et al.* [29] found that CTP binding was crucial but CTP hydrolysis was not required for DNA condensation [29], which suggests a third alternative where ParB dimers condense DNA without any opening after DNA loading and prior to ParB-ParB bridge formation (Fig. 5.4A).

To distinguish between these models and resolve whether ParB needs to open after loading to DNA$_{parS}$ to proceed with DNA condensation, we examined a variety of ParB variants, which were forced into either N-or C-terminal domain closure. Prior to spreading, ParB dimer binds as an 'open clamp' to the *parS*-site and sandwiches two CTP nucleotides at the N-termini interfaces that proceed to close, forming a 'closed clamp' [43]. To force the protein to remain N-terminally closed after binding the DNA, we used a previously described ParB variant, namely ParB$^{\mathbf{T22C}}$, which can be efficiently crosslinked by bismaleimidoethane (BMOE) via cysteine chemistry in its closed (but not in the open) form [27] (Fig. S5.5A-B). After incubating our 15 kbp DNA$_{parS}$ with a ParB$^{\mathbf{T22C}}$ variant at different concentrations, we collected MT force-distance curves that characterized the degree of condensation (Fig. 5.4B-D). Note that this was slightly different from the experimental procedure described in Fig. 5.1, since we needed to crosslink this ParB$^{\mathbf{T22C}}$ protein variant only after it had loaded onto the DNA$_{parS}$: we first loaded the ParB$^{\mathbf{T22C}}$ proteins for 5 min and then crosslinked them while bound to the DNA for 10 min, using a buffer containing BMOE and CTP but no protein (see Methods, Fig. S5.5A). A comparable experimental procedure increased the DNA residence time of ParB$^{\mathbf{T22C}}$ in a Biolayer Interference (BLI) assay, presumably by locking ParB clamps onto DNA by cysteine cross-linking [26-28] (Fig. S5.5C-D). After loading the ParB$^{\mathbf{T22C}}$ dimers on the DNA, we started the force-extension experiments (as in Fig. 5.1C) and observed two key differences (Fig. 5.4B) compared to wildtype ParB.

First, without the BMOE crosslinking, a significant condensation was observed, as can be seen from comparing the yellow curve (with ParB$^{\mathbf{T22C}}$) to the black curve (bare DNA), although the ParB$^{\mathbf{T22C}}$ variant condensed the DNA to a lesser degree than wild-type ParB (Fig. 5.4D). Secondly, and more interestingly, the ParB$^{\mathbf{T22C}}$ variant's ability to condense the DNA was hampered in the presence of BMOE. To compare with a mutant cross-linking in the C-terminal domain[29], we subsequently employed a ParB$^{\mathbf{S278C}}$ variant that can be efficiently crosslinked by BMOE at its C-terminus while still allowing both the CTP a *parS*-site binding [27]. The ParB$^{\mathbf{S278C}}$ mutant was crosslinked prior to the experiments, ensuring that upon their contact with the DNA$_{parS}$, they were already crosslinked at their C-terminus. In the MT experiments we observed no differences between the crosslinked and non-crosslinked variants (Fig. 5.4C)). In the presence of BMOE (and thus a covalent bond at the C-terminus), the ParB$^{\mathbf{S278C}}$ proteins could efficiently load and condense the DNA$_{parS}$ similar to the wild-type (Fig. 5.4D). We confirmed the crosslinking of both the ParB$^{\mathbf{T22C}}$ and ParB$^{\mathbf{S278C}}$ variants by denaturing SDS-PAGE (Fig. S5.5A-B).

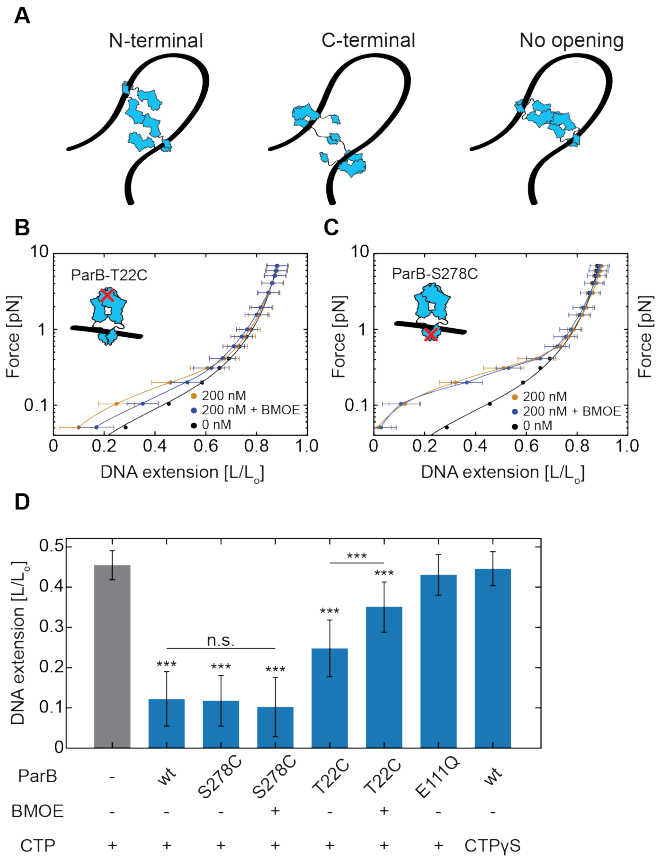


Figure 5.4. DNA$_{parS}$ condensation requires CTP hydrolysis at the N-terminal of ParB proteins. ***(A)*** *Potential scenarios leading to ParB-ParB bridging via different protein domains.* ***(B)*** *Average DNA$_{parS}$ extension (mean±SD) in MT when lowering force in the presence of ParB^{T22C} mutant with (purple; N = 36) or without (yellow; N = 43) 1 mM BMOE crosslinker added. Black line represents the WLC model fit to 0 nM ParB data (N = 32).* ***(C)*** *Same as in (B) for the C-terminal ParB^{S278C} mutant (N; 0 nM: 32, 200 nM: 13, 200 nM +BMOE: 13).* ***(D)*** *Relative DNA extension in different conditions at an applied force of F = 0.1 pN and 200 nM concentrations of all ParB variants. Statistical analyses consisted of unpaired, two-tailed t-tests (p: *** < 0.001; n.s. = non-significant).*

Furthermore, we examined the effects of CTP hydrolysis on ParB-mediated DNA-condensation. First, we measured the previously described ParB^{E111Q} mutant, which is deficient in CTP hydrolysis but not in DNA$_{parS}$ loading [27]. In MT force-extension

experiments under the same conditions as the experiments in Fig 1C, this variant did not show any apparent DNA condensation (Fig. 5.4D, S5.5E). This is in agreement with previous studies showing that catalytically inactive EQ-mutants do not form fluorescent foci characteristic of a functional partition complex in *B. subtilis* [27]. Finally, we performed MT experiments with replacing CTP with its non-hydrolyzable version CTPγS, which would force a clamped state of ParB after loading onto the DNA_{parS} [4,28]. First, we confirmed ParB binding and lack of condensation in the presence of CTPγS, in our fluorescence assay (Fig. S5.5E, F). In line with our previous results, we observed no condensation of DNA_{parS} molecules in MT, even in the presence of high protein concentrations (200 nM, Fig. 5.4D, S5.5G, H).

Taken together, we can conclude that our findings demonstrate that CTP hydrolysis at the N-terminal domain is essential for DNA condensation. Most likely, this involves an N-terminal opening, while C-terminal opening is not required.

5.2.5 Cooperativity of ParB multimers drives ParB:DNA condensation

We then questioned whether the interactions between ParB proteins involve merely dimer-dimer pairs or larger oligomers. In the case of "dimer of dimers" (DoD), ParB dimers behave as single bivalent bridges (Fig. 5.5A). By contrast, "Multimers of dimers" (MoD) can undergo oligomerization (Fig. 5.5A) into larger complexes. We tested these two scenarios in Molecular Dynamics (MD) simulations (Fig. 5.5B), where we modelled ParB dimers loading at *parS*, diffusing on a DNA substrate, and undergoing *cis/trans* recruitment. These computational models are based on the well-established framework of testing protein movements along the DNA by multiple previous studies [41-43]. We extended our previously published model that includes experimentally determined ParB loading rates, residence time of ParB on the DNA, and *cis/trans* recruitment rates (see Methods and Tišma et al. [36] for more details) to test the effects of valency. By varying the ratio κ of loading versus unloading rates, we accounted for different ParB concentrations in the bulk.

For all parameters, we observed a dramatic difference in the DNA polymer structure between DoD and MoD models. When ParB dimers could only interact as DoD (valency 1), DNA molecules remained in a linearly extended, non-condensed conformation (Fig. 5.5C). However, when we considered the MoD mode with valency 2, we observed the formation of a dense cluster (Fig. 5.5D) that resembled our fluorescence data (Fig. 5.1). Thus, for all other parameters being equal, the DoD-mode remained in fully extended conformation while MoD-mode dynamically collapsed the DNA into a condensed state. Notably, a recent model on the ParB:DNA condensation in *Caulobacter crescentus* suggests that DoD-mode could bring DNA into a condensed cluster [40].

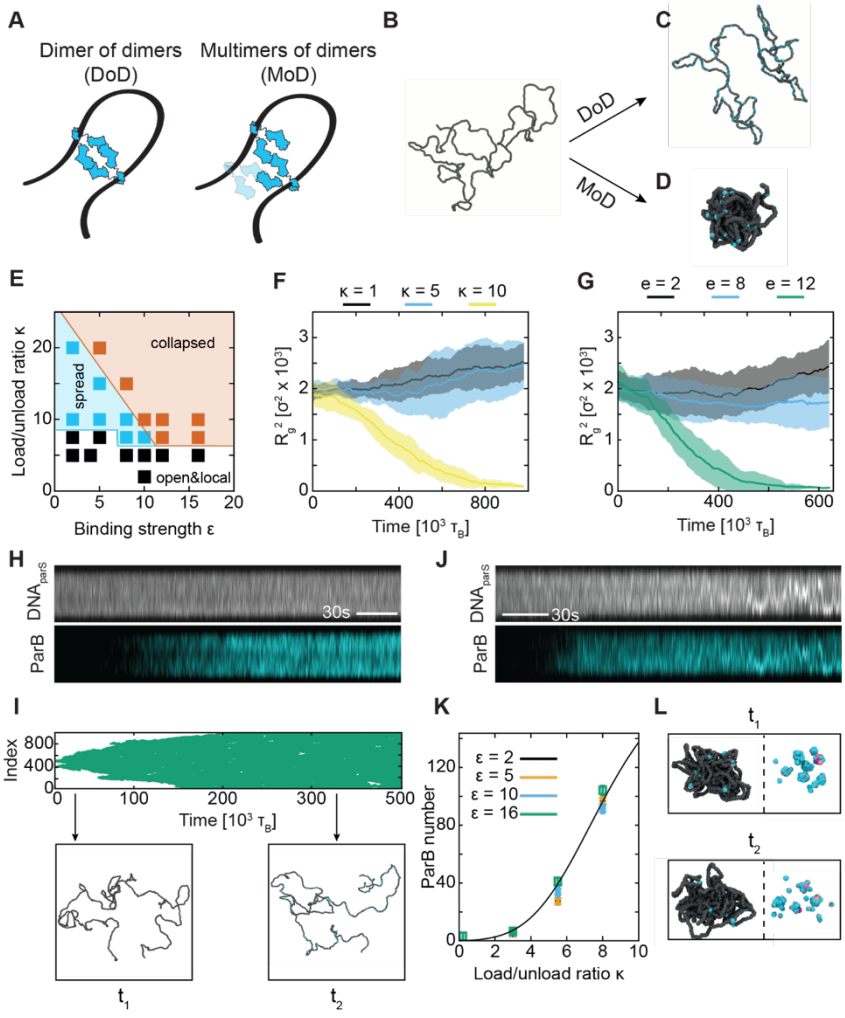


Figure 5.5. DNA cluster formation depends on bridging strength and ParB loading rate. ***(A)*** *Two possible scenarios for ParB-ParB bridging via the N-termini.* ***(B)*** *MD simulations image of a DNA polymer containing 1,000 beads with non-tethered ends.* ***(C)*** *'Open' DNA polymer conformation in the DoD (valency = 1) mode of ParB-ParB interaction.* ***(D)*** *Collapsed DNA polymer conformation in the MoD (valency = 2) mode of ParB-ParB interaction.* ***(E)*** *Phase diagram for the MoD model showing three distinct conformations with varying ParB-ParB interaction strength (ε) and load/unload ratios (κ). White area: local distribution of ParB and open DNA conformation; cyan area: spread distribution of ParB and open DNA conformation, and orange area: collapsed ParB:DNA conformation.* ***(F)*** *DNA collapse for varying loading/unloading ratios (with a fixed ε = 10, see Methods).* R_g^2 *represents the gyration radius of the DNA. Shaded area*

is SD among 10 replicas of the same system with a different initial configuration and seed. ***(G)*** *MD simulations of DNA collapse/condensation in the presence of a fixed loading/unloading ratio (κ = 10) at varying ParB-ParB binding strengths. Shaded area: same as in F.* ***(H)*** *Kymographs for DNA_{parS} stained with SxG (top) and $ParB^{TMR}$ (bottom) at 5 nM.* ***(I)*** *Top: simulated kymograph of ParB distribution at ε = 5, κ = 15, where no DNA polymer collapse was observed. Bottom: snapshots of DNA polymer conformations at selected timepoints in the kymograph above.* ***(J)*** *Same as H for the ParB concentration of 25 nM.* ***(K)*** *Total number of ParB bound to the DNA as a function of κ. Black line represents fit with a Hill coefficient of H = 4.5, indicating a cooperative, switch-like behavior.* ***(L)*** *Different timepoints after condensation of ParB:DNA cluster in MD simulations (ε = 10, κ = 10). Left: shows the ParB:DNA cluster conformation. Right: shows the ParB proteins within the cluster. Three ParB proteins labelled in shades of pink to show that they dynamically rearrange while the overall DNA structure remains collapsed.*

In this model, this is facilitated by the rapid re-formation of the ParB-ParB bridge after the protein-protein connection is broken, whereby both proteins remain bound to the DNA. In our model, ParB proteins are likely to dissociate from the DNA after the formation of a transient bridge due to their k_{off} rate. Hence the MoD-mode that ensures oligomerization is more efficient in collapsing the DNA cluster. Combination of structural data and computational modelling may in the future shed more light on the exact conformation of ParB dimers within a ParB-ParB bridge.

We then extended our MD simulations to test for DNA condensation at different values of the interaction strength ϵ between ParB proteins in the MoD model (i.e., the depth of the Morse potential): we observed three qualitatively different outcomes (see phase diagram in Fig. 5.5E): (i) extended DNA with merely localized ParB dimers (Fig. 5.5E, white area), (ii) extended DNA where ParB proteins spread to the whole DNA substrate driving no compaction (Fig. 5.5E, cyan area), and (iii) condensed DNA:ParB structures (Fig. 5.5E, orange area). In our MD simulations, we did not observe condensation without spreading, while we did observe spreading without condensation, e.g., DNA molecules showing ParB proteins across the full length of the DNA polymer but no collapse of the polymer (Fig. S5.6A, B). This was dependent on the loading/unloading rate κ and interaction strength ϵ (Fig. S5.6C-E). For a sufficiently large number of ParB proteins (Fig. 5.5F) and ParB-ParB bridge strengths (Fig. 5.5G), clusters would appear (Fig. S5.6F, G) and the DNA molecule would collapse (Fig. 5.5F, G). This is in line with the behavior we observed in our fluorescence imaging assay: at 5 nM, we observed DNA

molecules that displayed a uniform coverage of ParBs without evidence of condensation (Fig. 5.5H), just as in the MD simulations (Fig. 5.5I). On the contrary, at higher protein concentrations (25 nM), the DNA molecule collapsed shortly after ParB proteins spread over the entire DNA molecule (Fig. 5.5J).

This behavior can be attributed to the dynamic nature of ParB dimers on DNA. If the loading and recruitment rate (proportional to the concentration of ParB in the soluble pool) is slow compared with the unbinding time – set by the CTP hydrolysis rate[4,27,28] – it is not possible to reach a critical number of ParB proteins on the DNA to drive condensation. In our MD simulations, we therefore quantified the number of ParB bound to the DNA as a function of ParB concentration (κ_{on} in our simulations, Fig. S5.7A-B). We obtained a steep Hill coefficient (H = 4.5, Fig. 5.5K) indicating high cooperativity. For instance at κ = 8, we observed ~100 ParB molecules on the DNA polymer that drive the condensation (Fig. S5.7C). An abrupt transition was also observed in the radius of gyration of the DNA as a function of κ_{on} (Fig. 5.5G). This switch-like collapse behavior was also seen in both our fluorescence (Fig. 5.5J) and MT (Fig. 5.1C) experiments, where at ~10 nM ParB the DNA molecules were either found stretched or condensed, but never in between, indicating a bi-stable nature of this cooperative , first-order-like condensation.

Finally, by visual inspection of our simulation results, we could discern that the ParB:DNA condensate was maintained by a fluctuating number of ParB proteins. Figure 5.5L shows example time snapshots where ParB proteins were exchanged with proteins of the pool, whilst the DNA scaffold remained condensed. This turnover that we observed in MD simulations is in line with our FRAP experiments (Fig. 5.2).

5.2.6 Transcription by RNA Polymerase can occur in the presence of dynamic ParB:DNA clusters

It has been reported that gene expression can be downregulated in the vicinity of *parS* sites [44-50]. To address the long-standing question of whether ParB acts as transcriptional repressor by sterically hindering RNAP, we examined *in vitro* transcription in our single-molecule assays with DNA:ParB condensates. We included a single T7A1 promotor within the 16.5 kbp DNA_{parS} construct with a single *parS* site (Fig. 5.6A) together with a singly biotin-labeled bacterial RNAP from *E. coli* that efficiently binds to the T7A1 promotor and able to transcribe ~5,000 nt long RNA constructs (Fig. 5.6B, D). After stalling the RNAP at position A29 after the T7A1 promoter on the DNA_{parS} and tethering the DNA_{parS} to the surface via DIG:anti-DIG interaction (see Methods), we incubated the flow cell with streptavidin-coated magnetic beads that bound to the stalled biotin-RNAP on the DNA_{parS} [51]. To ensure that a transcribing RNAP moved towards the ParB-

cluster, the T7A1 promotor was located 1 kbp upstream of the *parS*. We first exposed the DNA_{parS} to a high concentration of ParB proteins (50 nM), which ensured efficient loading and DNA condensation, as in our previous experiments (e.g., Fig. 5.1). Unlike the DNA section between the surface tether point and RNAP, which was held at a constant force of 5 pN, the residual 12 kbp of DNA_{parS} experienced 0 pN force, ensuring effective DNA condensation by the high ParB concentration. We additionally confirm that a single-tethered DNA can be efficiently condensed in such orientation by testing the same DNA construct in our fluorescence assay in the presence of 20 nM ParB (Fig. S5.8A-C). After the DNA_{parS} was condensed by ParB, we initiated RNA transcription by adding 1 mM of all four NTPs (Fig. 5.6C).

Strikingly, we observed that RNAP molecules were able to efficiently translocate along DNA despite the presence of *parS* and ParB, with virtually no effect on the average processivity or pause-free elongation rate (Fig. 5.6D and Fig. S5.8D, respectively). Even at 200 nM ParB, the processivity was not affected (Fig. 5.6D), indicating that a ParB:DNA cluster does not act as a transcriptional roadblock. A decrease of ~20% in average transcription velocity was only detectable at 200 nM ParB (from 9.2 ± 0.8 nt/s to 7.3 ± 0.6 nt/s, mean ± SEM, Fig. 5.6E). Notably, the decrease in average velocity resulted from the increased pausing probability while the elongation rate remained the same (Fig. S5.8E, D, respectively). More specifically, a probabilistic dwell time analysis of transcriptional pausing (Fig. S5.8F) showed that the probability of long pauses increased, whereas short elemental pausing remained constant (Fig. S5.8F-G)[51,52], and revealed that the ParB:DNA condensate induced an increase in (reversible) RNAP backtracking [52].

While RNA transcription was remarkably unaffected by the presence of ParB, an opposite scenario can be envisioned, i.e., that the DNA condensation breaks down during transcription as RNAP might break ParB-ParB bridges or detach ParB proteins from the DNA. To examine this, we visualized the effect of transcription on the ParB:DNA cluster in real-time using our fluorescence DNA-stretching assay (Fig. 5.6F). For this, we constructed a 38 kbp $DNA_{parS/T7A1}$ that includes a T7A1 promotor 1 kbp downstream from the *parS* site (see Methods; Fig. S5.9A). We used a TMR-labelled ParB ($ParB^{TMR}$) and an Alexa647-labeled RNAP ($RNAP^{Alexa647}$, Fig. S5.9B) for visualization. We observed efficient DNA condensation by 25 nM ParB in the presence of non-transcribing RNAP (Fig. S5.9C,D). When we subsequently initiated $RNAP^{Alexa647}$ transcription in presence of ParB, we simultaneously observed both efficient transcription and DNA condensation (Fig. 5.6G), in agreement with the MT experiments. At both longer and shorter end-to-end tethering lengths, the RNAP appeared to translocate, independent of the cluster presence (Fig. 5.6G, S9E-H).

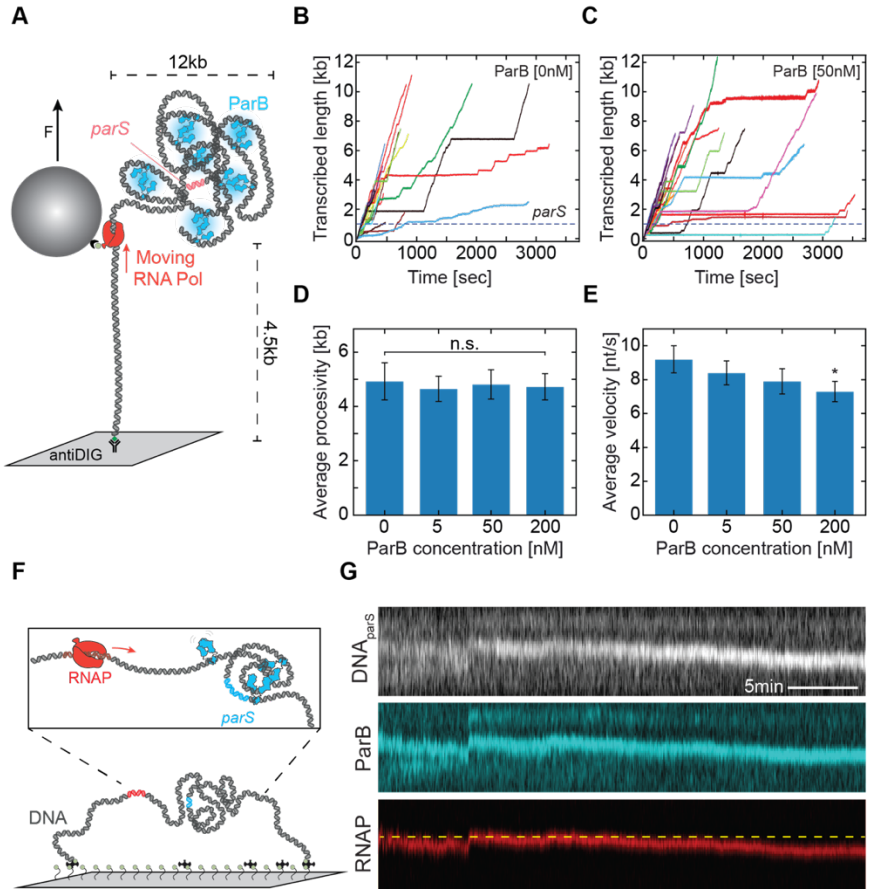


Figure 5.6. Transcription is unaffected by condensed ParB:DNA clusters. ***(A)*** *Single-molecule MT RNAP transcription assay.* ***(B, C)*** *Individual RNAP transcription trajectories in the absence (B; N = 27) and presence (C; N = 29) of 50 nM ParB.* ***(D)*** *RNAP processivity (mean±SEM) with increasing concentrations of ParB.* ***(E)*** *Average RNAP velocity (mean±SEM) with increasing ParB concentrations (0 nM: N = 27, 5 nM: N = 46, 50 nM: N = 29, 200 nM: N = 51). Statistical analyses consisted of an unpaired, two-tailed t-test (* = $p < 0.05$; n.s. = non-significant).* ***(F)*** *Co-visualization single-molecule fluorescence DNA-stretching assay.* ***G)*** *Kymographs for DNA_{parS} stained with SxG (top; grey), $ParB^{TMR}$ (middle; cyan, 25 nM), and $RNAP^{Alexa647}$ (bottom; red). Yellow dashed line represents initial location of the RNAP at the start of transcription.*

Thus, both RNAP transcription and ParB condensation were found to be unaffected in their corresponding functions and they can simultaneously operate. In our data, we

occasionally observed discrete jumps after the initial translocation by RNAP (Fig. 5.6G, S5.9H) which may be attributed to the dynamic ParB condensation that can induce large movement of the condensed regions across the DNA (as in Fig. 5.2D), and possibly to supercoiling that RNAP induces into the ParB cluster.

5.3 Discussion

The ParB partition complex is a key component for the maintenance of bacterial chromosome integrity. Here, we investigated the dynamics and molecular basis of the initiation of the partition complex formation and its maintenance. Our results provide an extensive description of the dynamics of partition complex formation, the ParB domains involved in it, and the effect the partition complex on key biological functions such as transcription. Our research expands on earlier work that inadvertently often focused on nonspecific interactions in the absence of CTP [8,9,20,21].

Using three single-molecule assays, we showed that a single *parS* site on a long DNA molecule can efficiently promote DNA condensation by ParB proteins. While previous studies using shorter DNA molecules showed a necessity for multiple *parS* sites [29], our MT experiments and fluorescence DNA stretching assay with long DNA molecules demonstrate that a single *parS* site is sufficient for efficient ParB loading and strong DNA condensation (Fig. 5.1). We hypothesize that this is due to the length of DNA molecules, where longer DNA (>10 kbp) allows for spontaneous self-looping via thermal fluctuations of the polymer much more frequently than for shorter DNA molecules. Partition complex formation via a single *parS* site is in line with *in vivo* data showing that a single *parS* site continues to exhibit an unaltered phenotype in bacteria with multiple signatures of functional ParB partition complexes (i.e. fluorescence foci, SMC loading, high fidelity chromosome segregation) being preserved [18,32,53,54].

The results from our single-molecule fluorescence and MT experiments revealed that ParB and DNA form a very dynamic structure that varies in the number of ParB molecules and amount of DNA in a condensate, with sizeable fluctuations of up to 10 kbp/minute (Fig. 5.1, S5.3, S5.4). This dynamic rearrangement of ParB:DNA partitions is well compatible with the observed high protein turnover within the condensate and the transiency of ParB-ParB bridge formation that underlies DNA condensation (Figs. 5.2, 5.3). Our FRAP recovery data also showed a high turnover of ParB proteins on the DNA molecule, while our hsAFM experiments directly observed that transient bonds can be formed between two ParB dimers to bring distal DNA segments close together (Fig. 5.3B-C, S5.6). Interestingly, the survival time of these DNA loops was

roughly similar of the ParB residence time on the DNA (Fig. 5.3D and Ref. by Tišma et al. [36]).

On the molecular scale, our data showed that CTP hydrolysis at the N-terminus is needed for DNA condensation. This contrasts a previous study[29] that reported that CTP hydrolysis and clamp opening was not required for DNA condensation, which may be due to the occurrence of multiple *parS* sites in that study, where ParB proteins nucleating on the multiple loading *parS* sites may bridge and condense the DNA, or due to recently reported ParB multimers[55] that could bridge from different *parS* sites. Our experiments using three different strategies for N-terminal closure (non-hydrolyzing protein mutant, non-hydrolyzable nucleotide, and crosslinked proteins) pointed towards a necessity for ParB opening at the N-terminus. CTP hydrolysis at the N-terminus (Fig. 5.4) appears to be necessary for DNA condensation *in vivo*, too [27,28], as hydrolysis-deficient ParB mutants did not efficiently form a bright foci in the cell even when they were efficiently loaded onto the chromosome[27]. Our MD simulations further showed that these bridges are formed in a way that allows for local oligomerization of ParB proteins (Fig. 5.5A-D).

Transiency is an essential feature for the maintenance of ParB:DNA partition complexes, which was well illustrated in our experiments as well as in previous *in vivo* research on plasmid-encoded ParB proteins [25]. Our MD simulations shed light on the cooperative and highly dynamic nature of ParB:DNA clusters. In line with computational models of generic DNA-bridging switchable proteins, we hypothesize that the high transiency yields condensates that are self-limiting in size and preferentially drive shorter-range contacts [56,57]. This may help the formation of the partition complex that does not include rigid structures that could hinder other cellular machineries. Previous studies showed a considerable difference in ParB residence time on the DNA after a buffer wash in presence or absence of CTP, which points to the possible CTP exchange [27,28]. As our previous work indicated that ParB can reside in an open state where dimer-dimer interaction can occur,[36] the N-terminus would be freely accessible for potential CTP exchange during this time. We hypothesize that CTP molecules can be exchanged within the ParB proteins prior to bridge formation, which allows for both ParB-ParB recruitment[36] and DNA-condensation[29].

Notably, the stalling force that we obtained for condensate growth is very low, i.e. a force of ~0.1 pN, which is more than two orders of magnitude lower than the stalling forces of DNA-processing motor proteins such as RNA polymerases and helicases [58-62] that can exert large forces up to 25 pN [60] and 35 pN [58], respectively. As the DNA machinery at such high forces will strip any ParB clamp from the DNA, a dynamic network of proteins

with a high turnover ensures to maintain the ParB:DNA partition complex. Indeed, our data showed that RNAP and ParB can simultaneously perform their respective functions, transcription and DNA-condensation (Fig. 5.6), respectively. We speculate that the difference in dynamics between the two processes is important to enabling them to co-function. While RNAP transcription is slow (~10 nt/s *in vitro* (this work and Janissen et al. [51]), ~70 nt/s *in vivo* [63]), ParB proteins exhibit fast and dynamic loading, diffusion, and DNA condensation of up to tens of kilobases within minutes. Continuous dynamic reforming of the ParB-DNA partition complex is likely necessary for maintaining uninterrupted RNA transcription of genes in the part of the genome that is entrapped in the partition complexes. The same likely holds for the replication machinery during the replication cycle.

Previous reports on plasmid-encoded ParB proteins showed suppression of gene expression in the vicinity of the *parS* site [44,46,48], whereas more recent reports indicate uninterrupted expression of genes around *parS* sites [30,44,64]. Based on our single-molecule RNAP results, we hypothesize that the reported suppression of transcription [44,46-50] could be caused by restricted excess of RNA polymerases to tightly packed ParB:DNA complexes during the initiation stage where RNA polymerase needs to access the promotor.

In light of our results, we propose a model where the DNA-ParB partition complex is initiated by DNA-ParB and ParB-ParB interactions (Fig. 5.7): ParB dimers load on the *parS* site by binding two CTP molecules, whereupon they diffuse away from the *parS* site as clamps (Fig. 5.7B) [4,27,28]. During diffusion, ParB is bound to the DNA *via* its C-terminus by non-specific interactions (Fig. 5.7C). Upon hydrolysis of both CTP molecules, the ParB dimer opens at the N-terminus (Fig. 5.7D) and at this moment [28] it is able to connect to another ParB dimer on a distal DNA segment, consequently forming a transient DNA loop (Fig. 5.7E). Subsequently, ParB can form oligomers which result in the formation of larger clusters (Fig. 5.7F) that are stable over time even after the initial bridge disruption (Fig. 5.7G). Previous work on *B. subtilis* ParB diffusion suggested that upon hydrolysis there is likely a ~15 s period of residual binding to the DNA before the dissociation occurs[36], and thus a post-hydrolysis open-clamp ParB might still reside on the DNA for some time and connect to a second dimer (also proposed by Taylor et al., [21] and Fisher et al. [20]). In the presence of a large number of ParB proteins within a partition complex (Lim et al., [10] and Guilhas et al. [25] reported ~400-800 molecules); a continuous occurrence of ParB-ParB bridges would allow for the maintenance of the metastable partition complex. An intrinsic transiency of such bridges would allow the cellular machineries to be unaffected in their respective functions. Further *in vivo* studies of the interaction between the ParB:DNA complex and

the DNA-replication/RNA-transcription machinery could further shed light on the dynamic structure of the ParB-DNA partition complex and its vital role in chromosome segregation.

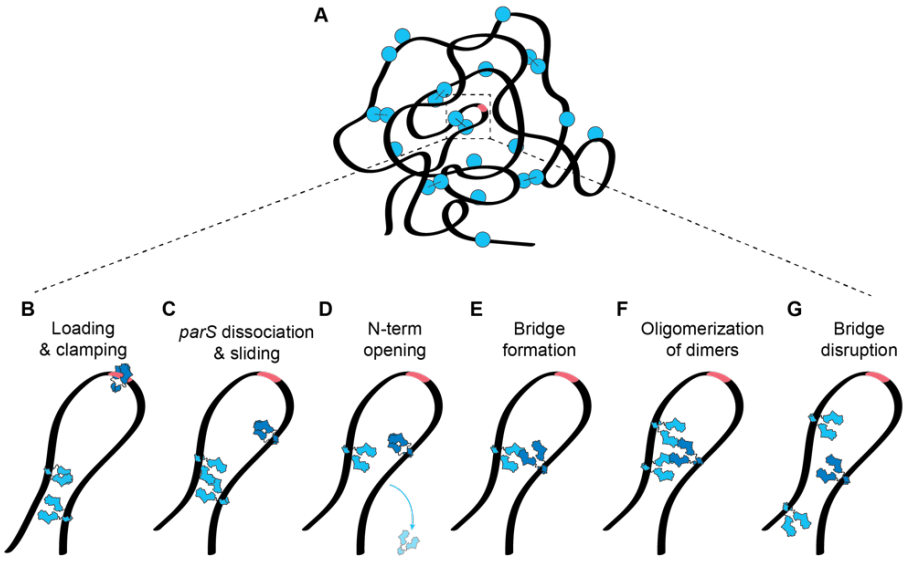


Figure 5.7. Model of dynamic ParB-ParB bridging via the N-terminal domains. (A) *Schematic representation of a ParB:DNA cluster where few ParB-ParB bridges maintain the DNA condensate. (**B-F**) Hypothesized timeline of events experienced by ParB protein (blue). (**B**) ParB proteins load at the parS site and form a DNA clamp via dimerization at the N-terminus[65,66]. (**C**) ParB loses the affinity to parS site and diffuses away along the DNA [67-69]. (**D**) After CTP hydrolysis, ParB clamp opens at the N-terminus[66], but (**E**) remains bound to the DNA via its C-terminal domain[70], to form a ParB-ParB bridge with another open clamp. This bridge is formed via their accessible N-termini. (**F**) Such interactions allow for oligomerization via Multimer-of-dimers mode which can stabilize the condensate over time. (**G**) After some time, a bridges can disrupt, allowing for dissociation of ParB from the DNA or connection to newly open ParB clamps, thus maintaining the fluid ParB:DNA condensate shown in panel A.*

5.4 Material & Methods

5.4.1 ParB purification and fluorescent labeling

We prepared *Bacillus subtilis* ParB expression constructs using pET-28a derived plasmids through Golden-gate cloning. We expressed untagged recombinant proteins in *E. coli* BL21-Gold (DE3) for 24 h in ZYM-5052 autoinduction medium at 24°C. Purifications of ParB and $ParB^{L5C}$ variants, used for fluorescent labeling, were performed as described before[27]. Briefly, we pelleted the cells by centrifugation and subjected them to lysis by sonication in the Buffer A (50 mM Tris-HCl pH 7.5, 1 mM EDTA pH 8, 500 mM NaCl, 5 mM β-mercaptoethanol, 5 % (v/v) glycerol, protease inhibitor cocktail (SigmaAldrich)). We then added ammonium sulfate to the supernatant to 40% (w/v) saturation and kept stirring at 4°C for 30 min. We centrifuged the sample and collected the supernatant, and subsequently added ammonium sulfate to 50% (w/v) saturation and kept stirring at 4°C for 30 min. We collected the pellet (containing extracted ParB proteins) and dissolved it in the Buffer B (50 mM Tris-HCl pH 7.5, 1 mM EDTA pH 8 and 2 mM β-mercaptoethanol). Before loading onto a Heparin column (GE Healthcare), the sample was diluted in Buffer B to achieve the conductivity of 18 mS/cm. We used a linear gradient of Buffer B containing 1 M NaCl to elute the protein. After collecting the peak fractions, we repeated the dilution in Buffer B to 18 mS/cm conductivity and loaded it onto HiTrap SP columns (GE Healthcare). For elution, we used a linear gradient of Buffer B containing 1 M NaCl. Collected peak fractions were loaded directly onto a Superdex 200-16/600 pg column (GE Healthcare) preequilibrated in 50 mM Tris-HCl pH 7.5, 300 mM NaCl, and 1 mM TCEP. For fluorescent labeling, we incubated purified $ParB^{L5C}$ variant with TMR-maleimide at a 1:2 molar ratio (protein:dye). We incubated the mixture for 15 min on ice, centrifuged it for 10 min, and then eluted it from a spin desalting column (Zeba) and flash frozen in liquid nitrogen. We estimated the fluorophore labelling efficiency at 70% for $ParB^{TMR}$ monomers (90% dimers labeled) by an inbuilt function on Nanodrop using extinction coefficients of ε = 60 000 $cm^{-1}M^{-1}$.

5.4.2 ParB storage and handling

We observed ParB proteins to be highly sensitive to handling and storage before the fluorescent imaging, thus handling of purified ParB protein solution is essential for high-quality experiments. Following the protein shipment between laboratories (from SG to CD lab) on dry ice, the protein solution was thawed on ice for 10 min. Concurrently, we prepared a fresh storage buffer solution 300 mM NaCl, 50 mM Tris-HCl (pH 7.5), and 1 mM TCEP and stored it on ice. We diluted the initial protein solution (~240μM ParB) to 1.29 μM in steps of consecutive 1:1 dilutions using cold storage buffer, split the

solution in 5 µl volumes and flash froze them using liquid nitrogen. On the day of the experiment, we diluted the protein once more in 1:1 ratio using a new fresh storage buffer before adding the protein at the desired concentration to either the imaging buffer in our fluorescence experiments (40 mM Tris-HCl, 65 mM KCl, 2.5 mM $MgCl_2$, 1 mM CTP, 2 mM Trolox, 1 mM TCEP, 10 nM Catalase, 18.75 nM Glucose Oxidase, 30 mM Glucose, 0.25 µg/ml BSA, 25 nM SYTOX Green (SxG, ThermoFisher Scientific)) or incubation buffer in our MT experiments (40 mM Tris-HCl, 65 mM KCl, 2.5 mM $MgCl_2$, 1 mM CTP, 0.25 µg/ml BSA, 1 mM TCEP). Omitting 1:1 dilutions or using buffers at different temperatures resulted in the presence of large protein aggregates in our field of view, as well as the binding of large protein aggregates to the DNA_{parS}.

5.4.3 ParBs crosslinking assays

The crosslinking experiments for $ParB^{T22C}$ and $ParB^{S278C}$ were performed under different conditions due to the following rationale: $ParB^{S278C}$ does not get influenced by *parS* binding because it dimerizes in solution, so the crosslinking experiment were performed and quenched before ever contacting the DNA_{parS}, while $ParB^{T22C}$ needs to interact with DNA_{parS} before closing at N-terminus binging C22 in proximity to be crosslinked, so the experiment was performed in presence of DNA_{parS}. The crosslinking experiments were setup to mimic the MT protocol as much as possible, with obvious limitations in lack of washing steps.

We prepared the $ParB^{S278C}$ stock at 10 µM final concentration in the storage buffer (50 mM Tris-HCl pH 7.5, 300 mM NaCl) and kept on ice. Following this, we added BMOE to this stock to a final concentration of 1 mM, and incubated on ice for 5 min and then at room temperature for 5 min. This protein:BMOE mix was diluted 1:10 in the imaging buffer containing the quencher (50 mM Tris-HCl pH 7.5, 65 mM KCl, 2.5 mM $MgCl_2$, 1 mM CTP, and 1 mM DTT) and incubated for 10 min at room temperature (equivalent to incubation/loading step in MT).

We prepared an initial loading reaction by incubating $ParB^{T22C}$ [2 µM] with ~200 bp fragment containing *parS* site – DNA_{parS} [2 µM] for 5 min at room temperature in MT imaging buffer (50 mM Tris-HCl pH 7.5, 65 mM KCl, 2.5 mM $MgCl_2$, 1 mM CTP). This represents the initial loading of $ParB^{T22C}$ in the flow cell. Next, we added the crosslinking buffer (50 mM Tris-HCl pH 7.5, 65 mM KCl, 2.5 mM $MgCl_2$, 1 mM CTP, 2 mM BMOE) in relation 1:1 and incubated for 15 min at room temperature. This represents the crosslinking via slow washing in the flow cell. We then added DTT to a final concentration of 2 mM to quench the reaction. While in our MT experiments we performed such loading and washing twice, here we could not wash away any residual components thus the final buffer contained (65 mM KCl, 50 mM Tris-HCl, 2.5 mM

$MgCl_2$, 1 mM CTP, 2 mM DTT, 0.5 mM BMOE leftover). We performed these experiments in multiple conditions mentioned in Fig. S5.5A, and such alterations to the protocol (omitting components) was performed such that the final volume remains the same, and concentration of other components remains unaltered. All conditions were ran on the 12% SDS-PAGE gel (SurePAGE™/Bis-Tris, M00668, GenScript) and the molecular weights were approximated using SeeBlue™ Plus2 Pre-stained Protein Standard (LC5925, Invitrogen).

The crosslinking efficiency was determined from a duplicate experiment (Fig. S5.5B) using GelAnalyzer (version 19.1).

5.4.4 Biolayer interferometry assay (BLI)

We performed BLI assay as described previously by Antar et al. [27] (Fig. S5.5C-D). In brief, we used in a buffer containing 150 mM NaCl, 50 mM Tris-HCl (pH 7.5), and 2.5 mM $MgCl_2$ on BLItz machine (FortéBio Sartorius). We first loaded 4 µl of 169 bp biotin-labeled DNA_{parS} (100 nM) on the biosensor for and incubated for 5 min (Fig. S5.5C-D). After this loading phase, we washed the biosensor briefly once with the reaction buffer and once with the reaction buffer containing 1 mM CTP. Next, we mixed 2× ParB solution and 2× CTP solution in 1:1 ratio (final concentration of 1 µM ParB and 1 mM CTP, both in the same buffer [150 mM NaCl, 50 mM Tris-HCl (pH 7.5), and 2.5 mM $MgCl_2$]), and we loaded the 4 µl of the mixture immediately on the biosensor for 2 min. In case of BMOE crosslinking test, both for ParB-wt and $ParB^{T22C}$, we performed a wash using a buffer containing 1 mM BMOE [150 mM NaCl, 50 mM Tris-HCl (pH 7.5), and 2.5 mM $MgCl_2$, 1 mM CTP, 1 mM BMOE] and no proteins, for 2 min. The dissociation phase was then carried for 5 min in 250 µl of protein-free reaction buffer in the absence of CTP nucleotide. We analyzed all measurements on the BLItz analysis software and replotted on GraphPad Prism for visualization.

5.4.5 Construction and purification of 42 kbp DNA_{parS} construct and 38 kbp T7A1+parS for fluorescence experiments

For the construction of a long linear DNA_{parS}, we used a large 42 kbp cosmid-i95 reported previously [71] and a synthetic construct containing the *parS* site (Integrated DNA Technologies, Table. S1, underlined sequence). First, we linearized the i95 cosmid using the PsiI-v2 restriction enzyme (New England Biolabs). Next, we dephosphorylated the remaining 5'-phosphate groups using Calf Intestinal Alkaline Phosphatase for 10 min at 37°C, followed by heat inactivation for 20 min at 80°C (Quick CIP, New England Biolabs). We added the 5'-phospho group on the synthetic *parS* fragment by adding a T4 kinase for 30 min at 37°C and heat-inactivated 20 min at 65°C in 1x PNK buffer supplemented with 1 mM ATP (T4 PNK, New England Biolabs). Next, we ligated the

two fragments together using a T4 DNA ligase in T4 ligase buffer (New England Biolabs), containing 1 mM ATP overnight at 16°C. The final cosmid construct was transformed into *E. coli* NEB10beta cells (New England Biolabs), and we verified the presence of insert by sequencing using JT138 and JT139 (Table S1).

The final 38kbp T7A1+*parS* construct was made from plasmid 189-pBS-T7A1-parS (Table S1). This plasmid was generated from plasmids 179, 66, 67, 69, 163 and 71 using a BsaI-HFv2 golden gate reaction mix (NEB E1601). The intermediate vectors were made using traditional cloning techniques (in details described in Table S1).

To prepare a linear fragment adapted for flow cell experiments, we isolated cosmid-i95 or pBS-T7A1-parS *via* a midiprep using a Qiafilater plasmid midi kit (Qiagen). We digested the cosmid-i95 for 2 h at 37°C using SpeI-HF restriction enzyme (New England Biolabs) and heat-inactivated for 20 min at 80°C. pBS-T7A1-parS was digested with NotI-HF and XhoI under the same conditions and heat-inactivated using the same procedure. Next, we constructed the 5'-biotin handles by a PCR from a pBluescript SK+ (Stratagene) using 5'-biotin primers JT337 and JT338 (Table S1), to get a final 1,246 bp fragment. We digested the PCR fragment using the same procedure described for cosmid-i95, resulting in ~600 bp 5'-biotin-handles. The handles for the 38 kbp T7A1-parS construct were made with the same primers, but on template plasmid 186 (Table S1, S2, S3) resulting in a final fragment of 514 bp. We further digested these PCR fragments were digested using NotI-HF or XhoI for 2 h at 37°C. This resulted in the handles of ~250 bp in length.

Finally, we mixed the digested constructs and handles in a 1:10 molar ratio and ligated them together using T4 DNA ligase in T4 ligase buffer (New England Biolabs) at 16°C overnight, which was subsequently heat-inactivated for 10 min at 65°C. The 38 kbp T7A1-parS + handle construct were subsequently digested for 1 h at 37°C and heat-inactivated for 20 min at 65°C using SrfI restriction enzyme (New England Biolabs).

We cleaned up the resulting linear (42 +1.2) or (38 + 0.5) kbp DNA_{parS} constructs from the access handles using an ÄKTA Start (Cytiva), with a homemade gel filtration column containing 46 ml of Sephacryl S-1000 SF gel filtration media, run with TE + 150 mM NaCl buffer at 0.5 ml/min. We stored the collected fractions as aliquots after snap-freezing them by submerging them in liquid nitrogen.

5.4.6 Single-molecule visualization assay

The surface of imaging coverslips was prepared as previously described [72], with the addition of surfaces being pegylated 5x 24 h. For immobilization of 42 kbp DNA_{parS}, we introduced 50 µl of ~1 pM of 5'-biotinylated-DNA_{parS} molecules at a flow rate of

1 – 4 µl/min, depending on the desired end-to-end length in the experiment, in T20 buffer (40 mM Tris-HCl (pH 7.5), 20 mM NaCl, 25 nM SxG). Immediately after the flow, we further flowed 100 µl of the wash buffer (40 mM Tris–HCl, pH 7.5, 20 mM NaCl, 65 mM KCl, 25 nM SxG) at the same flow rate to ensure stretching and tethering of the other end of the DNA to the surface. By adjusting the flow, we obtained a stretch of around 15−40% of the contour length of DNA. Next, we flowed in the imaging buffer (40 mM Tris-HCl, 2 mM Trolox, 1 mM TCEP, 10 nM Catalase, 18.75 nM Glucose Oxidase, 30 mM Glucose, 2.5 mM $MgCl_2$, 65 mM KCl, 0.25 µg/ml BSA, 1 mM CTP/, 25 nM SxG) without ParB protein at the low flow rate (0.2 µl/min) to enable minimal disturbances to the DNA molecules before and after protein addition. Experiments were performed in the same conditions with the exception of replacing 1 mM CTP with 1 mM CTPγS where mentioned. Real-time observation of ParB diffusion was carried out by introducing ParB (5-25 nM) in the imaging buffer.

For the RNAP transcription experiments, we prepared the RNAP ternary complex as described previously by Janissen et al. [51,52]. RNAP holoenzyme was stalled on the $DNA_{parS/T7A1}$ constructs at position A29 after the T7A1 promoter sequence. To do so, we added 3 nM of RNAP holoenzyme to 3 nM linear $DNA_{parS/T7A1}$ template in 20 mM Tris, 100 mM KCl, 10 mM $MgCl_2$, 0.05% (v/v) Tween 20 (SigmaAldrich) and 40 mg/mL BSA (New England Biolabs), pH 7.9, and incubated 10 min at 37°C. Afterwards, we added 50 µM ATP, CTP, GTP (GE Healthcare Europe), and 100 µM ApU (IBA Lifesciences GmbH) to the solution and incubated for 10 min at 30°C. To ensure that we measured the transcription dynamics of single RNAp ternary complexes, we sequestered free RNAP and RNAP that were weakly associated with the DNA by adding 100 µg/ml heparin and incubating for 10 min at 30°C. The ternary complex solution was then diluted to a final concentration of 100 pM of the RNAP:$DNA_{parS/T7A1}$ complex. The complex was flushed into the flow cell at the speed of 4 µl/min and subsequently washed for all unbound molecules in the buffer containing 40 mM Tris-HCl, 2 mM Trolox, 30 mM Glucose, 4 mM $MgCl_2$, 70 mM KCl, 0.25 µg/ml BSA, 1 mM CTP, 25 nM SxG. After the washing of unbound RNAP:$DNA_{parS/T7A1}$ complexes, we first subjected the buffer to the imaging buffer without ParB proteins and lacking all NTPs (40 mM Tris-HCl, 2 mM Trolox, 1 mM TCEP, 10 nM Catalase, 18.75 nM Glucose Oxidase, 30 mM Glucose, 4 mM $MgCl_2$, 70 mM KCl, 0.25 µg/ml BSA, 1 mM CTP, 25 nM SxG), for 3 min. This was followed by the same buffer with the addition of 25 nM ParB proteins (10 nM $ParB^{TMR}$ and 15 nM WT ParB), which we incubated for 5 min to allow for DNA condensation to start prior to RNAP transcription. Following this incubation we added the final imaging buffer which allows DNA condensation and RNAP transcription (40 mM Tris-HCl, 2 mM Trolox, 1 mM TCEP, 10 nM Catalase, 18.75 nM Glucose

Oxidase, 30 mM Glucose, 4 mM $MgCl_2$, 70 mM KCl, 0.25 µg/ml BSA, 25 nM SxG, 1 mM NTP and 2 µM GreB) and started the imaging. In these experiments the signals were obtained by alternate excitation with 100 ms exposure times for DNA-SxG (488 nm laser), $ParB^{TMR}$ (561 nm laser), and $RNAP^{Alexa647}$ (647 nm laser) followed by a 2700 ms pause before the next frame. We observed 40% of the $RNAP^{Alexa647}$ molecules undergo transcription in the absence of ParB molecules (N = 18/44, Fig. S5.9B shows an example trace).

We used a home-built objective-TIRF microscope to achieve fluorescence imaging. We used alternating excitation of 488 nm (0.1 mW), 561 nm (12 mW) and 647 nm (12 mW) lasers in Highly Inclined and Laminated Optical sheet (HiLo) microscopy mode, to image SxG-stained DNA and TMR-labelled ParB and Alexa647-RNAP respectively. All images were acquired with an PrimeBSI sCMOS camera at an exposure time of 100 ms, with a 60x oil immersion, 1.49 NA objective (CFI APO TIRF, Nikon).

5.4.7 Fluorescence recovery after photobleaching experiments

Our FRAP experiments were performed using the same 42 kbp DNA_{parS} mentioned above. For these experiments, we used Alexa647-labelled ParB proteins and SxG-labelled DNA, using the same experimental procedure and buffers mentioned above. The DNA was initially incubated with ParB for 15 min to ensure DNA molecules are sufficiently covered with ParB dimers and in large percentage condensed already. The final $ParB^{Alexa647}$ concentration was 25 nM to ensure strong DNA condensation in our fluorescence assay. Following the initial incubation we started co-imaging DNA-SxG and $ParB^{Alexa647}$ for the initial ~50s, before performing photobleaching of ParB proteins on the entire DNA molecule.

In these experiments the signals were obtained by alternate excitation with 200 ms exposure times for DNA-SxG (488 nm laser), $ParB^{Alexa647}$ (647 nm laser). The photobleaching was performed using 100 mW laser power (647 nm) for 100 bursts. We used a home-built objective-TIRF microscope to achieve fluorescence imaging. We used alternating excitation of 488 nm (0.5 mW), and 647 nm (15 mW) lasers in HiLo microscopy mode, to image SxG-stained DNA and TMR-labeled ParB. All images were acquired with iXon Ultra 897 EMCCD (X-7105) camera 100x oil immersion objective (X-Apo, 1.45NA, Olympus™).

5.4.8 Image processing and analysis

The areas with single DNA molecules were cropped from the raw image sequences and analyzed separately with custom-written, interactive python software [73]. The images were smoothened using a median filter with a window size of 10 pixels, and the

background was subtracted with the "white_tophat" operation provided in the *scipy* python module. The contrast of the images was further adjusted manually for visualization only (i.e. Fig. 5.2). The ends of a DNA were manually marked. The distance between DNA ends is the end-to-end length R of the DNA molecule. Total fluorescence intensity of 11 pixels (~1.3 µm) across the axis of the DNA was obtained for each time point and was stacked to obtain a kymograph (i.e. Fig. 5.2). The same image area was selected to obtain kymograph of the ParB fluorescence channel.

DNA condensates appear as spots of the increased fluorescence signal (i.e., Fig. 5.1D, 5.2A) compared to the surrounding fluorescence signal along the DNA. The position of the spots was identified and tracked using the *trackpy* python module (v0.4.2; 10.5281/zenodo.7670439). The amount of DNA contained within the condensate is computed as extensively described previously by Davidson et al. [74]. In brief, the condensate size is expressed as the fraction of intensity at the condensate position, I_{cond}, in relation to the total intensity along the entire DNA molecule, I, and the DNA length $L = 42.5\,kbp$

$$L_{cond} = \frac{I_{cond}}{I} \cdot L \tag{1}$$

The tension acting on the DNA is expressed in terms of the contour length of the DNA outside the condensate (in bp), $L_{out} = L - L_{cond}$, which is $L_{out}^{c} = \alpha \cdot L_{out} \cdot 0.342\,\frac{nm}{bp}$, accounting for the distance between base pairs of 0.324 nm and α is a correction factor accounting for the lengthening of the dsDNA contour length in the presence of intercalating dyes (for 25 nM SxG, $\alpha = 1.0357$ was used [74]). The relative extension of the DNA outside the condensate, $r = R/L_{out}^{c}$ is used to compute the momentary tension acting on the DNA via the empirically determined and well-established force-extension relationship [75]:

$$F = \frac{k_B T}{L_p}\left(\frac{1}{4(1-r)^2} - \frac{1}{4} + \sum_{i=1}^{7} a_i\, r^i\right) \tag{2}$$

where $k_B T = 1.3806503 \cdot 10^{-23} \cdot 293\,K \cdot 10^{-18}\,pN \cdot \mu m$, $L_p = 39.7\,nm$ is the persistence length of DNA at 25 nM SxG, $a_1 = 1, a_2 = -0.5164228, a_3 = -2.737418, a_4 = 16.07497, a_5 = -38.87607, a_6 = 39.49944, a_7 = -14.17718$.

5.4.9 Construction of DNA_{parS} construct for atomic force microscopy experiments

To construct the circular DNA for AFM experiments we used a commercially available pGGA plasmid backbone (New England Biolabs). We linearized the plasmid using MT032 and MT033 primers (Table S2). In parallel to this we extracted a region containing *parS* site downstream of *metS* gene in *B. subtilis* genome by a colony PCR using primers MT039 and MT040 (Table S2). We combined the plasmid backbone with the colony PCR insert by mixing them in molar ration 1:3 in the 2xHiFi mix (New England Biolabs). We incubated the reaction at 50°C for 60 min, and cooled down to 12°C for 30 min. We then transformed 2 µl of this reaction into the *E. coli* NEB5alpha cells (New England Biolabs), and we verified the presence of insert in grown colonies the following day by sequencing using MT030 and MT031 (Table S2). We grew sequence-positive clones for the plasmid extraction at 37°C overnight in presence of a selective antibiotic Chloramphenicol (30 µg/ml) and isolated the final plasmid using a QIAprep Spin Miniprep kit (Qiagen) the following day. The plasmids were nicked using a standard protocol for Nb. BbvCI nicking enzyme (New England Biolabs) capitalizing on a pre-existing recognition site in *metS* gene. This was done in order to remove any supercoiling from the isolated plasmids, which would alter the experimental conditions and conclusions via promoting in-trans interactions between different plasmid domains. We ligated the nicked plasmids using a T4 DNA ligase in T4 ligase buffer (New England Biolabs), containing 1 mM ATP overnight at 16°C. The following day we performed three more rounds of plasmid clean-up using the same QIAprep Spin Miniprep kit (Qiagen) to remove all the residual enzymes which could corrupt the AFM images.

5.4.10 Atomic force microscopy experiments and imaging

We obtained images in dry conditions using an AFM from Bruker (Massachusetts, USA) and Scanassyst-Air-HR tips from Bruker. AFM was operated using peakforce-tapping mode. We used WSxM [76] software for all image processing and data extraction from our raw data in AFM experiments.

We incubated samples with different molarity ratios of DNA, CTP and ParB in Eppendorf tubes for 2 to 5 min in a buffered solution (40 mM Tris, pH 7.5, 65 mM KCl, 7.5 mM $MgCl_2$). Then, we deposited the solution onto a freshly cleaved mica for 30 s. Afterwards, we thoroughly washed the surface with 3 ml of Milli-Q water and dried it under a flow of Nitrogen until visibly dry.

We took images in aqueous conditions using a high-speed AFM from RIBM (Tsukuba, Japan) and PRE-USC-F1.2-k0.15 tips from Nanotools. Here, we operated the AFM using tapping mode. The samples with DNA, CTP, and ParB were prepared in a buffered

solution (40 mM Tris, pH 7.5, 65 mM KCl, 10 mM $NiCl_2$) before depositing them onto a freshly cleaved and pre-incubated with Poly-L-lysine mica. Then, we thoroughly washed the surface 3 times with 8 µl of the same buffer.

5.4.11 Construction of DNA_{parS} construct for Magnetic Tweezers experiments

For the construction of a 14 kbp long linear DNA_{parS} for MT experiments, we used a #126-pSC-T7A1reverse-parS plasmid (Table S1). Due to the plasmid size (~20 kbp) we linearized it using 3xPCR reactions using primers MT234/MT237, MT235/MT238 and MT236/MT239 (Table S2). Concurrent with being used in linearization, MT237 primer contains an internal *parS* site - TGTTCCACGTGTAACA (Table S2). We visualized the three obtained fragments of sizes 7,783 bp, 7,638 bp and 5,594 bp for the corrected size using EtBr-agarose gel (1xTAE buffer (ThermoFisher Scientific, J63931.K2), 0.8% agarose (Promega, V3125), 0.5 µg/ml etidium-bromide (Sigma Aldrich, 1239-45-8), and extracted each from the gel using a standard protocol from PCR purification kit (Promega, A9282). We then mixed the three fragments together in 10 µl in molar ratio 1:2:1, respectively, and added to 10 µl of 2xHiFi mix (New England Biolabs). We incubated the reaction at 50°C for 60 min, and cooled down to 12°C for 30 min. We transformed 2 µl of this reaction into the *E. coli* NEB5alpha cells (New England Biolabs), and we verified the presence of desired insert (*parS* site) by sequencing using MT240 and MT241 (Table S2). We grew sequence-positive clones for the plasmid extraction at 30°C overnight in presence of a selective antibiotic Ampicillin (100 µg/ml) and isolated the final plasmid *via* a Midiprep using a Qiafilater plasmid midi kit (Qiagen) the following day.

To prepare linear fragment adapted for Magnetic Tweezer experiments, we digested #126-pSC-T7A1reverse-parS with SpeI-HF and BamHI-HF 1 h at 37°C and heat-inactivated for 20 min at 80°C (New England Biolabs). Subsequently we ran the digested fragment on a 1% TAE agarose gel and the desired ~14 kbp DNA fragment was isolated from an agarose gel using a gel purification kit (Promega, A9282).

We made two different construct and therefore we made three different handles. For the DNA condensation experiments (e.g., Fig. 5.1A-C, Fig. 5.4), we used DNA molecules with two attachment points; Digoxigenin handle at the surface side and Biotin handle towards the magnetic bead. We made both handles using primers CD21 and CD22 (Table S2) in a PCR on pBlueScriptSKII SK+ (Stratagene). This was done in the presence of 1/5 biotin-16-dUTP/dTTP or digoxigenin-11-dUTP/dTTP (two separate reactions) resulting in a 1246 bp fragment with Biotin or Digoxigenin at different ends (JenaBioscience, NU-803-DIGXS, NU-803-BIO16-L). We digested the Biotin PCR-fragment with BamHI-HF, and the Digoxigenin-PCR-fragment with SpeI-HF, both for

2 h at 37°C. This resulted in handles of ~600 bp in length with multi-biotin or multi-digoxigenin nucleotides present. Subsequently, for the condensation MT experiments a torsionally constrained construct was made by ligating, using T4 DNA ligase (NEB), the 14 kbp DNA fragment to multi-Biotin and multi-Digoxigenin handle in a 1:10 ratio.

For the experiments using RNAP we used a singly tethered DNA construct that only contained Digoxigenin handle at one end (attaching to the surface) while the second attachment point was on the RNAP (Fig. 5.6A). Thus, the second handle was a blunt end handle that did not attach to anything (Fig. 5.6A). Here, we made handles using the same primers CD21 and CD22 in a PCR on pBlueScriptSKII SK+ (Stratagene) either in the presence of digoxigenin-11-dUTP/dTTP, as previously, or no modified nucleotides (for blunt end side). This resulted in the same 1,246 bp fragment with Digoxigenin at one end and a second blunt end. We digested the no modification PCR-fragment with BamHI-HF, and the Digoxigenin-PCR-fragment with SpeI-HF, both for 2 h at 37°C. This resulted in the same length handles as previously (~600 bp) with blunt end side and a multi-digoxigenin nucleotides present at the other side. For the RNAP tweezer experiments a construct with on one side multi-digoxigenin was made by ligating the 14 kbp DNA fragment to multi-Digoxigenin and unmodified handle in a 1:10 ratio.

For both constructs, we cleaned up the resulting tweezer construct (14+1.2 kbp) from the access handles by running this on a 1% agarose gel and gel purify the right DNA fragment with a gel purification kit (Promega, A9282).

5.4.12 *E. coli* RNAP-biotin, GreB, and σ^{70} purification

Wild-type *E. coli* RNA polymerase (RNAP) holoenzyme (α2ββ′ω) with the transcription initiation factor σ^{70} was expressed and purified as described previously [77]. The RNAP contained a biotin-modification at the ß'-subunit [78] that served as an anchor to attach streptavidin-coated magnetic beads. GreB factor was obtained and purified following a previously established protocol [79]. The activity of all purified proteins was confirmed using standard bulk transcription assays.

5.4.13 Magnetic tweezers instrument and experiments

The MT implementation used in this study has been described previously[51,52]. In short, light transmitted through the sample was collected by a 50x oil-immersion objective (CFI Plan 50XH, Achromat; 50x; NA = 0.9, Nikon) and projected onto a 4-megapixel CMOS camera (#4M60, Falcon2; Teledyne Dalsa) with a sampling frequency of 50 Hz. The applied magnetic field was generated by a pair of vertically aligned permanent neodymium-iron-boron magnets (Supermagnete GmbH, Germany) separated by a distance of 1 mm, and suspended on a motorized stage (#M-126.PD2, Physik

Instrumente) above the flow cell. Additionally, the magnet pair can be rotated around the illumination axis by an applied DC servo step motor (C-150.PD; Physik Instrumente). Image processing of the collected light allows to track the real-time position of both surface attached reference beads and superparamagnetic beads coupled to DNA$_{parS}$ or RNAP in three dimensions over time. The bead x, y, z position tracking was achieved using a cross-correlation algorithm realized with custom-written software in LabView (2011, National Instruments Corporation)[80]. The software determined the bead positions with spectral corrections to correct for camera blur and aliasing.

The flow cell preparation for the MT experiments used in this study has been described in detail by Janissen et al. [51,52]. Briefly, polystyrene reference beads (Polysciences Europe) of 1.5 µm in diameter were diluted 1:1500 in PBS buffer (pH 7.4) and adhered to the KOH treated surface of the flow cell channel. Next, 0.5 mg/mL digoxigenin antibody Fab fragments (Roche Diagnostics) were incubated for 1 h within the flow cell channel, following incubation for 2 h of 10 mg/mL BSA (New England Biolabs) diluted in Buffer A containing 20 mM Tris-HCl pH 7.9, 100 mM KCl, 10 mM $MgCl_2$, 0.05% (v/v) Tween 20 (SigmaAldrich) and 40 mg/mL BSA (New England Biolabs).

For the force-extension experiments, 1 pM of the 15 kbp linear DNA$_{parS}$ was incubated in PBS buffer for 20 min in the flow cell channel. After washing with 500 ml PBS buffer, the addition of 100 µl streptavidin-coated superparamagnetic beads (diluted 1:400 in PBS buffer; MyOne #65601 Dynabeads, Invitrogen/Life Technologies) with a diameter of 1 µm for 5 min resulted in the attachment of the beads to biotinylated DNA$_{parS}$; non-attached beads were then washed out with PBS buffer. Prior to conducting the force-extension experiments, the DNA$_{parS}$ tethers were assessed by applying a high force (7 pN) and 30 rotations to each direction. Only DNA tethers with singly bound DNA$_{parS}$ and correct end-to-end lengths were used for the single-molecule experiments. In the force-extension experiments, the ParB proteins (or ParB variants; see main text) were induced to the flow cell channel while applying 7 pN to the DNA$_{parS}$ tethers. For wild type ParB, ParB$^{\mathbf{E111Q}}$ and ParB$^{\mathbf{S278C}}$ we first incubated the proteins for 15 min in the flow cell at such high force and directly after, the force was gradually reduced in steps (see Fig. 5.1B) from 7 pN to 0.05 pN within the 15 minutes the bead z-positions were recorded. For the ParB$^{\mathbf{T22C}}$ variant, we first incubated the proteins for 5 min without the presence of BMOE (65mM KCl, 50mM Tris-HCl, 2.5mM $MgCl_2$, 1mM CTP) and then crosslinked them using a buffer containing 1 mM BMOE, but not ParB$^{\mathbf{T22C}}$ for 10 min slow wash (65mM KCl, 50mM Tris-HCl, 2.5mM $MgCl_2$, 1mM CTP, 1 mM BMOE). We repeated this step twice to ensure high presence of ParB$^{\mathbf{T22C}}$ on the DNA$_{parS}$. Following these two rounds of loading and crosslinking ParB$^{\mathbf{T22C}}$ we performed a washing step in the buffer containing no ParB$^{\mathbf{T22C}}$ proteins and a quencher (65mM KCl,

50mM Tris-HCl, 2.5mM $MgCl_2$, 1mM CTP, 2 mM DTT), to ensure that any residual BMOE is quenched, while any non-crosslinked proteins are washed away before the force-extension experiments began. After this the force was gradually reduced and the z-positions of the beads were recorded, as mentioned above.

For the RNAP transcription experiments, the preparation of the RNAP ternary complex was performed as described previously[51,52]. Briefly, RNAP holoenzyme was stalled on the $DNA_{parS/T7A1}$ constructs at position A29 after the T7A1 promoter sequence. To do so, 3 nM of RNAP holoenzyme was added to 3 nM linear $DNA_{parS/T7A1}$ template in Buffer A and incubated 10 min at 37°C. Afterwards, 50 µM ATP, CTP, GTP (GE Healthcare Europe), and 100 µM ApU (IBA Lifesciences GmbH) were added to the solution and incubated for 10 min at 30°C. To ensure that we measured the transcription dynamics of single RNAP ternary complexes, we sequestered free RNAP and RNAP that were weakly associated with the DNA by adding 100 µg/ml heparin and incubating for 10 min at 30°C. The ternary complex solution was then diluted to a final concentration of 250 pM of the RNAP:$DNA_{parS/T7A1}$ complex. The complex was flushed into the flow cell and incubated for 30 min at room temperature. The subsequent addition of 100 µl streptavidin-coated superparamagnetic beads (diluted 1:400 in buffer A; MyOne #65601 Dynabeads, Invitrogen/Life Technologies) with a diameter of 1 µm resulted in the attachment of the beads to the stalled biotinylated RNAP. With the introduction of ParB proteins of different concentrations (see concentrations used main text), transcription was re-initiated by added ATP, CTP, GTP, and UTP (GE Healthcare Europe) at equimolar concentration of 1 mM and immediately starting the single-molecule measurements. The experiments were conducted for 2 h at constant force of 5 pN.

All MT data sets were processed and analyzed using custom-written Igor v6.37-based scripts [52]. From our raw data, we removed traces showing surface-adhered magnetic beads as well as tethers in our force-extension experiments where the DNA-bead attachment points were far from the magnetic equator of the beads using a previously described method [81]. Tethers that detached from the surface during the measurement were also rejected from further analysis. All traces resulting from experiments conducted at identical conditions were pooled. The absolute z-position of the RNAP during the transcription process was converted to transcribed RNA product as a function of time, using the end-to-end length determined by the extensible worm-like chain model [82]. The extensible worm-like chain model was also used for the fitting to the force-extension DNA_{parS} end-to-end length data in absence of ParB.

The transcription dynamics of *E. coli* RNAP was quantitatively assessed by a statistical analysis of transcription elongation and transcriptional pausing. Pause distributions were

assessed using unbiased dwell time analysis[52]. The times needed for RNAP to transcribe through consecutive dwell time windows of five base pairs – defined as 'dwell times' – were calculated for all RNAP trajectories and used to construct a dwell time probability distribution function. The data was filtered to 1 Hz (moving average) for analysis of all data sets. The expected error (standard deviation) in the constructed distributions were estimated by bootstrapping the data 100 times[52]. To characterize the dwell time distributions, we divided it into three separate time ranges, as described in detail previously[52]: the pause-free transcription elongation region (0.1-1 s), which contained the elongation peak; the short elemental pause region (1-5 s); and the long backtrack pause region (>5 s). The elongation rate is given by $k = \frac{N}{\bar{t}}$, where N is the dwell time window size in bp, and $\bar{t}$ denotes the peak position of the gamma-fitted distribution. To calculate the probabilities of the short and long pauses, we integrated the dwell time distribution over the corresponding dwell time regions.

5.4.14 Modelling and molecular dynamics simulations

We modelled the DNA as a semiflexible polymer made of $1{,}000$ spherical beads of size $\sigma = 5.5\ nm = 16\ bp$. We placed *parS* in the middle of the chain where ParB beads are recruited and diffuse. The beads interact purely by excluded volume following the shifted and truncated Lennard-Jones (LJ) force field

$$U_{LJ}(r,\sigma) = \begin{cases} 4\varepsilon\left[\left(\frac{\sigma}{r}\right)^{12} - \left(\frac{\sigma}{r}\right)^{6} + \frac{1}{4}\right] \ for\ r \le r_c, \\ 0\ otherwise \end{cases} \quad (3)$$

where r denotes the distance between any two beads and $r_c = 2^{\frac{1}{6}}\sigma$ is the cut-off. We defined the bonds between two monomers along the DNA contour length by the finite extensible nonlinear elastic (FENE) potential, given by:

$$U_{FENE}(r) = -0.5kR_o^2 \log\left(1 - \left(\frac{r}{R_o}\right)^2\right) \ for\ r \le R_o \quad (4)$$

with $k = 30\ \varepsilon/\sigma^2$ the spring constant and $R_o = 1.5\ \sigma$ the maximum length of the bond. We introduced the persistence length of the DNA chain as a bending potential energy between three consecutive beads given by:

$$U_{bend}(\theta) = k_\theta(1 - cos\theta) \quad (5)$$

where θ is the angle between two bonds and $k_\theta = 10\ k_BT$ is the bending stiffness constant, corresponding to a persistence length of about 10 beads or ~55 nm.

We performed the simulations in a constant-volume and constant-temperature (NVT) ensemble with implicit solvent utilizing the Langevin heat bath with local damping constant set to $\gamma = 1$ so that the inertial time equals the Lennard- Jones time $\tau_{MD} = \sigma\sqrt{m/\varepsilon} = 1$ and $m = 1$ is the mass of each bead. We let equilibrate the chain for long enough to reach a constant radius of gyration, before turning on the ParB recruitment and diffusion. We evolved the Langevin equation in LAMMPS (*40*) using a Velocity-Verlet integration scheme and a timestep $dt = 0.002$.

We performed mapping to real time and length units by using the Brownian time $\tau_B = 500\ dt = \frac{\gamma\sigma}{k_BT} = \frac{3\pi\eta_S\sigma^3}{k_BT}$. Using the viscosity of water $\eta_S = 1\ cP$ we obtained that $\tau_B = 0.5\ \mu s$. We typically dump the positions of the beads every $10^4\tau_B = 5\ ms$. It's also useful for later to note that with the coarse graining of 1 bead to 5.5 nm we also have that $1\ \mu m = 182\ \sigma$.

We modelled ParB in the system by calling, within the LAMMPS engine, an external program that modifies the types of the beads to account for the loading and diffusion of ParB on DNA; in other words, ParB is implicitly modelled. At $t = 0$ we loaded a ParB protein onto the *parS* site and allowed it to diffuse with a constant $D = 5\frac{\mu m^2}{s} = 5\left(\frac{182^2\sigma^2}{2.8\ 10^6\tau_B}\right) = 0.062\frac{\sigma^2}{\tau_B}$. Note that this is 100x faster than the real diffusion rate of ParB, around 0.05 $\frac{\mu m^2}{s}$. The diffusion is implemented by attempting the movement of a loaded ParB either to its left or to its right with probability 0.125 every $\tau_B = 500\ dt$ timesteps (recall that MSD = 2 Dt in a 1D system, hence why the jump probability is twice the diffusion coefficient D). The diffusion cannot happen (the move is rejected) if the attempt brings a ParB protein either on top of another ParB or beyond the ends of the DNA.

On top of diffusion, we add a loading rate at ParS at a variable rate κ_{on} and an unloading process at fixed rate $\kappa_{off} = 0.001\ 1/\tau_B$, i.e. at a timescale $T_{off} = 0.5\ ms$. This timescale is faster than the one seen experimentally but we argue that the overall behaviour of the system is controlled by the ratio of loading and unloading timescales. In line with our previous work on the recruitment mechanism of ParB proteins, we implement a stochastic recruitment at the same rate of the loading at ParS (κ_{on}), with the difference that the recruitment probability is associated with each loaded ParB and can happen *in-cis* (with probability $p_c = 0.083$) or *in-trans* (with probability $p_T = 1 - p_C = 0.9166$), in such a way that the trans recruitment is 11 times larger than the cis recruitment. If the cis-recruitment is selected, one of the two 1D adjacent beads to a ParB is selected at random and, if unoccupied, a new ParB is added onto the chain. Otherwise,

if the latter '*in-trans*' mechanism is selected, we compute the list of 3D proximal neighbors which must be (i) within a Euclidean cutoff distance of $2\sigma = 11\ nm$ and (ii) farther than the second-nearest neighbor in 1D (i.e. the first and second nearest neighbors cannot be picked). Once the list of 3D neighbors is compiled, we randomly pick one of these from the list (if not empty), load a new ParB protein, and resume the Langevin simulation.

5.4.15 Implementation of Dimer-of-Dimers and Multimer-of-Dimers bridging

To precisely regulate the binding mechanism between ParB and control the valence of interactions we decorate each polymer bead with 2 patches at antipodal positions of the spherical bead. The central bead and the patches rotate as a rigid body and there is no constraint on the rotation of the patches, e.g. no dihedral potential is imposed. The interaction between patches is turned on only if the polymer bead is occupied by a ParB protein and we decide whether to turn one or both on. The former situation leads to the formation of one-to-one bridges (dimer-of-dimers) while the latter to the formation of multimers-of-dimers. The interaction between patches is regulated by a Morse potential of the form

$$U_{Morse}(r) = D_0(Exp[-2\alpha\, r] - 2\, Exp[-\alpha\, r]\,) \qquad (6)$$

for $r < r_c = 2\,\sigma$ and 0 otherwise. D_0 is a parameter we vary in the simulations to explore the phase diagram, while $\alpha = 0.5$ to ensure short-range interactions. We note that the cut off $r_c = 2\,\sigma = 11\ nm$ is set on purpose to ensure that it is realistic for a pair-wise ParB interaction. The code to run this simulation can be found at https://git.ecdf.ed.ac.uk/taplab/parbcondensation.

5.5 Supplementary data

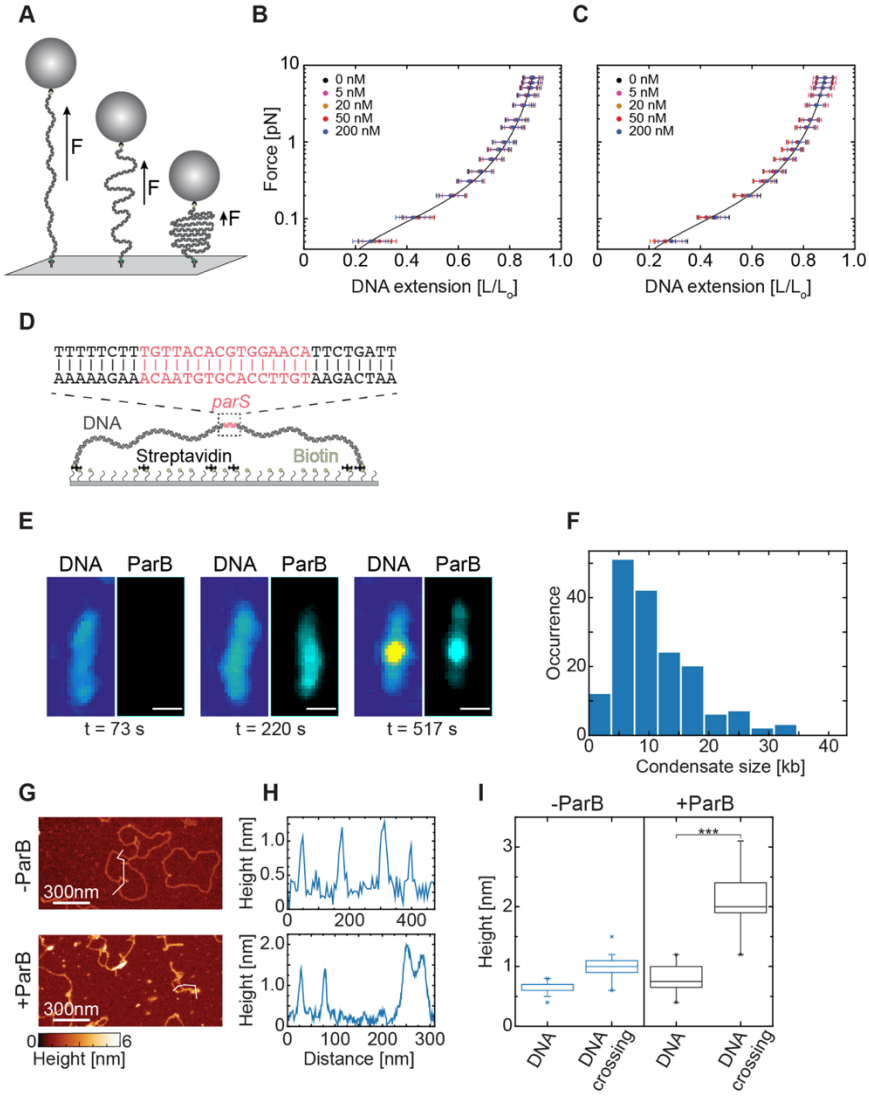


Figure S5.1. ParB proteins do not condense the DNA in the absence of CTP or without a parS site. ***(A)*** *Representation of experimental MT assay where the force is gradually lowered and the bead tethered to 12 kbp linear DNA moves towards the surface in presence of different ParB concentrations.* ***(B)*** *Average DNA extension (mean±SD) at lowering forces (N; 0 nM: 61, 5 nM: 61, 20 nM: 60, 50 nM: 60, 200 nM: 57) in the absence of a parS site on the DNA.* ***(C)*** *Average DNA extension (mean±SD) at lowering forces (N; 0 nM: 16, 5 nM: 15, 20 nM: 15, 50 nM: 17, 200 nM: 11) in the absence of*

CTP nucleotide. Black lines in (B) and (C) represent a WLC fit to the 0 nM ParB data. ***(D)*** *Schematic representation of DNA_{parS} tethered with both ends to a glass surface via streptavidin-biotin interactions (see Methods).* ***(E)*** *Representative fluorescence images of DNA_{parS} and $ParB^{TMR}$ signals at three time points during the experiment: (left) before ParB is present, (middle) at the moment that ParB covers the DNA_{parS}, and (right) after the DNA_{parS} is visibly condensed by ParB molecules. t = 0 s represents the imaging start time after the buffer exchange to the imaging buffer containing ParB protein* ***(F)*** *The size of ParB-induced DNA condensates on the 42 kbp DNA_{parS} molecule (N = 161)* ***(G)*** *Zoomed AFM image of DNA_{parS} molecules in the presence and absence of ParB (7 nM) from Fig. 6.1G, I. White line represents the path over which height profile was analyzed.* ***(H)*** *Height profiles over the lines presented in (G).* ***(I)*** *Height of the DNA_{parS} structures in the absence of ParB molecules (7 nM), both at single strands and at the section where two DNA strands cross each other (p: *** <0.001)*

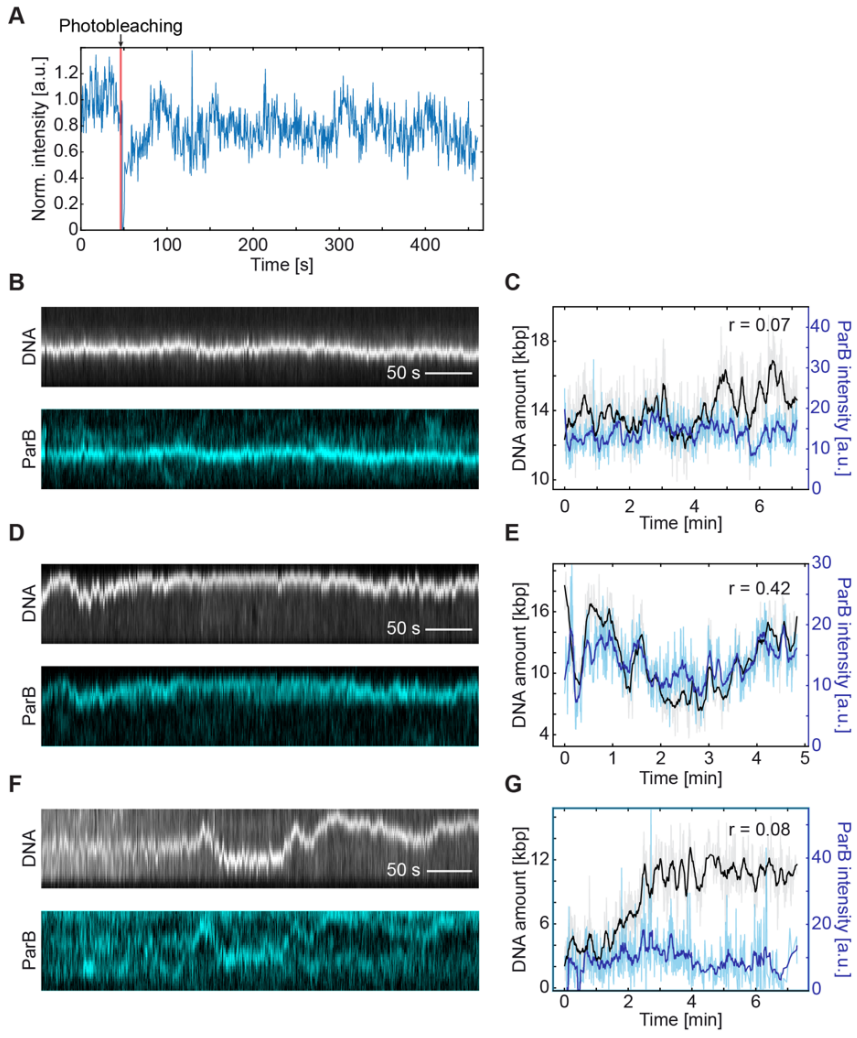


Figure S5.2. ParB:DNA clusters are dynamic and experience high ParB turnover. (A) *Example FRAP (fluorescence recovery after photobleaching) fluorescence intensity plot of a single DNA_{parS} molecule from Fig. 2A. The bleaching event is marked with red line.* ***(B)*** *Kymographs of DNA_{parS} (top, grey) and $ParB^{alexa647}$ (bottom, cyan) after the bleaching recovery events.* ***(C)*** *Quantification of the ParB signal intensity (light blue: raw data; purple: filtered data (Savitzky-Golay, time window =11 frames)) and the amount of DNA within the condensed region of the DNA_{parS} (light gray: raw data; black: filtered data). Pearson correlation coefficient (r) shown in legend.* ***(D-E)*** *Same as (B) and (C) for an example molecule with a higher r value.* ***(F-G)*** *Same as (B) and (C) for an example molecule with a lower r value. Related to Figure 5.2.*

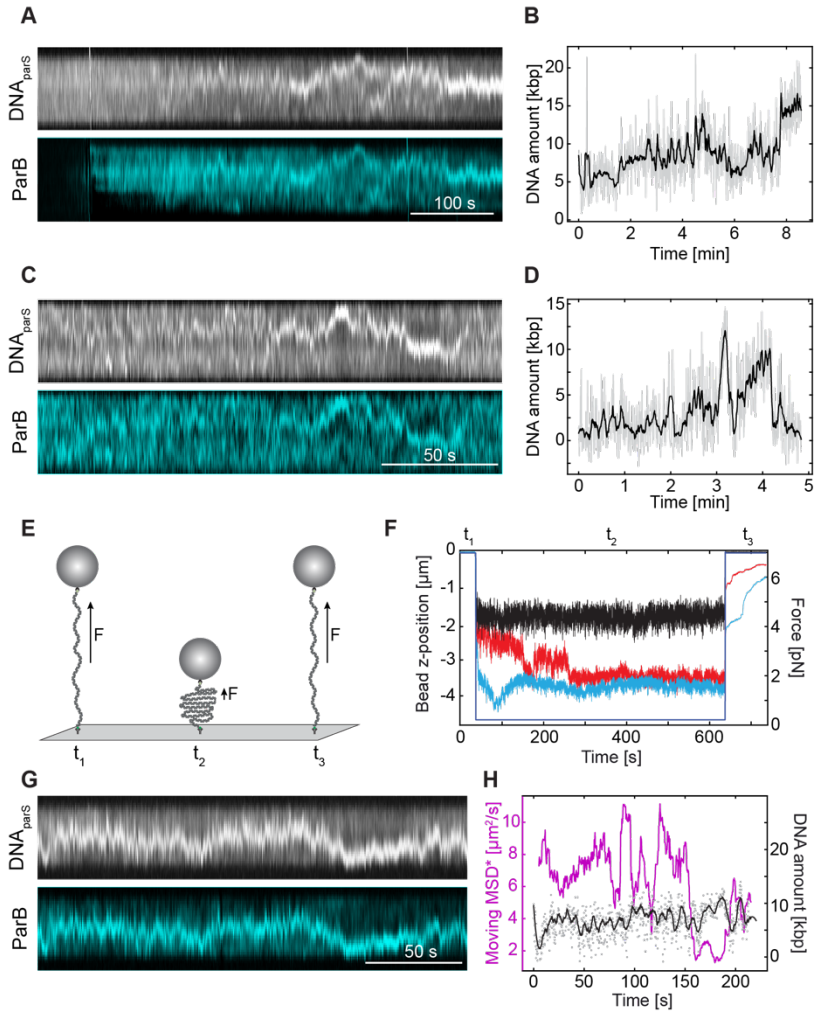


Figure S5.3. DNA$_{parS}$ molecules experience highly dynamic and fluctuating DNA condensation in the initial stages. ***(A)*** *Time course experiment of ParB inflow and ParB-induced DNA condensation. Kymographs of DNA$_{parS}$ (top, grey) and ParB^{alexa647} (bottom, cyan) from the beginning of ParB loading up to dynamic DNA condensation.* ***(B)*** *Quantification of the amount of DNA within the condensed region of the DNA$_{parS}$ (light grey: raw data; black: filtered data (Savitzky-Golay, time window =11 frames)).* ***C-D)*** *Same as in (A) and (B).* ***(E)*** *Time course experiment in MT assay. The DNA bead is lowered from 5 pN (t$_1$) to 0.3 pN for 5 min (t$_2$), and then back to 5 pN (t$_3$).* ***(F)*** *Magnetic bead z-position representing DNA$_{parS}$ extension in the presence of 25 nM ParB. Black trace without ParB does not show DNA condensation events, while in presence of ParB the DNA$_{parS}$ experiences diverse discrete condensation steps (blue, red).* ***(G)***

*Kymographs of DNA_{parS} (top, grey) and $ParB^{alexa647}$ (bottom, cyan) after ~20 min post ParB inflow, during the stable condensation stage. (**H)** Fluctuating DNA cluster position during a stable condensation. Magenta - apparent Mean Squared Displacement (MSD*, window size = 52 frames) of the ParB:DNA condensate tracked by the relative position along the 1D line of the tethered DNA. Gray dots – raw data of the DNA amount within the ParB:DNA condensate in each frame. Black – Savitzky-Golay filter (window size = 11 frames) of the DNA amount withing the condensate in shown in grey. Related to Figure 5.2.*

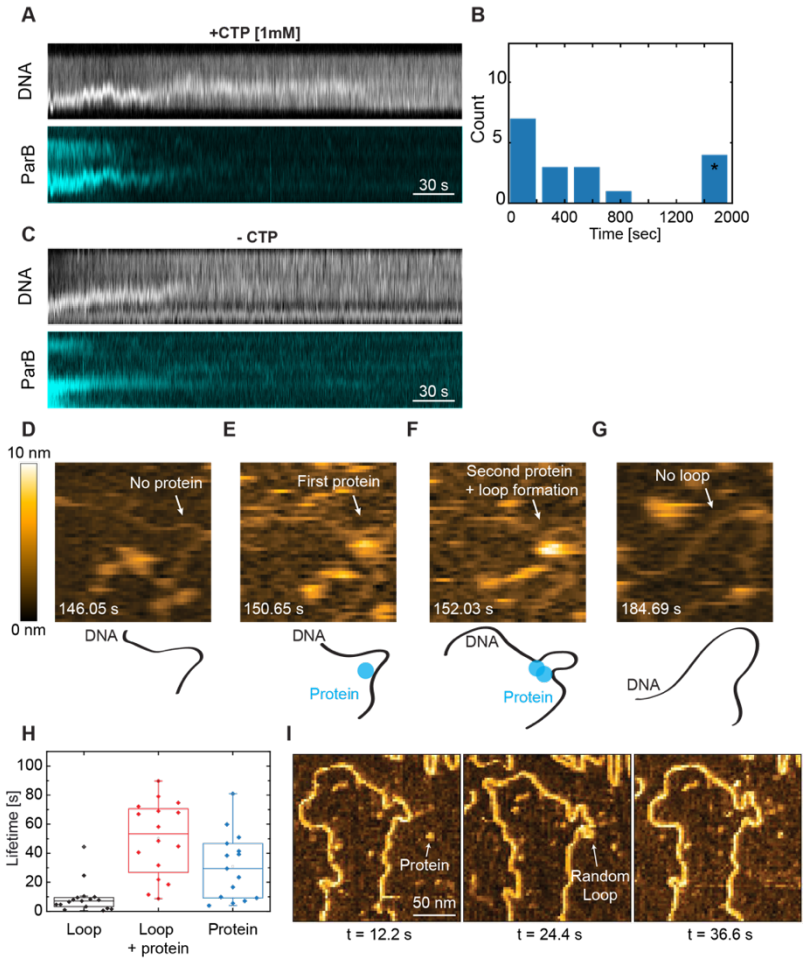


Figure S5.4. ParB-induced DNA condensation is reversible in the presence and absence of CTP. ***(A)*** *Kymographs of DNA_{parS} (top, grey) and $ParB^{TMR}$ (bottom, cyan) from the moment of buffer wash that does not contain $ParB^{TMR}$ molecules.* ***(B)*** *Time from the beginning of the washing until the condensate entirely disassembles. Starred bin represents condensates that did not wash during the entirety of the video.* ***(C)*** *Same as (A) for the washing experiment using the buffer containing neither CTP nor ParB molecules.* ***(D-G)*** *High-speed AFM snapshots of transient DNA loop formation in the presence of ParB and CTP (7 nM). Z-scale bar shown on the left.* ***(H)*** *Loop lifetimes on the DNA_{parS} in the absence (black; mean±SD: 5.6±3.3 s; N = 15) and presence (red; mean±SD: 50±25 s; N = 16) of ParB molecules, and protein lifetime under the same conditions (blue; mean±SD: 30.8±22.9 s; N = 15).* ***I)*** *High-speed AFM snapshots of transient DNA loop formation in the presence of ParB but in the absence of CTP.*

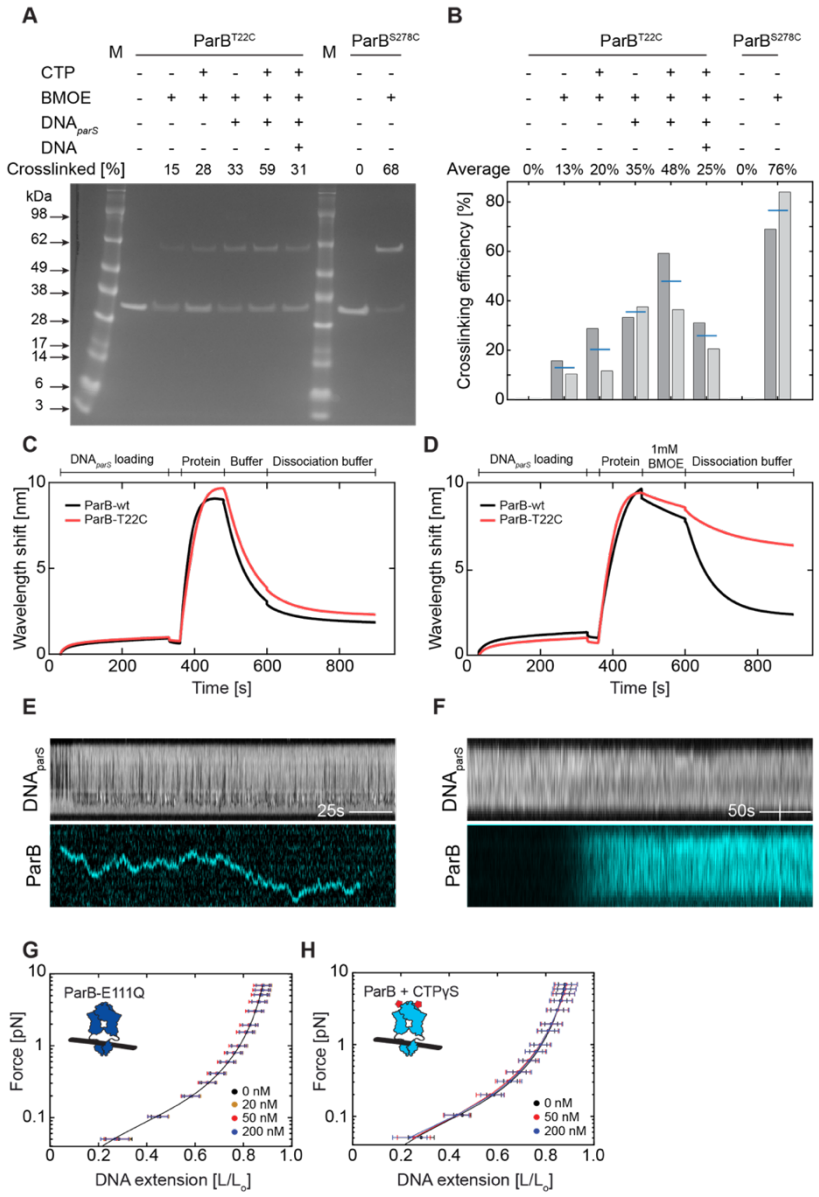


Figure S5.5. ParB mutants (T22C and S278C) can be crosslinked at their C-termini by BMOE. (A) *SDS-PAGE gel showing crosslinking efficiency of ParB^{T22C} (lanes 2-7) and ParB^{S278C} lanes (9-10) in the presence of 1 mM BMOE. Crosslinking efficiency is shown in the percentage of the total signal from both bands. Experimental conditions shown on top and more detailed in the Methods section.* ***(B)*** *Crosslinking efficiency from a duplicate experiment under the same conditions. Blue lines represent the average*

crosslinked fraction from two experiments. ***(C)*** *DNA loading and dissociation of ParB-wt and* $ParB^{T22C}$ *(1 μM) on* DNA_{parS} *measured by BLI in the presence of 1 mM CTP (see Methods). During dissociation, an equivalent buffer lacking ParB protein and CTP was applied.* ***(D)*** *Same as in (C), with the additional step of introducing 1 mM BMOE for cysteine-crosslinking between the loading and dissociation step.* ***(E)*** *Kymographs showing* DNA_{parS} *(top) and single ParB dimer diffusing on the DNA (bottom). The final* $ParB^{Alexa647}$ *concentration was 0.2 nM.* ***(F)*** *Same as in E) but in the presence of 25 nM* $ParB^{Alexa647}$*.* ***(G)*** *Average* DNA_{parS} *extension (mean±SD) in MT in the presence of catalytically inactive* $ParB^{E111Q}$ *mutant (N; 0 nM: 32, 20 nM: 36, 50 nM: 39, 200 nM: 36).* ***(H)*** *Same as in (G), but in the presence of the wild-type ParB protein with 1 mM CTPγS (N; 0 nM: 32, 50 nM: 33, 200 nM: 32).*

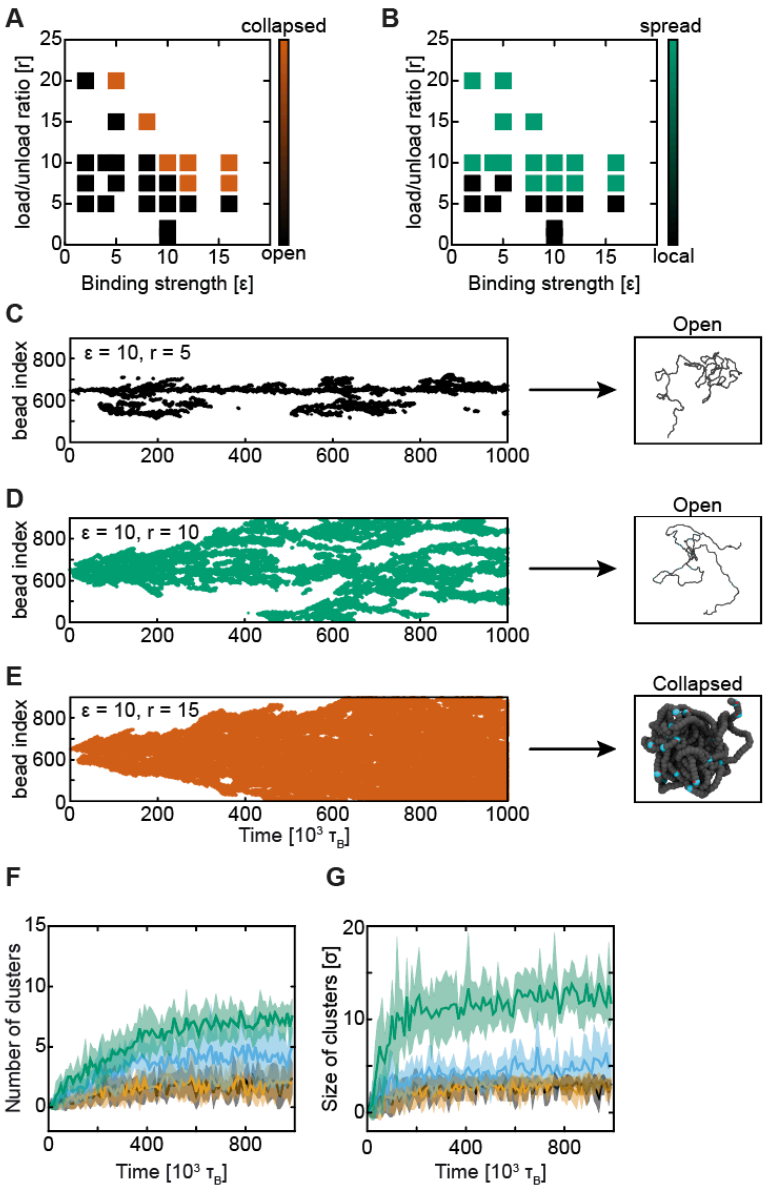


Figure S5.6. Efficient DNA condensation requires spreading and sufficient ParB interaction strength. ***(A)*** *Final DNA polymer conformation (collapsed or open) in relation to load/unload rate (κ) and binding strength (epsilon).* ***(B)*** *ParB distribution over the DNA polymer (local or spread) in relation to load/unload rate (k) and binding strength (ε).* ***(C)*** *Left - Kymograph showing ParB distribution along the simulated DNA polymer at ε = 10 and κ = 5. Right – a snapshot of the final polymer conformation.* ***(D-***

E) *Same as (C) for k = 10 and κ = 15, respectively.* ***(F)*** *The number of DNA clusters over time per DNA. Legend shown on top. κ = 10. Shaded area is SD among 10 replicas of the same system with different initial configuration and seed.* ***(G)*** *The size of individual DNA clusters over time within a single DNA. Legend same as in F). κ = 10. Related to Figure 5.5.*

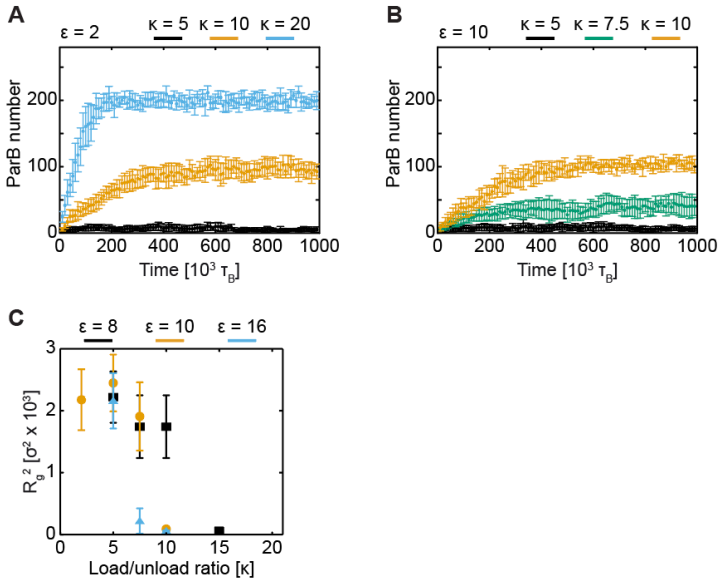


Figure S5.7. DNA-condensation by ParB experiences switch-like behavior due to a high ParB cooperativity. ***(A)*** *Total ParB numbers over time at increasing load/unload rates (κ) at a fixed interaction strength of ε = 2.* ***(B)*** *Same as (A) for ε = 10.* ***(C)*** *Radius of gyration of simulated DNA polymers as a function of κ. Related to Figure 5.5.*

5.6 References

1. Livny, J., Yamaichi, Y. & Waldor, M.K. Distribution of centromere-like parS sites in bacteria: Insights from comparative genomics. *Journal of Bacteriology* **189:8693-703**(2007).

2. Lin, D.C.H. & Grossman, A.D. Identification and characterization of a bacterial chromosome partitioning site. *Cell* **92**, 675–685 (1998).

3. Osorio-Valeriano, M. et al. ParB-type DNA Segregation Proteins Are CTP-Dependent Molecular Switches. *Cell* **179:1512–1524**(2019).

4. Soh, Y.M. et al. Self-organization of parS centromeres by the ParB CTP hydrolase. *Science* **366:1129–1133**(2019).

5. Surovtsev, I.V. & Jacobs-Wagner, C. Subcellular Organization: A Critical Feature of Bacterial Cell Replication. *Cell* **172:1271–1293**(2018).

6. Chen, B.W., Lin, M.H., Chu, C.H., Hsu, C.E. & Sun, Y.J. Insights into ParB spreading from the complex structure of Spo0J and parS. *Proceedings of the National Academy of Sciences of the United States of America* **112:6613-8**(2015).

7. Funnell, B.E. ParB partition proteins: Complex formation and spreading at bacterial and plasmid centromeres. *Frontiers in Molecular Biosciences* **3**, 44 (2016).

8. Graham, T.G.W. et al. ParB spreading requires DNA bridging. *Genes and Development* **28:1228–1238**(2014).

9. Song, D., Rodrigues, K., Graham, T.G.W. & Loparo, J.J. A network of cis and trans interactions is required for ParB spreading. *Nucleic Acids Research* **45**, 7106-7117 (2017).

10. Lim, H.C. et al. Evidence for a DNA-relay mechanism in ParABS-mediated chromosome segregation. *eLife* **3:e02758**, e02758 (2014).

11. Marston, A.L. & Errington, J. Dynamic movement of the ParA-like Soj protein of B. subtilis and its dual role in nucleoid organization and developmental regulation. *Molecular Cell* **4:673-82**(1999).

12. Bock, F.P., Liu, H.W., Anchimiuk, A., Diebold-Durand, M.-L. & Gruber, S. A joint-ParB interface promotes Smc DNA recruitment. *Cell reports* **40**, 111273 (2022).

13. Gruber, S. & Errington, J. Recruitment of Condensin to Replication Origin Regions by ParB/SpoOJ Promotes Chromosome Segregation in B. subtilis. *Cell* **137**, 685-96 (2009).

14. Sullivan, N.L., Marquis, K.A. & Rudner, D.Z. Recruitment of SMC by ParB-parS Organizes the Origin Region and Promotes Efficient Chromosome Segregation. *Cell* **137**, 697–707 (2009).

15. Böhm, K. et al. Chromosome organization by a conserved condensin-ParB system in the actinobacterium Corynebacterium glutamicum. *Nature Communications* **11**, 1485 (2020).

16. Minnen, A., Attaiech, L., Thon, M., Gruber, S. & Veening, J.W. SMC is recruited to oriC by ParB and promotes chromosome segregation in Streptococcus pneumoniae. *Molecular Microbiology* **81**, 676-88 (2011).

17. Tran, N.T., Laub, M.T. & Le, T.B.K. SMC Progressively Aligns Chromosomal Arms in Caulobacter crescentus but Is Antagonized by Convergent Transcription. *Cell Reports* **20**, 2057-2071 (2017).

18. Wang, X., Brandão, H.B., Le, T.B.K., Laub, M.T. & Rudner, D.Z. Bacillus subtilis SMC complexes juxtapose chromosome arms as they travel from origin to terminus. *Science* **355**, 524-527 (2017).

19. Jalal, A.S.B. & Le, T.B.K. Bacterial chromosome segregation by the ParABS system. *Open Biology* **10:200097**(2020).

20. Fisher, G.L.M. et al. The structural basis for dynamic DNA binding and bridging interactions which condense the bacterial centromere. *eLife* **6:e28086**(2017).

21. Taylor, J.A. et al. Specific and non-specific interactions of ParB with DNA: Implications for chromosome segregation. *Nucleic Acids Research* **43:719-31**(2015).

22. Debaugny, R.E. et al. A conserved mechanism drives partition complex assembly on bacterial chromosomes and plasmids. *Molecular Systems Biology* **14:e8516**(2018).

23. Sanchez, A. et al. Stochastic Self-Assembly of ParB Proteins Builds the Bacterial DNA Segregation Apparatus. *Cell Systems* **1:163–173**(2015).

24. Babl, L. et al. CTP-controlled liquid–liquid phase separation of ParB. *Journal of Molecular Biology* **434:167401**(2022).

25. Guilhas, B. et al. ATP-Driven Separation of Liquid Phase Condensates in Bacteria. *Molecular Cell* **79**, 293–303 (2019).

26. Jalal, A.S.B. et al. A CTP-dependent gating mechanism enables ParB spreading on DNA. *eLife* **10:e69676**(2021).

27. Antar, H. et al. Relief of ParB autoinhibition by parS DNA catalysis and ParB recycling by CTP hydrolysis promote bacterial centromere assembly. *Science Advances* **7**, eabj2854 (2021).

28. Osorio-Valeriano, M. et al. The CTPase activity of ParB determines the size and dynamics of prokaryotic DNA partition complexes. *Molecular Cell* **81:3992–4007**(2021).

29. Balaguer, F.d.A. et al. CTP promotes efficient ParB-dependent DNA condensation by facilitating one-dimensional diffusion from parS. *eLife* **10:e67554**(2021).

30. Broedersz, C.P. et al. Condensation and localization of the partitioning protein ParB on the bacterial chromosome. *Proceedings of the National Academy of Sciences of the United States of America* **111**, 8809-8814 (2014).

31. Madariaga-Marcos, J., Pastrana, C.L., Fisher, G.L.M., Dillingham, M.S. & Moreno-Herrero, F. ParB dynamics and the critical role of the CTD in DNA condensation unveiled by combined force-fluorescence measurements. *eLife* **8:e43812**(2019).

32. Wang, X. et al. Condensin promotes the juxtaposition of dna flanking its loading site in Bacillus subtilis. *Genes and Development* **29**, 1661-1675 (2015).

33. Kim, S.H. et al. DNA sequence encodes the position of DNA supercoils. *eLife* **7:e36557**(2018).

34. Jalal, A.S., Tran, N.T. & Le, T.B. ParB spreading on DNA requires cytidine triphosphate in vitro. *eLife* **9:e53515**(2020).

35. Taylor, J.A., Seol, Y., Budhathoki, J., Neuman, K.C. & Mizuuchi, K. CTP and parS coordinate ParB partition complex dynamics and ParA-ATPase activation for ParABS-mediated DNA partitioning. *Elife* **10:e65651**(2021).

36. Tišma, M. et al. ParB proteins can bypass DNA-bound roadblocks via dimer-dimer recruitment. *Science Advances* **8:eabn3299**(2022).

37. Ganji, M. et al. Real-time imaging of DNA loop extrusion by condensin. *Science* **360:102-105**(2018).

38. Quail, T. et al. Force generation by protein–DNA co-condensation. *Nature Physics* **17:1007–1012**(2021).

39. Ryu, J.K. et al. Bridging-induced phase separation induced by cohesin SMC protein complexes. *Science Advances* **7:eabe5905**(2021).

40. Connolley, L., Schnabel, L., Thanbichler, M. & Murray, S.M. Partition complex structure can arise from sliding and bridging of ParB dimers. *Nature Communications* **14:4567**(2023).

41. Brackley, C.A. et al. Nonequilibrium Chromosome Looping via Molecular Slip Links. *Phys Rev Lett* **119:138101**(2017).

42. Cagnetta, F., Michieletto, D. & Marenduzzo, D. Nonequilibrium Strategy for Fast Target Search on the Genome. *Phys Rev Lett* **124:198101**(2020).

43. Foglino, M. et al. Non-equilibrium effects of molecular motors on polymers. *Soft Matter* **15:5995-6005**(2019).

44. Rodionov, O., ŁObocka, M. & Yarmolinsky, M. Silencing of genes flanking the P1 plasmid centromere. *Science* **283:546–549**(1999).

45. Lynch, A.S. & Wang, J.C. SopB protein-mediated silencing of genes linked to the sopC locus of Escherichia coli F plasmid. *Proceedings of the National Academy of Sciences of the United States of America* **92:1896–1900**(1995).

46. Bartosik, A.A., Lasocki, K., Mierzejewska, J., Thomas, C.M. & Jagura-Burdzy, G. ParB of Pseudomonas aeruginosa: interactions with its partner ParA and its target parS and specific effects on bacterial growth. *J Bacteriol* **186:6983-98**(2004).

47. Kusiak, M., Gapczynska, A., Plochocka, D., Thomas, C.M. & Jagura-Burdzy, G. Binding and spreading of ParB on DNA determine its biological function in Pseudomonas aeruginosa. *J Bacteriol* **193:3342-55**(2011).

48. Jakimowicz, D., Chater, K. & Zakrzewska-Czerwinska, J. The ParB protein of Streptomyces coelicolor A3(2) recognizes a cluster of parS sequences within the origin-proximal region of the linear chromosome. *Mol Microbiol* **45:1365-77**(2002).

49. Venkova-Canova, T., Baek, J.H., Fitzgerald, P.C., Blokesch, M. & Chattoraj, D.K. Evidence for two different regulatory mechanisms linking replication and segregation of vibrio cholerae chromosome II. *PLoS Genet* **9:e1003579**(2013).

50. Kawalek, A., Glabski, K., Bartosik, A.A., Fogtman, A. & Jagura-Burdzy, G. Increased ParB level affects expression of stress response, adaptation and virulence operons and potentiates repression of promoters adjacent to the high affinity binding sites parS3 and parS4 in Pseudomonas aeruginosa. *PLoS One* **12:e0181726**(2017).

51. Janissen, R. et al. Global DNA Compaction in Stationary-Phase Bacteria Does Not Affect Transcription. *Cell* **174:1188-1199**(2018).

52. Janissen, R., Eslami-Mossallam, B., Artsimovitch, I., Depken, M. & Dekker, N.H. High-throughput single-molecule experiments reveal heterogeneity, state switching, and three interconnected pause states in transcription. *Cell Rep* **39:110749**(2022).

53. Anchimiuk, A. et al. A low Smc flux avoids collisions and facilitates chromosome organization in Bacillus subtilis. *eLife* **10:e65467**(2021).

54. Brandão, H.B., Ren, Z., Karaboja, X., Mirny, L.A. & Wang, X. DNA-loop-extruding SMC complexes can traverse one another in vivo. *Nature Structural and Molecular Biology* **28:642-651**(2021).

55. Guo, L. et al. Stochastically multimerized ParB orchestrates DNA assembly as unveiled by single-molecule analysis. *Nucleic Acids Res* **50:9294-9305**(2022).

56. Brackley, C.A. et al. Ephemeral Protein Binding to DNA Shapes Stable Nuclear Bodies and Chromatin Domains. *Biophys J* **112:1085-1093**(2017).

57. Michieletto, D., Coli, D., Marenduzzo, D. & Orlandini, E. Nonequilibrium Theory of Epigenomic Microphase Separation in the Cell Nucleus. *Phys Rev Lett* **123:228101**(2019).

58. Bianco, P.R. DNA Helicase-SSB Interactions Critical to the Regression and Restart of Stalled DNA Replication forks in Escherichia coli. *Genes (Basel)* **11:471**(2020).

59. Liu, N., Chistol, G., Cui, Y. & Bustamante, C. Mechanochemical coupling and bi-phasic force-velocity dependence in the ultra-fast ring ATPase SpoIIIE. *eLife* **7:e32354**(2018).

60. Wang, M.D. et al. Force and velocity measured for single molecules of RNA polymerase. *Science* **282:902-7**(1998).

61. Yin, H. et al. Transcription against an applied force. *Science* **270:1653-7**(1995).

62. Sun, B. et al. Impediment of E. coli UvrD by DNA-destabilizing force reveals a strained-inchworm mechanism of DNA unwinding. *EMBO J* **27:3279-87**(2008).

63. Johnson, G.E., Lalanne, J.B., Peters, M.L. & Li, G.W. Functionally uncoupled transcription-translation in Bacillus subtilis. *Nature* **585:124-128**(2020).

64. Breier, A.M. & Grossman, A.D. Whole-genome analysis of the chromosome partitioning and sporulation protein Spo0J (ParB) reveals spreading and origin-distal sites on the Bacillus subtilis chromosome. *Molecular Microbiology* **64:703-18**(2007).

65. Soh, Y.M. et al. Self-organization of parS centromeres by the ParB CTP hydrolase. *Science* (2019).

66. Jalal, A.S., Tran, N.T. & Le, T.B. ParB spreading on DNA requires cytidine triphosphate in vitro. *eLife* **9**(2020).

67. Antar, H. et al. Relief of ParB autoinhibition by parS DNA catalysis and ParB recycling by CTP hydrolysis promote bacterial centromere assembly. *Science Advances* (2021).

68. Osorio-Valeriano, M. et al. The CTPase activity of ParB determines the size and dynamics of prokaryotic DNA partition complexes. *Molecular Cell* **81**, 3992-4007.e10 (2021).

69. Jalal, A.S.B. et al. A CTP-dependent gating mechanism enables ParB spreading on DNA. *eLife* **10**(2021).

70. Tišma, M. et al. ParB proteins can bypass DNA-bound roadblocks via dimer-dimer recruitment. *Science Advances* **8**, eabn3299-eabn3299 (2022).

71. Pradhan, B. et al. SMC complexes can traverse physical roadblocks bigger than their ring size. *Cell Rep* **41:111491**(2022).

72. Kim, E., Kerssemakers, J., Shaltiel, I.A., Haering, C.H. & Dekker, C. DNA-loop extruding condensin complexes can traverse one another. *Nature* **579:438-442**(2020).

73. Pradhan, B. et al. The Smc5/6 complex is a DNA loop-extruding motor. *Nature* **616:843-848**(2023).

74. Davidson, I.F. et al. CTCF is a DNA-tension-dependent barrier to cohesin-mediated loop extrusion. *Nature* **616:822-827**(2023).

75. Bouchiat, C. et al. Estimating the persistence length of a worm-like chain molecule from force-extension measurements. *Biophysical Journal* **76:409-13**(1999).

76. Horcas, I. et al. WSXM: a software for scanning probe microscopy and a tool for nanotechnology. *Rev Sci Instrum* **78:013705**(2007).

77. Svetlov, V. & Artsimovitch, I. Purification of bacterial RNA polymerase: tools and protocols. *Methods Mol Biol* **1276:13-29**(2015).

78. Abbondanzieri, E.A., Greenleaf, W.J., Shaevitz, J.W., Landick, R. & Block, S.M. Direct observation of base-pair stepping by RNA polymerase. *Nature* **438:460-5**(2005).

79. Vassylyeva, M.N. et al. The carboxy-terminal coiled-coil of the RNA polymerase beta'-subunit is the main binding site for Gre factors. *EMBO Rep* **8:1038-43**(2007).

80. Cnossen, J.P., Dulin, D. & Dekker, N.H. An optimized software framework for real-time, high-throughput tracking of spherical beads. *Rev Sci Instrum* **85:103712**(2014).

81. Klaue, D. & Seidel, R. Torsional stiffness of single superparamagnetic microspheres in an external magnetic field. *Phys Rev Lett* **102:028302**(2009).

82. Odijk, T. Stiff Chains and Filaments under Tension. *Macromolecules* **28:7016–7018**(1995).

6

DIRECT OBSERVATION OF A CRESCENT-SHAPE CHROMOSOME IN BACILLUS SUBTILIS

Bacterial chromosomes are folded into tightly regulated three-dimensional structures to ensure proper transcription, replication, and segregation of the genetic information. Direct visualization of chromosomal shape within bacterial cells is hampered by cell-wall confinement and the optical diffraction limit. Here, we combine cell-shape manipulation strategies, high-resolution fluorescence microscopy techniques, and genetic engineering to visualize the intrinsic shape of the bacterial chromosome in real-time in live Bacillus subtilis cells. We show that the chromosomes exhibit crescent shapes with a non-uniform DNA density that is increased near the origin of replication (oriC). Additionally, we localized ParB and BsSMC proteins – the key drivers of chromosomal organization – along the contour of the crescent chromosome, showing the highest density near oriC. Opening of the BsSMC ring complex disrupted the crescent chromosome shape and instead yielded a torus shape. These findings help to understand the three-dimensional organization of the chromosome and the main protein complexes that underlie its structure.

This chapter was written by Tišma M, Bock F. P, Kerssemakers J, Japaridze A, Gruber S, Dekker C. and is under review in *Nature Communications*.

6.1 Introduction

Over the past decade, it has become evident that bacterial chromosomes are folded into a compact 3D architecture that regulates transcription and is necessary for cell survival[1-3]. As nuclear compartmentalization is absent in bacteria, a high abundance of DNA-binding proteins can locally bind and change the chromosomal structure [4]. Furthermore, the chromosome is subject to the crowding effects of cytosolic components and the genome has to fit within the confines of the cell boundary which squeezes the millimeter-long bacterial genome within the micron-size cell [5]. Although bacterial chromosomes have been imaged by microscopy in many earlier works [6-11], the tight confinement of the genome combined with the finite optical diffraction limit has been a hindrance towards resolving its unconfined shape and structure. Attempts to significantly increase the spatial resolution via super-resolution microscopy techniques often require synthetic dyes that include lengthy washing procedures or invasive crosslinking steps which may affect the DNA structure and dynamics in live cells [6,7,12,13]. Direct high-resolution imaging of the chromosome would shed light onto the chromosomal dynamics, macrodomain organization [14,15], and the roles of various proteins in its organization.

An indirect but powerful method of studying the chromosomal structure is provided by chromosome capture techniques (3C[16], 4C[17], 5C[18]), most notably 'Hi-C'[7,19-24]. This technique uses proximity-based ligation in combination with next-generation sequencing to uncover the average spatial organization of the DNA within a population of cells [21]. Over the past decade, Hi-C has been established as a major tool for studying the 3D chromosome organization and it has contributed key insights about the chromosome organization in many bacterial species [7,19,20,23-25]. Interestingly, the most well-studied bacterial model organisms *Escherichia coli* and *Bacillus subtilis* show an entirely different chromosomal structure in Hi-C maps. *E. coli* was deduced to have a textbook circular chromosomal shape with separately condensed chromosomal arms that are twisted within the cylindrical cell [19]. *Bacillus subtilis* however, shows a distinct "second diagonal" feature in the Hi-C maps which indicates that two chromosomal arms are spatially aligned, which presumably is facilitated by the action of bacterial structural maintenance of chromosome (SMC) proteins [7,23,24]. Aligned chromosome arms were also observed in other microorganisms [20,26-28], albeit for some (e.g., *Caulobacter crescentus*), the second diagonal did not span the full length of the chromosome, suggesting a segregation of the nascent origins but not a full zipping of the entire chromosome [20]. Many questions remain, however, as Hi-C methods involve extensive cell fixation which can alter the DNA organization [21], and conclusions are drawn from population averages where the single-cell structure and cell-to-cell variabilities are lost.

A promising way to spatially resolve the bacterial chromosome is to use cell-shape manipulation techniques [15,29-32] or expansion microscopy (ExM) [33-35]. While expansion microscopy, where bacteria are encapsulated in a hydrogel that is stretched, requires cell fixation that precludes live cell imaging [35], cell-shape manipulation techniques allow for imaging of live cells, where a single chromosome can be maintained via DNA replication halting. Using cells-shape manipulation approach, we previously visualized the *E. coli* chromosome at the single-cell level, showing a toroidal shape with fast local dynamics and interesting substructures within the genome [15,29].

Here, we use cell-shape manipulation with replication halting to capture the structure of the unconfined *Bacillus subtilis* chromosome in single live cells. Cell-shape manipulation relaxed the cell-boundary confinement of the chromosome in live bacteria, thus allowing standard super-resolution microscopy techniques to capture the intrinsic chromosome shape. We observed that the *B. subtilis* chromosome most frequently adopts a crescent shape, with an origin region at one tip of the crescent that is highly condensed. Furthermore, we measured the positioning of the key chromosome-organizing proteins ParB and BsSMC along the contour of the chromosome. Upon BsSMC disruption, the crescent chromosome shape changed into a torus shape, indicating that BsSMC is required for maintaining the crescent shape. The data provide insight into the chromosomal organization of the *B. subtilis* chromosome and its organizing proteins.

6.2 Results

6.2.1 Cell-shape manipulation of *Bacillus subtilis* bacteria

In standard growth conditions, both for nutrient-rich or in a minimal medium, *B. subtilis* cells grow into rod shapes with its chromosome residing close to the center of the cell as a confined object of ~1.3 μm x 0.7 μm (Fig. S6.1A-B) [5]. Due to the diffraction limits of microscopy, most of the chromosome's inner structure cannot be resolved. To eliminate the confining effects set by the cell wall, we converted the rod-shaped *B. subtilis* cells into spheroidal cells (also known as L-form cells [36,37]) similarly to the protocol described in Kawai *et al.* [38] (Figure 1A-B, *see Methods*). The physical conversion from a capped cylinder to a spheroid implies a change in surface-to-volume ratio. In our case, the total surface remains constant as it is set by the cell membrane that cannot substantially grow over the course of the fast conversion to spheroidal cells. To accommodate the change and increase the cell volume, we used different osmotic media to promote water uptake into the spheroidal cells, and accordingly a volume increase. We tested a variety of media ranging from highly hypoosmotic (100 mM osmolyte) to isoosmotic concentrations (500

mM osmolyte, see *Methods*), which did not affect the phenotype in cylindrical cells (Fig. S6.1C). Under wall-less conditions, we observed the highest increase in volume under slightly hypoosmotic conditions, viz., 300 mM osmolyte (Fig. 6.1C, S6.1D). Cylindrical cells of, on average, 3.3 x 0.8 x 0.8 μm^3 size then adopted an approximately spheroidal shape with an average size of 2.3 x 2.3 x 1.7 μm^3. This resulted in the average total volume change of up to about a factor of 3 of the original volume. This volume expansion increased the physical space where the chromosome can freely reside within a few minutes, allowing for observation of its intrinsic shape without confinement while avoiding long cell-reshaping treatments which could induce chromosome perturbations.

6.2.2 Observation of a crescent chromosome *in Bacillus subtilis* in single cells

To obtain the image of a single chromosome in individual cells, we used two replication halting strategies in separate strains. First, we constructed a strain containing temperature-sensitive DnaB protein (*dnaB134ts*, Fig. S6.2, Table 1) [9,39,40]. This protein is an essential component during the DNA replication process in *B. subtilis* as it facilitates new rounds of initiation by facilitating helicase loading [41,42]. Upon a temperature increase, the strain carrying $DnaB^{K85E}$ (*dnaB134ts* locus) experiences a strong inhibition of initiation of new DNA replication rounds [40]. To control for the possible denaturation of HbsU protein at high temperatures [43] (which would alter chromosomal structure), we grew the strain at a maximum of 39°C. Second, we constructed a separate strain carrying P_{lac}-*sirA* whose protein product can also efficiently halt the initiation of DNA replication by directly inhibiting the action of DnaA [44,45] (Table 1), whilst preserving HbsU stability at 30°C [43]. For DNA imaging, we used (i) a fluorescently labeled version of the HbsU protein which uniformly binds across the DNA [46,47], or (ii) synthetic DNA intercalating dyes (Fig. S6.2) that do not affect cell viability [48], or (iii) standardized DNA dyes (DAPI, SYTOXGreen, SYTOXOrange). All different fluorophores and replication-halting variants yielded similar results (Fig. S6.2).

In a large fraction (33-43%) of the cells, we could resolve the unconfined chromosome shape even under widefield microscopy and observed that the *B. subtilis* chromosome exhibited a crescent shape (Fig. 6.1D, S6.3A-D). This was observed irrespective of the chromosome labeling or replication-halting strategy (Fig. S6.2).

Interestingly, the size of the expanded chromosome in *B. subtilis* was smaller than the cell diameter (Fig. S6.4), which indicates that the chromosomes did largely expand to their intrinsic conformation. This contrasts our previous observations in *E. coli*, where chromosomes that assume a toroidal shape upon cell expansion, fully expand to the size of the cell [15]. A considerable cell-to-cell variability was observed where some

chromosomes appeared as a more condensed object that we were unable to resolve (Fig. S6.3C-D).

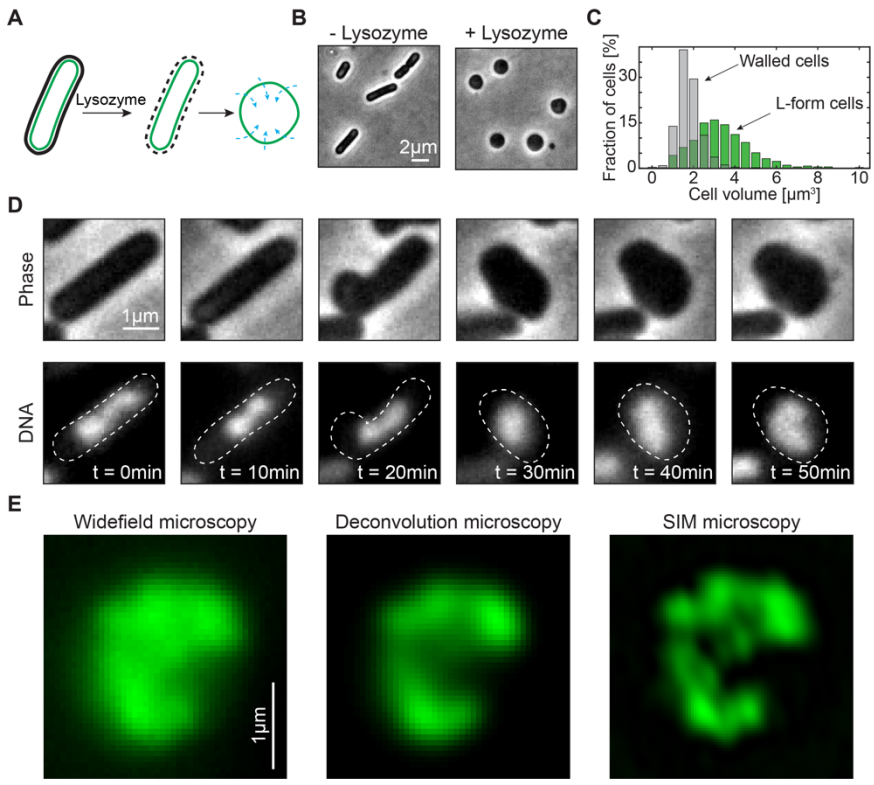


Figure 1. Bacillus subtilis chromosome adopts a crescent shape upon cell widening. ***A)*** *Graphical representation of the cell-shape conversion from rod-shaped to spheroidal shape.* ***B)*** *Conversion of rod-shaped cells to spheroidal cells under hypoosmotic conditions in SMM+MSM medium (300 mM succinate) upon addition of lysozyme.* ***C)*** *Total cell volume before (grey, V_{avg}=1.8 ± 0.6 µm^3, N=550) and after the lysozyme treatment (green, V_{avg}=3.4 ± 1.5 µm^3 N=1056). The results are pooled from three biological replicates.* ***D)*** *Example timelapse imaging of the conversion of a single cell from rod shape to spherical shape under an agar pad for the BSG217 strain at 39°C.* ***E)*** *Comparison of widefield (left), deconvolved (middle), and Structured Illumination Microscopy (SIM) (right) image of a crescent chromosome in the strain BSG217.*

Next, we used superresolution microscopy to obtain high-resolution images of single *B. subtilis* chromosomes. Deconvolution of widefield microscopy and structured illumination microscopy (SIM) allowed for the imaging of live cells with spatial resolution down to 150 nm and 120 nm, respectively. Images taken with both techniques consistently showed that chromosomes adopted a crescent shape (Fig. 6.1E, S5, Movie S1, S2). This is consistent with previous Hi-C data that suggested a close spatial alignment of left- and right-chromosomal arms [24]. Interestingly, the fluorescence intensity along the contour of the chromosome appeared to be quite variable between two ends as well as from cell to cell. This suggests a dynamic compaction level of the DNA along the chromosome where DNA is distributed non-uniformly (Fig. 6.1D-E). To quantitatively measure the physical characteristics of the crescent-shaped chromosomes, we ensured the presence of a single chromosome within each cell, as any unfinished replication round could result in large changes in the DNA amount and chromosome shape, thus obstructing quantitative assessments of the chromosome shape, size, and dynamics.

6.2.3 DNA is highly compacted in the origin region

First, we located the origin of replication (*oriC*) as the reference point. Conveniently, *B. subtilis* has multiple *parS* sites around the *oriC*, which bind partitioning protein B (ParB) in high numbers[49] (Fig. 6.2A). ParB proteins bridge multiple *parS* sites and form a single focus per chromosome [50,51], and they are commonly used as a proxy for the number of chromosomes per cell [24,52-55], given that newly replicated origins are quickly separated. We used a fluorescent fusion of ParB-mScarlet in addition to P_{lac}-*sirA* in order to select for cells with a single fluorescently labeled origin-proximal region [56] (Fig. 6.2B-E, Table 1). In growth assays, this strain behaved equivalent to wild-type *B. subtilis* (Fig. S6.6A) and it showed the same phenotype under the microscope (Fig. S6.6B), while experiencing severely halted growth during the SirA induction (Fig. S6.6C). In the absence of SirA induction, this strain shows multiple origins per single cell (Fig. 6.2B-C). Upon induction of SirA protein, up to 78% of the cells showed a single focus per cell, indicating successful replication halting (Fig. 6.2D-E). To ensure that this was not the effect of unresolved origins of multiple chromosomes, we performed a qPCR to quantify the *ori:ter* ratio and further constructed a strain that had fluorescently labeled replication termination protein (RTP-GFP) in addition to the origin label. By quantifying the *ori*:*ter* ratio in the cells upon replication halt using both qPCR and fluorescent readout, we confirmed that SirA expression indeed strongly suppressed replication due to the replication halt treatment (Fig. S6.7).

In origin-labeled cells, we observed *ori* to localize at the tip of the crescent chromosome (Fig. 6.2F, S6.8). The origin of replication was not notably mobile, residing within 86 nm (Fig. S6.9A-C) on the time scales of 10 s, which is comparable to the minor background movements of our cells under the soft agar (FWHM = 59 nm, Fig. S6.9D). Cells that had both *ori* and *ter* labeled, showed that these two important loci tend to localize at the opposite tips of the crescent-shaped chromosome (Fig. S6.10) albeit with a high flexibility in the *ter* region that can localize closer to the origin in some instances (Fig. S6.10E).

After thus successfully localizing the *oriC* and selecting the presence of a single fluorescent focus, we proceeded with the analysis of DNA compaction along the contour of the crescent chromosome (Fig. 6.2G, see Methods and Ref. 15). To stain the DNA we used either fluorescent intercalator dye – SyG (Fig. 6.2F-J)[57] or DNA-binding protein fusing HbsU-mTurquoise2 (Fig. S6.11A-C), allowing us to correlate the fluorescence intensity with the underlying amount of DNA. In all cells, we observed an increase in the DNA fluorescence intensity proximal to the ParB focus, i.e., at the origin of replication (Fig. 6.2H-I, S6.11D-E). We observed an uneven distribution of DNA along the contour of the chromosome, with a higher abundance of DNA present near the origin of replication and less DNA present towards the tail of the crescent chromosome. Using previously established analyses[15], we were able to detect DNA clusters along the chromosome based on the local fluorescence and intensity changes, where clusters were detected as a sub-group of point spread function-limited spots (see Methods for more detail). In our *B. subtilis* chromosomes, we observed clusters of DNA, representing more condensed regions along the contour of the chromosome (Fig. 6.2J). We termed the cluster with the highest amount of DNA as the 'primary cluster', and all other clusters found as 'secondary clusters' (Fig. 6.2J). We found that the primary clusters typically localized near the *ori* region (Fig. 6.2J – black data), i.e., coinciding with the ParB focus. Most of cells possessed a secondary condensed region, albeit variable in size and position along the chromosome (Fig. 6.2I – grey data). We did not observe a particularly preferred chromosome position for these secondary clusters, and such domains instead appeared to position at arbitrary locations along the chromosome contour shape as well as contained a variable amount of DNA.

As the primary clusters tended to be positioned near *ori*, we analyzed the total DNA percentage that was localized near *ori* (Fig. S6.8B-C). We observed that the majority of cells (67%) exhibited a very large fraction (>40%) of their entire genome within only 500nm from the origin of replication. Our data thus show a high DNA condensation proximal to the origin region, and concomitantly lower DNA condensation along the rest of the chromosome.

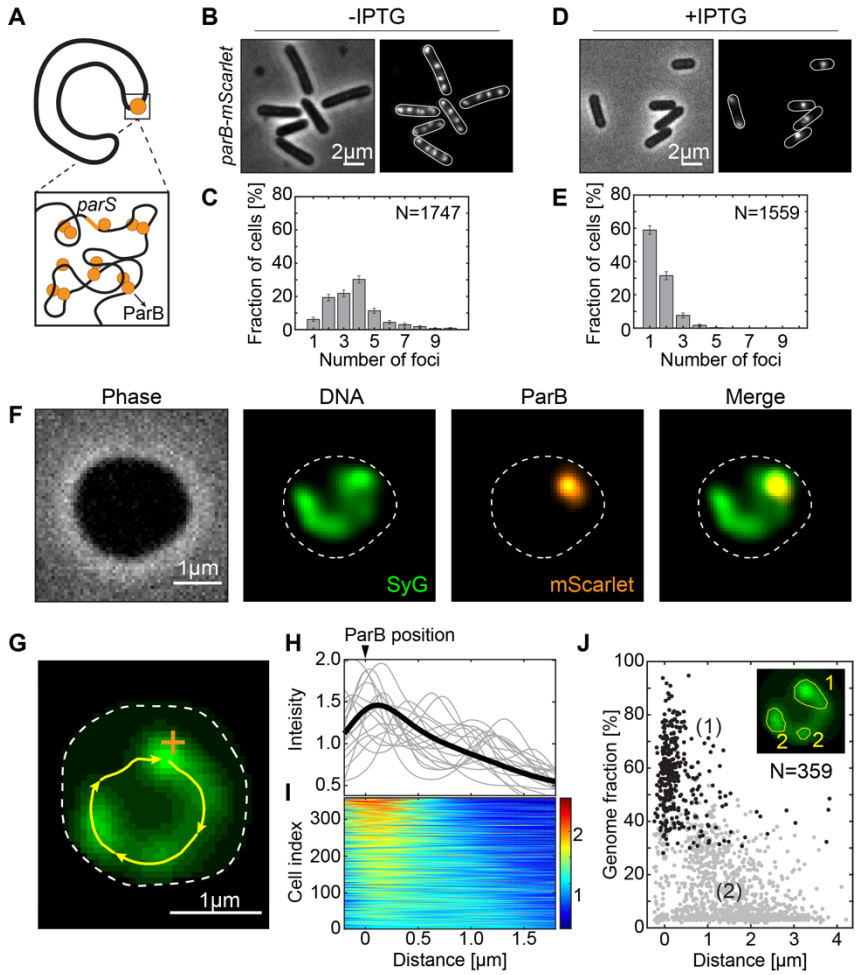


Figure 2. ParB complex co-localizes with a region of high DNA density. A) *Graphical representation of the crescent-shape chromosome. The zoom sketches the origin/parS region that is condensed by ParB proteins (orange).* ***B)*** *Phase (left) and fluorescence (right) images of the BSG4595 cells (parB-mScarlet; $P_{hyperspank}$-sirA) in the absence of ITPG.* ***C)*** *Quantification of the number of fluorescent ParB-mScarlet foci in single cells imaged as in panel B (N=1747, avg_{spots} = 3.56 ± 1.8). The results are pooled from three biological replicates. Error bars represent 95% confidence intervals.* ***D)*** *Same as panel B but for cells in the presence of 2 mM ITPG for 150 min.* ***E)*** *Quantification of the number of fluorescent ParB-mScarlet foci in single cells imaged as in panel D (N=1559, avg_{spots} = 1.42 ± 0.86). The results are pooled from four biological replicates. Error bars represent 95% confidence intervals.* ***F)*** *Representative example of a cell after treatment with lysozyme (400 μg/ml) for 30 min.* ***G)*** *Crescent-shaped chromosome. Cell outline is*

denoted by the white line; DNA contour track by yellow line; location of the ParB focus by the orange cross. ***H)*** *DNA intensity along the contour of the chromosome (cf. yellow line in panel G). Black line shows the average normalized intensity obtained from all cells (N=359). Gray lines display arbitrarily chosen individual examples. The position of the ParB focus is indicated on top (defining the 0 µm position).* ***I)*** *DNA density along the chromosome in all individual cells. Colorbar represents the fold-increase. Cells are ordered from top to bottom in terms of contrast.* ***J)*** *Cluster analysis of the chromosome. Inset shows an example output of the analysis with 1 primary and 2 secondary-size clusters. The fraction of the genome that is contained within the primary focus (1) (black dots) is plotted versus distance from the origin (ParB focus; n=359). Secondary condensation (2) foci are represented as gray dots.*

6.2.4 BsSMC proteins spread along the entire contour of the crescent chromosome

SMC proteins constitute key players in the large-scale chromosome organization in all domains of life [58]. For *B. subtilis,* this concerns the BsSMC complex [23,52,54]. Previous studies concluded that BsSMC is recruited to the origin of replication through interactions with ParB protein [52,54,59], whereupon it progressively "zips" the left and right chromosome arms together along the entire length of the chromosome [7,23,24] (Fig. 6.3A). We constructed a strain containing an origin label (ParB-mScarlet), DNA label (HbsU-mTurqoise2), and BsSMC label (BsSMC-mGFP) in order to co-visualize the chromosome along with ParB and BsSMC (Fig 3B, Table 1).

We observed that SMC proteins positioned as a combination of typically 1-2 fluorescent foci with an additional clear signal that colocalized with the DNA signal over the entire chromosome (Fig. 6.3B)[52,54]. This starkly contrasts data for the ParB protein that showed that virtually all of the intracellular ParBs was captured into one focus, with very little background in the rest of the cell (Fig. 6.2B, D, S8)[60]. We quantified the distance of BsSMC-mGFP and ParB-mScarlet foci in rod-shaped cells, and observed a close proximity between the foci, i.e. an average mutual distance of only 126 ± 28 nm (mean ± std, Fig. 6.3C). Upon performing the same procedure in widened cells, we again observed the HbsU-labelled chromosome to adopt a crescent shape, with a ParB-mScarlet focus at the tip of the crescent-shaped chromosome (Fig. 6.3D). BsSMC-mGFP appeared to spread over the entire chromosome, with the highest intensity proximal to the ParB-mScarlet focus (Fig. 6.3D). In a control strain containing a tag only on BsSMC

and not on ParB and HbsU, we observed the same distribution of BsSMC signal (Fig. S6.12).

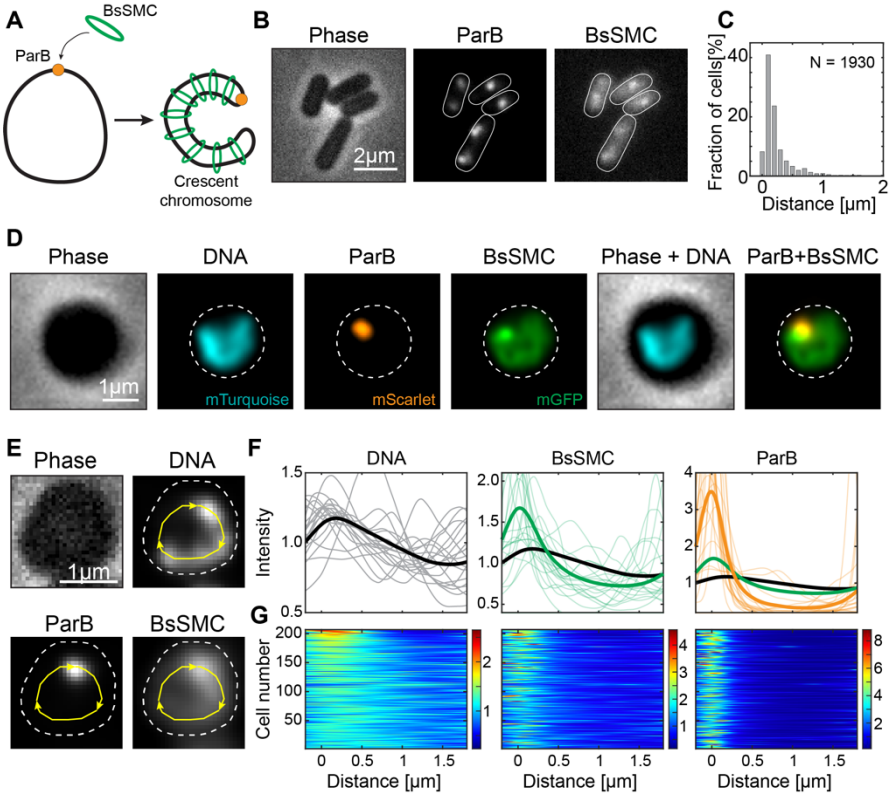


Figure 3. BsSMC proteins spread along the entire chromosome. A) *Graphical representation of the crescent chromosome and the BsSMC positioning (cf. Wang et al[1]).* ***B)*** *Phase (left) and fluorescent (right) images of BSG4623 strain (hbsu-mTurqoise2; smc-egfp; parB-mScarlet; $P_{hyperspank}$-sirA) after replication halt with 2 mM IPTG.* ***C)*** *Histogram of the distance between the BsSMC and ParB foci. The average distance between spots was $d_{avg} = 126 \pm 28$ nm (mean ± std, n=1930). The results for the histogram are pooled from three biological replicates.* ***D)*** *Images of bacterial strain BSG4623 strain after lysozyme (400 μg/ml) treatment for 30 min.* ***E)*** *Contour analysis of DNA, BsSMC, and ParB signals along the crescent chromosomes (cf. Fig. 2G.)* ***F)*** *Fluorescence intensity along the contour line of the chromosome, starting from the ParB locus: DNA signal (left, black line); BsSMC (middle, green); ParB (right, orange) (n = 215).* ***G)*** *Corresponding density plots along the chromosome in all individual cells. Colorbars represent the fold-increase.*

We quantified the intensities of all signals along the contour of the chromosome (Fig. 6.3E) similar to those described in Fig. 6.2G-I. The average DNA signal, from HbsU-mTurquoise2, showed an increased condensation at the origin and a gradual decrease towards the terminus (Fig. 6.3F, G – left). The BsSMC-mGFP intensity, however, did not linearly scale with the DNA signal, but rather had a 1.6-fold increase at the origin compared to the average signal along the chromosome (Fig. 6.3F, G - middle), while the signal also gradually decreased towards the *ter*. A decreasing signal from origin to terminus can be expected if BsSMC is loaded at *ori* by ParB [52,54,59] and removed at the *ter* by XerD [61], while BsSMC exhibits a finite rate to dissociate from the DNA. Such a distribution was captured previously by ChIP-seq [62], which was interpreted as stochastic unloading of BsSMC proteins along the chromosome arms [7,62]. In some cases, a secondary BsSMC focus was visible that did not correlate with the ParB location (Fig. 6.3G). ParB signal showed a pronounced peak near the tip of the chromosome and close to zero intensity signal along the rest of the contour length (Fig. 6.3F, G – right). Interestingly, while we did not observe that the intensity of ParB correlated with the amount of DNA within the main cluster (Fig. S6.13A), we did observe that higher SMC presence correlated with increased DNA content at the same site (Fig. S6.13B). This was true for both primary and secondary clusters, i.e., even away from the origin, an increase of SMC content correlated with an increase in the amount of local DNA (Fig. S6.13C).

6.2.5 Disruption of the BsSMC complex opens the crescent-shaped chromosome into a toroidal shape

Since BsSMC has been postulated to serve as the main connection between the left and right chromosome arms [7,23,24], we next tested for a potential reshaping of the chromosome after disruption of the BsSMC complex. For this, we constructed a strain with HbsU-mGFP as the chromosome label but included previously described ScpA-TEV3 [63] as well as P_{xyl}-*TEVp* (Table 1). ScpA is the kleisin subunit of the BsSMC complex that is a basic part of its ring-like structure, and it is essential in cells for fast growth [64]. The incorporated Tobacco Etch Virus (TEV) protease recognition site (TEV3) was within the ScpA protein (Fig. 6.4A), while the TEV protease itself was included at a different locus under a xylose-inducible promotor. This allowed us to controllably disrupt the BsSMC complex by opening the SMC-kleisin ring upon xylose addition, and subsequently observe the chromosome re-shaping (Fig. 6.4A). We demonstrated high specificity of SMC disruption that only occurred in the presence of both the TEV3 cleavage site and xylose (Fig. 6.4B).

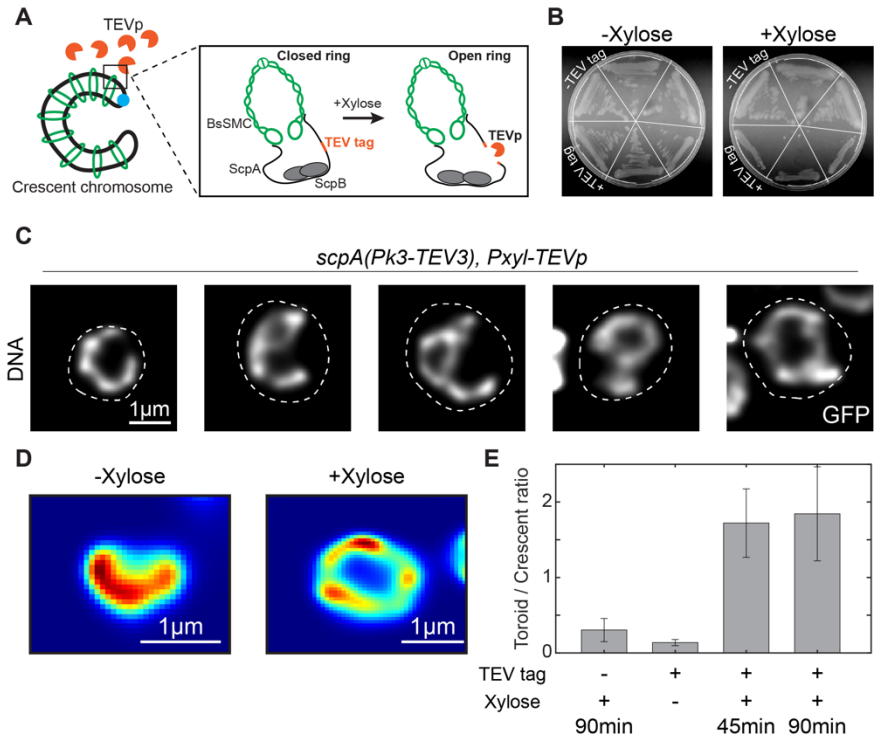


Figure 4. Disruption of BsSMC leads to the opening of the chromosome into a toroidal shape. A) *Graphical representation of BsSMC along the crescent-shape chromosome in strain BSG219 (dnaB(ts-134); hbsu-gfp; scpA(Pk3-tev3); P_{xyl}-TEVp). Zoomed region details the effect of the TEV protease that cuts the TEV cleavage site within the ScpA protein, which opens the BsSMC ring structure that supposedly is holding together the chromosome arms.* ***B)*** *Plating assay of strain BSG219 (depicted as +TEV) and its control BSG217 (depicted as -TEV) that is lacking the TEV cleavage site, in the absence (left) and presence (right) of 0.5% Xylose in the agar medium grown at 30°C.* ***C)*** *Selected examples of the disrupted chromosomes in strain BSG219 after 60 min of xylose (0.5%) in the liquid medium at 39°C.* ***D)*** *Representative examples of the crescent and toroidal chromosome shape with (right) and without (left) 0.5% xylose treatment.* ***E)*** *Relative ratios of toroidal to crescent chromosomes in four different conditions. See Supplementary Fig. S15 and Methods for details on these estimates. Each condition was performed using at least three biological replicates. Error bars represent 95% confidence interval.*

Expression of the protease resulted in dramatic macro-scale changes in the chromosome shape (Fig. 6.4C). Upon disruption of the BsSMC ring, the arms of crescent-shaped *B. subtilis* chromosomes opened. Sometimes, both arms separated entirely, resulting in a toroidal-shaped chromosome (Fig. 6.4C, S6.14). We observed that megabase-sized structural rearrangements of the chromosome occurred on the timescale of minutes, going from a well-defined crescent to a fully open state within ~30 min (Fig. S6.9A-B). These changes were never observed in the absence of xylose, nor in a control strain lacking the ScpA-TEV3 recognition site (Fig. 6.4D-E, and Fig. S6.14, S15). We further questioned whether the crescent shape of the chromosomes is affected in the absence of ParB proteins where SMC complexes can possibly load along the chromosome unspecifically. To examine this, we constructed a *ΔparB* strain containing the inducible P_{lac}-*sirA* replication halting system (see Methods). This strain showed an entirely disturbed chromosome shape and not the standard crescent-shaped chromosomes. Most chromosomes adopted a toroidal shape, similar to SMC depletion, or a rather undefined shape where the DNA was spread throughout all of the cell (Fig. S6.16). We were puzzled by cells that showed a persisting toroidal shape over time, indicating that there is a lateral compaction of the chromosomes even after the removal of SMC proteins. We hypothesized that lateral compaction of the chromosome might arise from a different source, namely transcription by RNAp which was recently proposed to underlie most bacterial chromosome structure in *E. coli*[65]. After treating the cells with Rifampicin, a potent transcription-blocking agent, we observed that the chromosomes in the expanded cells lost their compact crescent-shaped structures and exhibit either entirely dispersed or compacted structures (Fig. S6.17).

The results show that BsSMC proteins are indeed the sole agents that link the two arms of the circular chromosome of *B. subtilis* while transcription by RNAp is largely maintaining the lateral compaction of the chromosome. The data are also in line with the previously reported chromosome rearrangements upon BsSMC deletion or ParB deletion[7,23,24], whereupon chromosomes appeared to lose the second diagonal over time in ensemble Hi-C maps.

6.3 Discussion

Direct microscopy observation of bacterial chromosomes in single cells can reveal novel insights into the underlying organization and dynamics of the DNA within the nucleoid. In *E. coli*, for example, direct observation of chromosomes in expanded-volume cells did resolve the local DNA condensation in the left and right chromosomal arm as well as a lack of structure within the *ter* domain [15]. The approach furthermore yielded insights

into chromosome replication [29,32] and the role of the MukBEF SMC and MatP proteins [14,31] in chromosome organization.

Here, we applied a combination of cell-volume expansion with chromosome-copy control in *Bacillus subtilis* to directly resolve the structure of the chromosome with single-cell microscopy. This revealed that without a cell-boundary constraint, the unconfined shape of the chromosome is a crescent shape. Most of the time, the crescent chromosome was positioned with its convex side near the edge of the spheroidal cells. Our data showed only a weak correlation between the chromosome size and cell size (Fig. S6.4), suggesting that cell wall confinement in the spheroidal cells had only a minor effect on the crescent shape. While the crescent was the predominant chromosome phenotype, other shapes were also observed (Fig. S6.3) at smaller fractions (multilobed ~24%, compacted ~13%) which could arise from multiple chromosomes and not yet fully expanded chromosomes after the cell expansion, respectively. We found that the crescent shape was stably maintained over long time periods (at least 45 min) while still freely moving in the cell volume (Fig. S6.14B).

Our data show that the shape of the nonconfined *B. subtilis* chromosome is a crescent shape (Fig. 6.1, 2). This well compatible with the previous models where Hi-C data suggested a crescent shape or an S-shape[7]. This crescent shape chromosome is likely deformed when confining it to the rod shape of the bacterium. Previous studies indicated that the chromosome adopts a helicoidal structure in cylindrical cells [6,7]. As the crescent-shape chromosome needs to be tightly compacted within the cylindrical cell shape, introduced helicity might be the most efficient way for the compaction while still regulating origin and terminus regions to be at different cell poles.

The crescent shape may well be the predominant chromosomal shape in bacteria that possess an SMC-ScpAB complex that loads at the origin of replication. Multiple Hi-C studies point towards similar chromosomal features in various bacteria possessing a SMC-ScpAB/ParABS systems (e.g., ParB origin localization, a condensed origin, zipped chromosomal arms) [20,24,26-28,66]. By contrast, *E. coli* chromosomes do not adopt these features in Hi-C maps [67], while they also do not possess a ParABS system like most bacteria [68]. Interestingly, we found that acute knock-down of BsSMC resulted in large-scale chromosome reorganization where the left and right chromosomal arms lost proximity and the chromosome opened into a toroidal shape (Fig. 6.4, S9 and Refs. [7,24]), which is very reminiscent of the chromosome shape in widened *E. coli* cells [15]. While the two chromosomal arms thus are mutually connected with BsSMC complexes, one may ask what maintains the compaction of the individual chromosome arms. Recent work in *E. coli* suggests that such a compaction in chromosome interaction domains is

largely induced by transcription[65], which we observed in our rifampicin-treated cells too (Fig. S6.17). The stable crescent shape in *B. subtilis* chromosome could thus be maintained by a combination of the arm-zipping action of SMC proteins and the continuous presence of supercoiling arising from the interplay of RNA polymerases and topoisomerases.

The DNA density along the chromosome was found to be very inhomogeneous. Our work expands on previous work by the Nollmann and Koszul labs who used Hi-C in combination with super-resolution microscopy to resolve the chromosome structure including its underlying domains [7]. They observed that the replication origin contained a dense DNA region that they termed High-Density Region (HDR). Our method, which resolved the full chromosome structure in expanded single cells, also observed an increased DNA density in the origin region at the tip of the crescent-shaped chromosome. In many instances (67% of cells), the condensed DNA cluster close to origin contained even over 40% of the entire genome within it (Fig. S6.8). The increased density in the origin region may arise from multiple underlying biological processes. First, ParB proteins were proposed to condense the DNA near the *ori* site and form a partition complex by bringing multiple *parS* sites during the initial steps of chromosome segregation [7,50,69,70]. Second, ParB proteins have been proposed to recruit BsSMC proteins to the origin of the chromosome where a juxtaposition between the chromosomal arms is initiated [23,52,54,59]. As our data indeed show an increased BsSMC content near the origin of replication, higher DNA density regions may result from an increased frequency of chromosome folding by BsSMC proteins. Third, the origin-of-replication genomic section contains highly transcribed genes in most bacteria, including *B. subtilis* [71]. These genes are often accompanied by a high degree of supercoiling and plectoneme formation. This can further increase DNA condensation within the origin region compared to the rest of the chromosome. Maintaining the origin region in a condensed state could have important implications for chromosome segregations via entropic forces [72,73]; because highly condensed regions will be preferentially pushed towards the cell periphery in a cylindrical cell [73]. Accordingly, deletions of BsSMC and ParB proteins mostly result in delayed origin segregation [63,74] and aberrant chromosome segregation in *B. subtilis,* as nascent origins would stick together and reduce segregation fidelity [52,54].

Our data also showed an enrichment of BsSMC at the origin region (Fig. 6.3). This is in agreement with ChIP-seq data[7,23,24,75] and indicates that only a fraction of the total amount of BsSMC complexes on the chromosome are actively zipping the chromosomal arms, while the largest fraction resides at the origin close to ParB. The enrichment in the origin region might be exacerbated due to SMC:SMC collisions caused by an increased

SMC:chromosome ratio due to the replication halting condition [76,77]. Although a recent biochemical study points to the direct interaction between ParB and BsSMC proteins [59], the precise mechanism of BsSMC recruitment to the origin and its subsequent release to zip the entire chromosome is not yet well resolved. An observation that a higher local amount of SMC proteins results in higher DNA content (Fig. S6.13), also hints to the fact that SMC proteins that are locally stalled or blocked still remain on the DNA condensing it locally.

Our study investigated the *B. subtilis* chromosome organization via direct live-cell imaging. The data revealed the intrinsic crescent chromosome shape and the distribution of ParB and BsSMC proteins within single cells, as well as a disruption of chromosome shape in single cells upon BsSMC knock-down. We observed that the origin of the replication is maintained in a condensed state even under non-confining conditions. The cell-shape manipulation imaging approach can be applied to other bacteria, allowing for single-cell real-time imaging of the chromosome and the dynamics of intercellular processes.

6.4 Methods

6.4.1 Strain construction

All strains were constructed using the homologous recombination-based cloning described in detail in Diebond-Durant et al[78]. In brief, we used a transformation of recombinant DNA to create *B. subtilis* strains at the *smc*, *scpA*, *parB*, *amyE*, *hbsu* and *thrC* loci by allelic replacement harboring natural competence induced by the stationary phase growth as well as starvation due to media depletion (1-2 h incubation in SMM medium lacking amino acid supplements) the same as described in detail Diebold-Durand et al[78]. We selected the new strains on SMG-agar plates in the presence of the appropriate antibiotic at 30°C for 16 h. We verified the correct genotype of single colonies by antibiotic resistance profiling on solid agar plates, colony PCR, and locus sequencing and stored the correct clones at -80°C.

Strains with modified smc alleles were created as described in Ref [78]. In *Bacillus subtilis*, the *smc* gene is located in the operon containing *rncS-smc-ftsY* genes. To avoid potential adverse regulatory impacts on *ftsY* gene, the selection marker for *smc* modifications was positioned downstream of the operon, precisely after *ftsY*.

6.4.2 Bacterial growth conditions

Prior to all experiments, bacterial strains stored at -80°C, were streaked on a 1xNA (Oxoid) agar plate (1.5% agarose). Plates were incubated at 30°C for 10-16 h, overnight to obtain single colonies, and used for a maximum of 2 days after that. One day before the experiments we picked single colonies and incubated them in 5 ml liquid osmoprotective medium for 10-16 h, overnight. For all experiments performed, we examined at least three separate individual colonies which represent biological triplicates,and used them under the same procedure. Osmoprotective media (from now also referred to as SMM+MSM) used in this study were modified from Kawai et al. and composed of 2×MSM (40 mM magnesium chloride, 0.2 M-1 M succinate, 40 mM maleic acid, 0.2% yeast extract) mixed in 1:1 relation with 2xSMM (0.04% magnesium sulphate, 0.2% sodium citrate dehydrate, 0.4% ammonium sulphate, 1.2% potassium dihydrogen phosphate, 2.8% dipotassium phosphate) and supplemented with 0.2% L-tryptophan, 1 µg/ml ferric ammonium citrate, 0.1% glutamic acid, 0.02% casamino acids (Bacto™), 1 mg/ml L-threonine. We supplemented the overnight cultures with 5 µg/ml kanamycin, 1 µg/ml erythromycin, 5 µg/ml chloramphenicol, 100 µg/ml spectinomycin where applicable (see Table 1), but the cultures on the day of experiments were not exposed to selection antibiotics. We made 2xMSM solutions with the following range of succinate concentrations 0.2 M, 0.4 M, 0.6 M, 0.8 M, 1 M, for the purpose of

testing osmoprotective conditions with the sugar concentration ranging from 100-500 mM (see Fig. S6.1). On the day of the imaging experiments, we diluted the overnight cultures 50x in the total of 10 ml osmoprotective media. We grew the cultures for 3 h (30°C, 200rpm orbital shaking), until they reached the early exponential phase, and then induced replication halt either by supplementing with 2 mM IPTG or moving them to 39°C and 200rpm orbital shaking, depending on the strain, for a total of 30-180 min depending on the experiment. In the case of TEV protease expression experiments using the strains BSG217 and BSG219 (Table 1), we added 1.5% xylose 45 min before imaging for timecourse imaging (Fig. 6.4). For the real-time imaging of BsSMC degradation we included the xylose (at 1.5% final concentrations) into the agar pad just before imaging.

6.4.3 Conversion to L-form spheroid cells

After growing the bacteria for a targeted time of replication halting, we subjected the shaking bacterial cultures to lysozyme treatment. We made a 100 mg/ml fresh stock of lysozyme on the day of the experiment by mixing Lysozyme from chicken egg white (Sigma-Aldrich) with 1xPBS (140 mM NaCl, 10 mM phosphate buffer, and 3 mM KCl, pH 7.4, Phosphate Saline Buffer, (Sigma-Aldrich)) and kept it on ice for the duration of that day (4-6 h). Depending on the temperature of the cell growth we added the lysozyme to a final concentration of 400 µg/ml either 20 min, when grown at 39°C, or 30 min before, when grown at 30°C.

6.4.4 Fluorescence imaging

After cell growth and necessary treatments in liquid culture, we transferred ~3 ml of the liquid cell culture to the 35 mm glass bottom dish (MatTek), which we beforehand passivated with 100 µg/ml UltraPure™ BSA (Invitrogen) for 15-20 min. We specifically avoided using any pipetting steps after the lysozyme treatment to maintain the integrity of spheroidal cells and prevent them from lysis due to shear forces. We then centrifuged the imaging dishes custom-made holders at 400g for 4 min in a swingout centrifuge with 96-well plate holders (Centrifuge 5430 R, Eppendorf). We removed residual supernatant containing non-adherent cells by pipetting at the edge of the dish and placed an agarose pad (~ 4 x 4 mm) containing 1x osmoprotective medium (lacking yeast extract) and 0.2% low melting agarose (Promega, Madison, USA) on top of the glass bottom. Note that yeast extract needed to be removed from the medium used for making the soft imaging agar pad due to residual background fluorescence in the green channel (488 nm). We placed a small 11x11 mm glass coverslip on top of the agar pad to assure

the cells were not floating in the medium during imaging due to liquidity of 0.2% agarose and to prevent premature evaporation and drift.

We carried out widefield Z-scans out using a Nikon Ti-E microscope with a 100X CFI Plan Apo Lambda Oil objective (NA=1.45). The imaging stage was maintained at 39°C for experiments using temperature-sensitive mutants, and at room temperature for mutants affected by IPTG expressing of SirA protein. We excited DAPI using SpectraX LED (Lumencor) filter cube with λ_{ex}/ λ_{bs}/ λ_{em} = 363–391/425/435–438 nm, GFP and SYTOXGreen using filter cube with λ_{ex}/ λ_{bs}/ λ_{em} = 485-491 nm/506 nm/501-1100 nm, and mScarlet and STYOXOrange using filter cube with λ_{ex}/ λ_{bs}/ λ_{em} = 540–580/585/592–668 nm. We used an Andor Zyla USB3.0 CMOS Camera to collect the fluorescent signals. We took 9-11 Z-slices of step size l = 200 nm, which accounts for a total of 1.8-2.2 µm of scanning volume, that we fed into the deconvolution software (see below).

6.4.5 Solid agar plating assays

For testing the growth differences in presence/absence of xylose in the strains carrying *scpA(Pk3-TEV3)::specR* locus (Fig. 6.4B), we used a standard LB-agar (1.5% agarose). As described above, we grew the strains on separate plates carrying the selective antibiotic (here 5 µg/ml chloramphenicol and 100 µg/ml spectinomycin) one day before the experiment. We picked three single colonies from each plate and re-streaked them in a radial orientation on the plate containing LB-agar or LB-agar + 1.5% xylose. The plates were left to incubate at 30°C for 16 h, after which we imaged them on a Gel imager (BIO-RAD Chemidoc™).

6.4.6 Growth curves

For monitoring bulk growth (Fig. S6.6), we first grew the strains in the selective media overnight, as mentioned previously. On the day of the experiment, we diluted the overnight cultures 40x in the fresh SMM+MSM medium and grew them until the OD reached ~0.2 - 0.3. We then again diluted the cultures to the final OD of 0.01 and distributed in 96-well plate (Nunc), with the final volume of 170 µl. The plates were loaded into an Infinite 200Pro fluorescence plate reader (Tecan, Männedorf, Switzerland) and incubated at 30°C with the orbital shaking (2.5 mm amplitude) for a period of 24 - 48 h. Cell density was measured at 600 nm at 15 min intervals. We performed all experiments using at least biological triplicates, and in some instances more.

6.4.7 Quantitative RT-PCR on genomic DNA

To ensure the replication halt by expressible *sirA* gene, we performed qPCR using [PrimeTime, IDT]. We grew the bacterial cultures BSG4610 and BSG4595 under the same conditions and media mentioned above. We grew bacterial samples in biological triplicates for both treated and untreated sample (with or without IPTG). We induced the replication halt by adding 2 mM IPTG for 120 min. Following this incubation, all samples were centrifuged (13000g, 2 min) to collect cells and remove the surrounding medium. We next extracted the genomic DNA using [kit name] following the standard protocol for gram positive bacteria supplied with the kit.

To perform qPCR we used the premixed primer pairs that bind within the *ori* (Fw:CGAGCTGGTTCCTACAATATCA, Rev: ATGACGGCGGACAATCAA, with the qPCR probe: **FAM 520, ZEN / Iowa Black™** AGAGAGCGCTTGAAGCAGTAAAGCA) and *ter* region (Fw: GAACCTAATGTTAAGGAAGAAAGCC, Rev: GGACCAGTTAGGGCGATATTT, with the qPCR probe: **FAM 520, ZEN / Iowa Black™** CCTAGCAATGATGTCGACACTGATGGA) of the *B.subtilis* chromosome. The PrimeTime™ Gene Expression Master Mix, primers and qPCR probes were thawed on ice for 10 min. We then briefly vortexed the reagents and centrifuged them to collect all liquid at the bottom of the tube. Primers and probes were ordered premixed, upon arrival we spun the mixtures at 750g for 30 s. Dissolved these mixtures in 100 µl of TE buffer to obtain a 20x solutions. We mixed the solutions in water (final concentration of 9 mM of each Fw and Rev primer and 2.5 mM of the qPCR probe), together with the PrimeTime™ Gene Expression Master Mix (1x) as well as 3 ng of each of genomic DNA sample for the final volume of 20 µl for the reaction. Mixtures of primer pairs and probes for *ori* and *ter* were used in separate reactions. We initially set the sample to 95°C for 3 min. Following this step we set the amplification for 40 cycles (denaturation 95°C for 15 s, annealing and extension 60°C for 60 s). We obtained the primer efficiency for both *ori*-primer and *ter*-primer pairs at >91%. The *ori*:*ter* ratios were determined per individual technical triplicate sample (for each of biological triplicates) and represented in Fig. S6.7, S6.11.

6.4.8 Deconvolution microscopy

For deconvolution microscopy we used Huygens Professional deconvolution software (Scientific Volume Imaging, Hilversum, The Netherlands), using an iterative Classic Maximum Likelihood Estimate (CMLE) algorithm. We measured the point spread function (PSF) experimentally by using 200 nm Tetraspeck beads (Invitrogen) and the recommended Huygens Professional guidelines (*https://svi.nl/Point-Spread-Function-*

(PSF)). Stacks of 9-11 Z-slices were fed into the Huygens Professional software and we deconvolved each signal channel separately.

6.4.9 Structured illumination microscopy imaging

For SIM microscopy, samples were prepared as previously described, except using two rounds of centrifugation with 3 ml cell culture in order to obtain higher cell density to accommodate for the smaller camera FOV. We used a Nikon Ti-E microscope with an AiRSIM module and a 100X CFI Apo Oil objective (NA=1.49). We used a 3D-SIM option with the 5 pos x 3 angles for imaging our live samples, and a Z-stack of 11 positions with l = 200 nm in between. NIS-Elements (version 5.2.1) software was used for image reconstruction where we carefully adhered to the Nikon N-SIM reconstruction guidelines and parameters to avoid reconstruction artefacts (Fig. S6.5).

6.4.10 Image processing and analysis

For obtaining the cell outlines and counting fluorescent foci within each cell, as well as for measuring distances between ParB-mScarlet and BsSMC-GFP foci within each cell, we used the image segmentation and analysis software Oufti [79]. We obtained subpixel precision *B. subtilis* cell outlines using the cellDetection tool in Oufti with the parameters shown in Table 2. We used the detectSignal tool for fluorescent foci detection of the ParB-mScarlet and BsSMC-GFP signals using the selection parameters shown in Table 2.

We used custom-written MATLAB scripts, modified from the original publication of Kaljevic *et al*.[80], to extract the fluorescent foci positions, count the number of foci per cell, and determine the distances between foci in each channel. These scripts are open-source and available online (doi.org/10.5281/zenodo.7615509).

For a systematic and detailed analysis of the chromosome shape, shown in e.g. Fig. 6.2 and Fig. 6.3, we used home-developed Matlab code based on earlier work from Wu et al[15]. The image processing covered the following elements:

Selection - First, we used Fiji/ImageJ to user-select ROIs around round cells based on the phase image alone, yielding typically ~10^2 cells per field-of-view (FOV). This ROI list was imported in Matlab. For each ROI, we obtained a mask outlining the cell wall from the wide field image. Within this cell mask, we analysed the signals of the other colour labels, depicting the patterns representing DNA, SMC, and ParB.

Screening - For a randomly chosen FOV, the selected round cells displayed a large variety of patterns and artefacts and sometimes included misdetections due to the thresholding. The latter were screened out by a simple cell roundness criterion.

Furthermore, multiple ParB spots could lie in different focal planes such that only one was observed per focal plane. To make sure we selected single chromosomes, we applied a projection of maximum intensity along the defocus stack and accepted only those cells that had a single ParB spot appearing in maximum projection.

Backbone pattern analysis - Here, we made use of the characteristic shape of the chromosome pattern. As seen in-plane, the patterns formed crescent arcs that broadly followed the inside cell wall over a broad annular section of 90-180 degrees. As described before, such an arc-like structure could well be described in an annular coordinate system, where a 'backbone' centre line runs over the chromosome arc[15]. Using this backbone as a length axis, we sampled the relative intensity of the respective labels per unit annular section along this length. To compare many cells, we performed this sampling over a fixed, representative length, starting at the angle where the ParB signal maximizes, since this maximum represents the location of the *ori* site on the chromosome. We thus created intensity vs distance profiles for all labels. Notably, the cells with the crescent-shape chromosome may appear in a regular fashion or lie upside down. Therefore, starting from the *ori* location, the crescent may point clockwise or counter clockwise. To compare all cells, we flipped the profiles such that for all, the crescent intensity moved towards positive length values. We collected all these profiles in demographs shown in Fig. 6.2I and Fig. 6.3G. Each line in a demograph represents a heatmap of the DNA density profile from the origin (position of 0μm) to the end of the chromosome. These lines are stacked for all cells (y-axis) to make the common trends well visible.

Foci and cluster analysis - Following an earlier described method [15], we described the measured intensity patterns as a sum of clusters. Here, the chromosome pattern was described as a group of separate clusters. Each of these clusters was then described with a sub-group of psf-limited spots. For this sub-group, any of the spots was within one psf of at least one other. This resulted in a smooth, compact shape of this cluster. On the other hand, all spots in another cluster would be further away than one psf, so that there was always a distinguishable gap between each two neighboring clusters. In this way, the sometimes complicated 'blob patterns' can be described in a compact way as a limited set (typically, 4-5 per cell) of optically separable clusters, with each of these clusters coming with a particular xy position and a relative intensity (as compared with the intensity counted in the entire cell area). In the case of a compact focus, the cluster description simplifies in just one psf-sized spot. If a single cluster extended beyond one psf, such as the somewhat smeared-out spots observed for the ParB label, this approach still provided us with an intuitive description of the amount of fluorescence associated with one ParB spot. Finally, the xy positions of the cluster analysis can be correlated to

the above-described backbone length axis, allowing to readily and quantitatively compare the relative intensities of mutually associated clusters of DNA, ParB and SMC (Fig. 6.3).

6.4.11 Chromosome shape selection

We were unsuccessful in obtaining the ParB-mScarlet tag in strains BSG217 and BSG219, containing HbsU-tag, P_{xyl}-*TEV*p and/or ScpA-TEV3 in multiple cloning attempts. While we cannot distinguish between single and partially replicated chromosomes, due to strain construction issues, we attempted to quantitatively distinguish between torus-shaped chromosomes and crescent-shaped chromosomes in the presence of 0.5% xylose. For this, we performed the following manual user selection. We collected one image from four different samples (Fig. 6.4E, S15), which describe four experiments with different expected outcomes. Each of these was intensity thresholded to detect ROIs with separated DNA patterns based only on the continuous fluorescent signal. Next, a randomly picked ROI, containing a signal from a single cell, was presented to a user for classification of this pattern. The user could choose from one of four categories (toroid, crescent, compact, other/undefined) without knowing from which original image the ROI was taken. This was done for a series of 100 picks each, with no ROIs being presented to the user more than once within this series. To obtain an estimate for sampling variation, we repeated this series 20 times per user for a total of 2000 selected ROIs. To evaluate possible user bias, the procedure was done independently by two users (MT and JK) shown in Fig. S6.15. We then traced back the described ROIs (in one of those four categories) to the original images and plotted the selection distribution shown in Fig. 6.4E and Fig. S6.15.

6.4.12 Chromosomal loci counting – *ori* and *ter*

To quantify the *ori*:*ter* ratio (Fig. S6.7) and ensure that the replication-halted cells had a single chromosome, we imaged the strain BSG5522 under the same conditions as previously mentioned. We localized the cell outlines and positions of *ori* and *ter* loci using Oufti [79] and the parameters shown in Table 2. We performed additional filtering to account for the low signal-to-noise ratio in the *ter* signal channel (TRP-GFP), caused by the presence of only a few proteins at *Ter* sites,. We removed the detected spots that contained less than 15% of the total signal present in the cell, using custom-written MATLAB software (see *Data and materials availability*).

6.4.13 Visualization and representation

All fluorescent and phase images were visualized in the open-source image-analysis software Fiji[81]. We used a calculated microscopic pixel size of 65.35 nm/px in all images for scale bar creation. Adobe Illustrator 2020 was used for visualization and manuscript figures. After reconstructing the SIM microscopy images, we used SIMcheck software package for visualization [82] (Fig. S6.5) and a Fiji in-built function "3D project" to create a 3D reconstruction of the crescent chromosome (Movie S1), as well as the plug-in 3D viewer to create the isosurface plots of the same image (Movie S2). The same was used to visualize the deconvolved 3D stacks in Movie S3-S4.

6.5 Supplementary data

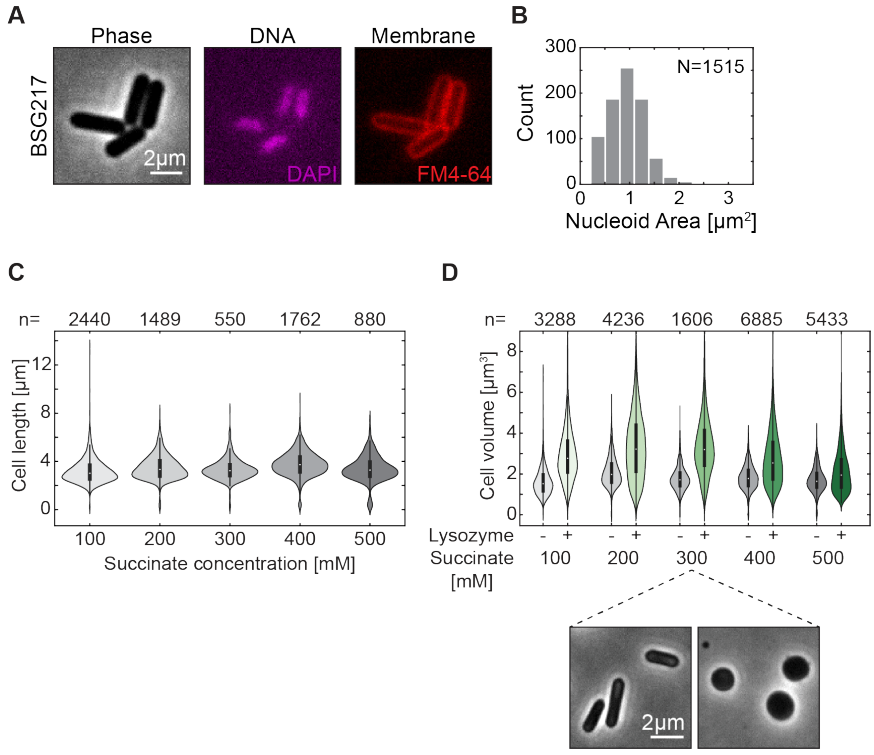


Figure S6.1. Transformation from cylindrical to spherical cell shape leads to an increase in volume. A) *Phase and fluorescent images of the BSG217 strain (see Table S1), with labelled DNA and cell membrane, after replication halt at 37°C for 60 min.* ***B)*** *Nucleoid area in replication halted cells shown in A). Mean nucleoid length and width were l=1.28 ± 0.49 μm and w=0.72 ± 0.09 μm (mean ± std, N = 1515).* ***C)*** *Longitudinal cell length of rod-shaped Bacillus subtilis cells (strain BSG217) grown in SMM+MSM medium of different osmolarities.* ***D)*** *Cell volumes of rod-shaped and spherical cells (see Methods and ref 2) grown in the same SMM+MSM medium of different osmolarities. Gray data represent samples that were not exposed to lysozyme treatments; green data represent cells exposed to lysozyme treatment (see Methods).*

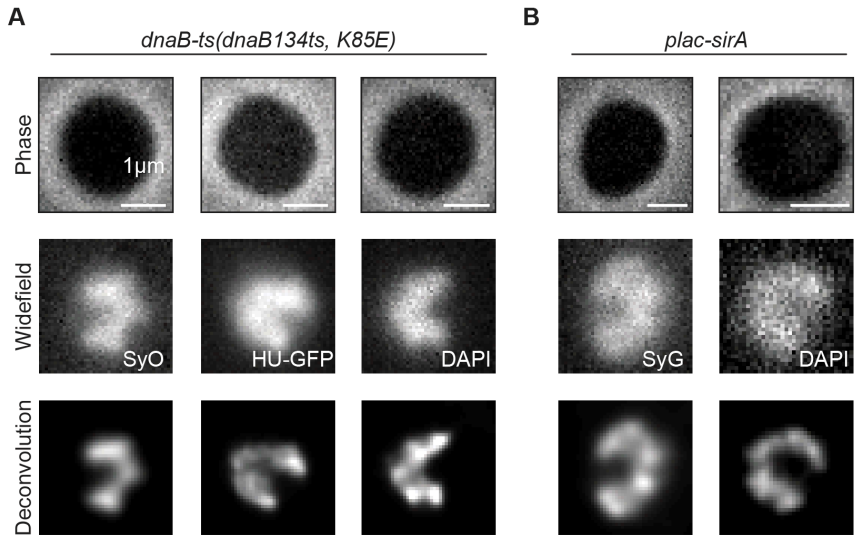


Figure S6.2. Bacillus subtilis chromosome adopts a crescent shape regardless of replication halt strategy or DNA-visualization dye. A) *Phase and fluorescent images of crescent chromosomes in BSG217 cells after lysozyme treatment (400 µg/ml for 20 min) using different DNA dyes (SYTOXOrange (250 µg/ml), GFP-fusion, DAPI (3 µg/ml)). Top to bottom – phase image of spherical bacterial cells, widefield fluorescence image, and the same images after deconvolution via Huygens Professional software (see Methods).* ***B)*** *Same as A) for the BSG4595 strain that is replication halted using 2 mM IPTG for 90 min.*

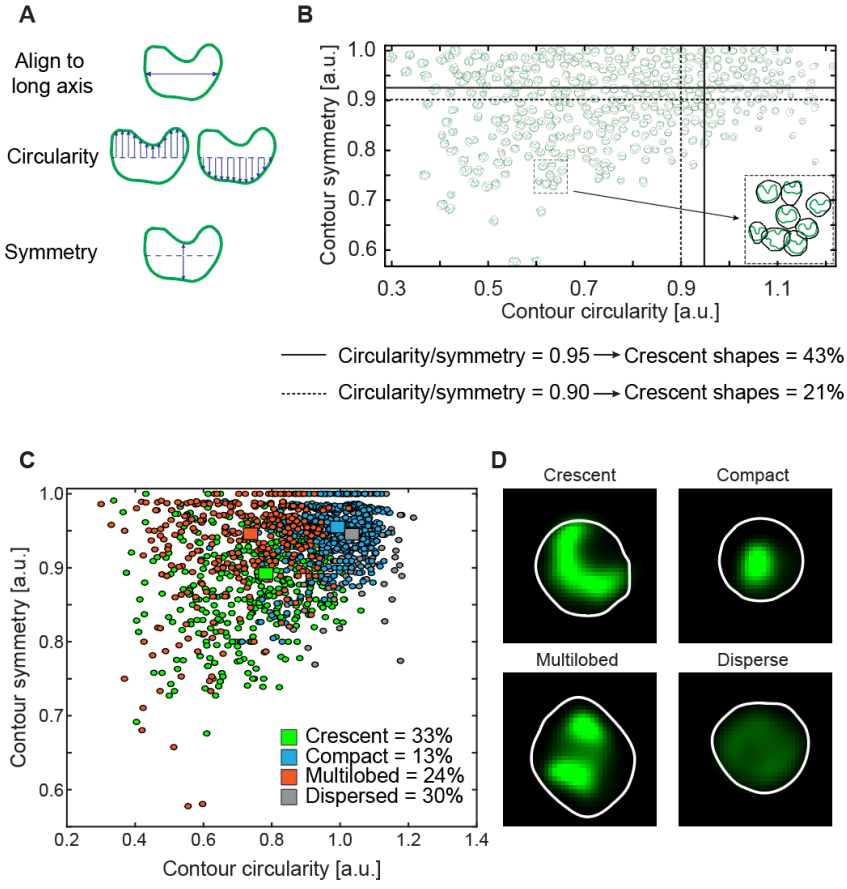


Figure S6.3. Quantification of crescent-shaped chromosomes in spherical cells that were exposed to hypoosmotic medium. ***A)*** *Graphical representation of the stepwise selection of crescent chromosomes. Initially selected chromosomes as Oufti objects (see Methods) are positioned along their long axis. Then a 'circularity estimator' is applied that estimates the number of equidistant points in the top and bottom of the mid-axis. Finally, a 'symmetry estimator' measures the relative difference in the distance from the midpoint to the mid-axis.* ***B)*** *Cells plotted by their circularity and symmetry. Green line represents the Oufti object outline (which characterizes the chromosome contour)*[2]*. n = 1321. Selection at threshold of 0.90 (dashed line) or 0.95 (full line) for the ration of circularity/symmetry results in 21% or 43% crescent shapes, respectively.* ***C)*** *Blinded manual classification of the chromosome shape shown in B).* ***The*** *colored squares represent a mean value of symmetry and circularity estimates for the corresponding population.* ***D)*** *Fluorescent images of the different shapes obtained in C). White line represents cell outline based on a brightfield image.*

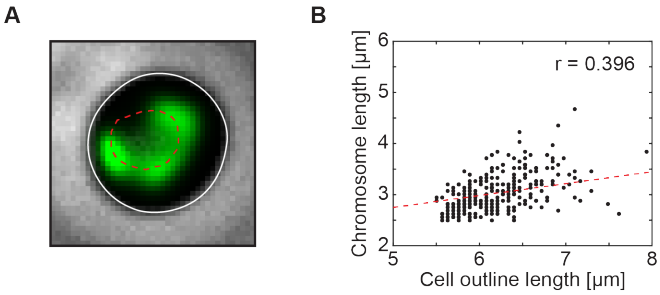


Figure S6.4. Crescent chromosome size is only weakly correlated with final cell size. ***A)*** *The micrograph shows the cell outline in white full line, and crescent chromosome contour in red dashed line.* ***B)*** *Chromosome contour length versus cell-boundary contour length in spherical cells BSG4595. Black dots represent individual data points. N = 292, r = 0.3965.*

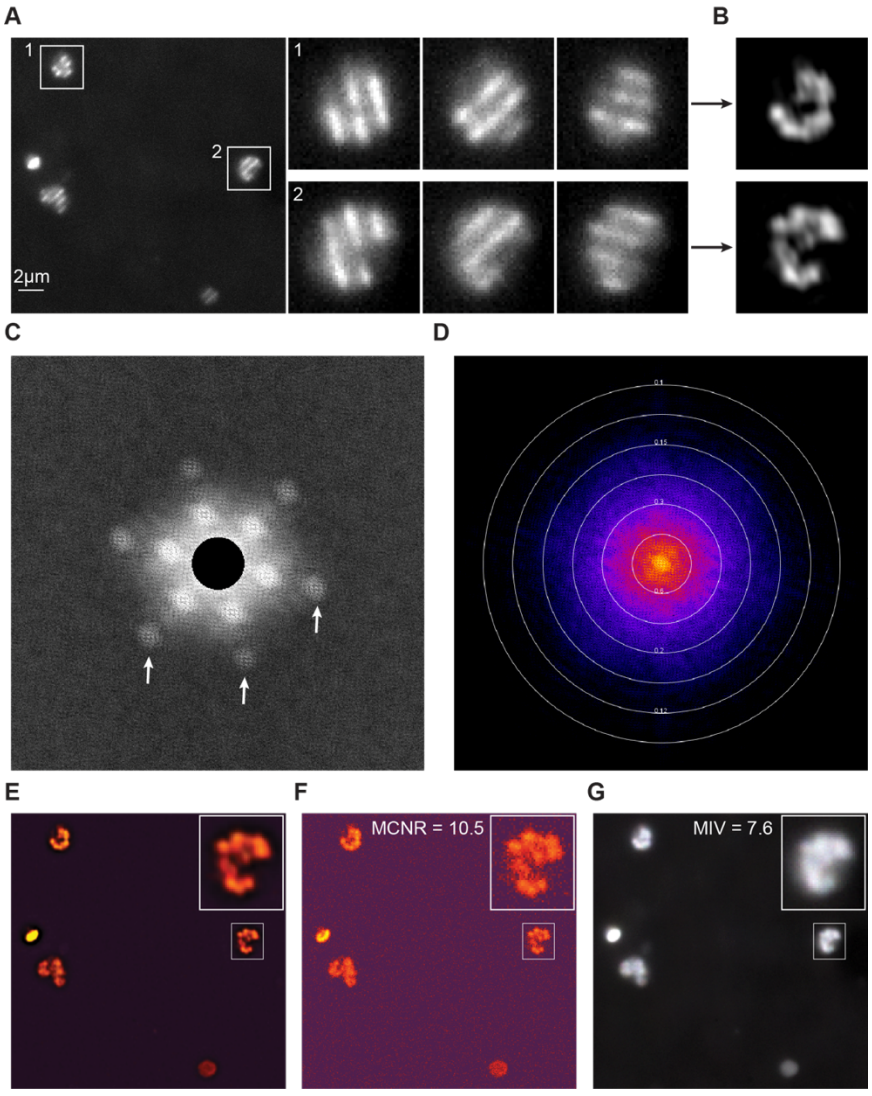


Figure S6.5. Structured Illumination Microscopy image controls. A) *Individual frame from the raw image sequences of 5x3 imaging (position x angle) in the SIM microscope. Two cells of the strain BSG217 (see Table S1) are zoomed and shown with the raw image in the three frames.* ***B)*** *Reconstructed SIM image of these individual cells.* ***C)*** *Fourier projection of the raw data of the full image (in panel A) in reciprocal space. The image shows the first and second order point of high frequency in all the angles (white arrows), which we used as mandatory to pass the quality control.* ***D)*** *Fourier-space image of the reconstructed image overlaid with concentric circles showing corresponding the spatial resolution (in µm). Based on the image, we estimate a resolution of ~0.16 µm.* ***E)***

Modulation Contrast map for reconstructed bottom image from panel A-B). ***F)*** *Same as in E) but for raw image. The MCNR (modulation contrast-to-noise ratio) passes the SIMCheck quality control*[3]*.* ***G)*** *Motion and illumination variation (MIV) in different angles and frames. The gray image with an absence of colors indicates a high stability and low variation between angles during illumination in the SIM imaging, which ensures that the total imaging sequence for one image is faster than any visible movements of the B. subtilis chromosome.*

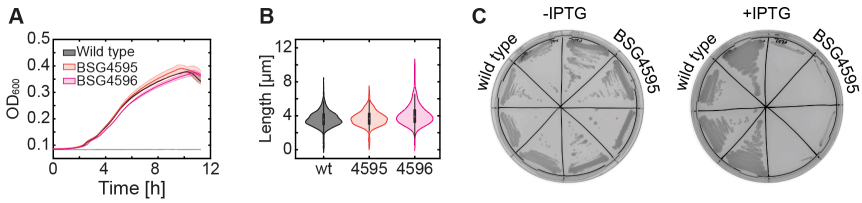


Figure S6.6. Bacterial growth and phenotype is not affected by genetic edits to parB and amyE loci. A) *Tecan plate reader growth curves (see Methods) for B. subtilis 1A700 strain and BSG4596, BSG4595 strains, carrying P_{lac}-sirA and P_{lac}-sirA + parB-mScarlet (used in extensive quantification in Fig. 6.2), respectively.* ***B)*** *Longitudinal cell length in phase images for the wild-type strain and P_{lac}-sirA containing modified strains.* ***C)*** *Plating assay showing replication halt in the absence (left) or presence (right) of 2 mM IPTG for the strain BSG4595.*

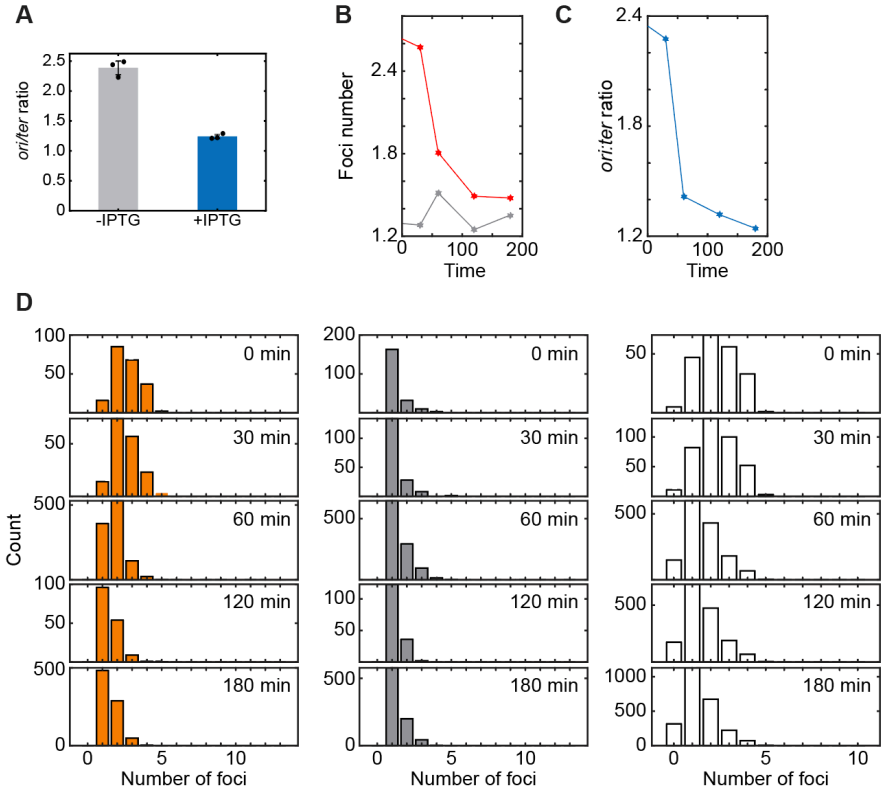


Figure S6.7. Chromosome replication is efficiently halted upon SirA expression. A) *qPCR determination of ori:ter ratio in the strain BSG4595. Gray bar shows an untreated sample, and the blue bar shows a sample treated with 2 mM IPTG for 2.5 h. Black dots represent and average value of a technical triplicate, for each biological triplicate. Both conditions were done in biological triplicates with technical triplicates for each of the colonies. Error bars represent a standard deviation from three biological triplicates.* ***B)*** *Number of ori (red) and ter (gray) foci in the strain BSG5522 upon replication halt via IPTG (2mM).* ***C)*** *Average ratio of ori to ter in the cell population.* ***D)*** *Timecourse measurement of the number of ori (orange), ter (gray) 0-180 min after the addition of IPTG (2mM). Individual ori-ter ratios are presented on the right.*

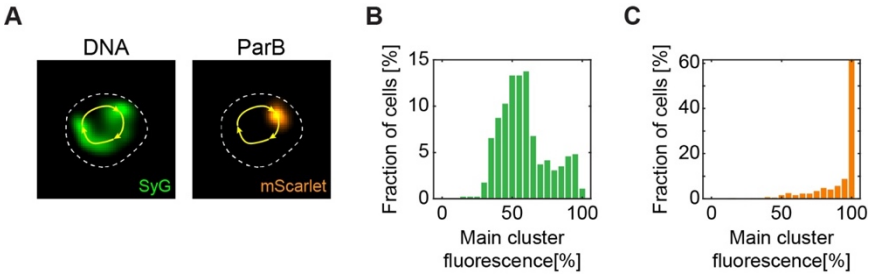


Figure S6.8. DNA and ParB clusters adopt different fractions of the total signal. A) *Representative fluorescence images of the crescent chromosome and ParB focus (cf. Fig. 6.2) in the strain BSG4595. Dashed white line represents cell outline, and yellow arrows represent a sketch of the contour line measurement along the crescent chromosome.* ***B)*** *Relative DNA presence (based on fluorescent signal, see Methods) in the main cluster compared to the total DNA signal within the crescent chromosome.* ***C)*** *Same for the ParB signal.*

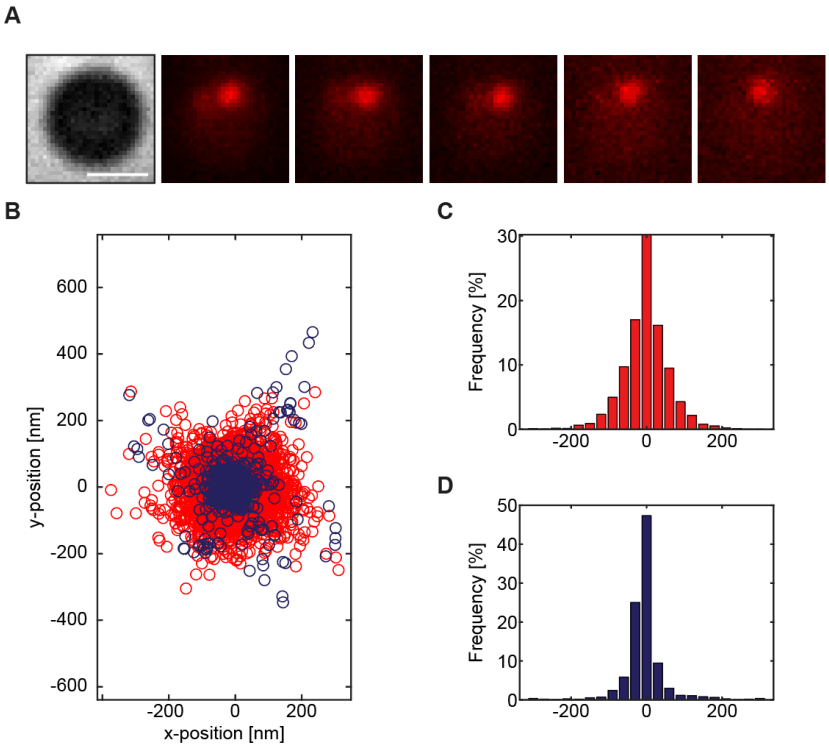


Figure S6.9. Dynamic movement of the origin of replication. A) *Timelapse imaging of ori (ParB-mScarlet) movement within the expanded cell. Scale bar – 1 µm. Frame rate – 1 s.* ***B)*** *Tracked positions of ParB-mScarlet signal in all cells (red, N = 643) and marker cells (purple, N = 101).* ***C)*** *Distribution of the ParB-mScarlet signal relative to the initial position (x = 0 nm point) at frame zero. Full-width half maximum – FWHM = 89 nm.* ***D)*** *Same as in C) but for tracked cells (FWHM = 56 nm).*

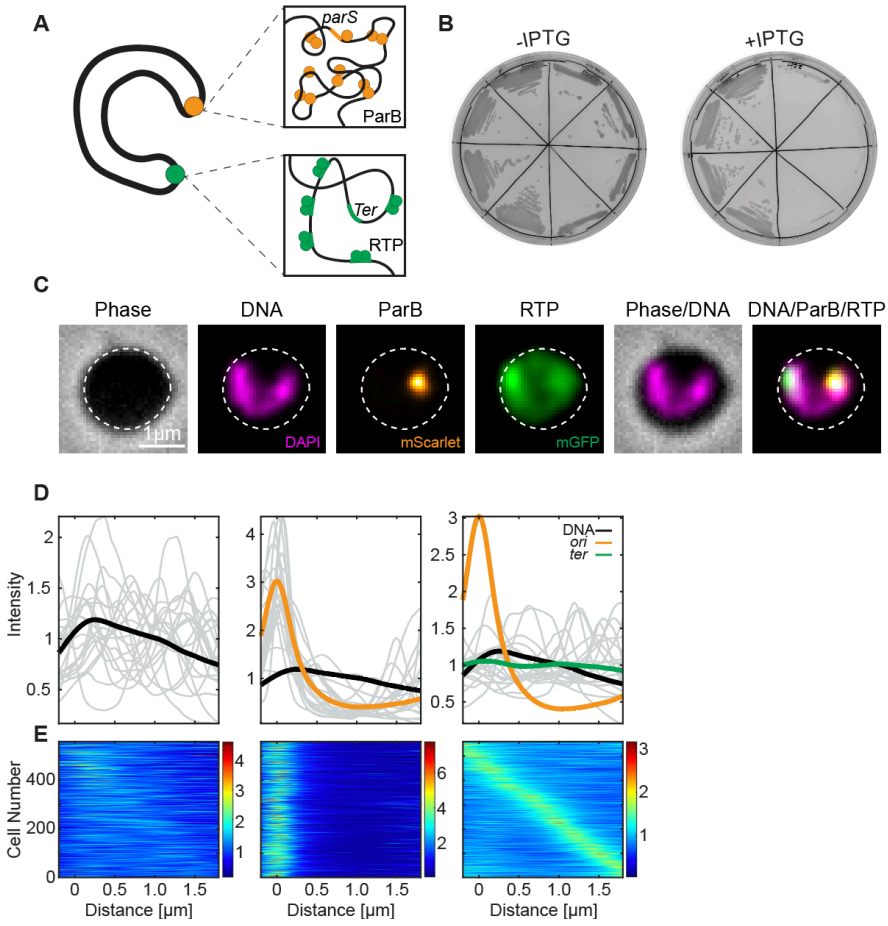


Figure S6.10. Origin and terminus of replication localize at different ends of the crescent chromosome. A) *Graphical representation of the crescent-shape chromosome and the positions of two main chromosomal loci – ori and ter.* ***B)*** *Plating assay showing replication halt in the absence (left) or presence (right) of 2 mM IPTG for the strain BSG5522.* ***C)*** *Images of bacterial strain BSG5522 strain after lysozyme (400 μg/ml) treatment for 30 min. Scale bar = 1 μm.* ***D)*** *DNA intensity along the contour of the chromosome. Black, orange and green line shows the average normalized intensity obtained from all cells (N=559) for fluorescently labelled DNA, ParB and RTP signals, respectively. Gray lines display arbitrarily chosen individual examples. The position of the ParB focus is indicated on top (defining the 0 μm position).* ***E)*** *DNA density along the chromosome in all individual cells starting from the 0μm position which represents ParB/ori. Colorbar represents the fold-increase. Cells are ordered from top to bottom in terms of contrast.*

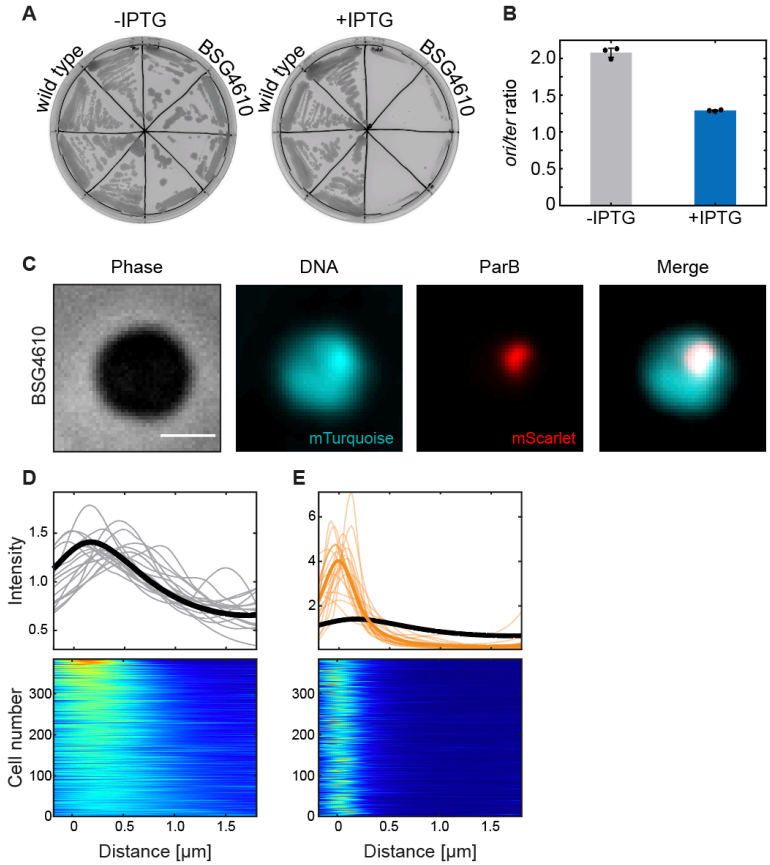


Figure S6.11. Origin of replication localizes within a region of high DNA density. A) *Plating assay showing replication halt in the absence (left) or presence (right) of 2 mM IPTG.* ***B)*** *qPCR determination of ori:ter ratio in the strain BSG4610. Gray bar shows an untreated sample, and the blue bar shows a sample treated with 2 mM IPTG for 2.5 h. Black dots represent and average value of a technical triplicate, for each biological triplicate. Both conditions were done in biological triplicates with technical triplicates for each of the colonies. Error bars represent a standard deviation from three biological triplicates.* ***C)*** *An example of a BSG4610 cell after treatment with lysozyme (400 µg/ml) for 30 min. Scale bar = 1 µm.* ***D)*** *Top - DNA intensity along the contour of the chromosome. Black line shows the average normalized intensity obtained from all cells (N= 384). Gray lines display individual examples. The position of the ParB focus is set as the 0 µm position. Bottom - Corresponding density plots along the chromosome in all individual cells. Results were pooled from biological duplicates.* ***E)*** *Same as in B for ParB-mScarlet signal. Thick orange line represents the averaged signal from all cells, while the thin orange lines represent arbitrarily chosen signals from individual cells.*

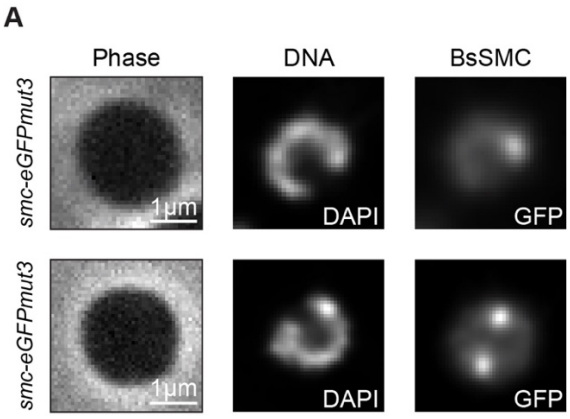


Figure S6.12. BsSMC proteins localize along the contour of the crescent shape and form fluorescent foci along it. A) *Phase and fluorescence images of BSG4612 strain (see Table S1) containing P_{lac}-sirA and BsSMC-eGFPmut3 label. Top: example with a single BsSMC fowcus close to the tip of the crescent chromosome. Bottom: example with multiple BsSMC foci.*

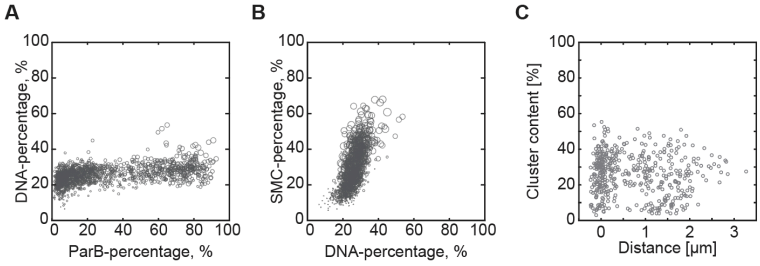


Figure S6.13. SMC proteins correlate with higher amount of DNA present. A) *DNA amount within the primary cluster in relation to ParB intensity.* ***B)*** *SMC amount in relation to ParB intensity.* ***C)*** *Local DNA content within secondary clusters in relation to secondary SMC clusters. Zero position represents the position of the secondary SMC cluster. Related to Fig. 6.3G.*

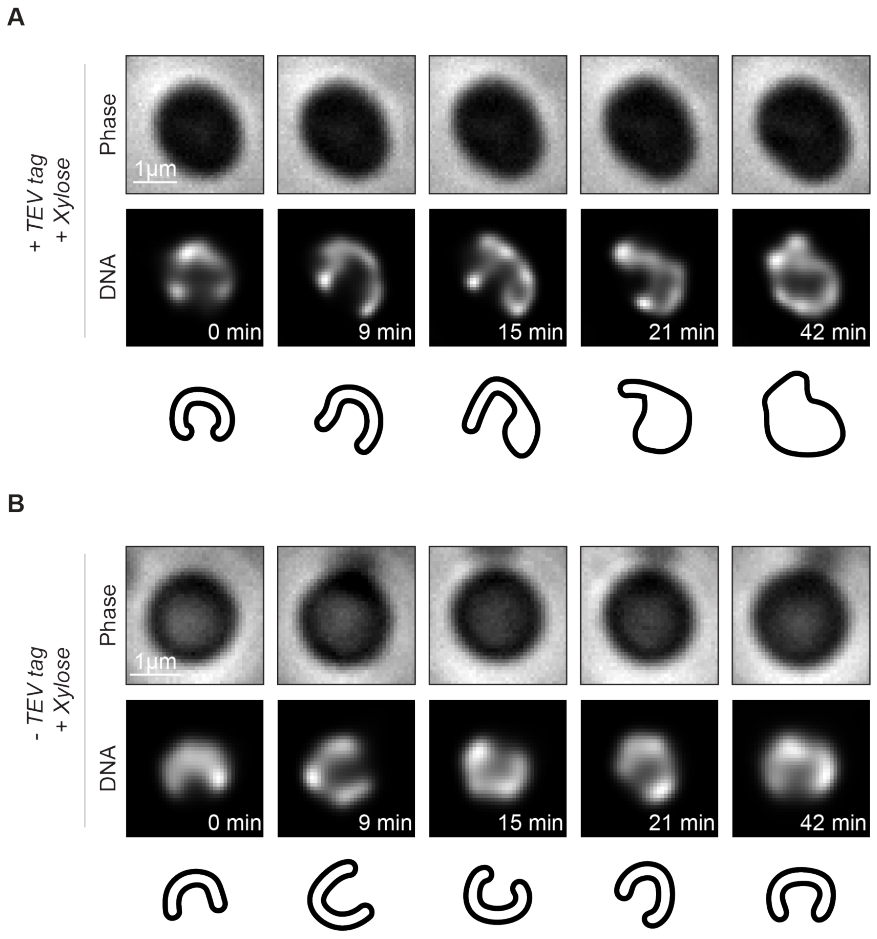


Figure S6.14. Real-time imaging of BsSMC protein knock-down via xylose-expressible TEV protease shows a reshaping of the chromosome which loses its crescent shape. A) *Timelapse imaging ofa single B. subtilis* ***chromosome*** *in strain BSG219, containing the ScpA-TEV3 in presence of xylose-expressed wTEV protease (0.5% xylose). Schematic representation of chromosome shapes is represented below.* ***B)*** *Control experiment showing timelapse images under the same conditions as in A) but for strain BSG217 that does not contain the TEV tag and TEV protease.*

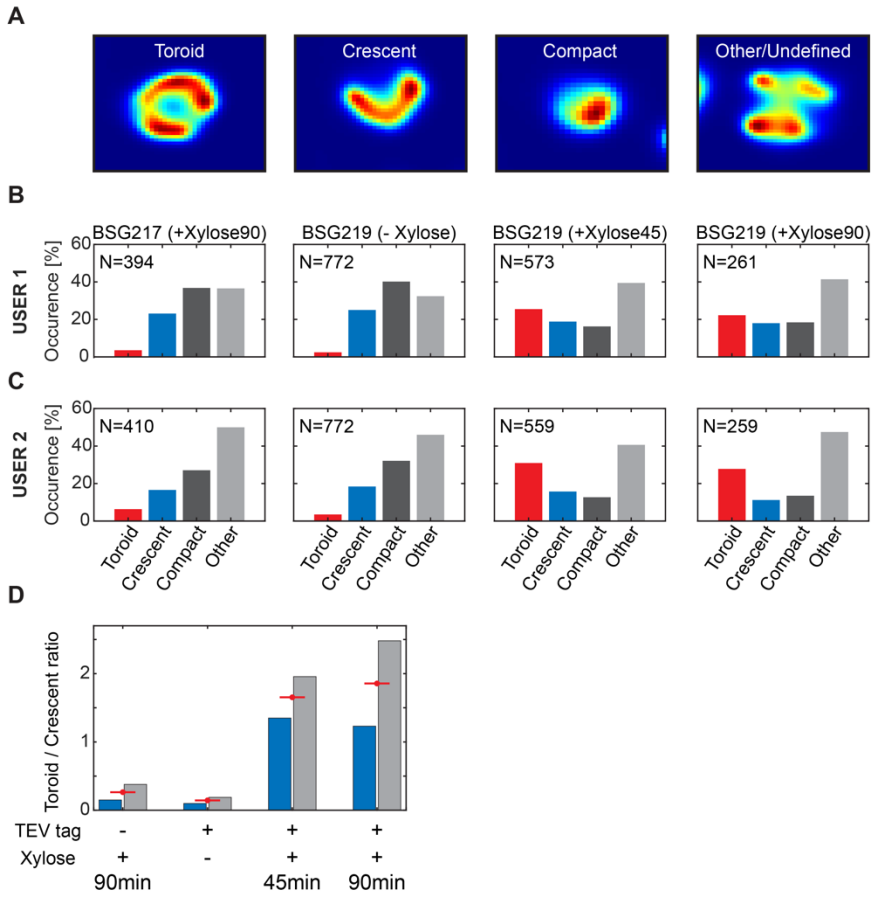


Figure S6.15. Identification of chromosome shapes under SMC knock-down conditions. ***A)*** *Example images representing four chromosome categories that were presented to two independent users for blinded identification (see Methods for detailed description).* ***B)*** *Distribution of four selected categories over different samples (shown on top) for user 1 (MT).* ***C)*** *Same for user 2 (JK).* ***D)*** *Ratio of torus-shaped to crescent-shaped chromosomes in all samples. Blue and grey bars represent the two users; mean values of the two users are represented by the red lines. Related to Fig 6.4.*

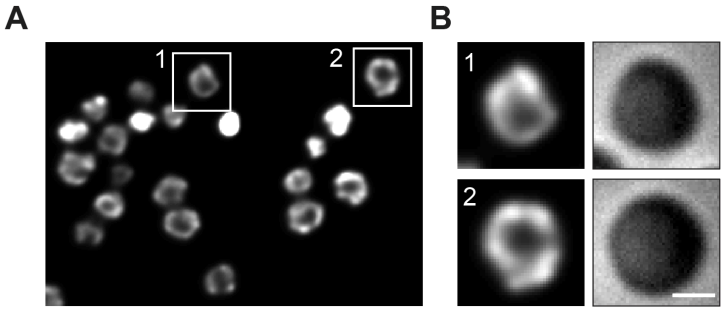


Figure S6.16. Chromosomes adopt a toroidal shape without chromosome arm-zipping in the absence of ParB protein. ***A)*** *Representative image of BSG5503 (containing ΔparB mutation) strain after replication halt using IPTG (2 mM) for 2.5h.* ***B)*** *Zoomed regions from A) showing high-resolution images of toroidal chromosomes in the absence of parB locus. Scale bar = 1 µm.*

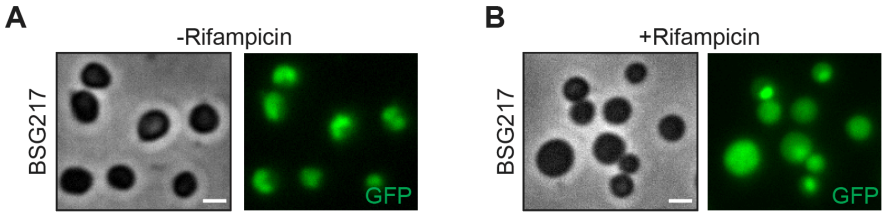


Figure S17. Transcription maintains the chromosome in a compact, crescent shape. ***A)*** *BSG217 (genotype) cells in the absence Rifampicin.* ***B)*** *Same cell line in the presence of 25µg/ml Rifampicin for 10 min. Scale bar = 2µm.*

6.6 References

1. Badrinarayanan, A., Le, T.B.K. & Laub, M.T. Bacterial Chromosome Organization and Segregation. *Annual Review of Cell and Developmental Biology* **31**, 171–199 (2015).

2. Dame, R.T., Noom, M.C. & Wuite, G.J.L. Bacterial chromatin organization by H-NS protein unravelled using dual DNA manipulation. *Nature* **444**, 387–390 (2006).

3. Wang, X., Llopis, P.M. & Rudner, D.Z. Organization and segregation of bacterial chromosomes. *Nature Reviews Genetics* **14**, 191–203 (2013).

4. Dillon, S.C. & Dorman, C.J. Bacterial nucleoid-associated proteins, nucleoid structure and gene expression. *Nature Reviews Microbiology* **8**, 185-95 (2010).

5. Gray, W.T. et al. Nucleoid Size Scaling and Intracellular Organization of Translation across Bacteria. *Cell* **177**, 1632-1648 (2019).

6. Berlatzky, I.A., Rouvinski, A. & Ben-Yehuda, S. Spatial organization of a replicating bacterial chromosome. *Proceedings of the National Academy of Sciences of the United States of America* **105**, 14136-14140 (2008).

7. Marbouty, M. et al. Condensin- and Replication-Mediated Bacterial Chromosome Folding and Origin Condensation Revealed by Hi-C and Super-resolution Imaging. *Molecular Cell* **59**, 588-602 (2015).

8. Le Gall, A., Cattoni, D.I. & Nollmann, M. Imaging of Bacterial Chromosome Organization by 3D Super-Resolution Microscopy. *Methods Mol Biol* **1624**, 253-268 (2017).

9. Wang, X., Llopis, P.M. & Rudner, D.Z. *Bacillus subtilis* chromosome organization oscillates between two distinct patterns. *Proceedings of the National Academy of Sciences of the United States of America* **111**, 12877-12882 (2014).

10. Hadizadeh Yazdi, N., Guet, C.C., Johnson, R.C. & Marko, J.F. Variation of the folding and dynamics of the Escherichia coli chromosome with growth conditions. *Molecular Microbiology* **86**, 1318-33 (2012).

11. Fisher, J.K. et al. Four-dimensional imaging of E. coli nucleoid organization and dynamics in living cells. *Cell* **153**, 882-95 (2013).

12. Spahn, C., Endesfelder, U. & Heilemann, M. Super-resolution imaging of Escherichia coli nucleoids reveals highly structured and asymmetric segregation during fast growth. *Journal of Structural Biology* **185**, 243-9 (2014).

13. Spahn, C.K. et al. A toolbox for multiplexed super-resolution imaging of the E. coli nucleoid and membrane using novel PAINT labels. *Scientific Reports* **8**, 14768 (2018).

14. Mäkelä, J. & Sherratt, D.J. Organization of the Escherichia coli Chromosome by a MukBEF Axial Core. *Molecular Cell* **78**, 250-260.e5 (2020).

15. Wu, F. et al. Direct imaging of the circular chromosome in a live bacterium. *Nature Communications* **10**, 2194 (2019).

16. Dekker, J., Rippe, K., Dekker, M. & Kleckner, N. Capturing chromosome conformation. *Science* **295**, 1306-11 (2002).

17. Simonis, M. et al. Nuclear organization of active and inactive chromatin domains uncovered by chromosome conformation capture-on-chip (4C). *Nature Genetics* **38**, 1348-54 (2006).

18. Dostie, J. et al. Chromosome Conformation Capture Carbon Copy (5C): A massively parallel solution for mapping interactions between genomic elements. *Genome Research* **16**, 1299-309 (2006).

19. Cagliero, C., Grand, R.S., Jones, M.B., Jin, D.J. & O'Sullivan, J.M. Genome conformation capture reveals that the Escherichia coli chromosome is organized by replication and transcription. *Nucleic Acids Research* **41**, 6058–6071 (2013).

20. Le, T.B.K., Imakaev, M.V., Mirny, L.A. & Laub, M.T. High-resolution mapping of the spatial organization of a bacterial chromosome. *Science* **342**, 731-4 (2013).

21. Lieberman-Aiden, E. et al. Comprehensive mapping of long-range interactions reveals folding principles of the human genome. *Science* **326**, 289-93 (2009).

22. Lioy, V.S. et al. Multiscale Structuring of the E. coli Chromosome by Nucleoid-Associated and Condensin Proteins. *Cell* **172**, 771-783.e18 (2018).

23. Wang, X., Brandão, H.B., Le, T.B.K., Laub, M.T. & Rudner, D.Z. Bacillus subtilis SMC complexes juxtapose chromosome arms as they travel from origin to terminus. *Science* **355**, 524-527 (2017).

24. Wang, X. et al. Condensin promotes the juxtaposition of dna flanking its loading site in Bacillus subtilis. *Genes and Development* **29**, 1661-1675 (2015).

25. Trussart, M. et al. Defined chromosome structure in the genome-reduced bacterium Mycoplasma pneumoniae. *Nature Communications* **8**, 14665 (2017).

26. Ren, Z. et al. Conformation and dynamic interactions of the multipartite genome in *Agrobacterium tumefaciens*. *Proceedings of the National Academy of Sciences of the United States of America* **119**, e2115854119 (2022).

27. Lioy, V.S., Junier, I., Lagage, V., Vallet, I. & Boccard, F. Distinct Activities of Bacterial Condensins for Chromosome Management in Pseudomonas aeruginosa. *Cell Reports* **33**, 108344 (2020).

28. Böhm, K. et al. Chromosome organization by a conserved condensin-ParB system in the actinobacterium Corynebacterium glutamicum. *Nature Communications* **11**, 1485 (2020).

29. Japaridze, A., Gogou, C., Kerssemakers, J.W.J., Nguyen, H.M. & Dekker, C. Direct observation of independently moving replisomes in Escherichia coli. *Nature Communications* **11**, 3109 (2020).

30. Karczmarek, A. et al. DNA and origin region segregation are not affected by the transition from rod to sphere after inhibition of Escherichia coli MreB by A22. *Molecular Microbiology* **65**, 51-63 (2007).

31. Japaridze, A. et al. MukBEF-dependent chromosomal organization in widened Escherichia coli. *Frontiers in Microbiology* **14**, 1107093 (2023).

32. Wang, X. & Sherratt, D.J. Independent segregation of the two arms of the Escherichia coli ori region requires neither RNA synthesis nor MreB dynamics. *Journal of Bacteriology* **192**, 6143–53 (2010).

33. Chen, F., Tillberg, P.W. & Boyden, E.S. Expansion microscopy. *Science* **347**, 543-548 (2015).

34. Chen, F. et al. Nanoscale imaging of RNA with expansion microscopy. *Nature Methods* **13**, 679–684 (2016).

35. Lim, Y. et al. Mechanically resolved imaging of bacteria using expansion microscopy. *PLoS Biology* **17**, e3000268 (2019).

36. Errington, J., Mickiewicz, K., Kawai, Y. & Wu, L.J. L-form bacteria, chronic diseases and the origins of life. *Philosophical Transactions of the Royal Society B: Biological Sciences* **371**, 20150494 (2016).

37. Leaver, M., Domínguez-Cuevas, P., Coxhead, J.M., Daniel, R.A. & Errington, J. Life without a wall or division machine in *Bacillus subtilis*. *Nature* **457**, 849–853 (2009).

38. Kawai, Y. et al. Crucial role for central carbon metabolism in the bacterial L-form switch and killing by β-lactam antibiotics. *Nature Microbiology* **4**, 1716-26 (2019).

39. Callister, H., Le Mesurier, S. & Wake, R.G. Initiation of deoxyribonucleic acid replication in germinating spores of Bacillus subtilis 168 carrying the dnaB (Ts)134 mutation. *Journal of Bacteriology* **130**, 1030-37 (1977).

40. Karamata, D. & Gross, J.D. Isolation and genetic analysis of temperature-sensitive mutants of B. subtilis defective in DNA synthesis. *Mol Gen Genet* **108**, 277-87 (1970).

41. Bruand, C., Farache, M., McGovern, S., Ehrlich, S.D. & Polard, P. DnaB, DnaD and DnaI proteins are components of the Bacillus subtilis replication restart primosome. *Molecular Microbiology* **42**, 245-55 (2001).

42. Jameson, K.H. & Wilkinson, A.J. Control of Initiation of DNA Replication in Bacillus subtilis and Escherichia coli. *Genes (Basel)* **8**, 22 (2017).

43. Christodoulou, E. & Vorgias, C.E. The thermostability of DNA-binding protein HU from mesophilic, thermophilic, and extreme thermophilic bacteria. *Extremophiles* **6**, 21-31 (2002).

44. Rahn-Lee, L., Gorbatyuk, B., Skovgaard, O. & Losick, R. The conserved sporulation protein YneE inhibits DNA replication in *Bacillus subtilis*. *Journal of Bacteriology* **191**, 3736–3739 (2009).

45. Wagner, J.K., Marquis, K.A. & Rudner, D.Z. SirA enforces diploidy by inhibiting the replication initiator DnaA durina snore formation in Bacillus subtilis. *Molecular Microbiology* **73**, 963-74 (2009).

46. Köhler, P. & Marahiel, M.A. Mutational analysis of the nucleoid-associated protein HBsu of Bacillus subtillus. *Molecular and General Genetics* **260**, 487-91 (1998).

47. Micka, B. & Marahiel, M.A. The DNA-binding protein HBsu is essential for normal growth and development in Bacillus subtilis. *Biochimie* **74**, 641-50 (1992).

48. Bakshi, S. et al. Nonperturbative imaging of nucleoid morphology in live bacterial cells during an antimicrobial peptide attack. *Applied and Environmental Microbiology* **80**, 4977-86 (2014).

49. Lin, D.C.H. & Grossman, A.D. Identification and characterization of a bacterial chromosome partitioning site. *Cell* **92**, 675–685 (1998).

50. Broedersz, C.P. et al. Condensation and localization of the partitioning protein ParB on the bacterial chromosome. *Proceedings of the National Academy of Sciences of the United States of America* **111**, 8809-8814 (2014).

51. Murray, H., Ferreira, H. & Errington, J. The bacterial chromosome segregation protein Spo0J spreads along DNA from parS nucleation sites. *Molecular Microbiology* **61**, 1352-61 (2006).

52. Gruber, S. & Errington, J. Recruitment of Condensin to Replication Origin Regions by ParB/SpoOJ Promotes Chromosome Segregation in B. subtilis. *Cell* **137**, 685-96 (2009).

53. Lewis, P.J. & Errington, J. Direct evidence for active segregation of oriC regions of the Bacillus subtilis chromosome and co-localization with the SpoOJ partitioning protein. *Molecular Microbiology* **25**, 945-54 (1997).

54. Sullivan, N.L., Marquis, K.A. & Rudner, D.Z. Recruitment of SMC by ParB-parS Organizes the Origin Region and Promotes Efficient Chromosome Segregation. *Cell* **137**, 697–707 (2009).

55. Teleman, A.A., Graumann, P.L., Lin, D.C.H., Grossman, A.D. & Losick, R. Chromosome arrangement within a bacterium. *Current Biology* **8**, 1102-9 (1998).

56. Antar, H. et al. Relief of ParB autoinhibition by parS DNA catalysis and ParB recycling by CTP hydrolysis promote bacterial centromere assembly. *Science Advances* **7**, eabj2854 (2021).

57. Glazer, A.N. & Rye, H.S. Stable dye-DNA intercalation complexes as reagents for high-sensitivity fluorescence detection. *Nature* **359**, 859-61 (1992).

58. Yatskevich, S., Rhodes, J. & Nasmyth, K. Organization of Chromosomal DNA by SMC Complexes. *Annual Review of Genetics* **53**, 445-482 (2019).

59. Bock, F.P., Liu, H.W., Anchimiuk, A., Diebold-Durand, M.-L. & Gruber, S. A joint-ParB interface promotes Smc DNA recruitment. *Cell reports* **40**, 111273 (2022).

60. Guilhas, B. et al. ATP-Driven Separation of Liquid Phase Condensates in Bacteria. *Molecular Cell* **79**, 293–303 (2019).

61. Karaboja, X. et al. XerD unloads bacterial SMC complexes at the replication terminus. *Molecular Cell* **81**, 756-766.e8 (2021).

62. Minnen, A., Attaiech, L., Thon, M., Gruber, S. & Veening, J.W. SMC is recruited to oriC by ParB and promotes chromosome segregation in Streptococcus pneumoniae. *Molecular Microbiology* **81**, 676-88 (2011).

63. Gruber, S. et al. Interlinked sister chromosomes arise in the absence of condensin during fast replication in B. subtilis. *Current Biology* **24**, 293-8 (2014).

64. Mascarenhas, J., Soppa, J., Strunnikov, A.V. & Graumann, P.L. Cell cycle-dependent localization of two novel prokaryotic chromosome segregation and condensation proteins in Bacillus subtilis that interact with SMC protein. *EMBO Journal* **21**, 3108–3118 (2002).

65. Bignaud, A. et al. Transcription-induced domains form the elementary constraining building blocks of bacterial chromosomes. *Nature Structural & Molecular Biology* (2024).

66. Tran, N.T., Laub, M.T. & Le, T.B.K. SMC Progressively Aligns Chromosomal Arms in Caulobacter crescentus but Is Antagonized by Convergent Transcription. *Cell Reports* **20**, 2057-2071 (2017).

67. Cockram, C., Thierry, A., Gorlas, A., Lestini, R. & Koszul, R. Euryarchaeal genomes are folded into SMC-dependent loops and domains, but lack transcription-mediated compartmentalization. *Molecular Cell* **81**, 459-472 e10 (2021).

68. Rybenkov, V.V., Herrera, V., Petrushenko, Z.M. & Zhao, H. MukBEF, a chromosomal organizer. *J Mol Microbiol Biotechnol* **24**, 371-83 (2014).

69. Funnell, B.E. ParB partition proteins: Complex formation and spreading at bacterial and plasmid centromeres. *Frontiers in Molecular Biosciences* **3**, 44 (2016).

70. Song, D., Rodrigues, K., Graham, T.G.W. & Loparo, J.J. A network of cis and trans interactions is required for ParB spreading. *Nucleic Acids Research* **45**, 7106-7117 (2017).

71. Kunst, F. et al. The complete genome sequence of the gram-positive bacterium *Bacillus subtilis*. *Nature* **390**, 249-56 (1997).

72. Jun, S. & Mulder, B. Entropy-driven spatial organization of highly confined polymers: Lessons for the bacterial chromosome. *Proceedings of the National Academy of Sciences of the United States of America* **103**, 12388-93 (2006).

73. Junier, I., Boccard, F. & Espéli, O. Polymer modeling of the E. coli genome reveals the involvement of locus positioning and macrodomain structuring for the control of chromosome conformation and segregation. *Nucleic Acids Research* **42**, 1461-73 (2014).

74. Wang, X., Tang, O.W., Riley, E.P. & Rudner, D.Z. The SMC condensin complex is required for origin segregation in Bacillus subtilis. *Current Biology* **24**, 287-92 (2014).

75. Wilhelm, L. et al. SMC condensin entraps chromosomal DNA by an ATP hydrolysis dependent loading mechanism in Bacillus subtilis. *eLife* **4**, e06659 (2015).

76. Anchimiuk, A. et al. A low Smc flux avoids collisions and facilitates chromosome organization in Bacillus subtilis. *eLife* **10**, e65467 (2021).

77. Brandão, H.B., Ren, Z., Karaboja, X., Mirny, L.A. & Wang, X. DNA-loop-extruding SMC complexes can traverse one another in vivo. *Nat Struct Mol Biol* **28**, 642-651 (2021).

78. Diebold-Durand, M.L., Bürmann, F. & Gruber, S. High-throughput allelic replacement screening in bacillus subtilis. *Methods Mol Biol* **2004**, 49-61 (2019).

79. Paintdakhi, A. et al. Oufti: An integrated software package for high-accuracy, high-throughput quantitative microscopy analysis. *Molecular Microbiology* **99**, 767-77 (2016).

80. Kaljević, J. et al. Chromosome choreography during the non-binary cell cycle of a predatory bacterium. *Current Biology* **31**, 3707-3720.e5 (2021).

81. Schindelin, J. et al. Fiji: An open-source platform for biological-image analysis. *Nature Methods* **9**, 676-82 (2012).

82. Ball, G. et al. SIMcheck: A toolbox for successful super-resolution structured illumination microscopy. *Scientific Reports* **5**, 15915 (2015).

6

7

FUTURE PERSPECTIVES AND OUTLOOK

In this chapter, I cover a few potential future avenues for studying the ParB mechanism as well as extending this to other major players in chromosome organization and segregation biology – ParA and SMC.

This thesis covered general principles of chromosome organization and segregation in the bacterium *B. subtilis* (Chapters 1 and 2), and extended further into the novel findings within ParB-mediated DNA organization on a single-molecule level (Chapter 4 and 5) as well as the macroscale chromosome organization in live cells (Chapter 6). These findings open up new avenues for deeper exploration of DNA organization within the same systems, and extending them to other organisms to gain a comprehensive overview of the mechanism involved in chromosome organization.

7.1 Mechanistic insights of ParB closure and dissociation using FRET

In Chapter 4, and 5, ParB was shown to experience transient ParB-ParB interactions likely via N-terminal part of the protein. This ensures efficient spreading in the presence of DNA-roadblocks (Chapter 4) and dynamic DNA condensation (Chapter 5), both of which are important for ParB functioning *in vivo*. In our proposed models, both ParB-ParB recruitment and ParB-mediated DNA condensation require a hypothetical protein conformation whereby ParB dimer is bound to the DNA via non-specific interactions using C-termini of both monomers. While previous studies suggested that upon CTP hydrolysis and clamp opening, ParB dimers would immediately diffuse away from the DNA[1,2], in Chapter 4 we suggest that ParB proteins reside on the DNA for an additional time in a state susceptible for *in trans* interactions.

This conformational change and dissociation timing cannot be efficiently explored in bulk assays or in *in vivo* studies. Since our hypothesized conformational state requires a dynamic conformational change of clamp opening at the N-terminus, the single-molecule technique FRET (Förster resonance energy transfer) is perfectly suitable for exploring such precise conformational changes. As FRET relies upon two fluorescent dyes that experience energy transfer prior to fluorescence [3], this technique could be incorporated into the assays covered in Chapters 3, 4, and 5. A powerful combination of FRET with the single-molecule fluorescence assay used throughout this thesis could simultaneously provide information about the ParB loading dynamics, ParB diffusion and the precise timing and conformational changes during ParB opening and dissociation. This would deepen the knowledge of the precise mechanistic events required for ParB-ParB *in trans* interactions that seem to underlie important ParB behaviors – recruitment and partition complex formation.

7.2 ParB interaction and DNA supercoiling

Chapter 3 of this thesis extensively covered the biophysics of ligand interactions with supercoiled DNA molecules. Undoubtedly, overtwisting and undertwisting the DNA molecule to induce supercoiling will affect small organic ligands and protein binding to the DNA. Notbaly, bacteria perpetually maintain their chromosomal DNA largely in a

negatively supercoiled state[4] (Chapter 1). To add to this, RNA polymerases continuously produce different levels of supercoiling in the vicinity of highly transcribed genes[5]. These notions point to the fact that within the cellular environment of bacteria, proteins (most importantly ParB), could have different binding dynamics and effects on the DNA.

ParB proteins form a partition complex by condensing a local region around the *parS* sites[6,7] (Chapters 1, 2, 4, 5). These sites are typically found near the origin region[8] which also harbors many highly transcribed genes (rRNA, tRNA, ribosomal proteins, etc)[9] which would locally induce the regions of high supercoiling. Studying the interaction between ParB and supercoiled DNA would bring us closer to understanding the effects of this protein on the DNA within its native region. The techniques shown in Chapter 3, 4, and 5 are well suited to the potential study of ParB effects on the DNA organization in the presence of DNA supercoiling. Reciprocally, the presence of supercoiling may hinder or facilitate ParB binding much alike organic ligands (Chapter 3) which would be of great interest to the field.

7.3 *In vitro* reconstitution of the ParABS system

Most previous single-molecule studies focused on isolated systems where single components are investigated (e.g. Chapter 2). Extending the study to comprehensively understand the interactions within the ParABS system, would be of great importance to the deep understanding of chromosome segregation in bacteria.

Chapters 4 and 5, cover the detailed mechanisms of ParB interaction with the DNA and with itself (ParB-ParB interactions). Extending this system to include ParB's most prominent interaction partner ParA, could offer new insight into the ParABS system functioning as a whole. While some previous studies tried to study both proteins simultaneously[10-12], new insights into the necessary nucleotide co-factors of ParA and ParB (ATP and CTP, respectively) could change the outcomes of the experiments. Furthermore studying both components of the ParABS system in the single-molecule stretching assay could bring new insights into the changing dynamics and forces exerted by these proteins on the DNA.

7.4 *In vitro* reconstitution of bacterial SMC loading onto the DNA

The most prominent chromosome organizers in all life forms are the SMC proteins[13]. In bacteria, they significantly contribute to origin segregation and DNA compaction, as well as maintaining the chromosome in its native arrangement[14-16] (Chapter 6). Interestingly, ParB proteins are the main interaction partners of SMC proteins in bacteria[17]. More specifically they actively load SMC proteins near the origin of replication which significantly increases the chromosome segregation fidelity[18,19].

The single-molecule assays shown in Chapters 3, 4, and 5, could be extended to include SMC proteins and observe their effect on the DNA. Similar assays have been used in other studies to in-detail investigate SMC proteins in eukaryotes. Similarly, Chapters 4 and 5 extensively cover different possibilities for ParB binding on the DNA (i.e., single proteins, large condensates, transiently looping DNA), which could have different effects on SMC loading. While eukaryotic SMC proteins have been shown to exhibit DNA cohesion and loop extrusion[20-22], no successful single-molecule study was realized so far on bacterial SMC proteins.

Future experiments combining single-molecule stretching assay (Chapter 2) with the *parS*-DNA could be the leading direction for the mechanism of bacterial SMC proteins. The mechanism of SMC loading and its specific action on the DNA molecule could be studied using a similar loading strategy for ParB protein (Chapters 4 and 5), the main recruiter of bacterial SMC. This future direction would elucidate whether loop extrusion is in fact an ancient mechanism, which is still essential for genome organization in all life domains.

Taken together, this thesis provides an excellent baseline for extending the study of bacterial SMC proteins *in vivo*.

7.5 *In vivo* investigation of SMC dynamics on bacterial chromosomes

Chapter 6 of this thesis covers the chromosome organization in the model bacterium *B. subtilis*. It shows the native shape of the bacterial chromosome in the absence of confinement, and it details how this shape is achieved only in the presence of functional ParB and SMC proteins.

SMC proteins were shown to progressively "zip" chromosome arms in both *B. subtilis*[23] and *C. crescentus*[24], whereby they load at the chromosome origin and juxtapose chromosomal arms until the chromosome terminus. These studies, and many others following them, were performed using Hi-C (chromosome capture) technique whereby a population of cells need to be fixed using invasive crosslinking agents that can affect the dynamic structure of the chromosome. Live-cell observations were impossible due to the very nature of the fixation techniques.

The gentle cell expansion technique, developed in Chapter 6, allows the chromosome to reside for a long time in its native state, while allowing the observation of the chromosome structure dynamics. Extending this study to real-time imaging of the progressive arm-zipping by SMC proteins could provide exciting insights into the mechanism of SMC proteins' action on the bacterial chromosome.

7.6 Final outlook

Given the nature of this thesis – dealing with *in silico* (Chapters 4, 5)*, in vitro* (Chapters 3, 4, and 5) and *in vivo* (Chapter 6) approaches to studying the essential machinery involved in chromosome organization in bacteria, new studies can be designed to complement each other and obtain a full, comprehensive picture of how ParABS system, SMC proteins and many others contribute to the beautiful processes of bacterial life.

7.7 References

1. Osorio-Valeriano, M. et al. The CTPase activity of ParB determines the size and dynamics of prokaryotic DNA partition complexes. *Molecular Cell* **81:3992–4007**(2021).

2. Antar, H. et al. Relief of ParB autoinhibition by parS DNA catalysis and ParB recycling by CTP hydrolysis promote bacterial centromere assembly. *Science Advances* **7**, eabj2854 (2021).

3. Ha, T. et al. Probing the interaction between two single molecules: fluorescence resonance energy transfer between a single donor and a single acceptor. *Proceedings of the National Academy of Sciences* **93**, 6264-6268 (1996).

4. Dillon, S.C. & Dorman, C.J. Bacterial nucleoid-associated proteins, nucleoid structure and gene expression. *Nat Rev Microbiol* **8**, 185-95 (2010).

5. Liu, L.F. & Wang, J.C. Supercoiling of the DNA template during transcription. *Proc Natl Acad Sci U S A* **84**, 7024-7 (1987).

6. Graham, T.G.W. et al. ParB spreading requires DNA bridging. *Genes and Development* **28:1228–1238**(2014).

7. Murray, H., Ferreira, H. & Errington, J. The bacterial chromosome segregation protein Spo0J spreads along DNA from parS nucleation sites. *Molecular Microbiology* **61**, 1352-61 (2006).

8. Breier, A.M. & Grossman, A.D. Whole-genome analysis of the chromosome partitioning and sporulation protein Spo0J (ParB) reveals spreading and origin-distal sites on the Bacillus subtilis chromosome. *Molecular Microbiology* **64:703-18**(2007).

9. Kunst, F. et al. The complete genome sequence of the gram-positive bacterium *Bacillus subtilis*. *Nature* **390**, 249-56 (1997).

10. Hu, L., Vecchiarelli, A.G., Mizuuchi, K., Neuman, K.C. & Liu, J. Directed and persistent movement arises from mechanochemistry of the ParA/ParB system. *Proceedings of the National Academy of Sciences of the United States of America* **112**(2015).

11. Vecchiarelli, A.G. et al. ATP control of dynamic P1 ParA-DNA interactions: a key role for the nucleoid in plasmid partition. *Mol Microbiol* **78**, 78-91 (2010).

12. Vecchiarelli, A.G., Neuman, K.C. & Mizuuchi, K. A propagating ATPase gradient drives transport of surface-confined cellular cargo. *Proceedings of the National Academy of Sciences of the United States of America* **111**(2014).

13. Kim, E., Barth, R. & Dekker, C. Looping the Genome with SMC Complexes. *Annu Rev Biochem* **92**, 15-41 (2023).

14. Le, T.B., Imakaev, M.V., Mirny, L.A. & Laub, M.T. High-resolution mapping of the spatial organization of a bacterial chromosome. *Science* **342**, 731-4 (2013).

15. Wang, X. et al. Condensin promotes the juxtaposition of dna flanking its loading site in Bacillus subtilis. *Genes and Development* **29**, 1661-1675 (2015).

16. Marbouty, M. et al. Condensin- and Replication-Mediated Bacterial Chromosome Folding and Origin Condensation Revealed by Hi-C and Super-resolution Imaging. *Molecular Cell* **59**, 588-602 (2015).

17. Bock, F.P., Liu, H.W., Anchimiuk, A., Diebold-Durand, M.-L. & Gruber, S. A joint-ParB interface promotes Smc DNA recruitment. *Cell reports* **40**, 111273 (2022).

18. Gruber, S. & Errington, J. Recruitment of Condensin to Replication Origin Regions by ParB/SpoOJ Promotes Chromosome Segregation in B. subtilis. *Cell* **137**, 685-96 (2009).

19. Sullivan, N.L., Marquis, K.A. & Rudner, D.Z. Recruitment of SMC by ParB-parS Organizes the Origin Region and Promotes Efficient Chromosome Segregation. *Cell* **137**, 697–707 (2009).

20. Davidson, I.F. et al. DNA loop extrusion by human cohesin. *Science* **366**, 1338-1345 (2019).

21. Ganji, M. et al. Real-time imaging of DNA loop extrusion by condensin. *Science* **360:102-105**(2018).

22. Pradhan, B. et al. The Smc5/6 complex is a DNA loop-extruding motor. *Nature* **616:843-848**(2023).

23. Wang, X., Brandão, H.B., Le, T.B.K., Laub, M.T. & Rudner, D.Z. Bacillus subtilis SMC complexes juxtapose chromosome arms as they travel from origin to terminus. *Science* **355**, 524-527 (2017).

24. Tran, N.T., Laub, M.T. & Le, T.B.K. SMC Progressively Aligns Chromosomal Arms in Caulobacter crescentus but Is Antagonized by Convergent Transcription. *Cell Reports* **20**, 2057-2071 (2017).

SAMENVATTING

Dit proefschrift onderzoekt de mechanismen die ten grondslag liggen aan de chromosomale organisatie van bacteriën. Bacteriën worden gezien als de meest eenvoudige vorm van leven op onze planeet. Ze missen de interne cellulaire organisatie die aanwezig is in de andere domeinen (Archaea of Eukaryoten) en hebben vaak eenvoudigere levenscycli. In het laatste decennium hebben we steeds meer inzichten gekregen die erop wijzen dat bacteriën veel middelen toebedelen aan het precies organiseren van het genoom in hun cellen en het scheiden van de twee genomen na DNA replicatie.

In dit proefschrift heb ik de DNA organisatie en segregatiesystemen van het model organisme *Bacillus subtilis* bestudeerd. Ik ben deze uitdaging aangegaan vanuit zowel het *in vivo* aspect – het in beeld brengen van een levende bacterie, als het *in vitro* aspect – het observeren van geïsoleerde eiwitten en DNA moleculen. Deze holistische aanpak heeft me in staat gesteld om zo een dieper inzicht te krijgen in de eiwitten en de mechanismen die benodigd zijn voor de organisatie en segregatie van DNA.

Hoofdstuk 1 introduceert de algemene principes van de genoom organisatie en segregatie van bacteriën. Het benadrukt het belang voor bacteriën om hun genoom-informatie snel en efficiënt te organiseren, repliceren, en segregeren binnen iedere celcyclus.

Hoofdstuk 2 geeft de achtergrond van biologische en mechanistische inzichten over de manier waarop ParB eiwitten het genoom van bacteriën organiseren. Ten eerste beschrijft het in detail de mechanismen van hoe ParB eiwitten interacties aangaan binnen een bredere context – het ParABS systeem, om het bacteriële genoom te segregeren. Het duikt dieper in hoe ParB eiwitten zich op het DNA laden met behulp van een specifieke bindingsplaats – *parS*, en hoe dit ze in staat stelt om het partitiecomplex te initiëren. Hoewel eerdere *in vivo* studies een stevig fundament en een overvloed aan biologische vragen over het ParABS systeem teweeg hebben gebracht, hebben recente ontwikkelingen op het gebied van *in vitro* enkel-molecuulstudies ons in staat gesteld een meer gedetailleerd begrip te verkrijgen van hoe dit systeem functioneert. Wij beschrijven de krachtige inzichten in het mechanisme van ParB eiwitten die verkregen zijn met enkel-molecuultechnieken. Tenslotte geven we een vooruitzicht in hoe deze technieken gebruikt kunnen worden om nieuwe, nog onverkende ParB varianten te bestuderen, eiwitten die lijken op ParB en ParB interactiepartners, om een algemeen begrip te verkrijgen van ParABS systemen over bacteriële soorten.

Hoofdstuk 3 van dit proefschrift focust op DNA-intercalerende kleurstoffen die standaard worden gebruikt in het kleuren van DNA voor bulktesten, alsook op een enkel-molecuul uitstrektest die is gebaseerd op tweevoudig vastgebonden DNA moleculen die gekleurd zijn met fluorescente intercalerende kleurstoffen die door dit gehele proefschrift heen worden gebruikt (Hoofdstukken 3, 4, 5). We focussen op fluorescente intercalerende stoffen, die topologisch vastgezet DNA opdraaien en ons in staat stellen om direct te kwantificeren. In dit hoofdstuk presenteren we een kwantitatief model voor hoe de globale beperkingen die worden opgelegd door topologie de binding beïnvloeden. Aanvankelijk beschrijft ons model bulktesten die gebruikmaken van plasmiden met verschillende initiële typologieën, verschillende intercalatoren, en een breed scala aan concentraties van intercalerende stoffen. Vervolgens demonstreren we de topologie-afhankelijke binding in een enkel-molecuultest, waarin we directe observaties maken van de intercalatordichtheid van opgedraaide naar ontspannen DNA.

Hoofdstuk 4 van dit proefschrift onderzoekt het gedrag van ParB eiwitten op het niveau van enkele moleculen. We gebruikten een uitstrekproef die in detail beschreven is in hoofdstuk 2, met een DNA molecuul dat de bindingsplaats (*parS)* bevat die efficiënt ParB eiwitten laadt en verspreiding mogelijk maakt. Door eiwitten fluorescent te labellen, konden we enkele ParB eiwitten observeren die binden en diffunderen in één dimensie. Een belangrijke vraag in het veld was: hoe kunnen ParB eiwitten diffunderen over grote afstanden in de aanwezigheid van een groot aantal aan DNA gebonden eiwitten? We bestudeerden dit door middel van een sterk gebonden DNA wegversperring die ParB diffusie eroverheen niet toestaat. Tot onze verrassing observeerden we dat ParB eiwitten bij hele kleine krachten en genoeg DNA flexibiliteit nieuwe ParB eiwitten kunnen recruteren vanuit de oplossing naar het DNA molecuul. Dit proces, genaamd ParB-ParB recrutering, gebeurt *in trans* over de DNA wegversperring heen, waarbij dit het mogelijk maakt dat eiwitten zich verspreiden over het gehele DNA molecuul. Dit hoofdstuk bevat ook verdere mechanistische details van dit proces en de afhankelijkheid van de aanwezigheid van CTP nucleotiden. Tenslotte bevat het Moleculaire Dynamica simulaties van dit proces (door het D. Michieletto lab) die bevestigen dat ParB eiwitten zich gezamenlijk kunnen verspreiden over het DNA zelfs in de aanwezigheid van wegversperringen.

In **Hoofdstuk 5** doken we dieper in de formatie van het partitiecomplex (ParB-DNA complex). Hoewel het een onderwerp was van menig hypothesen, zijn eerste stappen en de structuur van het partitiecomplex in bacteriën tot nog toe niet in detail beschreven. We bestudeerden dit met behulp van drie enkel-molecuultechnieken die omschreven zijn in Hoofdstuk 2. In de aanwezigheid van een grotere hoeveelheid eiwit, observeerden we dat DNA dynamisch condenseert en dat het complexen van nucleoproteïnen vormt. We

konden de grootte van het partitiecomplex en de krachten die het ParB-DNA complex uitoefent op het DNA molecuul meten. Dit hoofdstuk beschrijft de initiële stappen van het DNA condensatiefenomeen verder, waarbij we beargumenteren dat het ontstaat door de vorming van een vluchtige lus tussen twee ParB dimeren die een interactie aangaan *in trans*. We breidden onze studie uit om de veranderingen in conformaties te onderzoeken die benodigd zijn voor aan DNA-gebonden ParB eiwitten voor succesvolle DNA condensatie. Onze resultaten wijzen op de noodzaak van ParB klemopening waarbij het N-terminale domein van de monomeren van verschillende dimeren interacties aangaan *in trans* om DNA condensatie te initiëren. We breidden onze studie verder uit door de mogelijke conformaties van ParB dimeer-dimeer interacties *in trans* te bestuderen door middel van Moleculaire Dynamica simulaties (D. Michieletto lab). Deze simulaties toonden aan dat ParB het DNA zo efficiënt condenseert door de mogelijkheid om oligomeren te vormen tussen meerdere dimeren. Tenslotte pakt Hoofdstuk 5 de al lang bestaande vraag aan van genrepressie in de aanwezigheid van ParB moleculen in de omgeving. Hier observeerden we een zeer gering tot nihil effect van de aanwezigheid van ParB op de snelheid en de processiviteit van een actief transcriberende RNA polymerase. Deze inzichten leidden ons ertoe om een model voor te stellen van ParB verspreiding en vluchtige overbrugging in Hoofdstuk 5, dat oudere modellen en nieuwe inzichten combineert.

Hoofdstuk 6 van dit proefschrift onderzoekt de effecten van ParB en zijn interactiepartner – het SMC eiwit, op de chromosomale organisatie van *Bacillus subtilis*. Dit hoofdstuk begint met een nieuwe benadering om het bacteriële chromosoom in beeld te brengen zonder opsluitinhg in het celvolume. We waren in staat om de natuurlijke structuur van het *B. subtilis* chromosoom te observeren, dat een halvemaanvorm aanneemt. De lokalisatie van de ParB eiwitten, SMC eiwitten, en de replicatie terminus gaven ons inzichten in de oriëntatie van de chromosomale loci in de halvemaanvorm. Dit hoofdstuk bespreekt ook een extensieve kwantificatie van de DNA condensatie in de chromosomale origine *in vivo* – nabij de ParB en SMC signalen. We gebruiken verscheidene bacteriële stammen en mutanten om aan te tonen dat specifieke degradatie van SMC eiwitten of deletie van ParB eiwitten dervoor zorgen dat de natuurlijke halvemaanvorm niet wordt gevormd en dat de chromosomen een torusvorm aannemen.

Hoofdstuk 7 vat de kennis vergaard in dit proefschrift kort samen en geeft een vooruitzicht op toekomstige projecten op het gebied van zowel *in vitro* als *in vivo* studies van ParB, SMC, en hun effecten op chromosomale organisatie.

SUMMARY

This thesis explores the mechanisms that underlie chromosome organization in bacteria. Bacteria are considered amongst the simplest living organisms on our planet. They lack the cellular organization found in other domains of life (Archaea or Eukaryotics) and often have simpler life cycles. Over the past decade, we gained increasing knowledge pointing to the fact that bacteria allocate a lot of resources to precisely organize their genome within the cell, and to segregate two genomes after DNA replication to daughter cells.

In this thesis, I investigated DNA organization and segregation systems in a model system bacterium *Bacillus subtilis*. I approached this feat both from the *in vivo* aspect – imaging in a live bacterium, and from the *in vitro* aspect – observing isolated proteins and DNA molecules. This holistic approach allowed me to gain deep insight into the proteins and mechanisms needed for DNA organization and segregation.

Chapter 1 covers the general principles of bacterial genome organization and segregation. It highlights the importance of bacteria to organize, replicate, and segregate their genomic information fast and efficiently within every division cycle.

Chapter 2 provides a detailed background of biological and mechanistic insights into the way ParB proteins organize bacterial genomes. First, it covers in detail the mechanism of how ParB proteins interact within a broader context – the ParABS system, to segregate the bacterial genome. Further, it delves deeper into how ParB proteins load on the DNA using a specific binding site – *parS*, and how this allows them to initiate the partition complex formation. While previous i*n vivo* studies provided a solid foundation and a plethora of biological questions about the ParABS system, recent developments in *in vitro* single-molecule studies allowed a detailed understanding of how this system functions. We cover the powerful insights into ParB protein mechanism obtained from single-molecule techniques. Finally, we provide a future outlook into how these techniques could be used to study novel, unexplored ParB variants, and ParB-like proteins and ParB interaction partners in order to gain a general understanding of ParABS systems across bacterial species.

Chapter 3 of this thesis focuses on DNA-intercalating dyes that are standardly used in DNA staining for bulk assays as well as a single-molecule stretching assay that was used throughout this thesis (Chapters 3, 4, 5) which is based on double-tethered DNA molecules stained with fluorescent intercalating dyes. We focus on fluorescent intercalators, which unwind topologically constrained DNA and enable direct

quantification via fluorescence detection. We present a quantitative model of how the global constraints introduced by DNA topology modulate binding. Initially, our model describes bulk experiments using plasmids with different starting topologies, different intercalators, and over a broad range of intercalator and DNA concentrations. Subsequently, we demonstrate supercoiling-dependent binding in a single-molecule assay, where we directly observe the different intercalator densities when going from supercoiled to nicked DNA.

Chapter 4 of this thesis investigates the behavior of ParB proteins on a single-molecule level. We used the stretching assay described in detail in Chapter 2, with a DNA molecule that contains the loading site (*parS)*, which can efficiently load ParB proteins and allow their spreading. By fluorescently labeling the proteins, we were able to observe single ParB proteins binding and diffusing in one dimension. An important question in the field was: how can ParB proteins diffuse over large distances in the presence of a high number of DNA-binding proteins in their native environment? We investigated this using a strongly bound DNA-roadblock, which does not allow ParB diffusion over it. Surprisingly, we observed that at very low forces, and sufficient DNA flexibility, ParB proteins can recruit new ParB proteins from the solution to the DNA molecule. This process termed ParB-ParB recruitment, can occur *in trans* across the DNA-roadblock, thus allowing the proteins to cooperatively spread over the entire DNA molecule. This chapter also includes further mechanistic details of this process and its dependence on the presence of CTP nucleotide. Finally, it includes Molecular Dynamics simulations of this process (by D. Michieletto lab) which confirms that ParB proteins can collectively spread over the DNA even in the presence of DNA-roadblocks.

In **Chapter 5,** we delved deeper into the formation of the ParB-DNA partition complex. While a subject of many hypotheses, the initial steps and structure of the partition complex in bacteria were not heretofore described in detail. We investigated this using three single-molecule techniques described in Chapter 2. In the presence of a high amount of protein, we observed that the DNA could dynamically condense and form a nucleoprotein complex. We could precisely measure the partition complex size and forces that ParB-DNA complex exerts on the DNA molecule. This chapter further covers the initial steps of the DNA condensation phenomenon, where we argue that it forms by transient loop formation between two ParB dimers interacting *in trans*. We extended our investigation to test the conformational changes required for DNA-bound ParB proteins for successful DNA condensation. Our results point to the necessity of ParB clamp opening where N-terminal domain of the monomers of different dimers interacts *in trans* to initiate DNA condensation. We extended our investigation further by testing possible conformations of *in trans* ParB dimer-dimer interactions using Molecular Dynamics

simulations (D. Michieletto lab). These simulations showed that ParB condenses the DNA so efficiently due to the ability to form oligomers between multiple dimers. Finally, chapter 5 tackles the long-standing question of gene repression in the presence of ParB molecules in the surroundings. Here we observed a very low to no effect of ParB presence on the speed or processivity of an actively transcribing RNA polymerase. These insights led us to propose a model of ParB spreading and transient bridging in Chapter 5, which combines the older models and newly acquired insights.

Chapter 6 of this thesis investigates the macroscale effects of ParB and its interaction partner, SMC protein, on the chromosome organization in *Bacillus subtilis*. This chapter starts with a novel approach to image the bacterial chromosome in bacteria of relaxed shape. We were able to observe the native structure of the *B. subtilis* chromosome, which adopts a crescent shape. Further localization of the ParB, SMC proteins, and replication terminus provided us with insight into the orientation of the chromosomal loci within the crescent shape. This chapter also covers an extensive quantification of the *in vivo* DNA condensation in the chromosome origin – proximal to ParB and SMC signals. We use different bacterial strains and mutants to show that the specific degradation of SMC proteins or deletion of ParB proteins prevents the natural crescent shape formation, and the chromosomes adopt a toroidal shape.

Chapter 7 briefly summarizes the knowledge gained from this thesis and provides an outlook and future projects on the topic of *in vitro* and *in vivo* studies of ParB, SMC, and its effects on chromosome organization..

ACKNOWLEDGEMENTS

In pursuit of questions, many hands have lifted me.
To those who helped me, thank you!

CURRICULUM VITAE

Miloš TIŠMA

20-12-1994 Born in Belgrade, Serbia

EDUCATION

2001-2009 Elementary School at OŠ "Ivo Andrić", Belgrade, Serbia

2009-2013 High School at IV Gimnazija, Belgrade, Serbia

2013-2017 B.Sc. in Biology
Univerzitet u Beogradu, Belgrade, Serbia

2017-2019 M.Sc. in Molecular Bioengineering
Technische Universität Dresden, Dresden, Germany

2019-2024 Ph.D. Bionanoscience
Technische Universiteit Delft, Delft, The Netherlands

AWARDS AND SCHOLARSHIPS

2014-2015 Student Scholarship by the City of Belgrade

2015-2017 State Scholarship for Exceptionally Gifted Scholars and Students

2016-2017 Scholarship of Foundation for Young Talents – Dositeja

2015-2017 Private Scholarship by "Promedia doo"

2017-2019 Go West-Scholarship (Haniel and Tschira Stiftungs)

2020 Dresden Excellence Award – Best MSc thesis in Dresden (year 2019)

2022 EMBO Poster prize – (EMBO BacNet22)

2023 Emerging Talents in Microbiology Award (Molecular Microbiology)

LIST OF PUBLICATIONS

1. Gonzalez A. M*, **Tišma M***, Analikwu B. T, Antar H, Gruber S, Dekker C. *DNA supercoiling enhances ParB-mediated DNA condensation.* (2024) in preparation.

2. **Tišma M**, Bock F. P, Kerssemakers J, Japaridze A, Gruber S, Dekker C. *Direct observation of a crescent-shape chromosome in Bacillus subtilis.* Nature Communications (2024), under review.

3. **Tišma M***, Kaljević J*, Gruber S, Le T, Dekker C. *Connecting the dots: key insights into the ParB protein for chromosome segregation from single-molecule studies*. FEMS Microbiology Reviews (2023).

4. Kolbeck P. J*, **Tišma M***, Analikwu B. T, Vanderlinden W, Dekker C, Lipfert J. *Supercoiling-dependent DNA binding: quantitative modeling and applications to bulk and single-molecule experiments*. Nucleic Acids Res, gkad1055 (2023).

5. **Tišma M**, Janissen R, Antar H, Martin-Gonzalez A, Barth R, Beekman T, van der Torre J, Michieletto D, Gruber S, Dekker C. *Dynamic ParB-DNA interactions initiate and maintain a partition condensate for bacterial chromosome segregation*. Nucleic Acids Res, gkad868 (2023)

6. **Tišma M**, Panoukidou M, Antar H, Soh YM, Barth R, Pradhan B, Barth A, van der Torre J, Michieletto D, Gruber S, Dekker C. *ParB proteins can bypass DNA-bound roadblocks via dimer-dimer recruitment*. Science Advances. eabn3299 (2022)

7. Schärfen L*, **Tišma M***, Schlierf M. *Fast, Simultaneous Tagging and Mutagenesis of Genes on Bacterial Chromosomes.* ACS Synthetic Biology 9(8):2203-2207 (2020)

8. Schärfen L, **Tišma M***, Hartmann A*, Schlierf M. *Direct visualization of four diffusive LexA states controlling SOS response strength during antibiotic treatment.* bioRxiv 2020.07.14.201889 (2020)

* These authors have contributed equally to the work